BASIC MAGNETIC FIELD CONFIGURATIONS FOR SOLAR FILAMENT CHANNELS AND FILAMENTS

Duncan H. Mackay

A Thesis Submitted for the Degree of PhD
at the
University of St Andrews

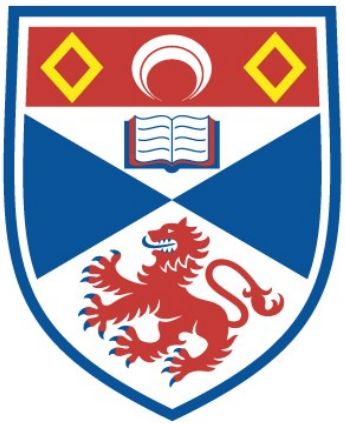

1997

Basic Magnetic Field Configurations for Solar Filament Channels and Filaments

Duncan H. Mackay

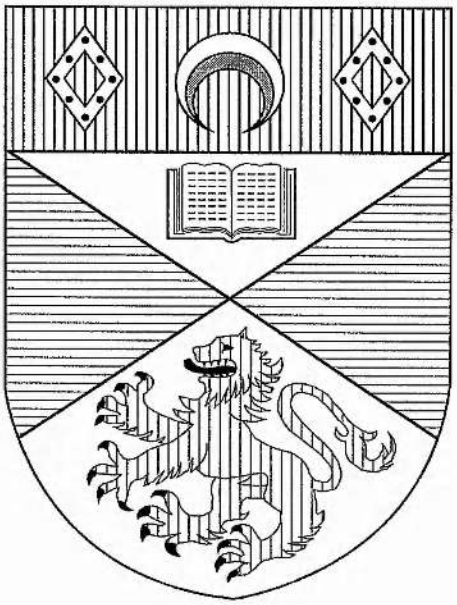

Thesis Submitted for the Degree of Doctor of Philosophy of
the University of St. Andrews on 18^{th} September 1997.

To my niece, Catherine Sarah Smith whose courage and willingness never to give up should be a lesson to us all.

Declarations

1. I, Duncan H Mackay, hereby certify that this thesis, which is approximately 50,000 words in length, has been written by me, that it is the record of work carried out by me and that it has not been submitted in any previous application for a higher degree.

   date 10/12/97. signature of candidate ..

2. I was admitted as a research student in October 1994 and as a candidate for the degree of PhD in October 1995 ; the higher study for which this is a record was carried out in the University of St. Andrews between October 1994 and October 1997 .

   date 10/12/97. signature of candidate

3. I hereby certify that the candidate has fulfilled the conditions of the Resolution and Regulations appropriate for the degree of PhD in the University of St. Andrews and that the candidate is qualified to submit this thesis in application for that degree.

   date 10.12.97. signature of supervisor .....

4. In submitting this thesis to the University of St. Andrews I understand that I am giving permission for it to be made available for use in accordance with the regulations of the University Library for the time being in force, subject to any copyright vested in the work not being affected thereby. I also understand that the title and abstract will be published, and that a copy of the work may be made and supplied to any bona fide library or research worker.

   date 10/12/97. signature of candidate .

Abstract

The three-dimensional magnetic structure of solar filament channels and filaments is considered. A simple analytical potential model of a filament channel is setup with line sources representing the overlying arcades and point sources the flux of the filament. A possible explanation of the distinct upper and lower bounds of a filament is given. A more detailed numerical force-free model with discrete flux sources is then developed and the effect of magnetic shear on the separatrix surface explored. Dextral channels are shown to exist for a wider range of negative values of the force-free alpha and sinistral channels for positive values of alpha.

Potential models of a variety of coronal structures are then considered. The bending of a filament is modelled and a method of determining the horizontal component of a filament's magnetic field is proposed. Next, the observed opposite skew of arcades lying above switchbacks of polarity inversion lines is shown to be produced by a local flux imbalance at the corner of the switchback. Then, the magnetic structure of a particular filament in a filament channel is modelled using observations from a photospheric magnetogram. It is shown that dips in the filaments magnetic field could result from opposite polarity fragments lying below the filament.

Finally, the formation of a specific filament channel and filament is modelled. The formation of the channel is shown to be due to the emergence of new flux in a sheared state. It is shown that convergence and reconnections between the new flux and old remnant flux is required for the filament to form. The field lines that represent the filament form a thin vertical sheet of flux. The changing angle of inclination of the sheet gives the appearance of twist. The method of formation is then generalised to other cases and it is shown that a hemispheric pattern consistent with the results of Martin et al. (1995) can be obtained.

Acknowledgements

I would like to thank the following people:

My Mum and Dad for supporting me throughout my years of study at University.

My supervisor Eric Priest for guiding me through this study.

The members of the PROM consortium and especially Vic Gaizauskas whose philosophy and guidance has been invaluable.

My fellow colleagues in the Solar Group.

Klaus Galsgaard, Tricia Heggie and Aaron Longbottom for providing computing support.

Gordon Inverarity, Jack Ireland and Aaron Longbottom for reading this thesis.

My friends and fellow students in University Hall for making life somewhat interesting.

My tennis partners and team colleagues of the St. Andrews 2^{nd} team namely Gus Grieve , David Eglinton, Ian Leith, Bob M^{c}Alinden, Fergus Muir and James Murray for constant support, entertainment and encouragement.

PPARC for financial support over the last three years.

The Solar Physics Research Corporation and NSF Grant ATM-9596070 for covering travel costs during my stay in Ottawa.

The National Research Council of Canada and the Herzberg Institute of Astrophysics for their warm hospitality.

The Medical Staff and Nurses of Ward 9, Kings Cross Hospital, Dundee.

Published Papers

The following publications resulted from this thesis:

1. **"A Model for Dextral and Sinistral Prominences"**, Priest, E.R. , van Ballegooijen, A.A. and Mackay, D.H. (1996), *Astrophys. J.*, **460**, 530.

2. **"A Potential Field Model for Dextral and Sinistral Filament Channels"**, Mackay, D.H. and Priest, E.R. (1996), *Solar Phys.*, **167**, 281.

3. **"Force Free and Potential Models of a Filament Channel In Which a Filament Forms"**, Mackay, D. H. , Gaizauskas, V. , Rickard, G. J. and Priest, E.R. (1997), *Astrophys. J*, **486**.

4. **"Role of Helicity in the Formation of Intermediate Filaments"**, Mackay, D.H., Priest, E.R., Gaizauskas, V. and van Ballegooijen, A.A. (1997), *Solar Phys.*, accepted.

5. **"The Skew of Polar Crown X-ray Arcades"**, M^{c}Allister, A.H., Mackay, D.H. and Hundhausen, J.R, (1997), in preparation.

Contents

Chapter 1

Introduction

The Sun is an object of beauty and wonder. Thousands of years ago, ancient eastern and Mediterranean societies worshipped the Sun as a god. Each society had its own folk lore for the constant rising, setting and passage of the sun across the sky, some more colourful than others. To the Egyptians it was the god Re, a fiery disc that travelled across the sky during the day, on a boat that sailed a great river. A solar eclipse was a serpent attacking the sun. The Babylonians worshipped the Sun as a living being called Shamash who emerged through a door in the east each morning and moved against the solid vault of sky to disappear in the west each evening.

In most societies today, the Sun is no longer worshipped as a god; however, it still plays an important role in our existence. Without its light and heat no life could exist on this planet. We were not created by the Sun but our existence is very much dependent on it. Today the Sun is known to be a great ball of hydrogen gas that lies 150×10^6 km (1 AU) from the earth. The earth orbits the Sun and the heat that allows our existence is generated in the Sun's core. This description may seem dull compared to the folk lore of ancient civilisations; however, modern science has not diminished the Sun's beauty. With today's generations of telescopes and filtergrams the Sun has been shown not to be a homogeneous ball of gas, but an object of much beauty and complexity. Even without the folk lore the beauty and wonder of the Sun still exists; at least for many of the scientists who study it. This PhD thesis will study objects found in the solar atmosphere called "solar prominences" or "solar filaments" and their places of birth, "filament channels". To begin with, a brief description of the Sun and the properties of solar prominences is given.

1.1 The Sun

Compared to other stars the Sun is fairly ordinary. It has a spectral classification G2 V and an absolute stellar magnitude of 4.8. Although it is an ordinary star it has special significance to us and can give us much insight into other stars and astrophysical plasmas. The Sun is mainly composed of hydrogen (90%) and helium (10%) and has no solid surface. It is around 4.5×10^9 years old and has a mass of 2×10^{31} kg (330,000 times that of earth) and a radius of 696, 000 km (116 times that of earth). The Sun rotates differentially with a period of 26 days near the equator and 30 days near the poles. The structure of the Sun may be described in terms of many different regions. Both temperatures and densities change drastically from one region to another and in each region different physical processes dominate, so let us now describe the main regions of the solar interior and atmosphere.

1.1.1 Interior

The solar interior is made up of three distinct regions and is shown in Figure 1.1 (Philips 1995, Priest 1982). The centre-most region of the Sun is its core. The core is the source of all the Sun's energy. In this region, which extends to $1/4R_\odot$, hydrogen is converted into helium by fusion reactions and energy is released. The temperature of the core is around 15×10^6 K and the density is 1.6×10^5 kg m^{-3}. These high temperatures and densities are required for fusion to take place since the hydrogen ions must overcome the electrostatic force that repels them. Similar fusion reactions take place in laboratory plasmas such as in Tokamaks; however, since the densities are much lower, temperatures need to be far higher and fusion reactions are more difficult to produce (Wesson, 1987).

Once the energy is generated in the core it needs to travel from the solar interior to the outer regions. Initially this is done by radiative transport. The radiative zone extends from the core to $0.7R_\odot$. In this region the temperature ranges from 8×10^6 K to 2×10^6 K and the density from 2×10^4 kg m^{-3} to 2×10^2 kg m^{-3}. Since the temperature is lower in the radiative zone compared to the core, hydrogen atoms are not fully ionised. These atoms can absorb and emit photons. The continual absorption and emission is a random process and it takes radiation 10^7 years to pass through the radiative zone. During the process of absorption and emission the wavelength of the

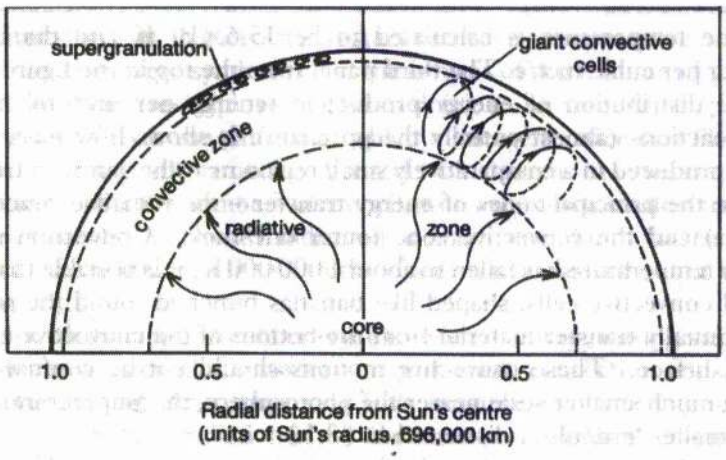

Figure 1.1: Zones of the solar interior (From Philips 1995).

radiation increases and it changes from gamma rays near to the core to visible light at the surface. As a result the photons lose energy as they pass through the solar interior.

Once out of the radiative zone the energy produced in the core uses another method of transport to reach the surface. At the top of the radiative zone convection takes over and transports heat to the surface. The convective zone runs from $0.7R_{\odot}$ to the visible surface of the Sun (the photosphere). In this zone the temperature changes from 2×10^6 K at the bottom to 6000 K at the top. At these temperatures convection is the most effective means of transport. In this region hot material at the bottom of the convective zone rises up to the photosphere and cooler material sinks to the bottom. As the hot material rises it cools down and energy is transported. This process can be seen on the solar surface as a series of bubbling convective cells called granules and supergranules. Granules are typically 1000 km in size and have convective flows with speeds of $1 - 3$ km s^{-1} and lifetimes of roughly tens of minutes. In contrast, the much larger supergranules are roughly 3×10^4 km in size and have flow velocities of 0.5 km s^{-1} and lifetimes of nearly one day.

The interior of the Sun is hidden from view; however, techniques have been developed to measure its properties. The temperature, composition and structure of the interior may be determined through helioseismology. This is the study of sound waves propagating in the solar interior. These waves can be seen as oscillations on the solar surface and have a distinctive period of 5 minutes. Another method is to measure the solar neutrino flux generated during the fusion reactions in the core. During the fusion reactions one of three types of neutrino, the electron neutrino (υ_e) is pro-

duced. The observed flux of these can be used to deduce the temperature of the core. However, only one third of the calculated neutrinos are observed. The problem here may be due to neutrinos having some mass: if they do have mass it would be possible for the neutrino created in the core (the electron neutrino, υ_e) to transform into one of the two other types, the muon (υ_μ) or tauon (υ_τ) neutrinos. The detectors at the moment can only detect the lowest energy neutrino, the electron neutrino (υ_e).

1.1.2 Atmosphere

The atmosphere of the Sun can be split up into four distinct regions: the photosphere, chromosphere, transition region and corona. As with the interior of the Sun, temperatures and densities change drastically from one region to the next. In Figure 1.2 the variation of temperature through the solar atmosphere can be seen.

The lowest part of the Sun's atmosphere is called the photosphere (or sphere of light). All of the white light that we observe from the Sun comes from this region. The photosphere is 500 km thick and is the "apparent" surface of the Sun. The temperature of the photosphere is $6,000$ K at the bottom and $4,300$ K at the top where it joins the chromosphere. Its density is much reduced compared to the interior and is roughly 3×10^{-4} kg m^{-3}. When the photosphere is viewed through a telescope dark spots can be seen on its surface. These are sunspots and are regions of intense magnetic fields ($2000 - 4000$ G). They appear dark since they are cooler than the surrounding atmosphere. Sunspots are 2×10^4 km in size and have lifetimes from days to months. The number and location of sunspots on the solar surface varies with an 11-year cycle.

The chromosphere (or sphere of colour) lies just above the photosphere. It is roughly $2,000$ km thick and through it the temperature increases with height. At the base of the chromosphere the temperature is $4,300$ K and at the top, where it joins the transition region, it has risen to $25,000$K. The rise in temperature through the chromosphere accompanies a sharp fall of density with height from 3×10^{-4} kg m^{-3} at the base to 1.4×10^{-10} kg m^{-3} at the top. The chromosphere is mainly observed in the red line of $H\alpha$ and in the CaII K line. Both of these lines are important for observing filaments and filament channels, since filament channels lie in the chromosphere and filaments exist at chromospheric temperatures. Above the chromosphere lies the transition region. It is a very thin layer of the Sun's atmosphere which is about 100 km thick. Across this

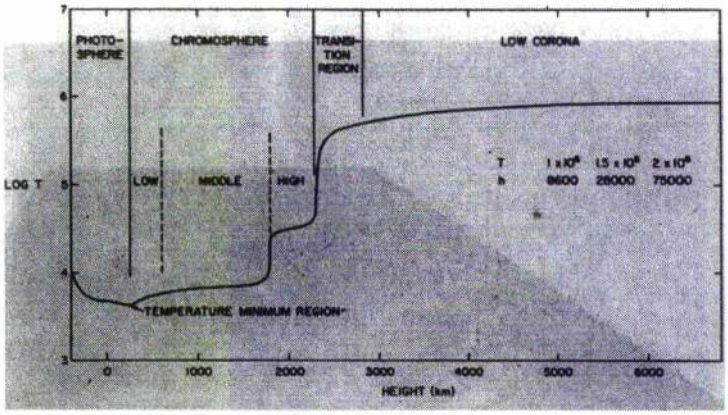

Figure 1.2: Variation of temperature with height in the solar atmosphere (Athay 1976).

small region the temperature rises from $25,000$ K to over 2×10^6 K in the corona. This sudden temperature rise is not well understood and is one of the main questions facing Solar Physics. A number of heating mechanisms have been put forward and it is widely believed that the heating is caused by the Sun's magnetic fields. A review of coronal heating mechanisms can be found in Zirker (1993) and Narain and Ulmschmieder (1990).

The outermost region of the Sun's atmosphere is called the corona. The corona extends from the transition region to outer space; therefore, the earth lies in the Sun's corona. The density of the corona is very low (4×10^{-12} kg m^{-3}), and so it is very faint. The corona can only be seen during solar eclipses or through a coronagraph. The shape of the corona is determined by the magnetic field of the Sun. A wide variety of structures can be seen including coronal loops, coronal holes and filaments. In loops, the magnetic field from the photosphere extends out into the corona and arches back to the solar surface. The plasma in these structures is very hot with temperatures ranging from $1.5 - 7 \times 10^6$ K. Due to these high temperatures the corona is often observed from space in X-rays. In contrast coronal holes are regions of open field lines. This is the source of the solar wind. Solar filaments are also found in the corona. They exist in the corona with temperatures much less than that of the corona and densities much higher. So let us now give an in-depth discussion of solar filaments and filament channels.

1.2 Solar Filaments and Filament Channels

Solar filaments are one of the most interesting but least understood of all solar phenomena. The unique sites of formation of these objects are filament channels (Martin 1990). To understand filaments we need to understand first the filament channel. Both of these objects provide the observer and theorist with demanding challenges. The theoretical study of filament channels and filaments can provide crucial physical insight into not only the solar atmosphere but a wide range of other astrophysical phenomena, where similar plasma processes are taking place. Through filaments, magnetic instabilities (which lead to eruptions) and thermal instabilities (which create their fine structure) can be studied. Filaments are not only interesting in their own right but are closely connected with coronal mass ejections (CME's) and solar flares, both of which affect the solar terrestrial environment. The main properties of filament channels and filaments are as follows.

In the simplest terms, a prominence or filament is a huge, almost vertical sheet of dense, cool plasma surrounded by a hotter and rarer coronal environment. Prominences are generally 500 times cooler than the surrounding corona and roughly 100 times denser. The prominence material would therefore be expected to fall through the solar atmosphere and to be heated up. In $H\alpha$ photographs these objects appear bright at the limb and are called prominences (Figure 1.3), while in Hα images of the disc they show up as thin, dark meandering ribbons called filaments (Figure 1.4). At any one time on the Sun, as Figure 1.4 shows, many filaments may exist. Throughout this thesis the names "Prominence" and "Filament" which describe the same object, will be used interchangeably.

The existence of a filament is due to the magnetic field of the filament channel which supports the mass against gravity and insulates it from the surrounding corona. As filaments weave and meander their way across the solar surface they lie along large scale polarity inversion lines (P.I.L.'s) (Babcock and Babcock 1955) in the photosphere. Polarity inversion lines are theoretical curves separating regions of opposite polarity flux in the photosphere, where the vertical component of field falls to zero. Filaments always form above polarity inversion lines, as long as a "filament channel" is also present. A filament channel is a path in the chromosphere characterised by chromospheric fibrils on either side of the P.I.L that are: (1) nearly parallel to one another;

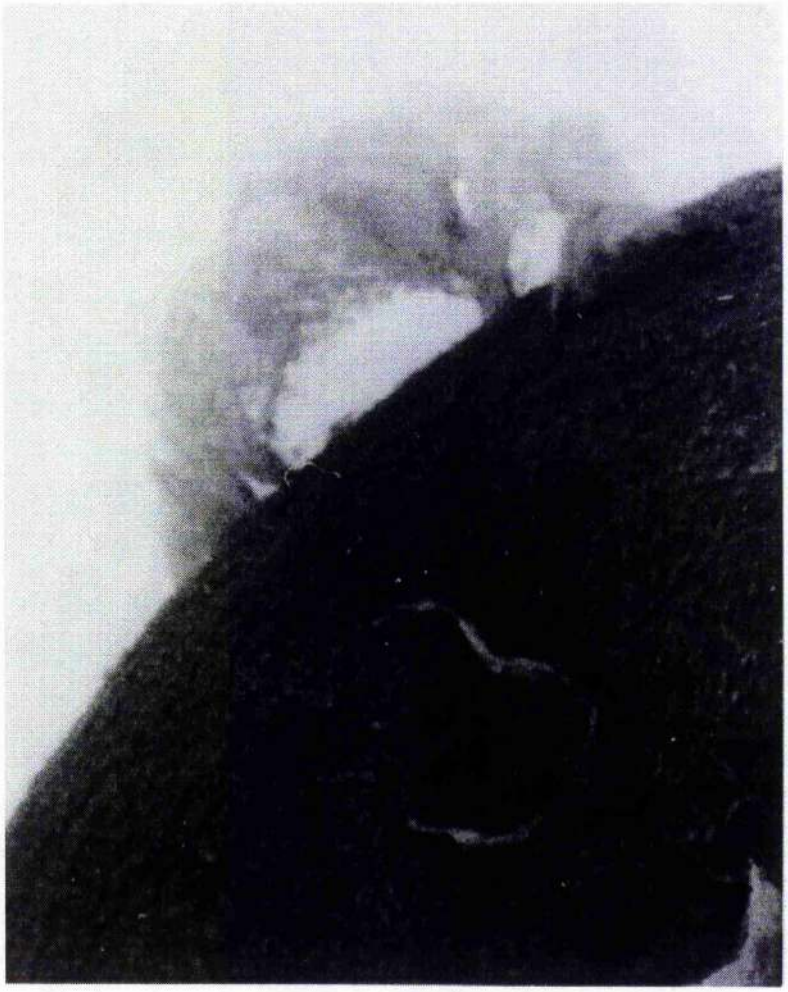

Figure 1.3: Example of a prominence seen at the limb (from Meudon).

and (2) nearly parallel to the path of the P.I.L. This alignment of fibrils tells us that the channel is a region of dominant horizontal field. The horizontal component points in the same direction on both sides of the channel and the filament forms in the centre of the channel where the field is most horizontal. In filament channels there is an absence of any structure crossing the P.I.L. between the regions of opposite polarity flux. Filament channels are more fundamental than the filaments that form within them. The channels appear prior to the appearance of visible filament mass and can survive successive filament formations and eruptions. Filament channels may be longer and broader than the filaments that form within them. In Figure 1.5 an example of a filament channel without a filament (left) and one with a filament (right) can be seen. On the right-hand side the

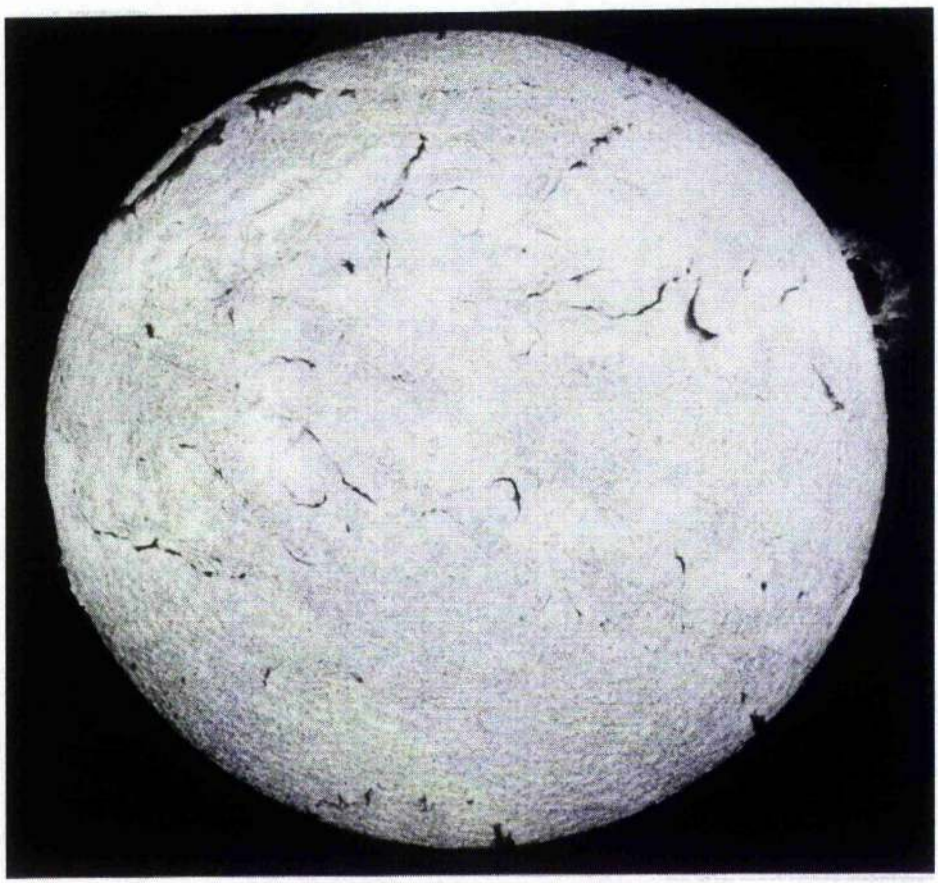

Figure 1.4: Full-disc image showing filaments on the disc (from Meudon).

filament only partially fills the channel. On both images fibrils can be seen on either side of the P.I.L. (shown as the dashed line). These fibrils outline the magnetic field vectors in the channel (Foukal 1970) and so may act in a similar way to a chromospheric magnetograph. On the left-hand image, a theoretical observer standing on the positive polarity side would see fibrils streaming to the left. This tells us that the dominant magnetic field of this channel points to the left and the channel is classified as "sinistral". In contrast, on the image on the right, the fibrils stream to the right when viewed from the positive polarity side. In this case the magnetic field vector points to the right and we have a "dextral" channel. There are therefore two classifications of filament channels and filaments given by the direction of the dominant horizontal component of field in the channel. They may be of "sinistral" or "dextral" type when viewed from the positive polarity side. In Section 1.3 a surprising hemispheric pattern for filament channels and filaments is described.

Figure 1.5: Example of a sinistral filament channel (left) and a dextral filament channel (right) (from Martin *et al.* 1995.)

Filament channels of the same orientation may connect together to form larger channels that can run across the whole solar surface, but channels of opposite orientation may not.

The significance of the filament channel was not realised until recently. Before this, filaments were classified depending on their size and location with respect to neighbouring flux regions. Filaments could be classified into two main types: the "quiescent prominence" and the "active region" prominence. Quiescent prominences are very stable structures which are located in quiet regions of the Sun. As their name suggests, they change shape very slowly. Their lifetime was thought to be anywhere from 1-300 days, but this is probably an overestimate. A single quiescent filament can probable last between one and two months (Gaizauskas, private communication). The filament channels, however, survive many filament formations and eruptions and have a much longer lifetime. New filaments can form within them and this leads to an overestimate in the lifetime of a single filament. The temperature of a quiescent prominence is around $5,000$-$10,000$ K and the ratio of protons to hydrogen atoms is roughly 1:10. They form in a wide range of sizes with lengths from $60,000 - 600,000$ km, heights from $10,000 - 100,000$ km and widths

of $4,000 - 15,000$ km. The average density lies between 10^{16} and 10^{17} particles m^{-3}. Many measurements of magnetic fields in quiescent prominences have been made. This can only be done so far when the prominence is at the limb, using Zeeman splitting or the Hanle effect. This shows that within prominences the magnetic field is mainly horizontal and makes an angle of 20° to the prominence axis (Athay *et al.* 1983, Querfield *et al.* 1985, Leroy *et al.* 1983). The magnetic field strength lies between 2 and 30 G (average 8 G) and increases with height through the prominence. Although quiescent prominences are stable structures they do sometimes erupt and eject mass into space. Not all of them erupt and some are seen slowly to disappear and break up or flow down to the chromosphere.

As their name suggests "active-region" filaments lie in the active-region belts of the sun. They are generally three to four times smaller than the quiescent prominences and are commonly associated with flares. They are very dynamic structures with lifetimes from hours to days. The maximum height of an active-region filament is around $20,000$ km, so they are situated much lower than their quiescent cousins. Although they are much lower they have a much higher density and magnetic field strength of around $20 - 100$ G.

As well as being classified in terms of their size and location, filaments have also been classified in terms of the direction in which the magnetic field passes through the plane of the filament (Priest, 1989). The two classifications are Normal (N) and Inverse (I) Polarity. In a normal polarity filament the magnetic field passing through the filament is in the same direction as that of the overlying potential field. An example of a normal polarity filament can be seen in the model of Kippenhahn and Schluter (1957). The opposite occurs for an Inverse (I) polarity filament. The field passes through the filament in a direction opposite to that of the overlying arcade, such as suggested by Kuperus and Raadu (1974). Most 2D models of filaments are based either on the Kippenhahn-Schluter-type solution or the Kuperus-Raadu solution. However both of these models do not include the dominant field component along the axis of the filament. The sinistral/dextral types of filaments do not correspond one-to-one with the normal and inverse categories of filaments. There are therefore four possible combinations between the sinistral/dextral and normal/inverse categories.

Overlying filaments are hot coronal arcades (Solberg, 1997) and above these lie helmet streamers (Tandberg-Hanssen 1974). The central part of the helmet streamer surrounding the prominence

is darker and less dense than its neighbouring parts. This is called the coronal cavity (Engvold, 1987) and is a region of reduced density surrounding the filament which can only be seen in eclipse or coronograph pictures. The cavity can reach as high as 4×10^5 km above the solar surface and a model for it has been proposed by Low and Hundhausen (1995). Filaments also have much fine structure in the form of vertical threads. Threads are roughly 5,000 km long and 300 km thick and have lifetimes from minutes to hours. Prominences also have distinct lower and upper bounds and reach down to the chromosphere in a series of regular spaced feet or barbs, as shown in Figure 1.3. A possible explanation for the lower and upper bounds is given in Chapter 2. The barbs of the filament also define two new structural classes of filaments (Martin *et al.* 1995). They are called "right-bearing" and "left-bearing" and describe the direction in which the barbs of the filament leave the main spine and reach down to the chromosphere. Filaments either have right-bearing or left-bearing barbs but not both. There is a one-to-one correspondence between the structural classes of filaments and the magnetic classes of the filament channel. All dextral channels have right-bearing filaments and all sinistral channels have left-bearing filaments (Martin *et al.* 1995).

The formation of filaments is a difficult and puzzling subject. Many theories have been put forward and include: formation through shear motion and thermal instability (eg. Antiochos and Klimchuck, 1993; and Antiochos *et al.* 1995); formation through subsurface shear and reconnection (eg. van Ballegooijen and Martens 1990 and Priest *et al.* 1996); formation in a twisted flux tube (Priest *et al.* 1989, van Ballegooijen and Martens 1990) or through the emergence of a buoyant flux tube (Rust and Kumar 1994). A review of formation processes is given by Malherbe (1989). However, observations by Martin (1973, 1986) show that filaments typically take a few hours to a day to form and the formation process requires cancellation of small fragments of opposite polarity magnetic flux at the polarity inversion line. This was reinforced by observations from Gaizauskas *et al.* (1997) who described an excellent example of a filament channel and filament formation through emergence, convergence and cancellation of flux. A hint about the formation mechanism may come from observations by Tang (1987) and Gaizauskas and Zwaan (1997). Both of these authors found that prominences prefer polarity inversion lines between bipolar regions compared to polarity inversion lines within bipolar regions. This suggests that the magnetic topology of the filament can develop through reconnection of field lines between adjacent regions. Modelling carried out in Chapter 4 also shows this.

Although filaments are relatively static a variety of flows has been observed. These include upflows, downflows and horizontal flows. Downflows have mainly been seen in prominences at the limb but are much less than free-fall speeds. Engvold (1976) observed downflows of $15 - 35$ km s^{-1} while Schmieder et al. (1985b) observed downflows of $5 - 10$ km s^{-1}. Upflows have been seen in filaments on the disc and range from 0.5 km s^{-1} (Martres *et al.* 1981) to 5 km s^{-1} (Schmieder *et al.* 1985b). As well as upflows, strong horizontal flows have been observed along the filament long axis or spine (Gaizauskas, private correspondence) and these are in the range of 5 km s^{-1} (Malherbe *et al.* 1983). A review of flows in filaments can be seen in Schmieder (1989).

1.3 Hemispheric Patterns

Hemispheric patterns on the Sun have been known for many years. An example is the clockwise or counterclockwise rotation of fibrils observed around sunspots (Richardson 1941). Other patterns include the helicity of erupting filaments and magnetic interplanetary clouds and the net helicity of active regions (Pevtsov *et al.* 1994, 1995). A review of these hemispheric patterns and others can be found in Zirker *et al.* (1997). More recently, hemispheric patterns have been found for filament channels and filaments and the arcades lying above them. These patterns are described below.

1.3.1 Filaments and Filament Channels

One of the most surprising observations to emerge in the last few years is that filament channels and filaments have a hemispheric pattern with respect to their sinistral/dextral classification. Martin *et al.* (1995) considered a sample of 154 filaments and found that quiescent filaments in the northern hemisphere are predominantly "dextral", while those in the southern hemisphere are predominantly "sinistral". This rule is statistical and exceptions do exist. In Figure 1.6(a) a graph of the number of sinistral and dextral quiescent filaments observed at each latitude can be seen for the period of September 1991 to June 1992. A further study showed that the pattern is independent of the solar cycle. However, when active-region filaments are considered over the same period no hemispheric pattern is found and equal numbers of sinistral/dextral filaments exist in each hemisphere (Figure 1.6(b)). Since there is a hemispheric pattern for quiescent filaments and not for

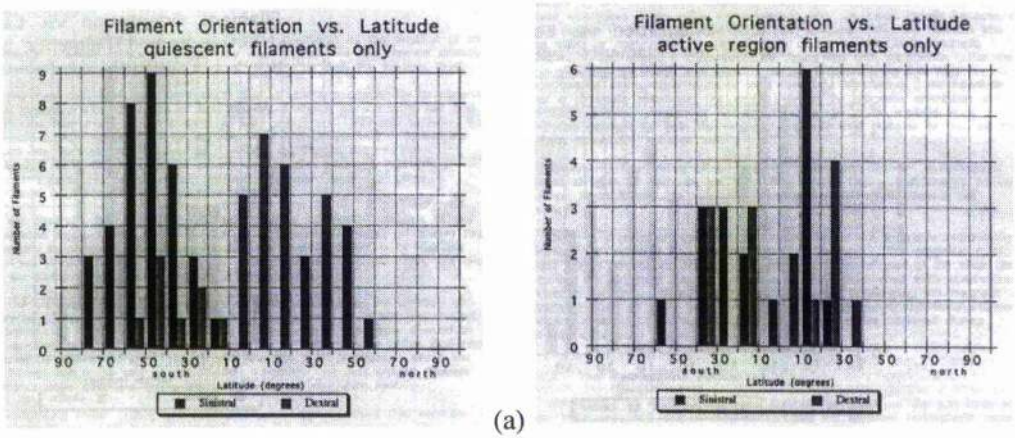

Figure 1.6: Number of (a) quiescent and (b) active-region filaments of sinistral/dextral type at each latitude on the Sun in the northern and southern hemispheres (from Martin *et al.* 1995).

active-region filaments, this suggests that there may be a mechanism that prefers the survival of dextral filaments in the northern hemisphere and sinistral in the southern. The obvious choice: differential rotation acting on pre-existing coronal arcades, however, tends to produce sinistral filaments in the northern hemisphere and dextral filaments in the southern (van Ballegooijen and Martens 1990, van Ballegooijen *et al.* 1997, Cartledge *et al.* 1997). New theories are now being put forward to explain this, such as, Priest et al. (1996), Rust and Kumar (1995), Zirker *et al.* (1997), Kuperus (1997) and Mackay *et al.* (1997). The origin of the hemispheric pattern will be discussed in more detail in Chapter 5.

1.3.2 Arcade Orientation Above Filaments.

In the paper by Martin and M^{c}Allister (1996) the relationship between filament structures in Hα and their overlying coronal loops in X-rays is given. Both stationary (static) arcades above filaments and post-eruption (dynamical arcades) are studied. They find that above filaments there is a systematic orientation and development of the arcades. To show this the skew of the arcades is considered. The skew (α) of an arcade is the angle between a tangent to the top of the loop, in the plane of the loop, relative to the long axis of the filament (or the long axis of the filament channel or the polarity inversion line) as shown in Figure 1.7. With this definition, the coronal loops may be defined as being left-skewed or right-skewed. A left-skewed coronal loop (Figure 1.7) points

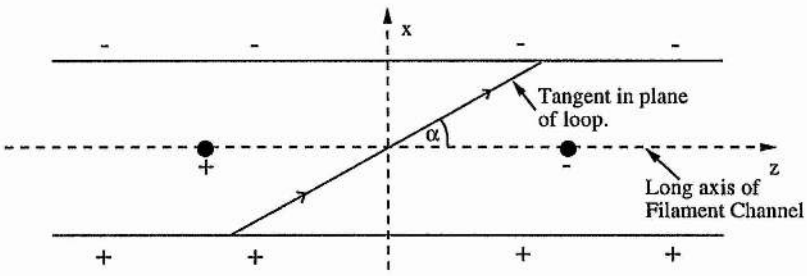

Figure 1.7: Schematic diagram showing the definition of the skew of an arcade as the angle between a tangent to the top of the loop and in the plane of the loop to the long axis of the channel.

from the observer's left to right when seen from above ($0° \leq \alpha \leq 90°$), while a right-skewed coronal loop points from the observer's right to left ($90° \leq \alpha \leq 180°$). With this definition it was found that, for stable arcades, all dextral filaments (filament channels) have left-skewed coronal arcades and all sinistral filaments (filament channels) have right-skewed coronal arcades giving a one-to-one relationship. The results are shown in Table 1.1.

	Dextral/RS	Dextral/LS	Sinistral/RS	Sinistral/LS
Northern Hemisphere	0	13	2	0
Southern Hemisphere	0	2	17	0

Table 1.1 : Relationship between filament channel and arcade orientation in each hemisphere.

Secondly, when dynamic post-eruption arcades are observed following a filament eruption they show a systematic change in their orientation with height. As successive loops develop there is a change in skew angle as higher loops form. All sinistral filaments with right-skewed arcades show a clockwise evolution with height and all dextral filaments with left-skewed arcades display a counter-clockwise evolution with height such that the field becomes more normal with increasing height. These results show that the association between the skew of the coronal loops and the sinistral/dextral filament categories is stronger than the association with hemisphere. This suggests that the axial component of field in the filament channel and that of the overlying arcade have a common origin. This will be investigated more in Chapter 5. The equations and assumptions used in modelling filament channels and filaments are now discussed.

1.4 MHD Equations and Assumptions

The MHD equations are used to describe the interaction of the Sun's atmosphere with its magnetic field. The plasma atmosphere is treated as a continuous medium so the interaction of individual particles is not considered. The length-scales considered must therefore be larger than the particle mean-free path, which is about 3cm in the chromosphere and 30 km in the corona. In the study of solar filaments both of these conditions are easily satisfied. The MHD equations are a set of nine equations, which include those of conservation of mass, Newton's second law, an energy equation, ideal gas law, Maxwell's equations (assuming $v << c$) and a generalised Ohm's law. In these equations the magnetic field is coupled to the plasma velocity through the induction equation.

$$\frac{\partial \mathbf{B}}{\partial t} = \nabla \times (\mathbf{v} \times \mathbf{B}) + \eta \nabla^2 \mathbf{B}, \tag{1.4.1}$$

where $\mathbf{B}$ is the magnetic induction (magnetic field), $\mathbf{v}$ the plasma velocity and η the magnetic diffusivity ($\eta = 1/(\mu\sigma)$, μ - magnetic permeability, σ - electrical conductivity). In 3D these equations are difficult to solve, but simplifications can be made to ease the analysis. According to Tandberg-Hansen (1974), " The single, physical, most important parameter to study in prominences may be the magnetic field. Shapes, motions and in fact the very existence of prominences depends on the nature of the magnetic field threading the prominence plasma ....."

To study the magnetic field of prominences it will be assumed that all plasma velocities are negligible and that there is no time variation, ($\frac{\partial}{\partial t} = 0$). These approximations are reasonable since prominences are relativity static objects. The MHD equations then reduce to

$$0 = -\nabla p + \mathbf{j} \times \mathbf{B} + \rho \mathbf{g}, \tag{1.4.2}$$

coupled with

$$\nabla . \mathbf{B} = 0, \tag{1.4.3}$$

$$\mathbf{j} = \frac{1}{\mu} \nabla \times \mathbf{B}, \tag{1.4.4}$$

$$p = \rho \frac{R}{\tilde{\mu}} T, \tag{1.4.5}$$

where p is the plasma pressure, $\mathbf{j}$ the current density, ρ the plasma density, R the gas constant ($R = 8.3 \times 10^3$ JK^{-1}kg^{-1}), T the temperature, $\mathbf{g}$ the Sun's gravity and $\tilde{\mu}$ the mean atomic weight (or average mass per particle in terms of m_p, for fully ionised hydrogen plasma $\tilde{\mu} = 0.5$). The first term in Equation 1.4.2 is the pressure gradient force, the second the Lorentz force (the force exerted by a magnetic field) and the final term the gravitational force. The temperature also satisfies an energy equation.

The equation of motion, (1.4.2) can be simplified even further by considering the relative sizes of each of the terms on the right-hand side. To do this, first consider the pressure scale height (Λ) at constant temperature and the plasma beta (β),

$$\Lambda = \frac{RT}{\tilde{\mu} g}, \tag{1.4.6}$$

$$\beta = \frac{2\mu p}{B^2} = \frac{2}{\gamma}\frac{c_s^2}{v_a^2}, \tag{1.4.7}$$

where c_s is the sound speed and v_a the Alfven speed and γ the ratio of specific heats ($\gamma = \frac{c_p}{c_v}$). The pressure scale height is the distance over which the pressure falls exponentially along field lines in a static state. At coronal temperatures it is 1.5×10^5 km. The plasma beta (β) is the ratio of the plasma pressure to magnetic pressure. For the corona it is typically 0.01.

Now consider the relative size of the terms on the right-hand side. First, the pressure force ($-\nabla p$) and gravity ($\rho \mathbf{g}$) may be compared by dimensional analysis, where L is the typical length scale.

$$\nabla p \sim \frac{p}{L}, \quad \rho g \sim \frac{p}{\Lambda}.$$

When $L << \Lambda$ the effect of gravity may be neglected with respect to the pressure force. For prominences, their height is less than the pressure scale height of the corona so this is a reasonable approximation. Now consider the pressure force ($-\nabla p$) and the Lorentz force ($\mathbf{j} \times \mathbf{B}$).

$$\nabla p \sim \frac{p}{L}, \quad \mathbf{j} \times \mathbf{B} \sim \frac{B^2}{\mu L}.$$

Therefore if

$$\frac{p}{L} << \frac{B^2}{\mu L},$$

or

$$\frac{p\mu}{B^2} << 1,$$

the pressure force may be neglected with respect to the Lorentz force. This is the case for the corona since $\beta \approx 0.01$. Therefore with the approximations of $L << \Lambda$ and $\beta << 1$ the equation of motion to the zeroth order becomes the force-free equation (Marsh 1996),

$$\mathbf{j} \times \mathbf{B} = 0. \tag{1.4.8}$$

1.4.1 Properties of Force-Free Fields

The Lorentz force $\mathbf{j} \times \mathbf{B}$ may be split into two terms such that

$$\mathbf{j} \times \mathbf{B} = \frac{1}{\mu}(\mathbf{B}.\nabla)\mathbf{B} - \nabla(\frac{B^2}{2\mu}), \tag{1.4.9}$$

where the first term on the right-hand side is the magnetic tension force and acts to straighten field lines when they are curved. The second term is the magnetic pressure force, which is similar to the plasma pressure force and acts from regions of high field strength to regions of low field strength. Since we have the force-free condition these two terms must cancel out everywhere.

Since the field is force-free, Equation 1.4.8 tells us that the current must be parallel to the field, so

$$\nabla \times \mathbf{B} = \alpha(\mathbf{r})\mathbf{B}, \tag{1.4.10}$$

for some scalar function $\alpha(\mathbf{r})$ which varies with position. The function $\alpha(\mathbf{r})$ is not completely arbitrary since the magnetic field must satisfy Equation 1.4.3. Taking the divergence of Equation 1.4.10 we find that

$$\mathbf{B}.\nabla\alpha = 0, \tag{1.4.11}$$

so that alpha must be constant along a field line but may vary from one field line to another. The force-free equation is very difficult to solve for a spatially dependent alpha. However, many simplifications occur when α = constant. When this occurs Equation 1.4.10 is reduced after-taking its curl to

$$\nabla^2\mathbf{B} = -\alpha^2\mathbf{B}, \tag{1.4.12}$$

namely, a linear Helmoltz equation. When α = constant linear theory may be applied. A further simplification can occur when $\mathbf{j} = 0$ (α=0) and a potential field is considered. In this case the

magnetic field is such that

$$\nabla \times \mathbf{B} = 0, \tag{1.4.13}$$

or

$$B = -\nabla\phi, \tag{1.4.14}$$

where

$$\nabla^2\phi = 0. \tag{1.4.15}$$

Hence finding a potential field reduces to solving Laplace's equation for the scalar potential (ϕ). Throughout this thesis various methods both analytical and numerical will be used to determine potential and force-free fields. In all cases the results will be shown by plotting field lines in 3D, which are obtained by solving the equations

$$\frac{dx}{ds} = \frac{B_x}{|B|} \tag{1.4.16}$$

$$\frac{dy}{ds} = \frac{B_y}{|B|} \tag{1.4.17}$$

$$\frac{dz}{ds} = \frac{B_z}{|B|} \tag{1.4.18}$$

to obtain a point $(x(s), y(s), z(s))$ at arclength s along the field line from the initial point $(x(0), y(0), z(0))$.

1.5 Outline of Thesis

This thesis will mainly deal with the magnetic configurations associated with filament channels and filaments. Throughout, an emphasis will be given on modelling actual observations. To begin with, in Chapter 2, potential and force-free models of a filament channel will be constructed, both analytically and numerically. Network flux on each side of the channel and concentrations of flux along the channel are included. These represent the overlying arcades and flux of the filament. By doing this a filament-type structure can be seen to connect along the channel (Mackay and Priest 1996). In Chapter 3 potential models are used to describe a variety of coronal structures including the bending of a filament (Section 3.1), arcades overlying switchbacks of polarity inversion lines

(Section 3.2, M^{c}Allister *et al.* 1997) and a filament in a filament channel (Section 3.3, Mackay and Priest 1996). In each case the potential models give a useful physical insight into the process being modelled. In Chapter 4 a series of $H\alpha$ and magnetogram observations showing a filament channel and filament formation are considered. It is shown that the formation of the channel is due to the emergence of an activity complex in a sheared state. However, further modelling shows that interaction between the activity complex and a neighbouring remnant region is required before a filament can form (Mackay *et al.* 1997(a)). The process described in Chapter 4 is then generalised in Chapter 5 to give a formation mechanism for intermediate filaments. A possible explanation for the hemispheric pattern of filaments is then put forward (Mackay *et al.* 1997(b)). Finally, in Chapter 6 the conclusions and a discussion of future work is given.

Chapter 2

Potential and Force-Free Models of a Filament Channel

The nature of a filament channel is first considered. Since they are the birth places of filaments (no filament may exist without a channel) any model that wishes adequately to describe filaments should also include the channel. It is therefore surprising that most models to date neglect to include a channel. In the first part of the chapter, a simple analytical potential model of a filament channel is constructed (Section 2.1). The model, which is consistent with the new observations of Martin *et al.* (1995), consists of magnetic sources and sinks that represent the network flux on both sides of the channel. The flux of the filament is then given by extra concentrations of flux that produce a strong field component along the channel. It is the asymmetry of flux locations along the channel that produces the dominant direction of field in the channel. From this the resulting separatrix surface of the flux connecting along the channel is computed. The surface has distinct upper and lower bounds that may produce the upper boundary of a filament cavity or filament and the lower bound of the filament, respectively. Section 2.2 then considers the effect of a weak background uniform field on this surface. From this initial modelling, a more detailed numerical model is then constructed with more realistic flux distributions (Section 2.3). With the numerical model, the channel is considered for both potential and non-potential cases. The effect of magnetic shear on the separatrix surface is considered. A comparison between the potential case of the analytical and numerical models is then given (Section 2.4).

2.1 A Simple Potential Model for a Filament Channel.

2.1.1 Equations and Assumptions.

A simple potential model for a sinistral or dextral filament channel is set up here, consisting of a set of magnetic sources and sinks that are believed to produce the basic components of a channel's field. Two point sources are used to produce the flux of a filament, while two line sources are used to represent the overlying coronal arcade. Thus, we suggest that a filament channel is created by an asymmetry in the location of opposite fluxes along the inversion line which produces the strong field component along the inversion line. Such a field may, but need not be, force-free and so for simplicity we first consider the case when it is potential. By contrast, in the traditional explanation, the global prominence field is force-free and is produced by the shearing of an infinitely long and initially potential field. Here, instead, it is the finite length of the channel and the asymmetry in flux distribution which are crucial (see Antiochos *et al.* 1995).

The field lines emerge radially from the point sources, and the field description for a single source in terms of either the radial coordinate ($\mathbf{r}$) in spherical polars or cartesian coordinates (x,y,z) is :

$$\mathbf{B_{point}} = \frac{f\mathbf{r}}{2r^3} = \left(\frac{f}{2}\frac{x}{(x^2+y^2+z^2)^{3/2}}, \frac{f}{2}\frac{y}{(x^2+y^2+z^2)^{3/2}}, \frac{f}{2}\frac{z}{(x^2+y^2+z^2)^{3/2}}\right), \tag{2.1.1}$$

when the pole is positioned at the origin $(0,0,0)$ and πf is its strength.

The line source field depends only on either the radial coordinate ($\mathbf{R}$) in cylindrical polars or the cartesian coordinates (x,y) and has two components

$$\begin{aligned}\mathbf{B_{line}} &= (\mathbf{B_x}, \mathbf{B_y}) \\ &= \frac{F\mathbf{R}}{R^2} = \left(F\frac{x}{x^2+y^2}, F\frac{y}{x^2+y^2}\right),\end{aligned} \tag{2.1.2}$$

when the line source of strength πF is positioned at $x=0, y=0$ and extends infinitely in the z-direction. An example of the field produced by two line sources can be seen in Figure 2.1(a), while

Figure 2.1(b) shows the coordinate system used and the positions of the sources in the filament channel.

The basic field in the filament channel is given by :

$$\begin{aligned} \mathbf{B_{channel}} &= \mathbf{B_{filament}} + \mathbf{B_{arcade}} \\ &= \frac{f}{2}\left(\frac{\mathbf{r_1}}{{r_1}^3} - \frac{\mathbf{r_2}}{{r_2}^3}\right) + F\left(\frac{\mathbf{R_3}}{{R_3}^2} - \frac{\mathbf{R_4}}{{R_4}^2}\right), \end{aligned} \tag{2.1.3}$$

where

$$\begin{aligned} \mathbf{r_1} &= x\hat{\mathbf{x}} + y\hat{\mathbf{y}} + (z+a)\hat{\mathbf{z}}, \\ \mathbf{r_2} &= x\hat{\mathbf{x}} + y\hat{\mathbf{y}} + (z-a)\hat{\mathbf{z}}, \\ \mathbf{R_3} &= (x+b)\hat{\mathbf{x}} + y\hat{\mathbf{y}}, \\ \mathbf{R_4} &= (x-b)\hat{\mathbf{x}} + y\hat{\mathbf{y}}, \end{aligned} \tag{2.1.4}$$

are the distances of a point P(x,y,z) from the two point sources and two line sources, respectively.

It is assumed that all the sources are in the $y = 0$ (photospheric) plane. $\mathbf{R_3}$ and $\mathbf{R_4}$ are the perpendicular distances from the line sources to any point P(x,y). The field is potential and satisfies the equations

$$\mathbf{j} = \frac{1}{\mu}\nabla \times \mathbf{B} = \mathbf{0}, \tag{2.1.5}$$

and $\nabla \cdot \mathbf{B} = 0$, so that

$$\nabla^2 \mathbf{B} = \mathbf{0}. \tag{2.1.6}$$

When standing on the positive polarity side it can be seen that the field points to the right. Thus the configuration is that of a dextral filament channel (northern hemisphere). If the polarities of the two poles are reversed, the field would go to the left and a sinistral channel (southern hemisphere) would be produced. Sub-photospheric motions can create dextral channels in the northern hemisphere and sinistral in the southern hemisphere (Priest *et al.* 1995). The flux values are chosen so that

$$F = 1.0 \tag{2.1.7}$$

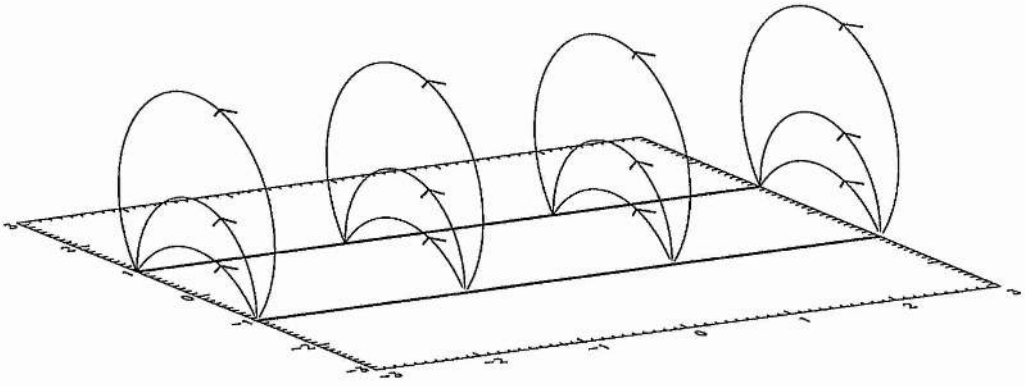

1(a)

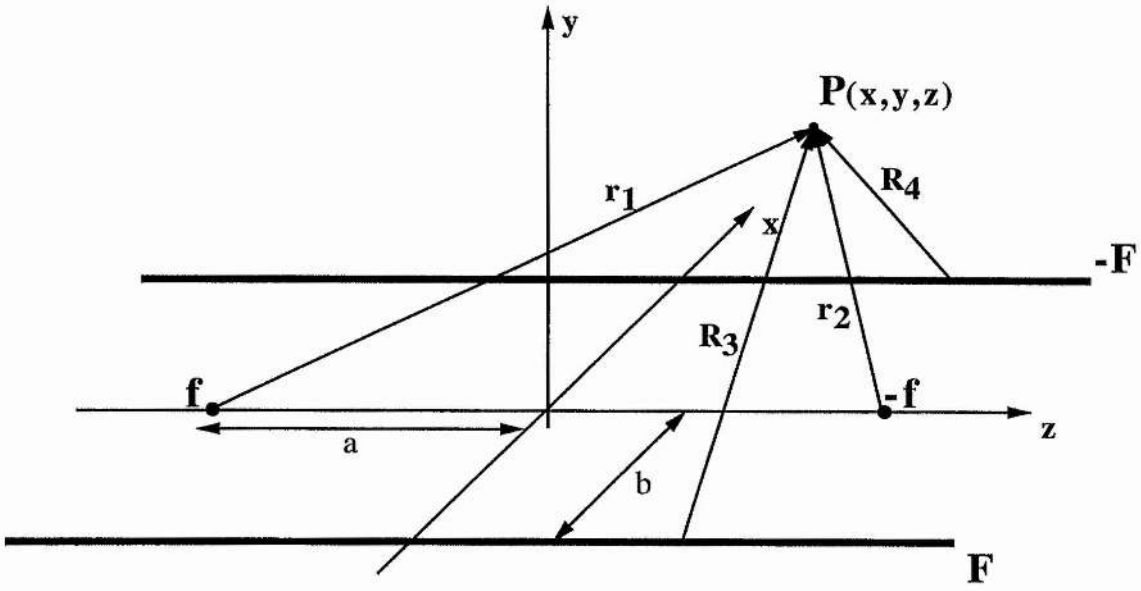

1(b)

Figure 2.1: (a) Magnetic field created by two line sources of strength πF and -πF. (b) Cartesian coordinate system and notation, showing the positions of the sources in the filament channel and the distances to the point P.

and the sizes so that

$$b = 1.0. \tag{2.1.8}$$

In other words, we nondimensionalise fluxes with respect to the line source flux and distances with respect to the half-width of the filament channel (half the distance between the network line sources). We shall take one unit in size to correspond to 30,000 km (i.e a typical supergranule width on the quiet Sun) so that the separation of the line sources of the arcade is typically 60,000 km as seen in Figure 3.12. From now on without loss of generality, only a dextral channel will be considered.

2.1.2 Separatrices.

The separatrix surfaces of the filament channel are the surfaces that divide up regions of different magnetic connectivity. On one side of the surface the field lines connect certain sources while on the other side the field lines connect different sources. Field lines that lie on the separatrix surface have the property that they extend from a pole to a neutral point or from a neutral point to a pole. For the filament to form in the channel the poles must be connected, which means by symmetry for this configuration, that the separatrix surface must cross the y-axis at some height, H_s. In order to find the range of heights of field lines that connect the poles, the height of the separatrix as a function of the flux must be found.

First of all, we make a simple order of magnitude estimate to show how the separatrix height varies with flux, since an analytical expression for the separatrix surface is unavailable. The poles are estimated to connect on the y-axis if the field from the poles dominates the field from the line sources, so that

$$| B_{poles} | \; > \; | B_{lines} |$$

or

$$\frac{f}{2r^2} \; > \; \frac{F}{R}, \tag{2.1.9}$$

where

$$\begin{aligned} r^2 &= x^2 + y^2 + (z+a)^2, \\ R^2 &= (x+b)^2 + y^2. \end{aligned}$$

Using the dimensionless values of Equations (2.1.7) and (2.1.8) we consider the inequality (2.1.9) for the two cases $y = 0$ and $y \neq 0$.

For a point in the photosphere $(y = 0)$ at $(z = 0, x = 0)$, Equation (2.1.9) reduces to

$$f > 2a^2, \tag{2.1.10}$$

which is the rough condition that the poles be joined in the photospheric plane. For a point above the photosphere, the poles connect according to (2.1.9) when

$$f > \frac{2(y^2 + a^2)}{(1 + y^2)^{1/2}}. \tag{2.1.11}$$

If the inequality is reversed the poles are not connected, and so the separatrix which divides regions of different magnetic connectivity crosses the y-axis at a point y given by :

$$f = \frac{2(y^2 + a^2)}{(1 + y^2)^{1/2}}. \tag{2.1.12}$$

Solving for y^2 gives the separatrix height as a function of a and f as

$$y^2 = -a^2 + \frac{f^2}{8} \pm \frac{1}{2}\sqrt{f^2\left(\frac{f^2}{16} - a^2 + 1\right)}. \tag{2.1.13}$$

There is therefore an upper separatrix height (H_s) defined by

$$H_s^2 = -a^2 + \frac{f^2}{8} + \frac{1}{2}\sqrt{f^2\left(\frac{f^2}{16} - a^2 + 1\right)} \tag{2.1.14}$$

and a lower separatrix height (h_s) given by

$$h_s^2 = -a^2 + \frac{f^2}{8} - \frac{1}{2}\sqrt{f^2\left(\frac{f^2}{16} - a^2 + 1\right)}. \tag{2.1.15}$$

Let us now evaluate these for values of a that are physically realistic for filament channels. If $a = 1$, the filament has the same length as the channel width, which may be appropriate in some cases for short active-region filaments or for one segment of a filament between two feet or barbs. The upper separatrix, H_s, is given by

$${H_s}^2 = -1 + \frac{f^2}{4}. \tag{2.1.16}$$

${H_s}^2$ is positive definite when $f > 2$, which is the same as condition (2.1.10) for the poles to join in the $y = 0$ plane. As the flux increases, the separatrix height increases. The lower separatrix

does not exist in this case since (2.1.15) gives a negative value for ${h_s}^2({h_s}^2 = -a^2)$. Therefore when $a = 1.0$ the poles initially join in the $y = 0$ plane.

If $a > 1$, the filament is longer than the channel width, which is more appropriate for most observed filament channels. The upper separatrix boundary given by Equation (2.1.14) exists for all flux values such that

$$f > 4\left(a^2 - 1\right)^{1/2}. \tag{2.1.17}$$

This is less strict than condition (2.1.10) for the poles to join in the $y = 0$ plane, so initially as f increases the poles will first join at a certain height above the photosphere depending on the value of a, while remaining unjoined in the photosphere. As the flux increases, the height of the upper separatrix increases.

The lower separatrix (2.1.15) exists when (2.1.17) holds along with

$$\frac{f^2}{8} > a^2 + \frac{1}{2}\sqrt{f^2\left(\frac{f^2}{16} - a^2 + 1\right)}. \tag{2.1.18}$$

The second condition is not satisfied when $f = 2a^2$, i.e. when the poles join in the $y = 0$ plane. Thus a lower bound on the height of the filament channel will exist when

$$4\left(a^2 - 1\right)^{1/2} < f < 2a^2. \tag{2.1.19}$$

When $f > 4(a^2 - 1)^{1/2}$ the poles connect over a certain range of heights and, as the flux f increases, the lower height of the separatrix decreases until it reaches the $y = 0$ plane. Thus when $a > 1$, the upper and lower surfaces of the separatrix exist for a range of flux values and they produce upper and lower bounds on the flux required to connect the poles.

The separatrix surface has also been found by numerical integration. The graph of how its height varies with flux (f) between the poles is shown in Figure 2.2 for the cases when $a = 1, 2, 3, 5$ and is found to agree qualitatively with the order-of-magnitude estimate. For $a = 1$, the separatrix only intersects the y-axis at one point, but for $a > 1$ it does so at an upper and lower surface .

In Table 2.1 a comparison between the order of magnitude estimates of when the poles join and the exact values obtained numerically for the case when $a = 2$ are shown. It can be seen that the order of magnitude calculation gives a reasonable estimate in most cases. Close estimates

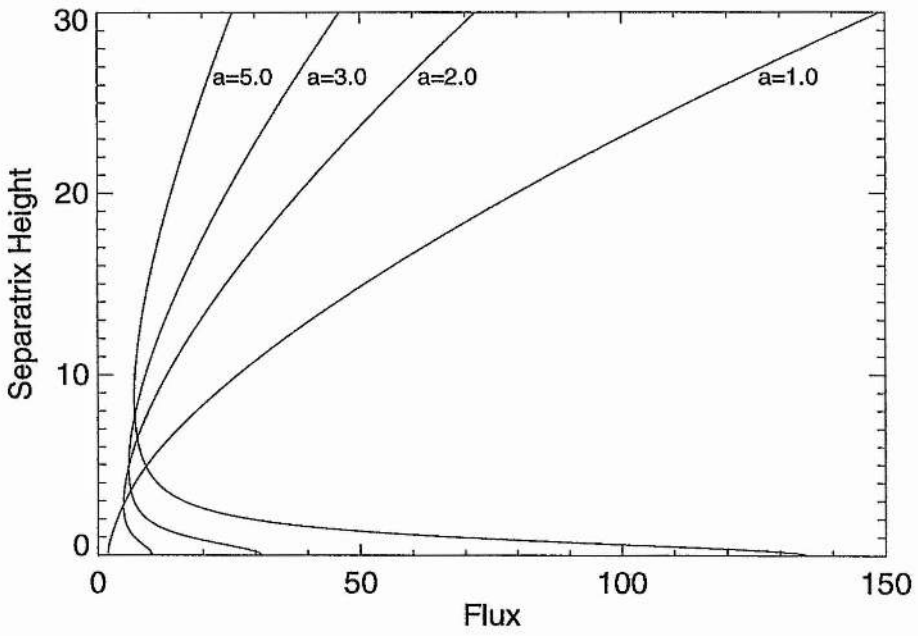

Figure 2.2: Separatrix height versus flux (f) for several values of the half-separation (a) of the point sources in units of the channels half-width.

are also obtained for $a = 1.0, 3.0, 5.0$. However as a and f grow larger the estimate gets worse (Appendix A).

The separatrix surface of the filament channel is shown in Figure 2.3. Figure 2.3(a) shows the three-dimensional structure viewed obliquely, while plots (b) and (c) show the surface from the side and the top. The field lines shown lie on the separatrix surface. There are two neutral points in the photospheric ($y = 0$) plane lying between the positive pole and line source and the negative pole and line source. The field lines all lie out of the $y = 0$ plane but pass near to the neutral points. All field lines inside the surface connect the poles, while field lines lying outside connect a pole to a line source or a line source to a line source. The field lines below the lower separatrix connect the positive and negative line sources, while the field lines that emerge from the positive pole that are not within the surface connect to the negative line source. On either side of the poles and over the top of the surface the line sources are connected. The surface is shown for $a = 2$ and a flux value of $f = 8.0$. This means that the poles are eight times stronger than the line sources.

Property	Order of Magnitude Estimate	Numerical Value
Poles join in $y = 0$ plane	$f > 8.0$	$f > 10.3$
Poles initially join	$f = 6.9$ $y = 1.44$	$f = 4.9$ $y = 2.9$
Sep. heights when $f = 7.0$	1.7 1.1	6.0 1.0

Table 2.1 : Comparison between order of magnitude estimate and numerical values for $a = 2$.

These large flux values are required so that field lines will connect between the poles at heights at which filaments form. This is consistent with the fact that a strong component of the field is inferred from the parallel fibril structure along the axes of a filament channel. For this flux value the poles are not connected in the $y = 0$ plane, so that the separatrix has both an upper and lower surface. Their heights are

$$H_s = 6.8 \text{ units } (2.0 \times 10^5 \text{ km})$$

$$h_s = 0.73 \text{ units } (2.2 \times 10^4 \text{ km}).$$

The lower part of the separatrix creates a lower bound for the filament that is consistent with observations ($10 - 30,000$ km). On the other hand, the value for the upper part of the separatrix is much higher than the observed top of filaments, but it does correspond to the height of the coronal cavity. One possibility, therefore, is that the coronal cavity seen around prominences is the region bounded by the upper part of the separatrix surface; another is that the filament top (or spine, Engvold, private correspondence) is indeed the upper part of the separatrix but that the present calculation overestimates its height since gravity and force-free effects may well lower it. The lower bound to the filament exists when the separation of the sources of the filament is greater than that of the overlying arcade. The effect of the arcade is to create both a lower and an upper bound on the field lines that connect the poles.

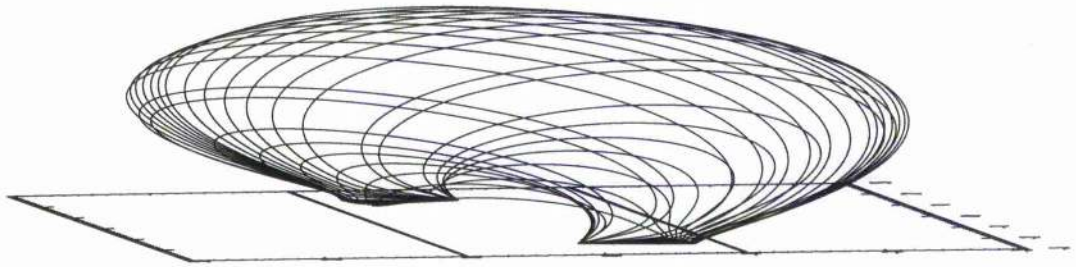

(a)

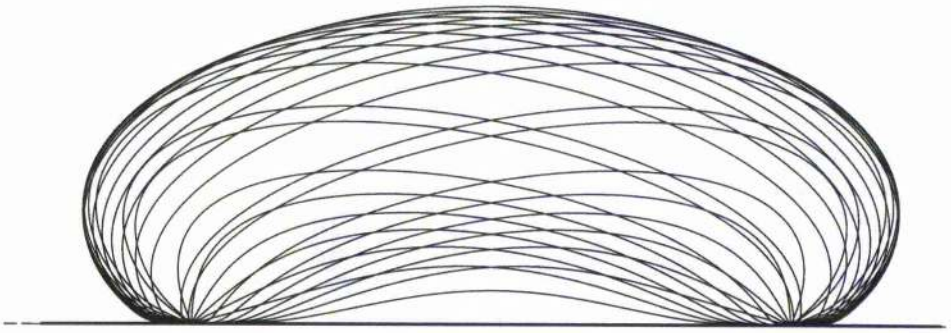

(b)

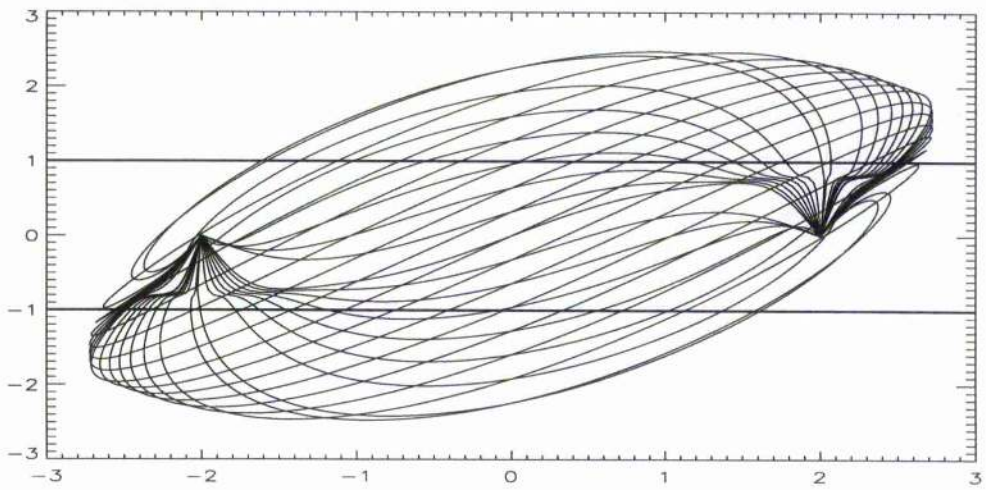

(c)

Figure 2.3: The separatrix surface when $a = 2$ and $f = 8.0$ viewed from (a) an angle, (b) the side, and (c) above.

2.1.3 Free-Fall Time.

The free-fall time for mass to fall down the field lines within the separatrix surface is now calculated. If the free-fall time is greater than the coronal condensation time (τ_c), which is around 3000s (Hood 1992), then it may be possible for dense cool material to condense along the field lines. Under the effect of gravity the cool dense material may then dip down the field lines and produce a configuration within the separatrix surface that can partially support the filament's mass. In simulations of Antiochos and Klimchuck (1991) it was found that if there is a long low-lying loop then there is a possibility for condensations to form at the apex of the loop. This will, however, only occur if there is highly localised heating near the footpoints of the loop (see also Poland and Mariska, 1986). Fielder and Hood (1993) found that the magnetic field of the filament must be highly sheared from the initial, circular, "potential-like" loop for the free-fall time to be greater than the condensation time. In the model here, the field lines are not skewed by shear of footpoints as in Fielder and Hood (1993). However, they are skewed by the configuration and direction of field in the channel. The field lines within the separatrix surface take the form of much longer and lower-lying loops than those of a simple potential arcade.

Two methods are used to calculate the free-fall time. First, the field lines within the separatrix are classed as a plane which is held at a constant angle (θ) to the horizontal. The component of gravity is therefore constant along the field line. In the second method, the free-fall time is calculated for a particle following the path of the field lines. In this case, gravity varies as a function of distance (s) along the field line ($g(s)$) and therefore the field line is not at a constant angle to the horizontal.

Method1.

In Figure 2.4(a) a schematic of the field line is shown and in Figure 2.4(b) its representation in the model is given. The angle θ of the plane to the horizontal is given by

$$\sin\theta = \frac{y_{max}}{s}, \tag{2.1.20}$$

where y_{max} is the height at which the particle starts from rest (the height of the apex of the loop) and s is the total length of the field line that it falls down. Therefore, the field lines are stretched

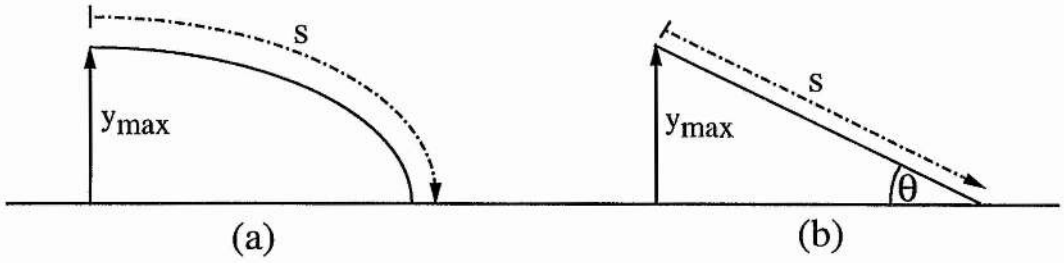

Figure 2.4: (a) Field line showing distance s along it and starting height y_{max}. (b) Representation in model.

out along their entire length and assumed to be at a constant angle to the horizontal. The equation of motion of the particle along the field line is

$$\frac{d^2s}{dt^2} = g_\odot \sin\theta. \tag{2.1.21}$$

Assuming that the particle starts from rest with velocity ($v = 0$) at time ($t = 0$) and from the point $s = 0$, the free-fall time for the particle to fall from a height y_{max} along a field line of length s is

$$t = \sqrt{\frac{2s}{g_\odot \sin\theta}} = \sqrt{\frac{2s^2}{g_\odot y_{max}}}, \tag{2.1.22}$$

and the end velocity at time t is

$$v = g_\odot t \sin\theta = g_\odot t \frac{y_{max}}{s}. \tag{2.1.23}$$

The length of the field lines that lie within the separatrix surface shown in Figure 2.3 are now calculated for field lines lying above the point ($x = 0, z = 0$). For these field lines we are at the apex of the loop. Using Equations (2.1.22) and (2.1.23) the free-fall time in seconds and final velocity in kms^{-1} are shown in Figure 2.5. As can be seen, the free-fall time in the calculation is at best half that of the condensation time, so all of the material that condenses would fall away before the condensation could form a dip. The final velocities on the other hand are two orders of magnitude greater then those observed ($1 \sim 5$ kms^{-1}). This means that the material in the filament cannot attain free-fall speeds. A possible explanation for this is that effects such as wave support (Verwichte 1997) and viscosity prevent the material from reaching free-fall speeds. These effects may therefore aid the filament formation process by keeping the mass in the corona for longer times. At the observed velocities of around 5 kms^{-1} it would take $4\frac{1}{2}$ hours to fall down the lower part of the separatrix, allowing time for the condensation to form.

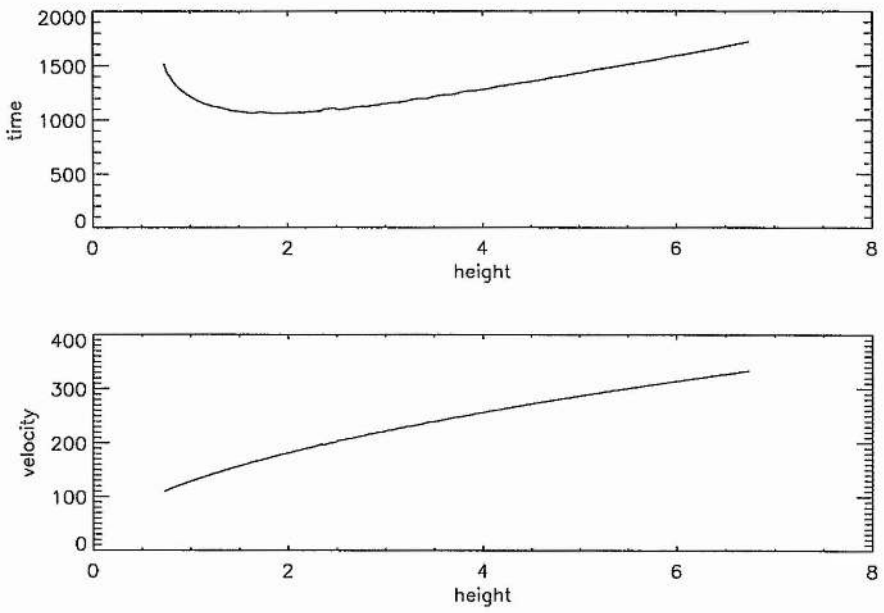

Figure 2.5: Top graph: free-fall time as a function of starting height for constant gravity. Bottom graph: end velocity of particle as a function of starting height for constant gravity.

Method2.

The free-fall time is now calculated using the second method. In this case gravity varies along the loop. The equation of motion along a field line then becomes,

$$\frac{d^2s}{dt^2} = v\frac{dv}{ds} = -g_{\odot}\sin\theta(s), \tag{2.1.24}$$

where

$$\sin\theta(s) = -\frac{B_z(s)}{|\mathbf{B(s)}|}. \tag{2.1.25}$$

Again assuming that the particle starts from rest ($v = 0$) from the point $s = 0$ at $t = 0$, the free-fall time and velocity of the particle now become,

$$v(s) = \sqrt{2\int_0^s g_{\odot} sin\theta(s)ds} \tag{2.1.26}$$

and

$$t = \int_0^s \frac{ds}{v(s)}. \tag{2.1.27}$$

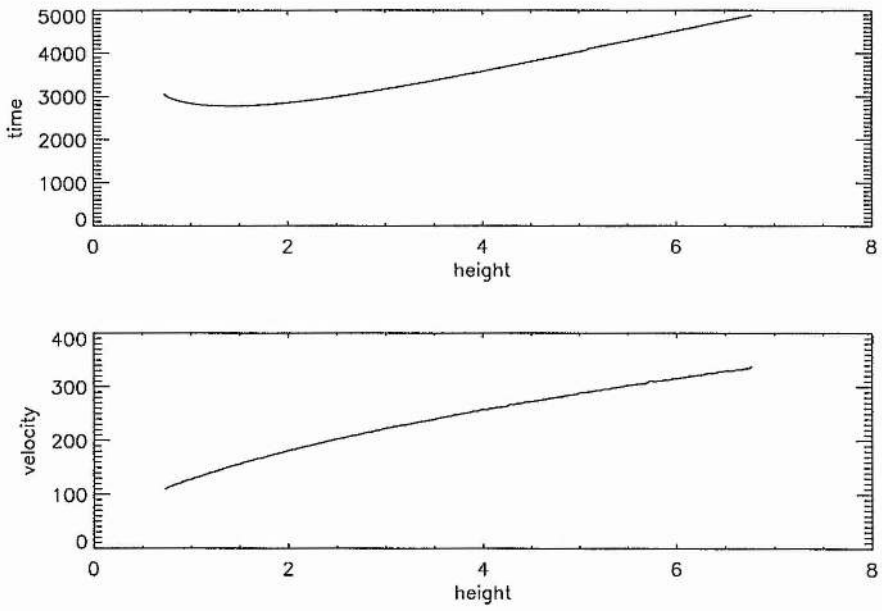

Figure 2.6: Top graph: free-fall time as a function of starting height for variable gravity. Bottom graph: end velocity of particle as a function of starting height for variable gravity.

The free-fall time and final velocity are now calculated for the same set of field lines and are shown in Figure 2.6. With the more accurate model, the free-fall time for the lowest field lines is now of the same magnitude as the condensation time. However, the velocities are very similar to the ones obtained before. By computing a more accurate model the free-fall time has increased by a factor of 2 and the possibility for a condensation producing a dip on the field lines is now greater. The free-fall time increases with height even though the velocities also increase since the field lines are much longer.

The question can now be asked, " Why does the free-fall time increase by more than a factor of two when similar end velocities are obtained as before?" The reason for this is shown in Figure 2.7. The plots show the velocity as a function of distance along the field lines for three heights, $h =$ 0.73 units (lower separatrix), 0.3765 units, and 6.8 units (upper separatrix). The solid curves represent the free-fall velocity using the second method with variable gravity along the field lines and the dashed curve the first method with constant gravity along the field lines. With variable gravity the speed at the top of the loop is much less than with constant gravity. This is because the

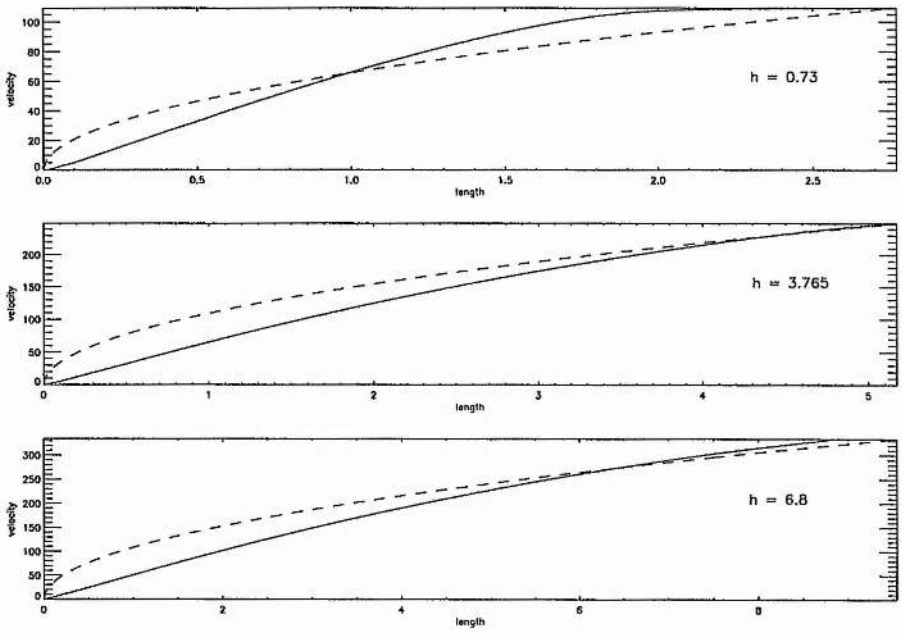

Figure 2.7: Comparison of velocities along field line for variable gravity (solid lines) and constant gravity (dashed lines) for heights of 0.73 units (top), 0.3765 units (middle) and 6.8 units (bottom).

field lines are much flatter at the top. It is only further down the loop that the two velocities become comparable, or the velocity under constant gravity less than that under variable gravity. However, the average velocity across the loop with variable gravity is much less than that with constant gravity and therefore the free-fall time is much longer. This shows that the constant gravity case is not a good approximation to the true geometry and velocities along the loop.

Since the entire enclosed region is too high and wide to represent the whole filament, the next question that can be asked is "On which field lines within the separatrix does the filament form?". Since it is generally accepted that a dip in magnetic field lines must occur before a prominence can form, the flatness of field lines in the separatrix has important consequences for the formation of the filament. The flatter a field line along its entire length, the much larger a chance of forming a dip through condensation. An alternate way of forming dips is shown in Chapter 3, where it is shown that dips in filament structures can be due to the locations of positive and negative regions of flux below the filament. The angles that the field lines make to the horizontal along their length is shown in Figure 2.8. The lower separatrix makes an angle of less than 30° to the horizontal

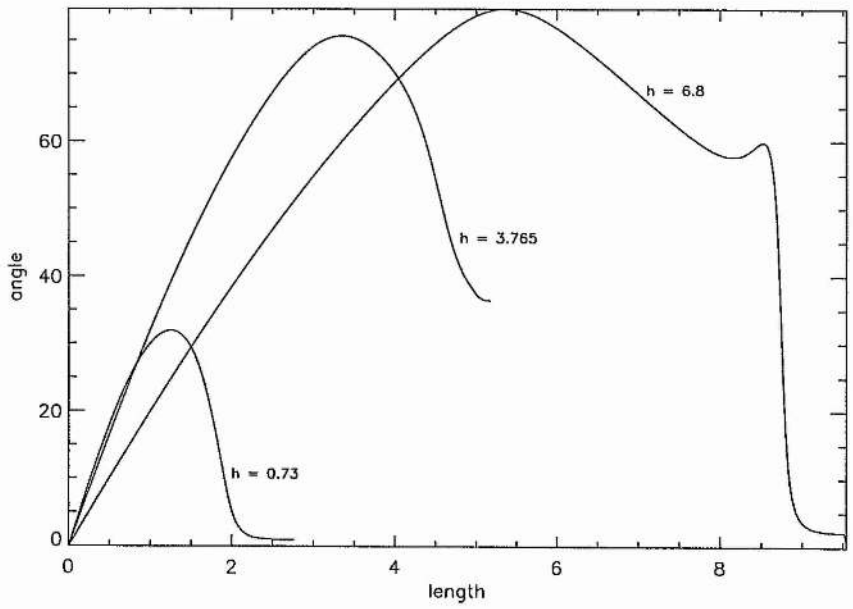

Figure 2.8: Angle of field line to the horizontal for starting heights of 0.73 units, 0.3765 units and 6.8 units.

along its entire length. However, the higher field lines make much larger angles to the horizontal. If a condensation occurred it would be much easier to dip a larger part of the lower field lines than the higher ones since the lower field lines are flatter. As their height increases, the field lines become steeper and less suitable for the support of mass. The filament would therefore be more likely to form in the lower part of the separatrix than in the upper part since in the upper part the field lines have a large concave-down structure which is too steep to support mass. These in fact would be the field lines of the coronal cavity. The cavity is perhaps a region surrounding the prominence which has the same magnetic connectivity as the field lines of the prominence but with field lines that are too steep to support mass, which would just fall down along the field lines. For further details of mass supply and support in this kind of model see Priest *et al.* (1995) and Cartledge (1995). In the next section the field lines in the filament channel are considered for both in and out of the $y = 0$ plane.

2.1.4 Magnetic Field Lines.

In this section the field lines in the filament channel are plotted, first in the $y = 0$ (photospheric) plane and then out of the plane. For some flux values the sources are joined by field lines out of the plane but not in the plane.

The plots in Figure 2.9 show how the field lines for $a = 2$ behave in the $y = 0$ plane for flux values at which the poles are either connected or not connected. In Figure 2.9(a) the flux of the poles is $f = 8.0$, the same flux value used in drawing the separatrix surfaces in Figure 2.3. The field lines are the solid curves and the separatrix lines are dashed. The separatrices go to, or emerge from, the two neutral points where the magnetic field **B** falls to zero (Parnell 1994). These points lie in the $y = 0$ plane between the positive pole and line source and the negative pole and line source. By inspecting the separatrices (which divide up regions of magnetic connectivity) it can be seen that the poles are not joined in the $y = 0$ plane. All of the field lines in that plane from the positive pole goes to the negative line source. In between the two point sources the line sources are connected with each other and on the outside edges they are also connected. From the graph of the separatrix height (Figure 2.2) it can be seen, however, that for $f = 8$ the poles are joined out of the $y = 0$ plane.

In Figure 2.9(b) the field lines are plotted for a flux value of $f = 10$. The poles are nearly connected in the photosphere and the neutral points lie closer to the line sources. The separatrix curves in the centre lie closer to each other and less field lines connect the line sources in the corridor between the poles. Although the field lines do not connect in the $y = 0$ plane they do connect out of the $y = 0$ plane. The upper and lower separatrix surfaces have heights of $H_s = 8.2$ units and $h_s = 0.22$ units, respectively.

As the strength of the poles increases, the separatrix lines become closer. Just before they connect, only one field line joins the line sources between the poles and it passes through the origin.

In Figure 2.9(c) the field lines are plotted for a flux of $f = 20$. The poles are now connected in the $y = 0$ plane. As the strength of the poles increases, the separatrices move further apart and more flux connects between the poles. With this flux value only the upper part of the separatrix exists.

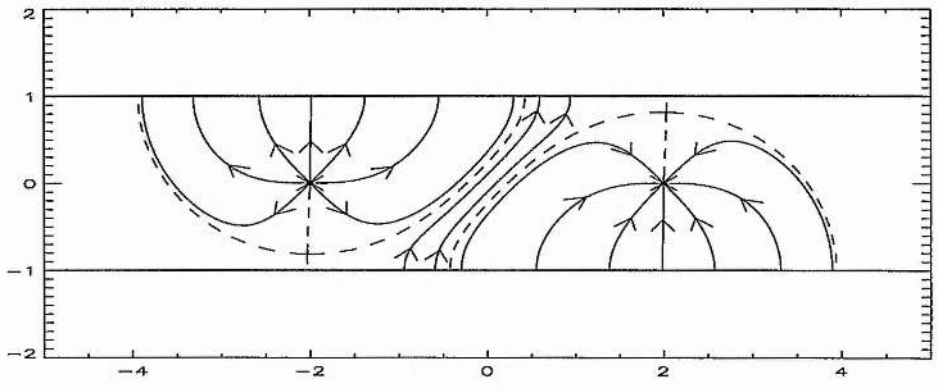

(a)

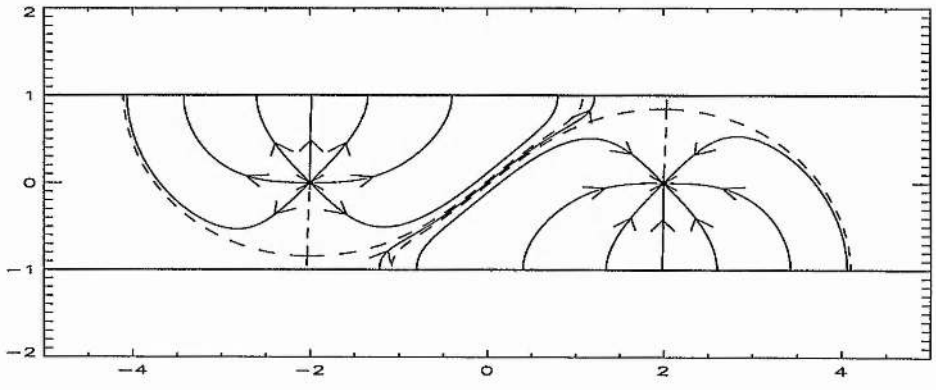

(b)

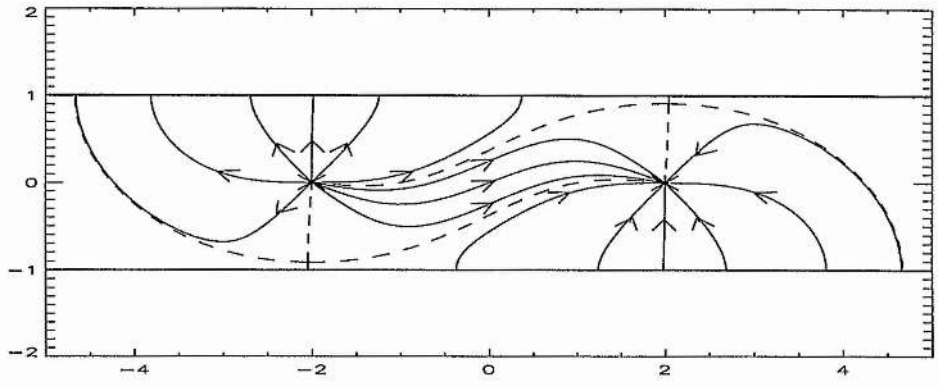

(c)

Figure 2.9: Field lines in the photospheric ($y = 0$) plane for a flux f of (a) 8, (b)10 and (c) 20.

A selection of field lines out of the $y = 0$ plane is plotted in Figure 2.10 for $f = 8$ and $a = 2$. The selected field lines, originate from a circle of radius 0.16 units about the point (0,1.1,0). They lie within the separatrix surface and are in the range of heights observed for filaments. They show a possible structure that could be seen if these field lines were to support condensed material and are some of the flattest in the channel. Figure 2.10(a) shows the 3D structure of the field lines, whereas Figure 2.10(c) is a view from above (i.e. on the solar disc). The flux tube is a long, thin structure with a length of 4 units (120,000 km) and a width of 9,600 km. These values are well within the observed range of values associated with filaments.

Figure 2.10(b) is a view of the field lines looking side on, as would be seen at the limb in which the height of the magnetic field lines can be seen. The lowest field line has a maximum height of 28,000 km while the highest field line has a maximum height of 38,000 km. The field lines are low-lying structures that are flatter at the top, the kind of structure that may be suitable for the accumulation of mass, as already described. This type of model can also explain why there are so many different shapes and types of prominence. The field lines here are just the basic components of the channel field. Different surrounding fields would cause changes in the magnetic topology. These changes would mean that different field lines would be better able to support the accumulation of mass than others. Different surrounding fields would cause different shapes and thus different filament structures.

2.1.5 Arcade Orientation.

The field lines of the arcade overlying the filament channel are now drawn (for $f = 8.0$ and $a = 2.0$). They are initially drawn for the dextral channel and so to be consistent with the results of Martin and M^{c}Allister (1996) the arcades should be left-bearing. In Figure 2.11(a) the field lines of the arcade can be seen from above and they are indeed left-bearing. They are drawn just above the separatrix surface that encloses the flux of the filament and coronal cavity (h $\sim$ 200,000 km , $\frac{1}{3}\ R_{\odot}$). In the simple potential model constructed here the dextral channel will always have left-bearing arcades as the skew of the arcades is due to the direction of the axial component of field in the channel. The axial component itself is a result of the asymmetry of flux locations along the channel. Due to this there will always be a one-to-one correspondence between the filament channel axial component and the large-scale fields overlying the channel.

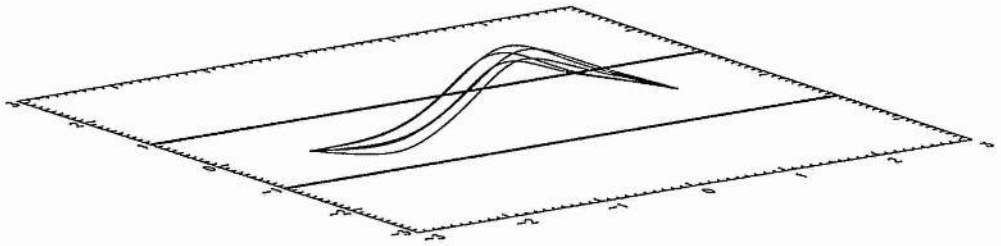

(a)

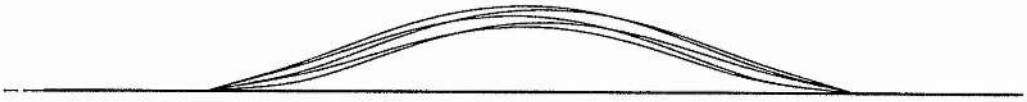

(b)

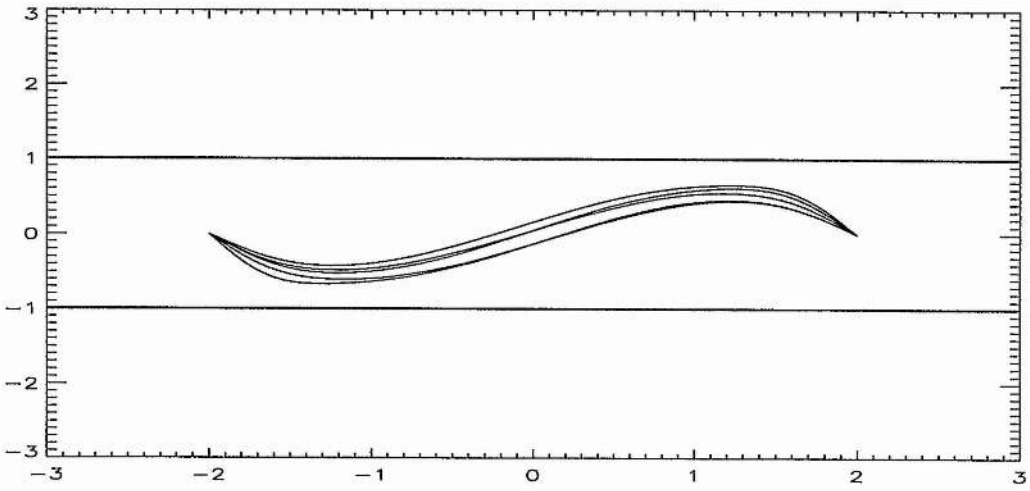

(c)

Figure 2.10: A selection of field lines joining the poles when the flux f is 8 and the pole separation ($2a$) is twice the line source separation ($2b$), viewed (a) obliquely , (b) from the side and (c) from above.

The same is now done for the sinistral channel and the field lines are plotted for the same flux values as before. This time the positive pole is placed at $z = +2$ and the negative pole at $z = -2$ to give an axial component to the left. When the field lines are plotted again at the same height as before it can be seen that the sinistral channel has right-bearing arcades as the observations suggest (Figure 2.11(b)), showing that the arcade orientation above the filament channel just represents that of the underlying axial component. This explanation is, however, a little simple and for a more detailed explanation see Chapter 4.

From the observations of Martin and M^{c}Allister (1996) it was found that all post-eruption dextral channel arcades show a counter-clockwise evolution with increasing height and all post-eruption sinistral channel arcades show a clockwise evolution with increasing height. In Figure 2.11(c) the field lines are plotted at heights of $h_1 = 210,000$ km, $h_2 = 360,000$ km, $h_3 = 510,000$ km and $h_4 = 650,000$ km above the point $z = 0, x = 0$ for the dextral channel and in (d) for the sinistral channel. As expected, there is a counter-clockwise evolution of the arcades with height above the dextral channel and a clockwise evolution of the arcades with height above the sinistral channel. The skew of these field lines as a function of height is now calculated, but only calculated for the dextral channel as the results for the sinistral channel should be exactly the same by symmetry. The skew angle, α, is defined as shown in Figure 1.7 and calculated for points above the origin. A field line that has a large shear due to the axial field of the filament channel will have small α, while a field line that is not sheared will have $\alpha = 90°$. The skew angle of the field lines is given by,

$$\begin{aligned} \tan\alpha &= \frac{B_x(0,y,0)}{B_z(0,y,0)} \\ &= 2\frac{F}{f}\frac{b}{a}\frac{(a^2+y^2)^{\frac{3}{2}}}{(b^2+y^2)} \end{aligned} \tag{2.1.28}$$

For this channel $a = 2.0, b = 1.0, F = 1.0$ giving,

$$\tan\alpha = \frac{1}{f}\frac{(4+y^2)^{\frac{3}{2}}}{(1+y^2)}. \tag{2.1.29}$$

The values of α are now calculated for all heights when $f = 8.0$ and are shown in Figure 2.11(e). On the graph the two dashed lines represent the heights of the lower separatrices (h_s) and upper

separatrix (H_s). At the photosphere ($y = 0.0$ plane) the field lines have a skew of 45°. As the height increases, the skew angle decreases until a minimum value is reached. This is when

$$\frac{d\alpha}{dy} = 0, \tag{2.1.30}$$

where

$$\alpha = \arctan(\theta) \quad , \quad \theta = \frac{1}{f}\frac{(4+y^2)^{\frac{3}{2}}}{(1+y^2)}. \tag{2.1.31}$$

Now

$$\begin{aligned} \frac{d\alpha}{dy} &= \frac{d\alpha}{d\theta}\frac{d\theta}{dy} \\ &= \frac{3y(1+y^2)(4+y^2)^{\frac{1}{2}} - 2y(4+y^2)^{\frac{3}{2}}}{f(1+y^2)^2 + \frac{(4+y^2)^3}{f}}. \end{aligned} \tag{2.1.32}$$

Therefore Equation (2.1.30) is satisfied when

$$3y(1+y^2)(4+y^2)^{\frac{1}{2}} - 2y(4+y^2)^{\frac{3}{2}} = 0 \tag{2.1.33}$$

or $y = +\sqrt{5}$ (67,000 km). At this point we have the maximum shear of the field lines due to the axial component. The skew angle then increases with height and at the height of the upper separatrix (H_s), $\alpha = 43°$. The skew angle continues to increase with height, and due to the decreasing axial component as $y \to \infty$, $\alpha \to 90°$. This shows that we have a changing skew of the field with height or shear from a potential field due to the increasing and decreasing axial component with height.

Although the results give qualitatively the same answer as the observations, we are not fully representing all the physical processes with this model. In the model the change in skew is due to the fact that the axial component grows weaker with height due to the field of the point sources diminishing faster than that of the line sources. A more detailed description is given in chapter 4.

The arcades seen by Martin and M^{c}Allister (1996) are post-eruption arcades, in which an eruption has taken place. These loops appear bright as some of the magnetic energy stored in the field has been converted into internal energy in the plasma. However, insufficient energy conservation takes place for the final magnetic field to be potential - the minimum energy state after an eruption. The changing skew with height probably represents the fact that the field higher

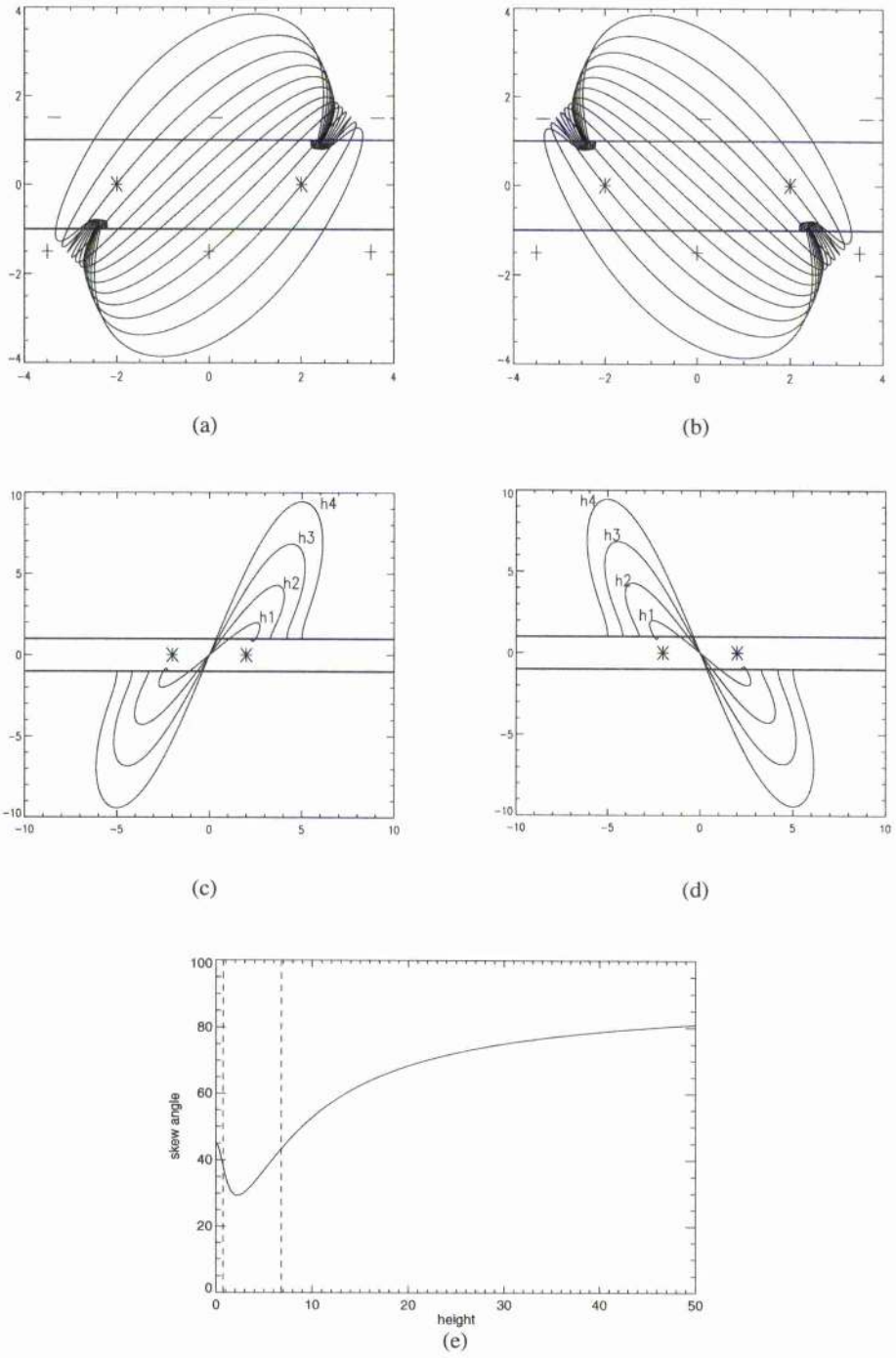

Figure 2.11: Arcade orientation for filament channel with (a) dextral channel $\sim$ left-bearing arcades, (b) sinistral channel $\sim$ right-bearing arcades, (c) dextral channel $\sim$ counterclockwise evolution with height, (d) sinistral channel $\sim$ clockwise evolution with height and (e) graph of skew angle α versus height.

up in the corona is relaxing to a potential field faster through reconnections than the field lower down. The axial field component is partly due to the shear of the field which decreases with height due to field relaxation. The arcades therefore become more transverse with height and rotate in the clockwise direction for sinistral channels and counterclockwise direction for dextral channels. It is these field lines which appear bright at what ever wavelength they are observed following an eruption.

2.1.6 Critical Flux Values.

Important quantities for a filament channel are the critical flux values at which the poles first join in and out of the $y = 0$ plane and the height at which they join (Figure 2.12). Figure 2.12(a) shows how the critical flux (F_{crit}) for the poles to join out of the $y = 0$ plane varies with the pole half-separation (a). It is plotted for $a > 1.0$ and shows that the poles join at relatively small flux values. Figure 2.12(b) plots the critical height (H_{crit}) for the poles to join out of the $y = 0$ plane and how it varies with a. When $a = 1$, the poles join in the $y = 0$ plane. As a increases, the height at which the poles join increases. Thus, as the pole separation increases, larger flux values are required for the poles to connect at heights at which filaments form (< 3 units). Figure 2.12(c) shows the variation with a of the critical flux (f_{crit}) at which the poles join in the $y = 0$ plane. The values of f_{crit} are an order of magnitude greater than those of F_{crit}. This means that, although the poles initially connect at small flux values and large heights, much larger flux values are required for the poles to connect at heights corresponding to filaments, for which a strong field component along the axis is required.

2.1.7 Filament Channel Field Strength.

The model may now be tested to see how the magnitude of the field at the centre of the channel varies with the network flux. To do this, it is assumed that the total line source flux in a length $(-L, L)$ of the channel is F_{total}, typical values of which are about 10^{21} Maxwells (Mx). The length $(-L, L)$ is chosen so that it encloses all of the field lines from the poles. The strength of the line sources is then

$$\pi F = \frac{F_{total}}{2Ll_{unit}}, \tag{2.1.34}$$

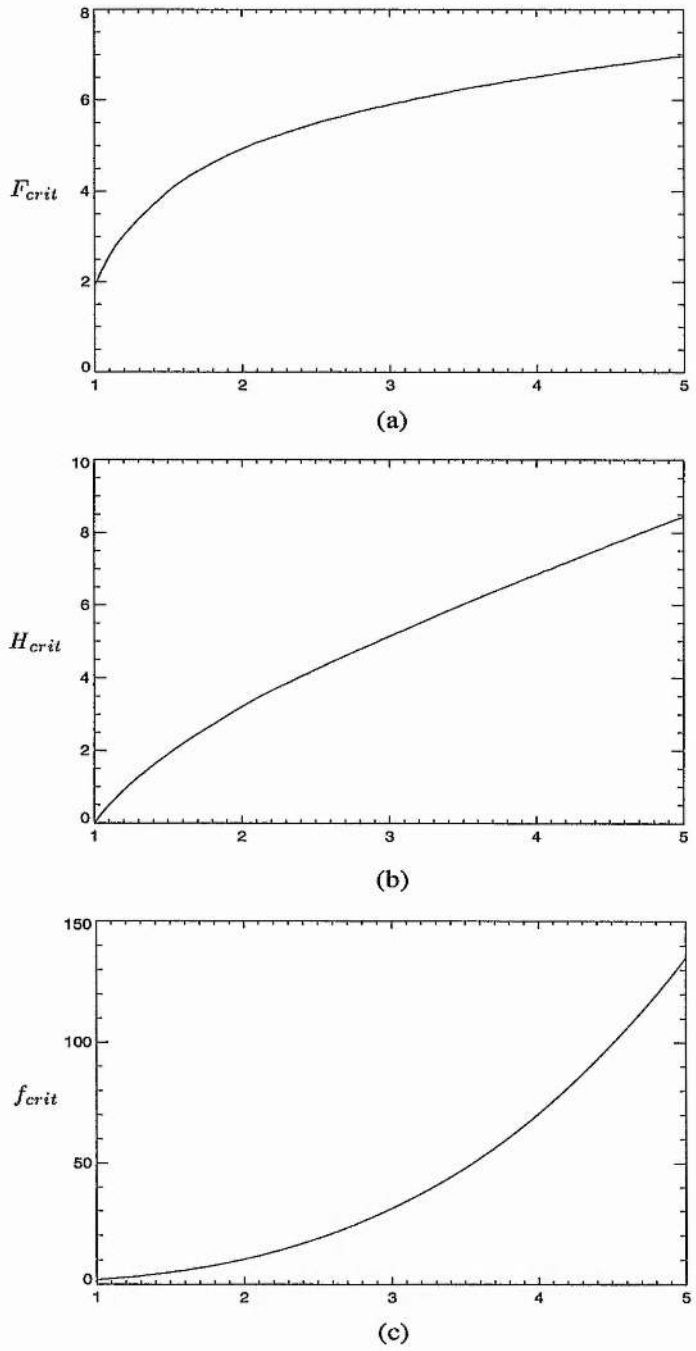

Figure 2.12: The variation with the pole half-separation, a, in units of the channel half-width of (a) the critical flux at which the poles join, (b) the critical height at which they join, and (c) the critical flux for the poles to be joined by field lines lying in the $y = 0$ plane.

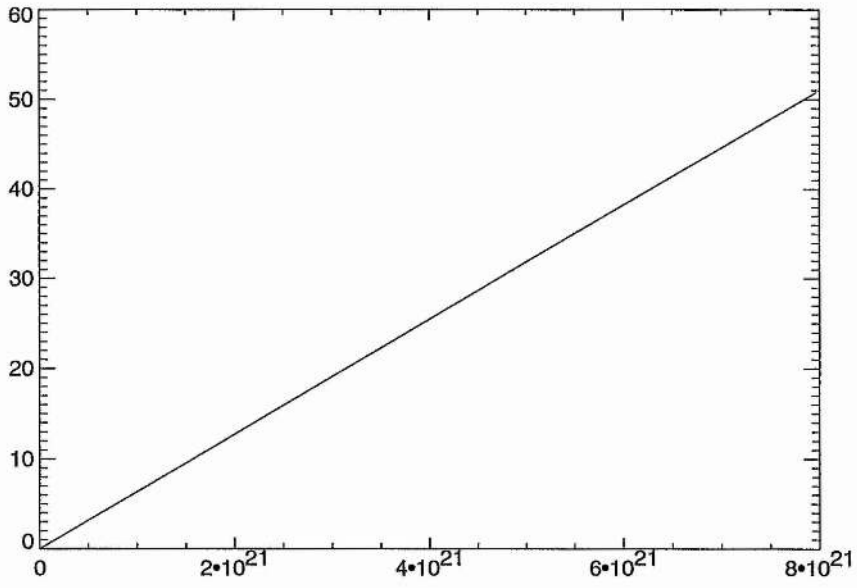

Figure 2.13: Magnetic field (in Gauss) against network flux (in Mx) for a=2,γ = 8 and L = 4.5 at the point (0,0,1.1)

where $l_{unit} = 30,000$ km and is the scale factor used to give πF in Mx/m. Correspondingly the point source strength is

$$\pi f = \gamma \pi F l_{unit} = \frac{\gamma F_{total}}{2L}, \tag{2.1.35}$$

where γ is the ratio between the line and point source fluxes. The units of πf are Mx. The values of the magnitude of the magnetic field B given in Gauss (G) were then plotted against F_{total}, the total network flux, for $\gamma = 8$ and $L = 4.5$ units. This corresponds to the channel shown in Sections 2.1.2 and 2.1.4. The field strength is calculated at the point $(0, 1.1, 0)$, which is in the middle of the field lines plotted in section 2.1.4. From Figure 2.13 it can be seen that reasonable field strengths are obtained for the flux values. When, for example, the network flux is 2×10^{21} Mx the field strength at the centre is 13 G.

2.1.8 Conclusions.

In this section a simple three-dimensional potential model for a filament channel has been set up. A pair of opposite-polarity line sources represents the network flux on both sides of the

polarity inversion line and a pair of point sources models the asymmetry in locations of flux along the channel. It is the asymmetry of magnetic flux locations along a finite length of the polarity inversion line that is crucial in creating the filament channel with its strong field component along the inversion line. A strong horizontal component along the channel is required for the poles to connect at heights at which filaments form. An interesting feature of the model is the presence of a separatrix surface which envelops the flux that joins the point sources along the filament channel. The lower bound of the surface may account for the distinct lower bound that is often observed for prominences on the limb, whereas the upper surface may create the boundary of the coronal cavity. The free-fall time for the field lines within the separatrix is around 3000s, which is the same as the condensation time of the corona, so it may be possible for filaments to form on the lower field lines which are the flattest. It is shown that the arcades lying above the channel have the correct right/left-bearing structure for sinistral/dextral filament channels as observed by Martin and M^{c}Allister (1996). The one-to-one correspondence was due to the arcades being consistent with the underlying axial component of field in the channel.

2.2 Background Uniform Field.

In the filament channel model so far we have two line sources representing the flux of the arcade and two point sources representing the flux of the filament. However, the top of the separatrix is too high to represent the top of the filament, although it does correspond to the top of the coronal cavity. To see if the top separatrix can be lowered to the observed heights of filaments a uniform background field component is now added along the channel. The field of the channel then becomes

$$\begin{aligned} \mathbf{B_{channel}} &= \mathbf{B_{filament}} + \mathbf{B_{arcade}} + \mathbf{B_o} \\ &= \frac{f}{2}\left(\frac{\mathbf{r_1}}{{r_1}^3} - \frac{\mathbf{r_2}}{{r_2}^3}\right) + F\left(\frac{\mathbf{R_3}}{{R_3}^2} - \frac{\mathbf{R_4}}{{R_4}^2}\right) + B_o\hat{\mathbf{z}}, \end{aligned} \tag{2.2.1}$$

where $\mathbf{r_1}, \mathbf{r_2}, \mathbf{R_3}, \mathbf{R_4}$ are given by Equations (2.1.5) and the uniform component is added in the z-direction. The same channel configuration is modelled as before (Fig. 2.1). When $B_o > 0$ the uniform component points to the right when standing on the positive polarity side, in the direction of the field in the channel. However, when $B_o < 0$ it points to the left and is opposite to the field direction in the channel. We now examine whether longer, lower-lying field lines can be created by adding a background uniform field, whilst still keeping the lower and upper bound on the poles joining. The same channel will be modelled as before with

$$a = 2.0, b = 1.0, F = 1.0 \text{ and } 1 \text{ unit} = 30,000 \text{ km}.$$

The strength of the uniform field is chosen relative to the line-source flux. When $B_o = 1.0$, the strength of the uniform field is the same as the strength of the field from a line source at a radius of 1 unit. At all points within this radius, the field of the line source is dominant whereas at all points outside the radius the uniform field dominates. If $B_o = 0.5$, the uniform field has half the strength of the field of the line source at a distance of one unit. The strength of the uniform field is not chosen any greater than 1.0, as we are considering the effect of a weak background component on already existing flux regions. Therefore, at low levels the dominant component must still be due to the sources and sinks of the channel. When $B_o = 1.0$, a field line that passes through a point above the z-axis on $x = 0$ and at a height of 1 unit will be skewed by 45°.

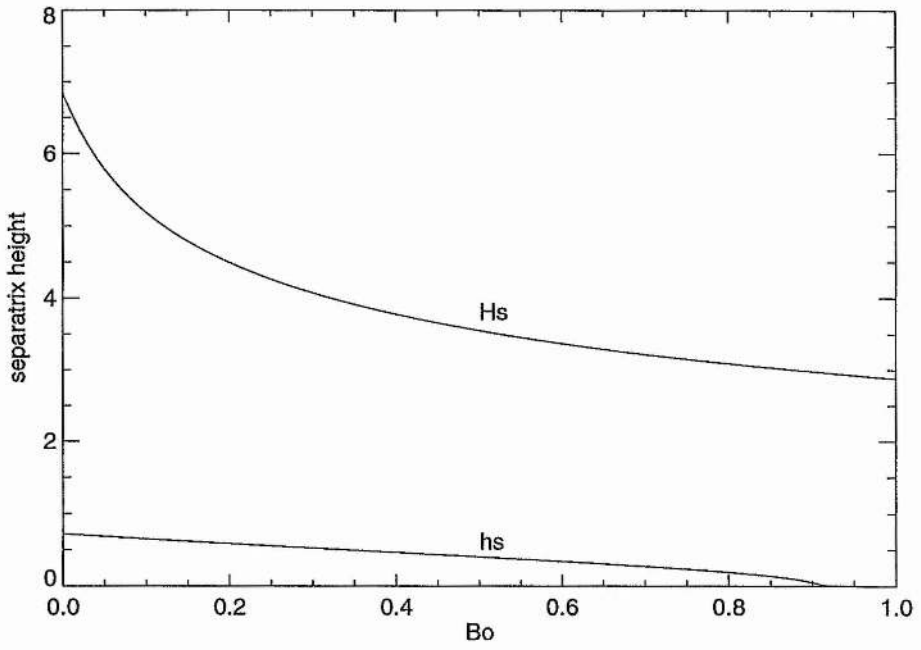

Figure 2.14: Graph of separatrix height versus strength of uniform field for $f = 8.0$

2.2.1 Separatrix Heights.

The uniform field is now added into the filament channel to see by how much it lowers the height of the upper separatrix while still having a lower separatrix for the poles joining. Initially the flux between the poles is kept constant and the heights of the upper (H_s) and lower (h_s) separatrices is calculated as B_o increases from 0 to 1. This is done for the channel modelled before when $f = 8.0$ (Figure 2.14). When $B_o = 0.0$, the separatrix heights are the same as before and as the value of B_o increases the heights decrease. The height of the upper separatrix changes the most, falling from 2×10^5 km to 86,000 km when $B_o = 1.0$. At this field strength the lower separatrix does not exist and the poles are joined in the $y = 0$ plane (h_s initially zero when $B_o = 0.92$). So the uniform field does lower the height of the separatrices, but if it becomes too strong it removes the lower bound. When $B_o = 0.8$, the upper and lower bounds have heights of $H_s = 86,000$ km and $h_s = 6,000$ km, respectively, which are closer to the observed range of heights for filaments. This shows that a background field may easily lower the height of the upper separatrix to more reasonable values for filaments. In the next graph (Figure 2.15), the heights of the lower and upper separatrices are

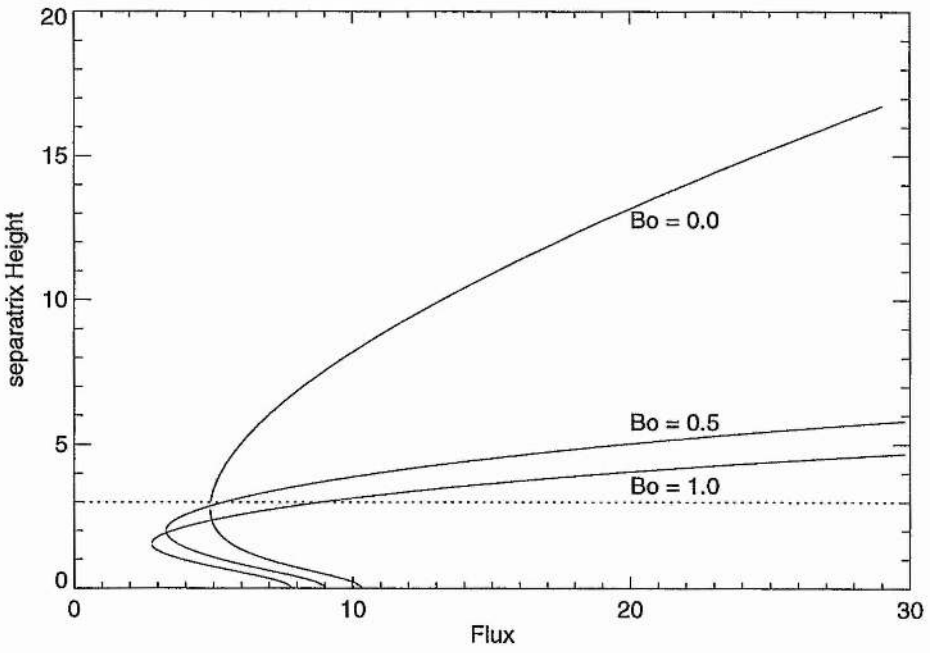

Figure 2.15: Graph of separatrix height versus pole strength for various values of B_o.

calculated as the flux between the poles is increased for fixed values of B_o ($B_o = 0.0, 0.5, 1.0$). The dotted line shows the maximum height that the top of the separatrix should be for a realistic filament structure ($h < 90,000$ km). When $B_o = 0.5$ and 1.0, a larger proportion of the upper and lower separatrices lie below the dashed line compared to when $B_o = 0.0$. As the value of B_o increases, the poles initially join for smaller flux values and the height at which they initially join decreases. All heights of the lower separatrices are now consistent with the height of the lower bound of filaments. Also, as B_o increases, the poles join in the $y = 0$ plane for small flux values compared to when $B_o = 0.0$. Therefore, the effect of adding a uniform field with $B_o > 0$ is to shift the graph to the left of its initial position where smaller flux values are required. This is just an effect of adding a constant component of field in the direction of the field in the channel. If $B_o < 0$ the graph would be shifted to the right and larger flux values would be required since the constant component is added opposite to the direction of the field in the channel. This can be seen in Figure 2.16 where the separatrix heights are shown for background fields of $B_o = 1.0, -1.0$ in the z-direction (solid lines) and for $B_o = 1.0$ in the x-direction (dashed line), which is parallel to

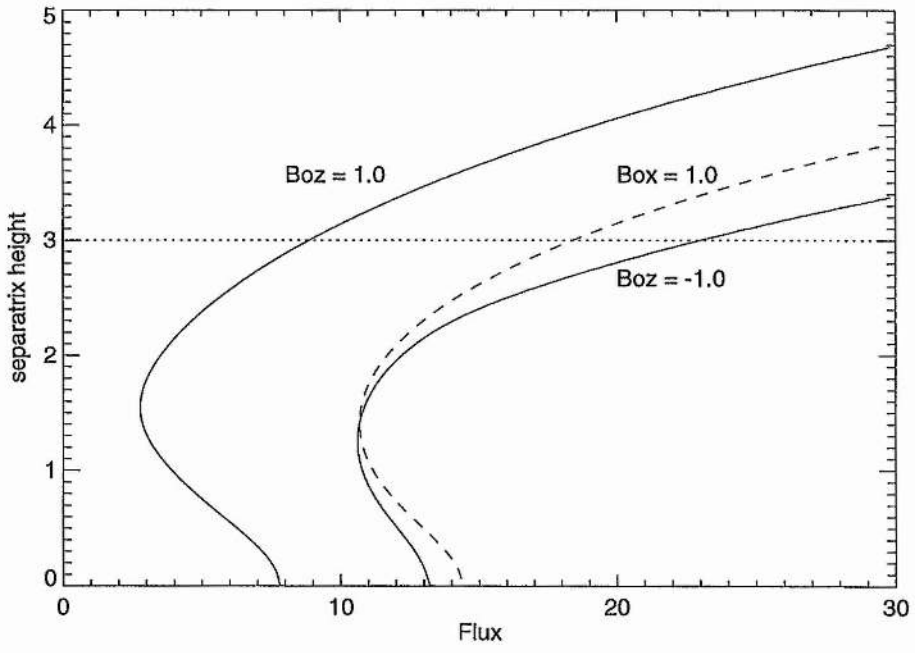

Figure 2.16: Separatrix height when a background field is added in different directions.

the direction of the field of the arcade.

In all cases similar results are obtained as before with the graph just shifted to the right or left from the $B_o = 0$ position. This shows that the upper and lower bound of the separatrix surface can be made more consistent with heights of filaments when a weak uniform field is added. It does not matter in which direction the field is added as similar results are always obtained. However, larger flux values are required when the background field is not added in the same direction as the field of the channel. When $B_o = 1.0\,\hat{\mathbf{z}}$, the curve lies below a height of $90,000$ km for all flux values below $f = 9.0$, and therefore there is a large range of values for which the separatrix heights are consistent with the upper and lower bounds of filaments. From this it can be seen that the upper separatrix height is dramatically reduced when a background uniform field is applied.

2.2.2 Separatrix Surface.

The separatrix surface of the flux connecting along the channel is now calculated when $B_o = 1.0$ and shown in Figure 2.18 for $f = 3.25$. The poles were not connected for this flux value before the

uniform field was added. The height of the upper separatrix is $54,000$ km and the lower separatrix is $36,000$ km. Both of these values are well within the observed range of values for prominences. The field lines lying on the surface can be seen side-on in Figure 2.18 (a). Again distinct upper and lower bounds can be seen. The structure now looks much closer to the observed structure of filaments at the limb. The field lines are flatter than before and are of a topology that may be dipped down if condensed material is present. In Figure 2.18 (b) the field lines can be seen from above. With the uniform field added we have a much thinner structure (12,000 km wide) which is more realistic for a filament. The filament would again exist in the centre-most region where the field lines are the flattest and most able to support mass. The field lines that could not support mass would again be the field lines of the coronal cavity, although its size is much reduced compared to the last example. The field lines and separatrix lines for the channel in the $y = 0$ plane are shown in Figure 2.18 (c). Again the field lines are given by the solid lines and the separatrix lines by the dashed lines. The two neutral points this time are located at $x = \pm 2.2, z = \pm 0.64$. The separatrix lines on the outside are now more compressed, while the lines on the inside are more elongated. The background uniform field does not have a large effect on the field lines in this plane. It only affects the field higher up where the field strength due to the sources is weaker. By introducing a background uniform field the main characteristics of the channel are kept, but the scales are made much more consistent with those observed for filaments.

The free-fall time is also calculated for the separatrix structure. Again gravity is taken to be a function of distance along the field line and the same formulation is used as in the last section. In Figure 2.17 the two graphs of free-fall time and velocity versus height are shown. With a much flatter structure the free-fall time is longer than in the previous case. For field lines within the separatrix it runs from 3900s to 4800s which is now much longer than the condensation time. At the previous heights the free-fall time was around 2800s. There is therefore a much higher chance of forming a dip in this structure through condensation than in the previous case. The free-fall velocities are in the range 140 kms^{-1} to 170 kms^{-1} which are very similar to those before but far above the observed velocities. If a particle fell at the observed velocities ($\sim$ 5 kms^{-1}) it would take $4 - 6$ hrs to fall down the lower and upper bounds of the separatrix thus giving plenty of time to form a dip. This time-scale is also in the range of the time required for a filament to form.

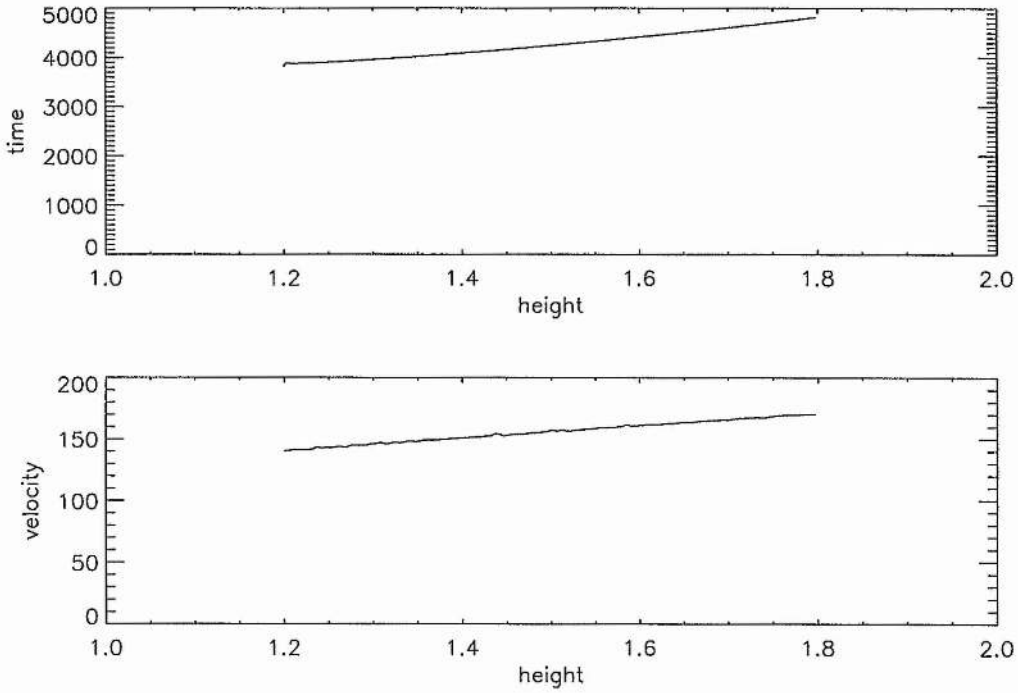

Figure 2.17: Top graph: free-fall time as a function of starting height for variable gravity. Bottom graph: end velocity of particle as a function of starting height for variable gravity.

2.2.3 Strength of Background Field.

In the analytical filament channel model a uniform field component has been added to represent an overlying background field. This component of field would be due to the neighbouring flux regions that surround the filament channel. It is required to lower the separatrix to heights that are more consistent with filaments, something best achieved for $B_o = 1.0$, i.e. when the strength of the uniform field is the same as the strength of the line source at a distance of 1 unit. In Table 2.2 the strength of the background field is shown for various flux values. The total flux F_{total} is defined by Equation (2.1.34) and L is again 4.5 units.

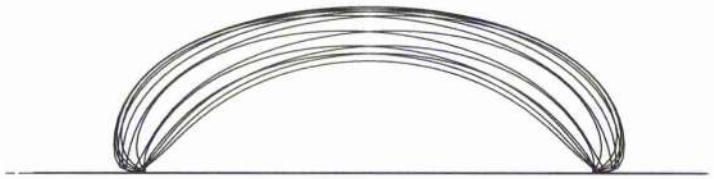

(a)

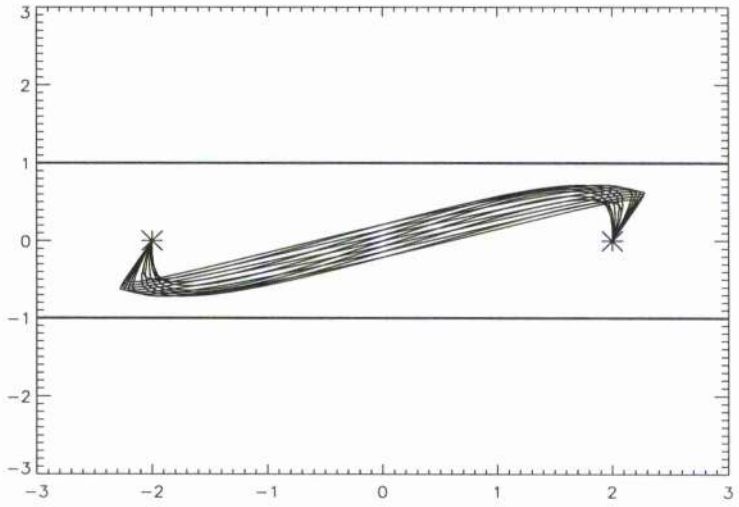

(b)

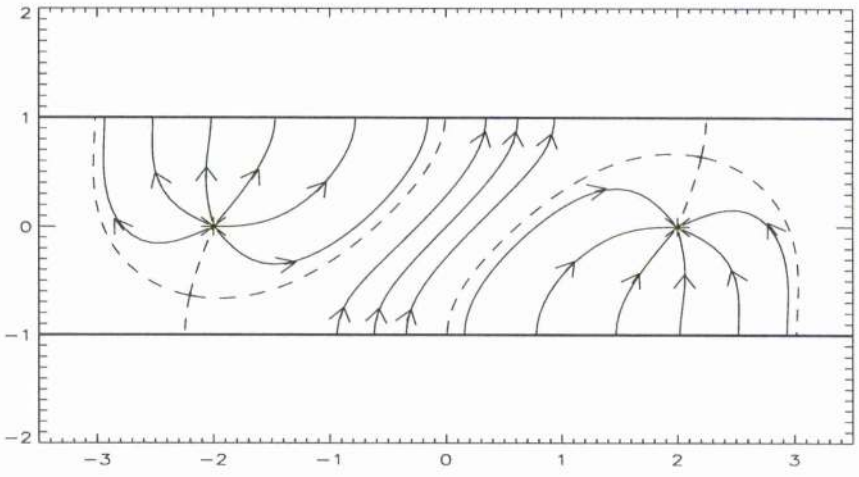

(c)

Figure 2.18: The separatrix surface when $a = 2.0, f = 3.5$ and $B_o = 1.0$ viewed from (a) the side, (b) above for field lines out of $y = 0$ plane and (c) for field lines in $y = 0$ plane.

F_{total} (Mx)	F ($\mathrm{Mxm^{-1}}$)	B_O (G)
1×10^{20}	1.179×10^{9}	0.4
2.5×10^{20}	2.947×10^{9}	1.0
1×10^{21}	1.179×10^{10}	4.0
1×10^{22}	1.179×10^{11}	40.0

Table 2.2 : Strength of uniform field for different values of the network flux.

For quiet regions on the Sun, where the network flux on either side of the channel is around 2.5×10^{20} Mx, a background field of around 1G is sufficient to lower the separatrix to observed heights. These quiet-region flux values would represent channels at higher latitudes on the Sun or on the polar crown. The 1G background field could then be due to the large region of weak unipolar flux on the pole. However, at lower latitudes, where the fields are much stronger and the network flux is around 1.0×10^{22} Mx, a background field of 40 G is required to lower the separatrix to the same height as for the weak field case. Active-region filaments tend to be much lower than the high-latitude quiescent filaments with heights generally below 20,000 km. From Figure 2.15 it can be seen that when $B_o = 1.0$ at no point on the curve are both the upper and lower bounds below this height, suggesting that a much stronger uniform field (> 40 G) would be required to achieve heights below 20,000 km. However, a background field of this magnitude cannot be accounted for (see Chapter 4). Thus, the filament channel model with a weak background field can easily fit the observed ranges of heights for large quiescent filaments at high latitudes; but the modelling is not consistent with the low-lying active-region filaments. The formation and structure of these objects is more likely related to the large-scale emergences of new flux and therefore the potential model may not be suitable for these, where magnetic shear may play an important effect as shown in Chapter 4.

2.2.4 Conclusions.

With a weak overlying background field added to the filament channel model of the last section, it is found that a large change in height of the lower and upper separatrices can occur compared to previous values. For quiet-region flux values, the upper and lower separatrices can be reduced

to the heights of the upper and lower bounds of quiescent filaments when a 1G background field is added. This size of field can easily be accounted for, as it could be due to the polar field of the Sun. The field lines within the separatrix are then much flatter than before and, with this, the free-fall time increased by over $1 - 2000$s which in turn, increased the chance of a condensation forming a dip and then a filament. For lower latitudes a background field in excess of 40 G would be required to describe active-region filaments. This size of field cannot be accounted for and therefore the potential model cannot describe those kinds of structures. The potential model with a background field added may, however, be a reasonable approximation for the higher-latitude quiescent filaments. However, with this type of modelling many different scales of structure can be found depending on the strength of the poles and uniform field. It is therefore important to model real examples from observations as shown in Chapters 3 and 4.

2.3 Force-Free Filament Channel Model.

So far, a simple, analytical, potential filament channel model has been constructed. In this model (Section 2.1) it was found that if, the separation of the sources representing the flux of the filament is greater than that of the overlying arcade, both an upper and lower bound can be produced for the sources connecting along the channel. The lower bound represents the lower bound of the filament and the upper bound at best the top of the coronal cavity. The modelling is now repeated but this time, numerically. Using the multigrid code described in Chapter 4 the filament channel will be considered for both the potential and non-potential (linear force-free field) cases. More realistic flux distributions that represent the filament flux and arcade flux are chosen. The linear force-free field case should give a more realistic structure since filaments are much denser than their surroundings and therefore some support of mass has to occur, thus requiring a current. To lowest order the magnetic forces dominate the momentum equation and therefore a force-free model may give a good representation of the field in a filament. Furthermore, a non-potential magnetic field can store the excess energy required for a filament to erupt. The modelling will consider how the structure that represents the filament changes as the value of alpha (Equation 1.4.10) is changed for fixed flux values, in particular, whether magnetic shear raises or lowers the top of the separatrix. In Figure 2.19 a schematic diagram of the channel and coordinate system used is shown.

For the numerical code, only the vertical component of field at the $z = -1$ (photospheric) plane is specified. For the circular sources that represent the flux of the filament it is given by

$$B_z = \pm\frac{B_{oc}}{2}\left(1+\cos\left(\frac{\pi r}{r_c}\right)\right), \quad 0 \le r \le r_c, \tag{2.3.1}$$

where r_c is the radius of the source which is centred at either $(-a,0)$ or $(a,0)$, B_{oc} is the central strength and r is the distance from the centre of the respective source, $r^2 = (x \pm a)^2 + y^2$. The source centred at (-a,0) is taken to represent the region of positive flux and the source at (a,0) the region of negative flux. The flux passing through one of the circular regions is

$$Flux = \int_A \mathbf{B}.\mathbf{dA} = \frac{\pi}{2}B_{oc}\left(1-\frac{4}{\pi^2}\right)r_c^2, \tag{2.3.2}$$

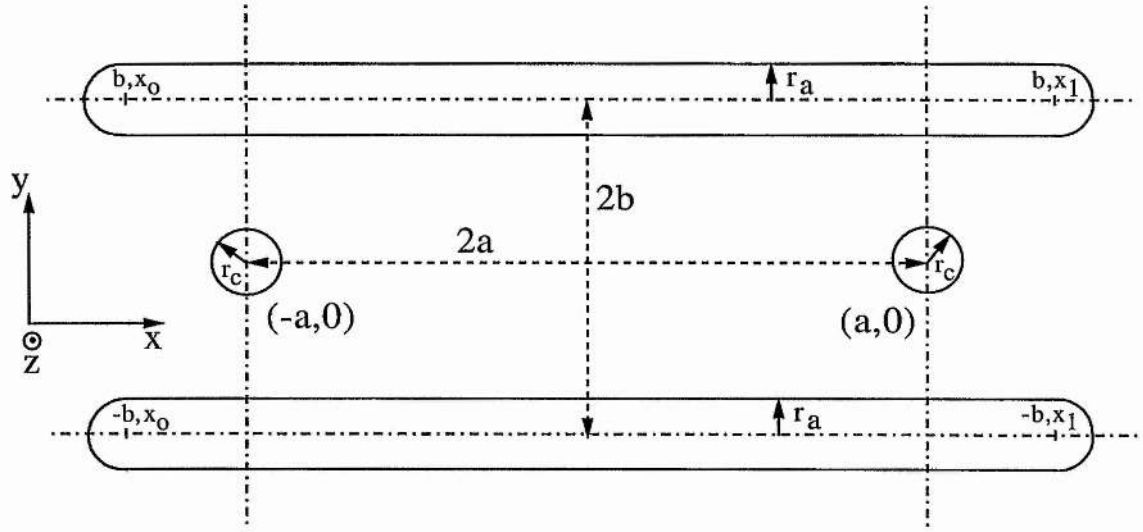

Figure 2.19: Schematic diagram of the locations of sources and sinks in the channel.

where **dA** = rdrdθ $\hat{z}$. For the elongated regions of flux that represent the arcades, the vertical component of field is given by

$$B_z = \pm\frac{B_{oa}}{2}\left(1+\cos\left(\frac{\pi d}{r_a}\right)\right), \quad x_o \le x \le x_1, \quad 0 \le d \le r_a \tag{2.3.3}$$

and

$$B_z = \pm\frac{B_{oa}}{2}\left(1+\cos\left(\frac{\pi r}{r_a}\right)\right), \quad x \le x_o, x \ge x_1, \quad 0 \le r \le r_a, \tag{2.3.4}$$

where B_{oa} is the central strength of the elongated source and r_a its half width. Also,

$$d = y \pm b \tag{2.3.5}$$

$$r^2 = (x-x_o)^2 + (y \pm b)^2, x \le x_o \tag{2.3.6}$$

$$r^2 = (x-x_1)^2 + (y \pm b)^2, x \ge x_1.$$

From this it can be seen that the arcade flux regions have two components. The first is the main body given by Equation (2.3.3). It runs from $x_o \rightarrow x_1$ and has width $2r_a$. The vertical component of field across it depends only on the y-distance from the centre ($y = \pm b$) and falls off with the cosine in the y-direction. At the end of each of these regions a semicircular region of flux

given by Equation (2.3.4) is placed to complete the shape. The source placed on the $y = -b$ line is the region of positive flux and the source placed along the $y = b$ line represents the region of negative flux. With this source configuration a dextral channel is produced; i.e the direction of the field points to the right when standing on the positive polarity side.

The flux passing through the arcade sources is given by

$$Flux = \int_A \mathbf{B}.\mathbf{dA} = B_{oa}\left[\frac{\pi}{2}\left(1 - \frac{4}{\pi^2}\right)r_a^2 + Lr_a\right], \tag{2.3.7}$$

where $L = x_1 - x_0$ is the length of the main body of the elongated area. The channel will now be computed when $a = b$ and $a = 2b$. Each of these cases will be modelled twice with different boundary conditions and compared with the analytical potential model. By doing this it will be seen how well the point source representation (Section 2.1) compares with the present numerical model and more realistic flux distributions. Also, by considering two cases it will be seen how the solution depends on or is affected by the bottom and side boundary conditions of the box (Chapter 4). For each case, the height of the lower and upper separatrix surface of the flux tube connecting the two circular sources along the channel is calculated for points above the origin $x = 0, y = 0$. The width of the structure is also calculated as alpha is varied.

2.3.1 Case1.

In the first case the sources are positioned such that,

$$\begin{aligned} x_o &= \text{-0.84375} \\ x_1 &= 0.84375 \\ b &= 0.34375 \\ r_a &= 0.1 \\ r_c &= 0.1 \\ L &= 1.6875. \end{aligned}$$

As with the simple potential model all lengths and fluxes are scaled such that

$$\begin{aligned} b &= 1 \text{ unit} = 30{,}000 \text{ km} \\ B_{oa} &= 1.0. \end{aligned}$$

With this scaling the maximum height above the photosphere that can be reached, due to the top of the box is 5.8 units or 175,000 km. The field lines in the channel will now be computed for flux ratios of $\frac{F_c}{F_a} = 1.0, 0.75, 0.5, 0.25, 0.1$. The more realistic solutions should be when the flux of the circular sources is much less than the flux of the arcade sources. The ratio of fluxes is given by

$$\frac{F_c}{F_a} = \frac{\frac{\pi}{2} B_{oc} \left(1 - \frac{4}{\pi^2}\right) r_c^2}{B_{oa} \left[\frac{\pi}{2} \left(1 - \frac{4}{\pi^2}\right) r_a^2 + L r_a\right]}, \tag{2.3.8}$$

and for this case it is

$$\frac{F_c}{F_a} = 0.05245 \frac{B_{oc}}{B_{oa}}. \tag{2.3.9}$$

The table below shows the central strength of the circular sources for each of the flux values when $B_{oa} = 1.0$.

F_c/F_a	B_{oc}
1.0	19.0
0.75	14.3
0.5	9.53
0.25	4.766
0.1	1.9

Table 2.3: Flux ratio of circular and arcade sources and maximum field strength at centre of each circular region for case1.

a=b.

The numerical code is first run for the case when $a = b = 0.34375$, when the separation of the two circles is the same as that of the two arcades. The separatrix height and width of the flux tube connecting the two circular regions of flux are calculated for each flux ratio and value of alpha (Figure 2.20). The top graph gives the separatrix height (H_s/b) versus alpha. Since we have a confined box system the top of the separatrix is constrained to be below the top of the box (5.8 units). This boundary is shown as the solid line. However when the field lines approach the

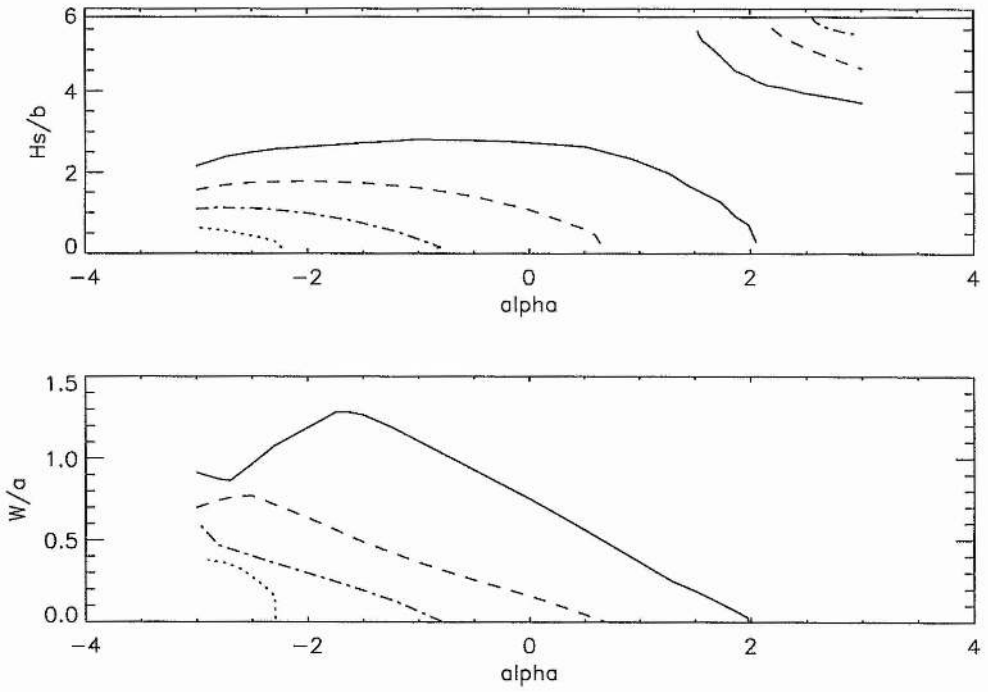

Figure 2.20: Graph of separatrix height (H_s/b, top) and width of flux tube (W/a,bottom) versus alpha for various flux ratios. The separatrix height is shown for the flux ratios of $\frac{F_c}{F_a} = 1.0$ (solid), 0.5 (dashed), 0.25 (dash-dot), 0.1 (dot).

top or sides of the box they become affected by the boundary conditions and become unphysical. The second graph gives the width of the flux tube (W/a) versus alpha. For a realistic filament we would require the width of the structure to be much less than its length. Similar results are obtained to those of the analytical potential model, but there are some differences. Again, as in the corresponding analytical case, when the flux regions connect they do so with only an upper bound and no lower bound, since they are connected in the photospheric plane through $x = 0, y = 0$. It is interesting to note that if the flux is too weak to connect the circular sources in the potential case ($\frac{F_c}{F_a} = 0.25, 0.1$), connections can be made by varying alpha.

For $\frac{F_c}{F_a} = 1.0$ (solid line) as alpha is increased from zero to positive values the height of the upper bound of the separatrix decreases and, with that, the width of the structure also decreases. This can be seen in Figure 2.21 which shows the separatrix surface for $\alpha = 0.0$ (left) and 1.4

(right) with the surface seen from the (a) top, (b) the side and (c) an oblique angle in each case. The changes in the structure are due to the type of twisting that is being added to the field. In Figure 2.22 we see the horizontal field vectors (B_x, B_y) plotted at a height of 7 grid points (19,000 km). The vectors are shown for both the potential case (black arrows) and the force-free case with $\alpha = 1.4$ (red arrows). It can be seen that when a positive value of alpha is used, the field vectors at the centre of the channel rotate in an anti-clockwise direction from that of the potential field. This rotation of the field makes it easier for the flux of the positive circular source to connect to the negative arcade at the top of the channel as more flux from the circular source can now connect across the channel rather than along it. Therefore the flux tube connecting the two circular sources decreases with height and width as the value of alpha is increased as shown in Figure 2.21. At the bottom left-hand corner and top right-hand corner of the channel (Figure 2.22), the horizontal field vectors are very small compared to the ones at the centre of the channel. This is due to the two positive regions of flux and two negative regions of flux interacting with each other. The flux emerging from the two positive and two negative regions is such that their horizontal components are oppositely directed at these two locations. The horizontal components nearly cancel out, leaving only a dominant vertical component which points upwards at the bottom left of the channel and downwards at the top right.

Once a value of $\alpha = 1.5$ is reached, the two circular flux regions connect over two ranges of height. They are connected from the photospheric plane to the height of the upper separatrix ($\alpha = 1.8$, $H_s = 1.2$ units) and then they are connected over the top of the arcade sources from a height of 4.5 units (135,000 km) to the top of the box. In Figure 2.23 the field lines can be seen over the two domains of connectivity. The second domain of connection is due to the boundary conditions in the box and is unphysical. As the value of alpha is increased from $\alpha = 0.0$, the region of dominant vertical field at the lower left-hand and upper right-hand corners in Figure 2.22 becomes stronger. Eventually, when enough twisting is added, the field is directed up the side wall of the box, along the top and down the other side into the negative region of flux leading to the second unphysical domain of connectivity.

The same type of graph is obtained for $\frac{F_c}{F_a} = 0.5$. However, since the flux is much weaker, the two circular sources become disconnected for a much lower (positive) value of alpha. Correspondingly, a much larger value of alpha is required for the sources to connect over the top of the arcade.

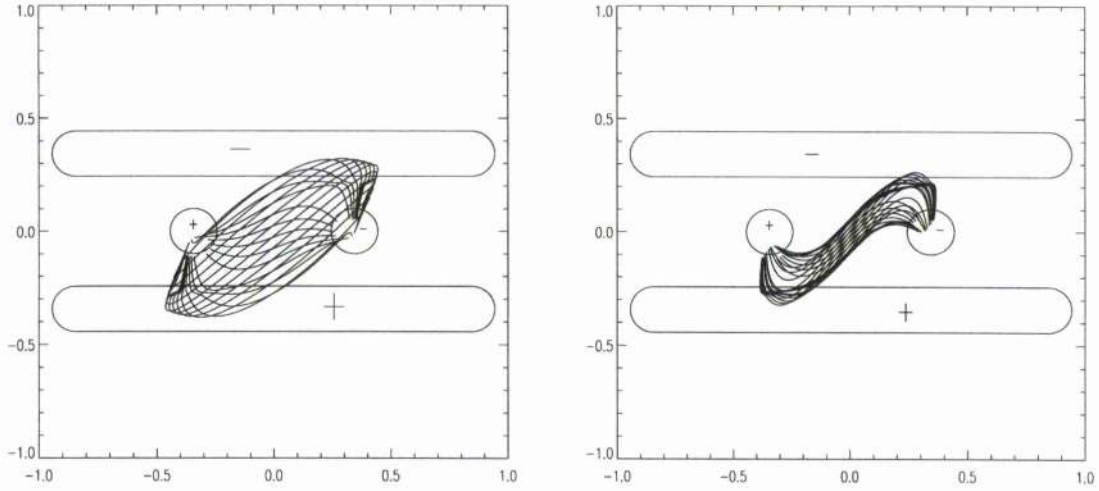

(a)

(b)

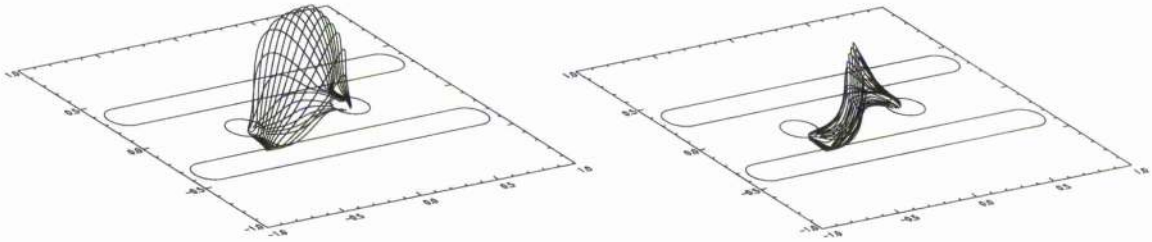

(c)

Figure 2.21: Separatrix surface for flux connecting circular sources for $\alpha = 0.0$ (left) and 1.4 (right). $F_c/F_a = 1.0$ and $a = b$ in each case.

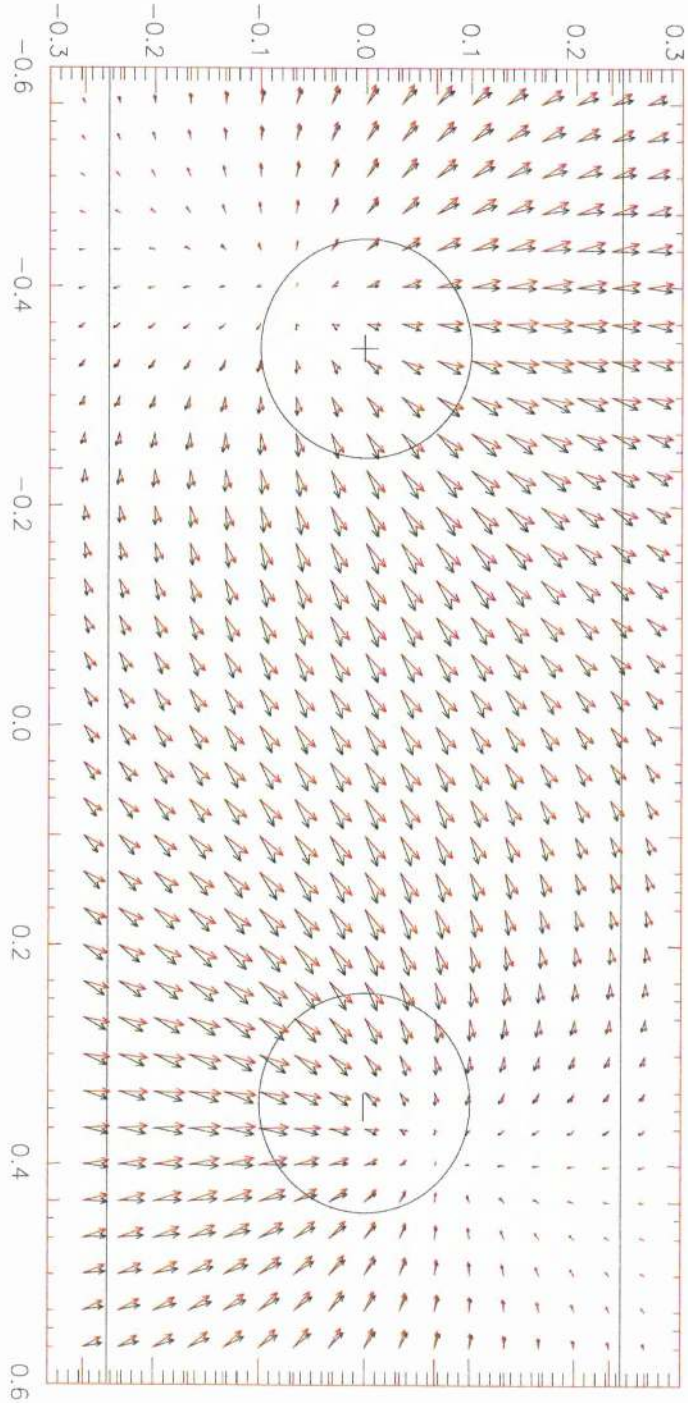

Figure 2.22: Horizontal field vectors (B_x, B_y) for the potential ($\alpha = 0.0$) field (black) and linear force-free ($\alpha = 1.4$) field (red) for $F_c/F_a = 1.0$ and $a = b$.

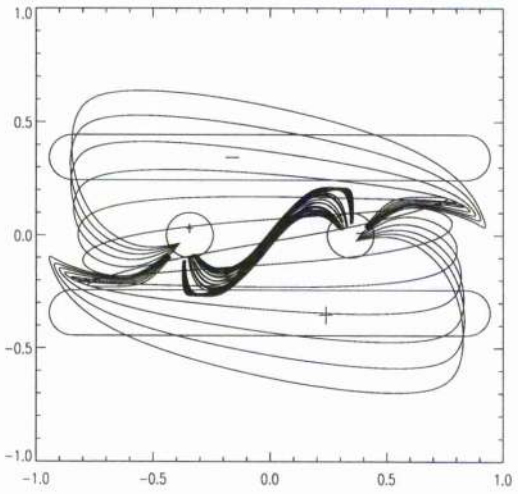

(a)

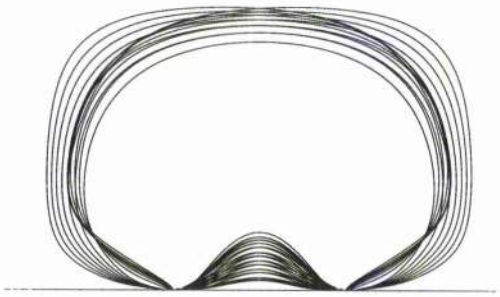

(b)

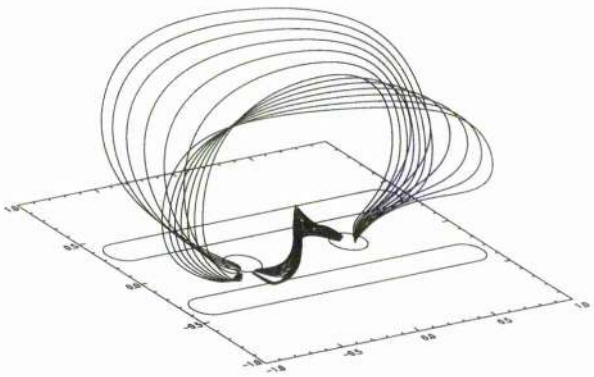

(c)

Figure 2.23: Separatrix surface for flux connecting circular sources for $\alpha = 1.8\,(F_c/F_a = 1.0, a = b)$ showing the two domains of connectivity.

The opposite now occurs for $\frac{F_c}{F_a} = 0.25$ and 0.1. For these cases, the flux of the circular sources is too weak to connect in the potential case with an upper bound. The value of alpha needs to be negative for the two circular sources to connect. As the value of alpha is decreased, the height of the flux tube connecting the two structures increases along with the width. Again, this is due to the type of twisting that is being added to the field. As the value of alpha is changed to negative values the field vector of the horizontal field (B_x, B_y) is rotated in a clockwise direction compared to that of the potential field. This can be seen in Figure 2.24 where the potential ($\alpha = 0.0$) field direction is shown in black and the sheared field ($\alpha = -2.0$) direction is shown in red. The flux from the positive circular source is directed more along the channel than across it compared to the potential case. When the shear is great enough, the two circular regions of flux can connect. By decreasing the value of alpha more flux is twisted along the channel and the height of the separatrix and the width increase.

a=2b.

The separation of the circular sources representing the flux of the filament is now twice that of the arcade sources. This is a much more realistic configuration for larger filaments. Again, the graph of separatrix height (H_s/b) versus alpha and width (W/a) versus alpha is shown in Figure 2.25. Similar results are obtained to the simple analytical model. The two regions of flux are connected with both an upper and lower bound. From the graph it can be seen that we have two different types of curve. For $\frac{F_c}{F_a} = 1.0$ we have both an upper and a lower bound for the potential case. As the value of alpha increases, the heights of both separatrices increase until a value of $\alpha = 0.4$, when the upper separatrix reaches the top of the box, at which point the solution becomes unphysical. When taking a wider spacing we are much closer to the sides of the box and, for strong flux values, the walls have a large effect on the solution. If the flux of the sources is decreased, the effect of the walls becomes less. For $\frac{F_c}{F_a} = 0.75$, the two circular sources are not connected for the potential case. However, if alpha is decreased to negative values, at $\alpha = -0.3$ they connect at a height of 2.2 units (66,000 km). As alpha is further decreased the lower separatrix extends down to the photosphere and the upper bound stays roughly at the same height. The sources become connected over a much larger range of heights and the width of the structure also increases, again due to the type of twisting that turns more flux to connect along the channel than across it, as described

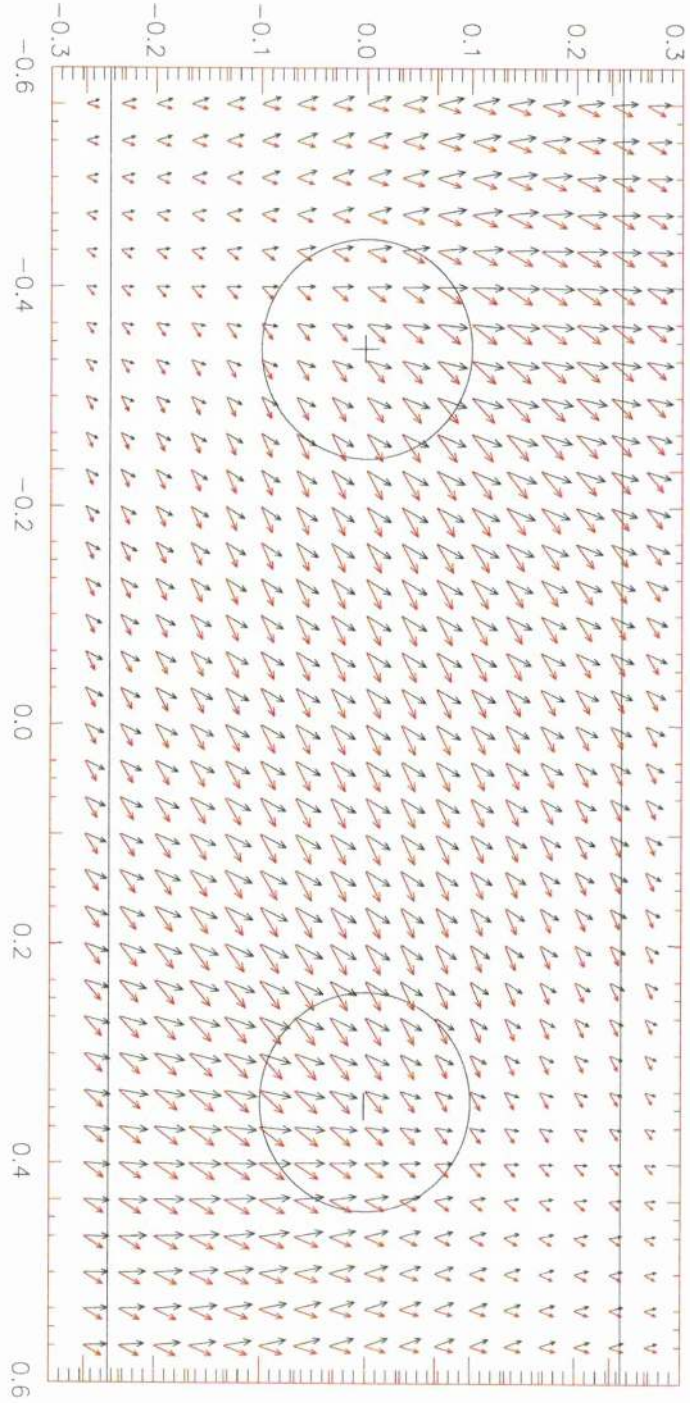

Figure 2.24: Horizontal field vectors (B_x, B_y) for the potential ($\alpha = 0.0$) field (black) and linear force-free ($\alpha = -2.0$) field (red) for $F_c/F_a = 0.25$ and $a = b$.

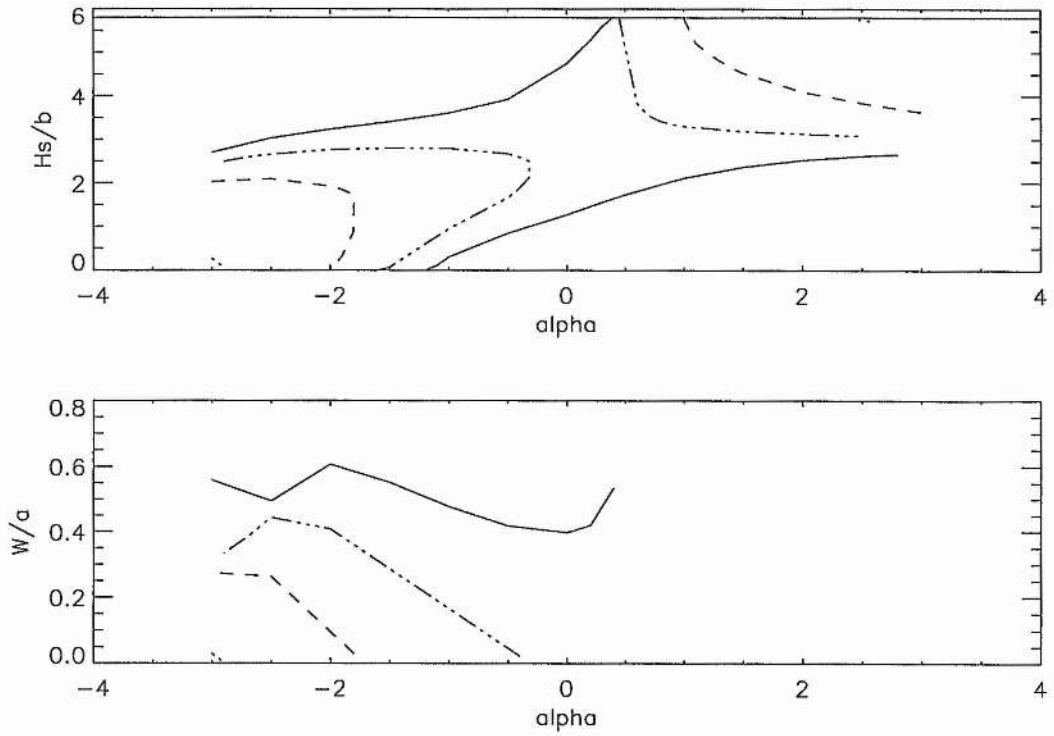

Figure 2.25: Graph of separatrix height (H_s/b, top) and width of flux tube (W/a,bottom) versus alpha for various flux ratios when $a = 2b$. The graph shows results for flux values of $\frac{F_c}{F_a} = 1.0$ (solid), 0.75 (dash-dot-dot-dot) 0.5 (dashed), 0.1 (dot).

before. In Figure 2.26 the flux tube connecting the circular sources is shown for $\alpha = -1.8$, $F_c/F_a = 0.5$. For this value of alpha the height of the upper bound is 57,000 km and lower bound is 20,000 km, while the structure is 2,000 km wide. All these dimensions being well within the observed range of values for filaments. For this value of alpha we have a very long, thin structure. Thus connections can be made along the channel even if the flux of the circular sources is much less than that of the arcade, but only if there is shear in the magnetic field. When the flux of the circular sources is less than that of the arcade more realistic structures for the filament can be obtained than in Section 2.1 since the structure is much longer and thinner. For all of the fluxes considered in this example the range of heights and widths are within the ranges observed for filaments. The results here are also consistent with those in Section 2.1. However, a much wider variety of separatrix structures and widths is possible as the value of alpha is changed. Finally,

if alpha is increased to positive values, connections can be made at the top of the box, but again these are unphysical.

Thus it can be seen that as the value of alpha is changed to both positive and negative values, in both cases a wide range of possible connections over many heights and widths is possible. Connections can occur where there were no connections before and disconnections can also occur as the value of alpha is changed, leading to a wide variety of possible structures that resemble filaments. It will therefore be useful to model some observed channels since this helps to fix some of the free parameters. For a dextral channel the widest range of connections are for negative values of alpha. By symmetry, for a sinistral channel positive values of alpha give the widest range of connections. The connection of helicity with the sinistral/dextral patterns of filaments will be dealt with in more detail in Chapter 4.

2.3.2 Case2.

In the last example the effect of the boundary conditions is large for large fluxes, leading to the generation of unphysical results. The modelling is now repeated but with different boundary conditions to see how this affects the solution. The sources are placed closer together and their radii are reduced. This has the effect of making the box larger so the solution should be affected less by the boundary conditions of the box. The sources are placed such that

$$\begin{aligned} x_o &= \text{-0.84375} \\ x_1 &= 0.84375 \\ b &= 0.21825 \\ r_a &= 0.09 \\ r_c &= 0.09 \\ L &= 1.6875. \end{aligned}$$

The sources are placed 8 grid points closer together. It should be noted that the length of the arcade source has been left the same as in the last example. By doing this the arcade extension becomes longer compared to the filament extension and the configuration becomes more like that of the analytical potential model. Again the structures are scaled such that

$$\begin{aligned} b &= 1 \text{ unit} = 30{,}000 \text{ km} \\ B_{oa} &= 1.0 \end{aligned}$$

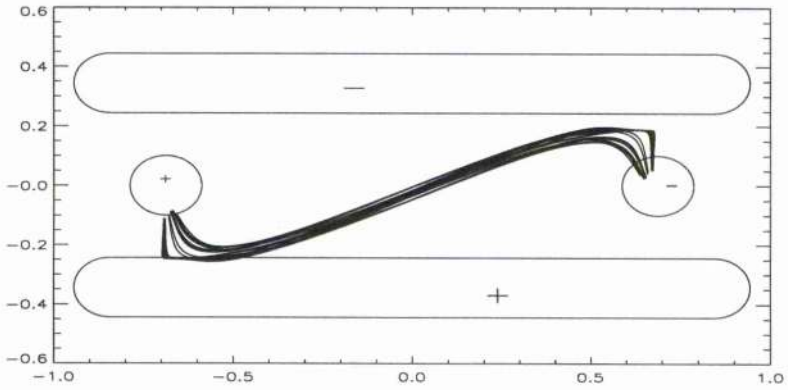

(a)

(b)

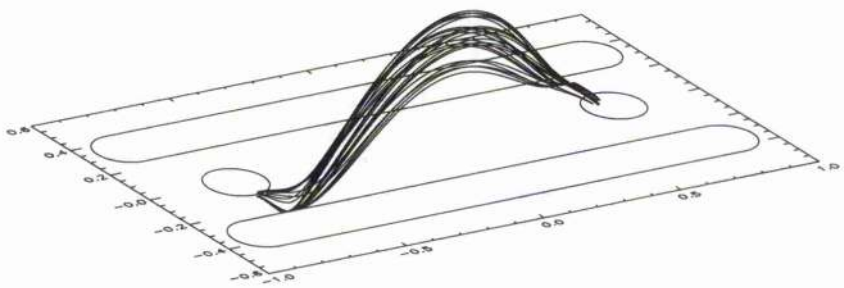

(c)

Figure 2.26: Separatrix surface for flux connecting circular sources for $F_c/F_a = 0.5$, $\alpha = -1.8$ and $a = 2b$, showing the upper and lower bounds of connectivity.

The heights of both the upper and lower separatrices and the width of the flux tube are again calculated for the flux ratios $\frac{F_c}{F_a} = 1.0, 0.75, 0.5, 0.25, 0.1$. Since the radii of the sources has changed, the flux ratio of $\frac{F_c}{F_a}$ (Equation 2.3.8) now becomes

$$\frac{F_c}{F_a} = 0.04745 \frac{B_{oc}}{B_{oa}}. \tag{2.3.10}$$

Table 2.4 shows the strength (B_{oc}) of the circular sources for each of the flux values, when $B_{oa} = 1.0$.

F_c/F_a	B_{oc}
1.0	21.0
0.75	15.8
0.5	10.5
0.25	5.3
0.1	2.1

Table 2.4: Flux ratio of circular and arcade sources and maximum field strength at centre of each circular region for case2.

a=b.

The experiment is first repeated for $a = b$. The results are shown in Figure 2.27 where the solid line at the top of the box again represents the top boundary which is at 9.16 units or 275,000 km. Again the results are plotted for the flux ratios of $\frac{F_c}{F_a} = 1.0$ (solid), 0.5 (dashed), 0.25 (dash-dot), 0.1 (dot). Only an upper bound exists for the flux tube connecting the circular sources. As the value of alpha is changed to both positive and negative values the separatrix height and width change in the same manner as before. The width in general decreases as the value of alpha is increased to positive values, and increases as alpha is changed towards negative values. The results are similar to those obtained in case 1 but there are differences. Since the walls have less effect than in case 1 the results obtained for $\alpha = 0.0$ should be closer to that of the simple potential model constructed in Section 2.1. A comparison of the two methods of modelling is carried out in the next section. This time, a larger value of alpha ($\alpha = 1.9$) has to be reached before the unphysical nature of the walls of the box comes into play and the sources connect at the top of the box. This larger

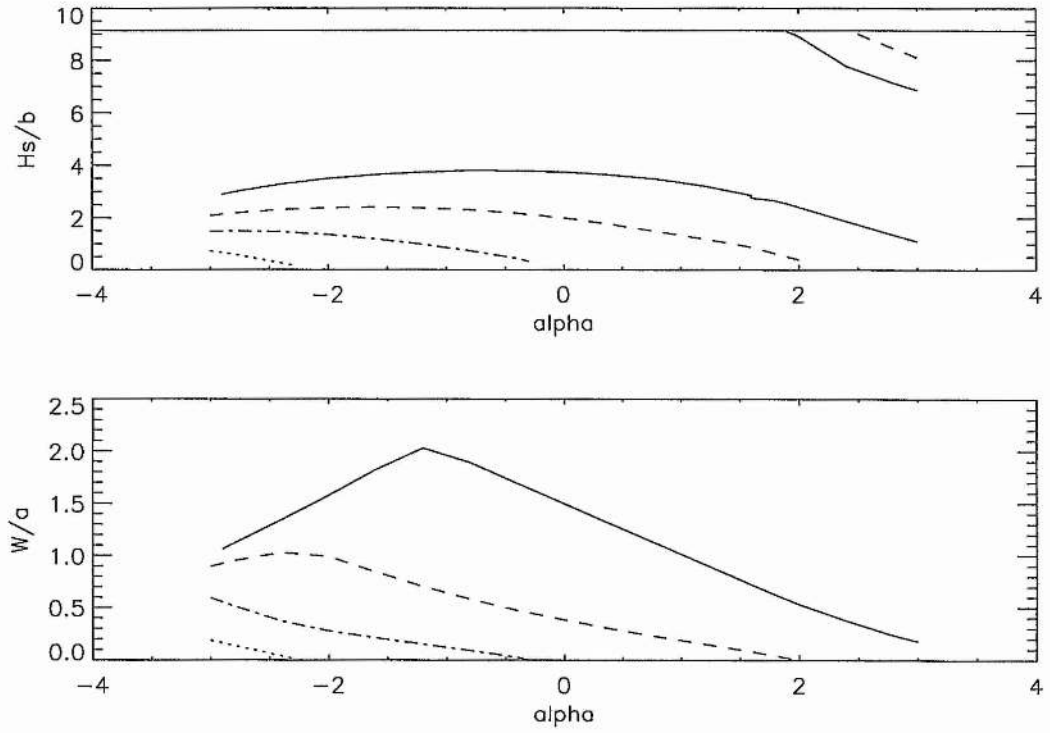

Figure 2.27: Graph of Separatrix Height (H_s/b, top) and Width of flux tube (W/a,bottom) versus alpha for various flux ratios in case2 when $a = b$.

value is due to the fact that the boundary of the box is further away from the flux regions being considered. Since it is further away, a much larger amount of twisting has to be added before the effect described earlier takes place.

A major difference in the two sets of results is the height of the upper separatrix in each case. Table 2.5 compares some of the values for the same flux ratios and values of alpha. All of the heights are higher in case 2 than in case 1, due to the fact that magnetic fields are space-filling. Since the box is effectively larger in case 2, the field expands to fill it giving larger separatrix heights. The width of the flux tube connecting the sources is also larger and this can be seen by comparing Figure 2.20 and Figure 2.27. Although in both cases different heights and widths are obtained, the same type of dependence of height and width on alpha is obtained.

α	F_c/F_a	Case 1	Case2
0.0	1.0	2.75	3.75
0.0	0.75	1.1	2.0
0.5	1.0	2.6	3.6
0.5	0.5	0.65	1.6
-1.5	0.5	1.7	2.4
-1.5	0.25	0.75	1.1

Table 2.5: Comparison of separatrix heights for different flux ratios and values of alpha.

a=2b.

The separation of the sources is now chosen so that $a = 2b$ and the process repeated. The results are shown in Figure 2.28, for the flux ratios of $\frac{F_c}{F_a} = 1.0$ (solid), 0.75 (dash-dot-dot-dot) 0.5 (dashed), 0.25 (dash-dot). The top of the box is again shown as the solid line. Again the same type of graph is obtained as in the last case. The sources are connected in general with both an upper and lower bound. As alpha is changed towards negative values the sources become connected over a wider range of heights due to the type of twisting that allows more flux to connect along the channel. For $F_c/F_a = 1.0$ as the value of alpha is changed to a higher positive value a point is again reached when there is only a lower bound and no upper bound ($\alpha = 1.4$). This time a larger value of alpha is required for this point to be reached. This is again due to the fact that the boundary conditions of the box have a smaller effect. As when $a = b$, the sources are connected over a larger range of heights and widths due to the lessening effect of the box. However, the same principle of solution is obtained as before, i.e. a lower and upper bound for the flux tube connecting along the channel.

2.3.3 Conclusions.

In this section the effect of magnetic shear on the separatrix surface of the simple potential model constructed in the last two sections is considered. Results similar to those of the potential case were found with either an upper, or upper and lower bounds existing for different separations of the circular sources. The surface increases or decreases with height and width as the sign of

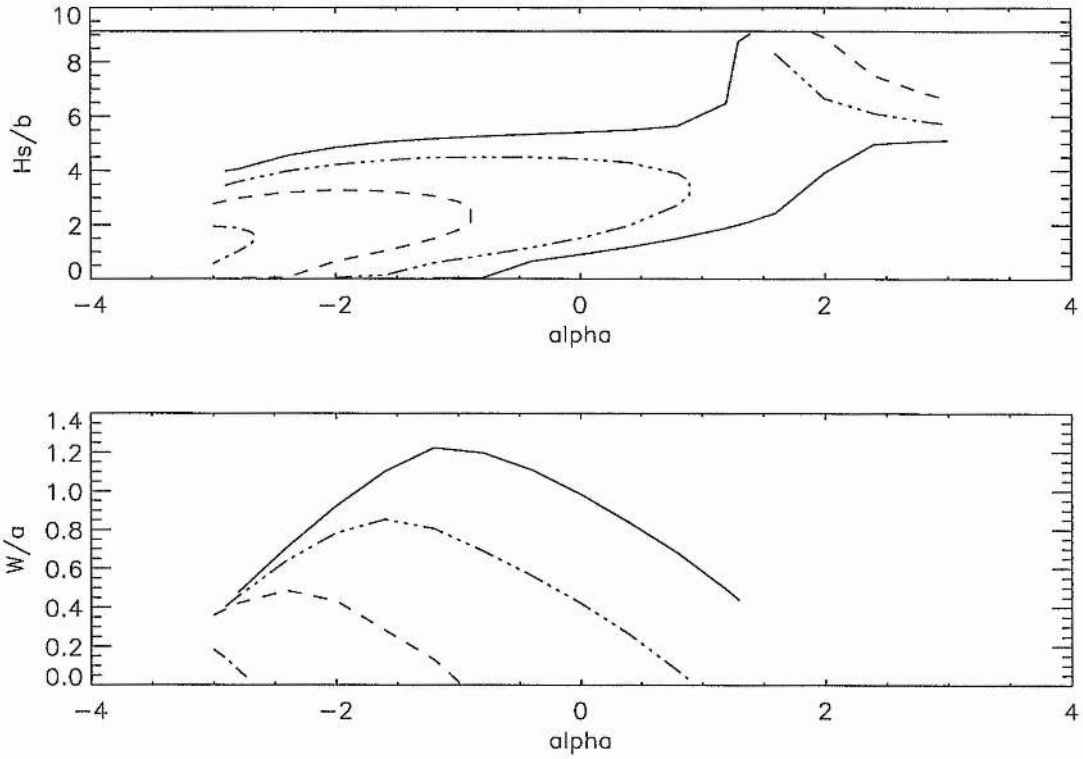

Figure 2.28: Graph of separatrix height (H_s/b, top) and width of flux tube (W/a,bottom) versus alpha for various flux ratios in case2 when $a = 2b$.

alpha is changed to both positive and negative values. It is found that the circular flux regions can connect for much smaller flux values when helicity is added. For the cases studied here, there are many possible heights and widths for the flux tube connecting the two circular sources as alpha is changed, with many of them lying within the observed range of values for filaments.

The modelling shows that the exact details of the solution (such as heights and widths) depend very much on the boundary conditions of the box, i.e how far away the sides and top of the box are from the flux regions. However, different boundary conditions give qualitatively the same behaviour and dependence with alpha. To model a specific filament accurately, the boundary conditions of the surrounding region would have to be adequately modelled. These conditions may include the helmet streamers that overlie filaments and have a confining effect on the filament channel field, like the top of the box. Also, neighbouring active regions may play a similar role

as the sides of the box by confining the field into a certain width. Again there are many free parameters in the modelling, many of which will be fixed by modelling observed channels. In the next section the results of the analytical model and the potential case of the numerical model are compared.

2.4 Comparison of Analytical and Numerical Models.

It is now useful to compare the results of the potential case of the numerical method with the results from the simple analytical potential model, to give an indication of the differences in results due to the two different methods of modelling. In each case we are dealing with potential fields so the total relative helicity is zero and the results can be directly compared . Below, the main differences between the two different methods are outlined.

1. The simple potential model uses:

   (a) Magnetic point sources (or singularities) to represent the field where B_x, B_y, B_z are specified.

   (b) Open system with radial field at infinity.

   (c) Two different types of source:

$$\text{point source (filament)} \sim \frac{1}{r^2} \text{ as } r \to \infty$$
$$\text{line source (arcade)} \sim \frac{1}{R} \text{ as } R \to \infty.$$

2. The numerical model uses

   (a) Diffuse regions of flux .

   (b) Closed box — flux only enters or leaves through bottom surface.

   (c) Vertical component of field zero at top of box, normal component zero at sides.

   (d) Specify only B_z at photosphere.

   (e) Both flux regions have same type of dependence.

From this it can be seen that there are many differences between the two methods. It is therefore promising that both methods give similar qualitative results, namely, that when $a = b$ there is only an upper bound for the flux tube connecting the filament flux sources and when $a = 2b$ there is both an upper and a lower bound for the flux tube.

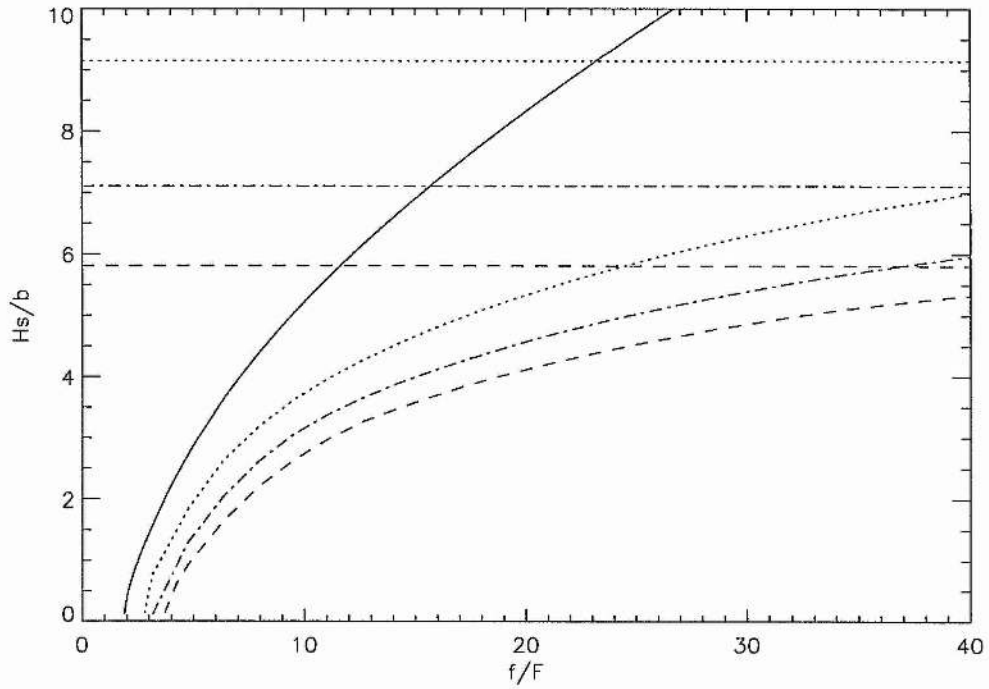

Figure 2.29: Comparison of potential field results for analytical model and three different configurations of the numerical model for $a = b$.

Figure 2.29 shows the comparison for $a = b$, plotting the separatrix height (H_s/b) versus the ratios f/F (for analytical model) and $B_{oc}/B_{oa}(L + 2r_a)$ (for the numerical model). The solid line represents the results of the analytical potential model. The separatrix heights are computed in the numerical model for $b = 0.34375$ (dashed), 0.28125 (dash-dot) and 0.21875 (dot). The lines drawn across the graph show the top of the box for each separation of b.

The analytical model gives a much higher upper separatrix surface. For $b = 0.34375$ the worst comparison between the two methods is found. For this value of b the sources fill up most of the box and the boundaries have a strong effect on the solution. As smaller values of b $(0.28125, 0.21875)$ are used, better agreement with the analytical model is found. By going to smaller values of b the box is made effectively larger and more like the analytical model. The field of the sources expands to fill the box. Consequently, since the simple potential model has open boundary conditions, it should represent the highest possible height for the separatrix. As b is decreased it can be seen that the effect of the top of the box becomes less as the final height gets

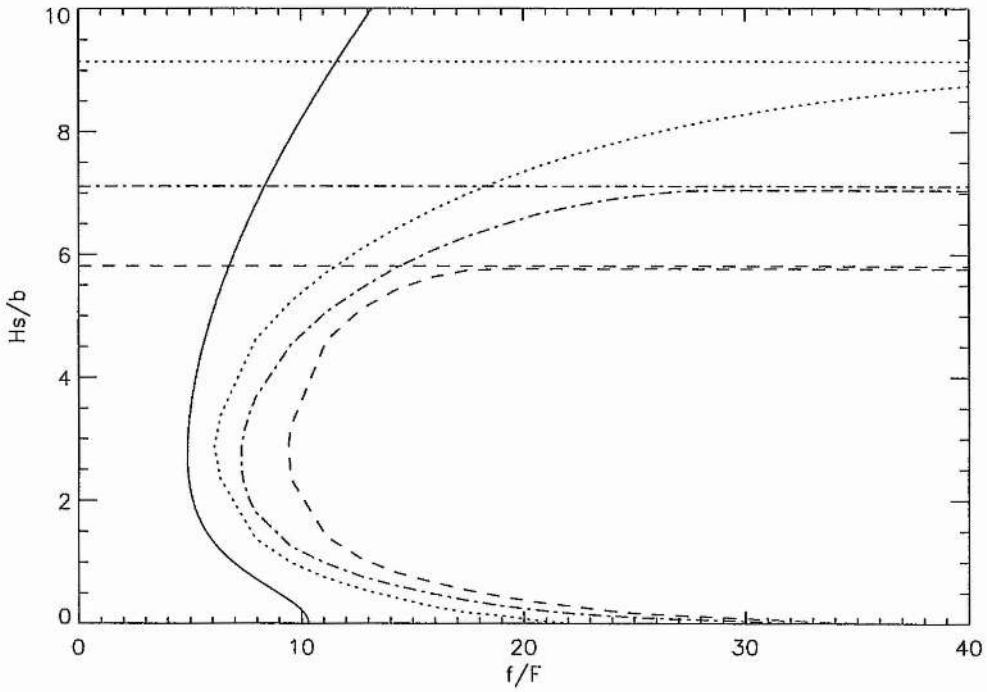

Figure 2.30: Comparison of potential field results for analytical model and three different configurations of the numerical model for $a = 2b$.

much further away from it. For $b = 0.34375$ units the difference in height of the top of the box and top of the separatrix for $f/F = 40.0$ is 0.5 units, for $b = 0.28125$ it is 1.2 units and finally for $b = 0.21875$ it is 2.2 units. For the three cases studied here it can clearly be seen that as the system of flux sources is shrunk, the solution grows closer to that of the potential model. This indicates that, if the boundary of the box could be placed at infinity, the solution may give the same results as in the analytical model. However, a more detailed study would have to be carried out to show this. For numerical reasons the sources cannot be placed any closer than 0.21875 units (7 grid points). To compute any configuration below this spacing the number of grid points will have to be increased from 65^3 to 129^3. On 65^3 grid points each program takes 720s to run and generates 6Mb worth of data. On each graph 30 points are used (21600s, 6 hrs, 180 Mb). To increase the spacing to 129^3, roughly 35 hrs of RAL J90 time would be required and 1530 Mb worth of data produced. It is therefore too expensive to test the result any further. In Figure 2.30 the results are shown for the same spacing and $a = 2b$. Again similar results are obtained as before with the

solution becoming closer to the analytical model as the sources are shrunk into the box.

For the potential case the height and width of the flux tube connecting the circular sources can vary by a large margin depending on the boundary conditions. For filaments that are closely bounded by active regions on either side and held down by low-lying arcades, the results for $b = 0.34375$ may be more realistic. However, for high-latitude quiescent polar-crown filaments which have open radial field near to them, the larger box or analytical model may be more realistic. A wide possible range of heights can be obtained with most being within the observed range for filaments.

Chapter 3

Application of Potential Models.

In this chapter potential modelling will be used to describe a variety of coronal structures. Potential models are very useful since they may be constructed analytically and can cover a wide region of parameter space. For the cases considered here it will be shown that potential models are a good first approximation. However, it should be noted that potential models cannot always represent the full nature of coronal fields and essential aspects of the physics involved may only come to light when force-free or magnetostatic models are considered. To begin with (Section 3.1), potential models will be used to describe the bending of a filament in a filament channel as it passes between regions of opposite polarity flux, called plagettes. The modelling describes one mechanism by which a filament may break up. After that (Section 3.2), arcades lying above switchbacks of polarity inversion lines at high latitudes on the Sun are considered. The potential modelling shows that the opposite skew of the arcades on each arm of a switchback may be due to a local flux imbalance at the corner of the switchback. Finally (Section 3.3), potential models are constructed of a filament in a filament channel. The modelling shows that dips in the magnetic field of a filament may be due to the locations of positive and negative flux lying below the filament.

3.1 Bending of a Filament.

3.1.1 Observations.

In Figure 3.12 a filament can be seen lying in a filament channel. On the left-hand side there are two Hα images and on the right-hand side the corresponding magnetograms. On the Hα images the filament is the dark elongated structure in the centre of the channel that bends and weaves its way past the regions of opposite polarity flux. On the magnetograms which give the vertical component of field through the photosphere, white represents regions of positive flux and black regions of negative flux. On the top magnetogram at the right-hand side there are two regions of opposite polarity flux that lie close together, regions 4 and 5. As the filament approaches these two regions (called plagettes), it bends or kinks and passes between them. As it does so, it also becomes narrower. This feature of filaments will now be modelled.

To model the bending of the filament, the magnetic field of the filament is regarded as a uniform field B_o in the x-direction. The plagettes are represented by two poles, one of strength $+f$ placed at $y = -a$ and the other of strength $-f$ placed at $y = a$. The schematic of the channel can be seen in Figure 3.1. By representing the channel in this manner we suggest that the bending of the filament is a result of the plagettes acting on the horizontal component of the filaments field in the channel. Since the region of bending of the filament (Figure 3.12) is small compared to the entire length of the filament the horizontal component of the filaments field is assumed to be uniform in the region of the plagettes.

The magnetic field of the channel is given by

$$\mathbf{B} = B_o\hat{\mathbf{x}} + \frac{f}{2\pi}\left(\frac{\mathbf{r_2}}{{r_2}^3} - \frac{\mathbf{r_1}}{r_1^3}\right), \tag{3.1.1}$$

where B_o is the strength of the uniform field ($B_o > 0$) and f is the strength of the plagettes. The vectors $\mathbf{r_1}$ and $\mathbf{r_2}$ are given by

$$\begin{aligned} \mathbf{r_1} &= x\hat{\mathbf{x}} + (y-a)\hat{\mathbf{y}} + z\hat{\mathbf{z}}, \\ \mathbf{r_2} &= x\hat{\mathbf{x}} + (y+a)\hat{\mathbf{y}} + z\hat{\mathbf{z}}, \end{aligned} \tag{3.1.2}$$

and all fluxes are normalised such that

$$B_o = 1.0. \tag{3.1.3}$$

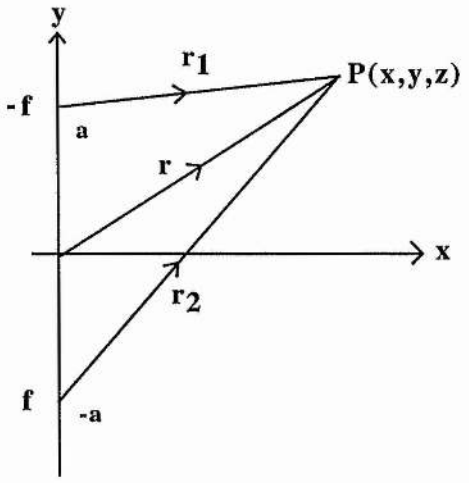

Figure 3.1: Schematic of channel showing coordinate system and location of plagettes in channel.

3.1.2 Field Lines.

The field lines in the $z = 0$ plane are first considered. In Figure 3.2(a) the field lines are plotted for $f = 1.25$ and $a = 1.3$. The dashed lines represent the separatrix lines and the solid lines the field lines. Two neutral points exist at the intersection of the separatrices, in front of the positive pole and behind the negative pole. The separatrix lines separate the flux of the plagettes from the body of the filament and it can be seen that the plagettes are not connected. The field lines that emerge from the plagettes lie anti-parallel to one another and parallel to the body of the filament, in agreement with the observations of Martin *et al.* (1995). The body of the filament passes between the plagettes and as it does so it bends or kinks and becomes narrower.

In the second plot, Figure 3.2(b), the strength of the plagettes is increased to $f = 2.5$. With this the filament is bent more and is much thinner. The separatrix surfaces that contain the plagettes are much larger and lie closer together. For this flux value the effect of the plagettes on the horizontal field of the filament can be clearly seen. In the final plot (Figure 3.2(c)) the strength of the poles is increased to $f = 10.0$. The two plagettes are now connected together and no flux can pass between them. The plagettes have become too strong and have broken up the filament.

In Figure 3.3(a) the field lines out of the $z = 0$ plane are shown from an oblique angle. It is

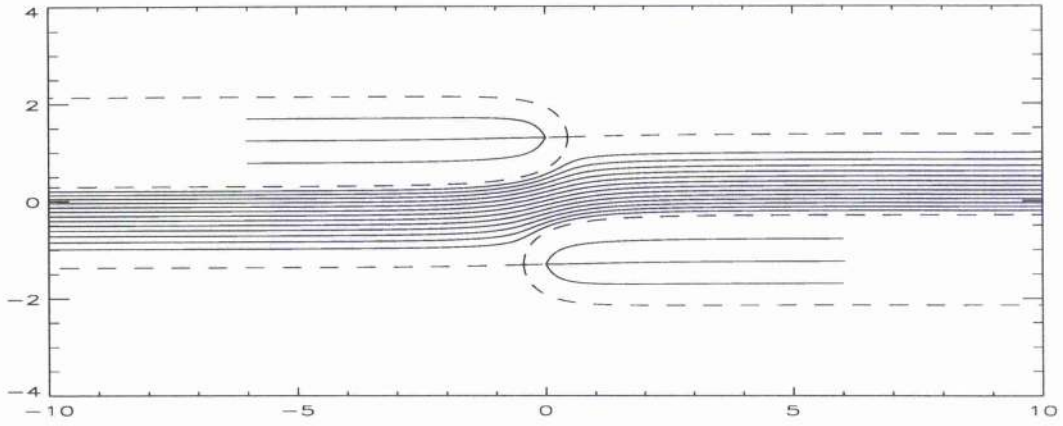

(a)

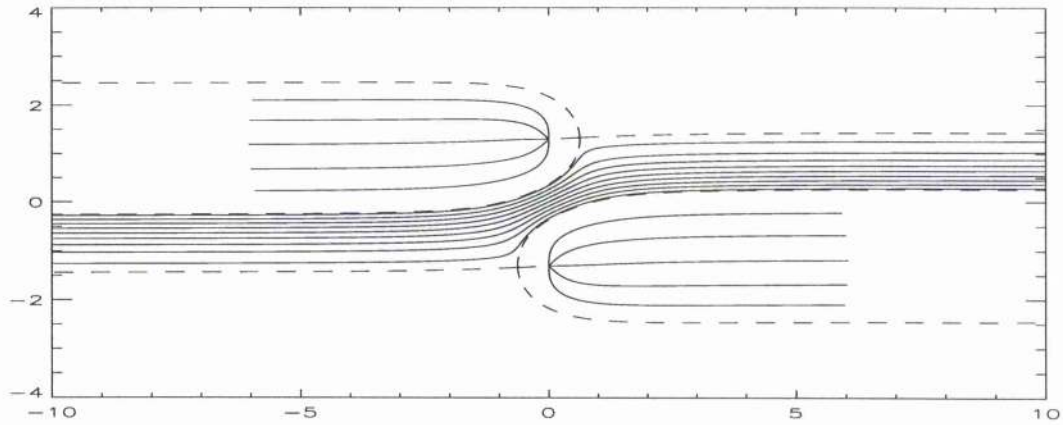

(b)

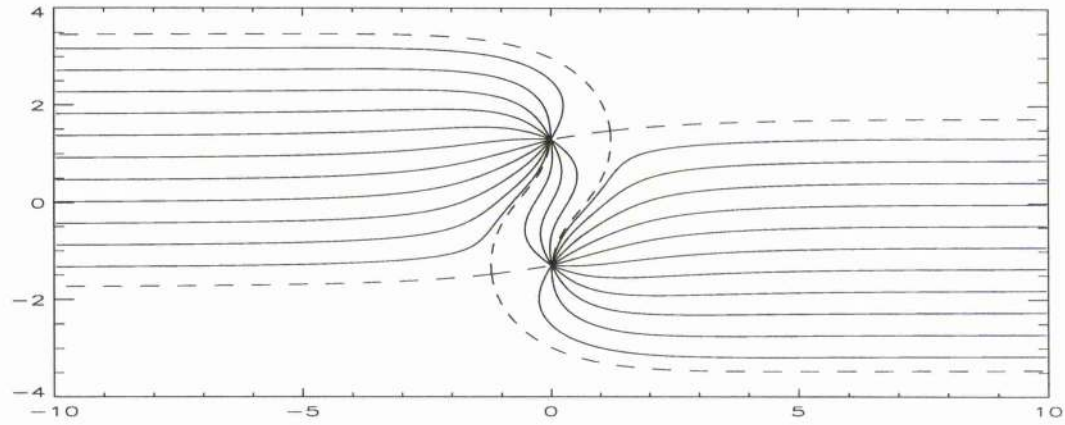

(c)

Figure 3.2: Field lines in the $z = 0$ plane for (a) $f = 1.25$, (b) $f = 2.5$ and (c) $f = 10.0$

shown for $a = 1.3$ and $f = 1.25$. The dashed lines are again the separatrix lines and the field lines in bold represent the ones out of the $z = 0$ plane, while the light ones are in the $z = 0$ plane. As the body of the filament approaches the plagettes it bends or kinks its way between them. The field lines closest to the positive pole bend away and rise up to avoid it, while the field lines closest to the negative pole bend down and towards it. The plagettes are not connected to the body of the filament and are separated from it by a type of "plagette magnetosphere", which is outlined in the $z = 0$ plane by the dashed line. The bold field lines are plotted at a height of 0.5 units for the field lines representing the filament and at 0.35 units for those representing the fibrils. In Figure 3.3(b) the same set of field lines is seen but from the side.

3.1.3 Displacement and Width of Filament.

From the field line plots it can be seen that the effect of the plagettes on the structure that resembles the filament is to make it bend or kink. The amount of bending or kinking will depend on the ratio of the strength of the filament field (B_o) to the strength of the plagette flux (f). In Figure 3.4(a) the displacement of a field line from a uniform field caused by the plagettes is shown. The graph plots d/a versus the flux ratio $f/(B_o a^2)$. Where d is the displacement of the field line that passes through the origin and lies in the $z = 0$ plane. As the flux of the plagettes increases, the displacement of the field lines also increases. The maximum displacement of the field at $f/(B_o a^2) = 2.56$ corresponds to the two poles joining together and the filament field can no longer pass between them.

If this is a reasonable representation of the filament bending process then this graph could be used to find the horizontal component of field within the filament from $H\alpha$ and magnetogram images. From the $H\alpha$ image, the displacement "d" of the filament from its uniform (straight) structure and the separation "a" of the plagettes can be measured. The magnetogram then gives the flux "f" of the plagettes. By finding the location on the graph given by "d/a" the value of B_o could be indirectly calculated. The practical application of this procedure should be considered in the future. As the filament passes between the plagettes its width decreases. In the next graph Figure 3.4(b) the ratio of the width of the filament (w_o) before it passes through the plagettes to the width (w_1) as it passes between the plagettes is given versus the same flux ratio as before. Again the widths are measured in the $z = 0$ plane. For all flux values the width ratio is less than one,

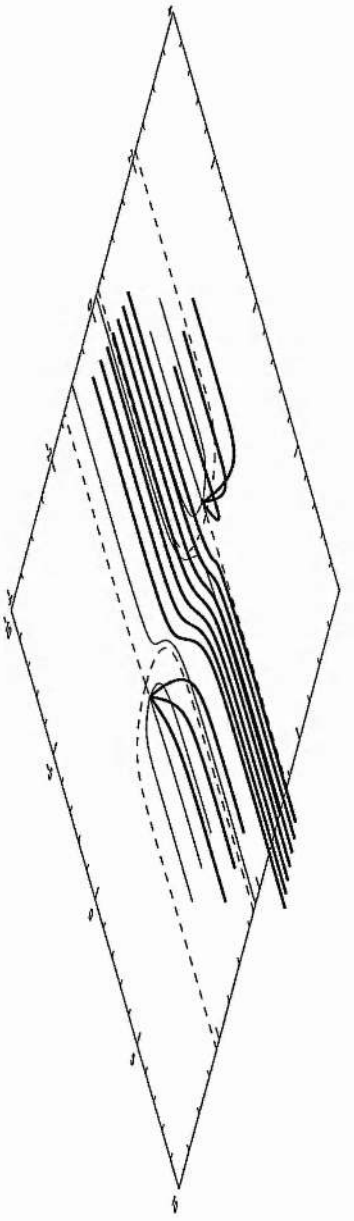

4(a)

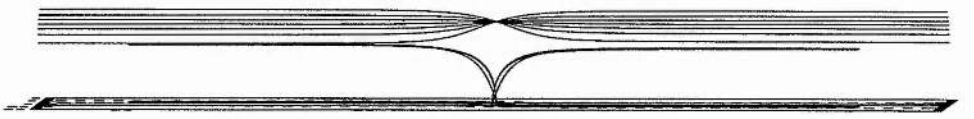

4(b)

Figure 3.3: Field lines out of the $z = 0$ plane for $a = 1.3$, $f = 1.25$ seen from (a) an oblique angle and (b) the side.

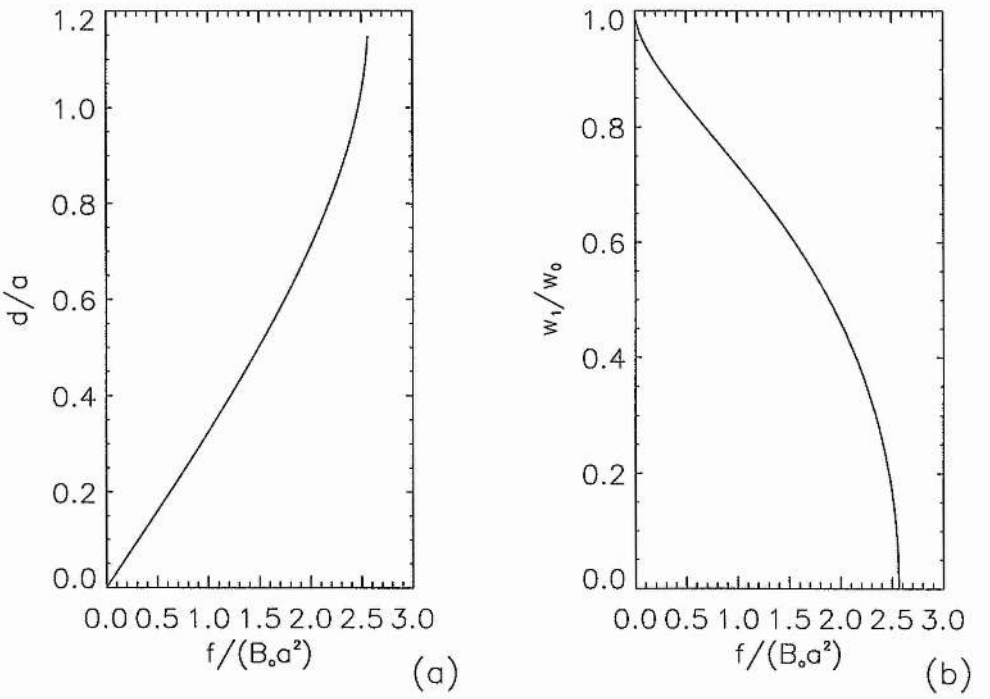

Figure 3.4: Graphs of (a) displacement d/a of field line from uniform field versus the flux ratio $f/(B_o a^2)$ and (b) width ratio w_1/w_o versus the same flux ratio.

showing that the structure becomes thinner as it passes between the plagettes. As the strength of the poles increases, the ratio decreases until $f/B_o a^2 = 2.56$ and the width is zero. This is again when the two poles connect. This graph together with Hα and magnetogram images could again be used to infer the strength of the uniform field through the filament.

3.1.4 Conclusions.

In this section a simple potential model has been constructed to represent the bending of a filament in a filament channel. The model consists of a uniform field that represents the filament and a pair of point sources that represents the plagettes. A good representation of the bending is found and a possible mechanism for obtaining the strength of the horizontal field in a filament is given.

3.2 Orientation of Arcades above Switchbacks of Polarity Inversion Lines.

3.2.1 Introduction.

A "switchback" of a Polarity Inversion Line (P.I.L.) and the skew of the overlying coronal arcades are modelled next. The polarity inversion lines considered here generally lie at high latitudes on the Sun and tend to be those of the polar crown. In Figure 3.5(a) a schematic diagram of the type of polarity inversion line and the typical skew of the coronal arcades can be seen. On one arm of the switchback the arcades have one type of skew and on the other arm the opposite skew. The arcades are post-eruption arcades and in a recent survey by A M^{c}Allister (Private Communication) it was found that, for the majority of cases of this type of P.I.L. in each hemisphere, the arcades have this form of opposite skew. Since the arcades have opposite skew the direction of the horizontal component of field is opposite on each arm. This has important consequences for the type of filaments that would lie under the arcades, since there is a one-to-one correspondence between the arcades and filaments. On one arm of the switchback there would be a dextral filament and on the other arm a sinistral filament, both lying on the same P.I.L. This would contradict the results of Martin *et al.* (1995). In this section the origin of the skew of the arcades is considered. A potential model of the switchback is developed which gives qualitatively the observed skewing of the coronal arcades. Potential models are considered since the arcades observed are post-eruption and therefore have lost some energy. The initial modelling will therefore consider the lowest-energy state of the field. The model is then applied to a specific set of observations where magnetograms are used to deduce the locations and strengths of flux sources at the photosphere and Yohkoh images are used to compare the orientations of the deduced model coronal arcades with those given by observations.

3.2.2 General Model

For the general model we consider two regions of flux nested together as shown in Figure 3.5(b) with the positive flux region nested inside the negative flux region. It is assumed that the two regions have the same flux density. Since the positive region is nested inside the negative region

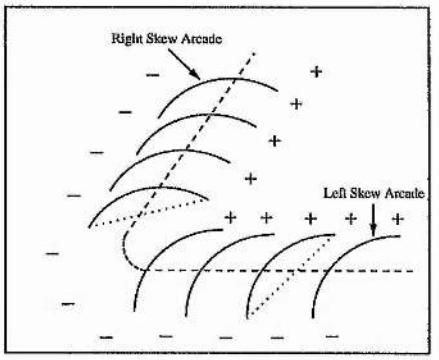

(a)

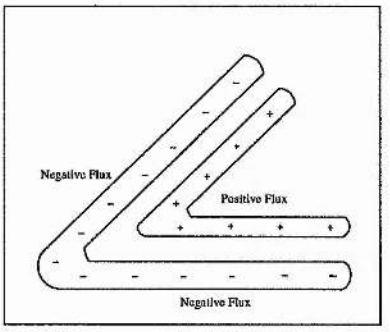

(b)

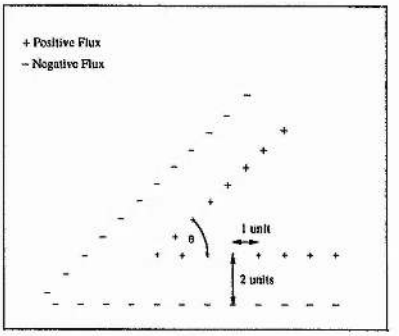

(c)

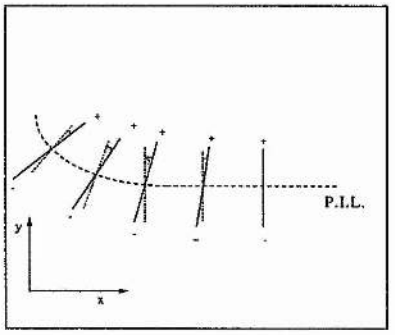

(d)

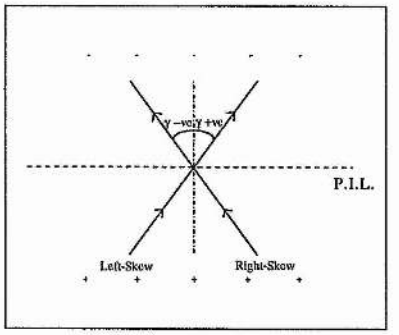

(e)

Figure 3.5: (a) Polarity inversion line with opposite skew of arcades on each arm. (b) Nested magnetic flux regions with a positive region nested inside a negative region. (c) Representation of a nested flux region by point sources (plus sign) and sinks (minus sign). (d) Shear angle (γ) of field lines along the P.I.L. measured from the normal to P.I.L. (e) Definition of left-skew and right-skew arcades as having γ positive and negative, respectively.

its area is less and so its total flux is smaller than that of the negative region. Locally, at the corner of the switchback, there is an imbalance in location of flux towards the negative flux. It is this imbalance at the corner of the switchback which creates the skew of the arcade, which can then be compared with observations.

The flux region shown in Figure 3.5(b) can be represented in a potential field model by placing a series of point sources and sinks along both arms of the positive and negative regions. The magnetic field of each source or sink relative to its location is again given by Equation 2.1.1. The positive sources (all of strength πf) are positioned as shown in Figure 3.5(c) with the distance between the centres of successive sources being 1 unit, which corresponds to 30,000 km (i.e. a typical supergranule width on the quiet Sun). The switchback angle (θ_s) is defined as the angle between the two lines of sources (i.e the angle between the horizontal and diagonal arms of the switchback). Opposite each of the positive sources a negative sink of strength $-\pi f$ is placed at a distance of 2 units. By doing this a negative sink is matched to each of the positive sources. Extra negative sinks are then added onto the horizontal and diagonal arms of the negative flux region with separations of 1 unit until the corner of the switchback is complete. These are balanced by positive sources at large distances (out of the field of view considered) and equally spaced in angle. The field lines at the switchback are then plotted at various heights to show how the skew varies with height and distance along the arms, for switchback angles θ_s of $\pi/4$, $\pi/3$ and $\pi/6$.

(i) $\theta_s = \pi/4$

The field lines are first plotted when the angle of the switchback is $\pi/4$, as shown in Figures 3.6(a-e). There are 17 positive sources; opposite each of these a negative sink is placed. Eight negative sinks are then added (four on each arm) to complete the corner of the switchback. The system is in flux imbalance of -9 units. It is this imbalance in flux location at the corner of the switchback that generates the skew of the field lines. The dashed curve on each of the plots represents the P.I.L., which we define to be the photospheric location above which the field lines at unit height are horizontal; along the arms of the switchback the P.I.L. lies in the centre of the polarity inversion zone midway between the two rows of sources. Near the centre, the P.I.L. curves round closer to the inside positive sources because of the local flux imbalance.

The length of each of the arms of the switchback is 10 units or 300,000 km, which is almost

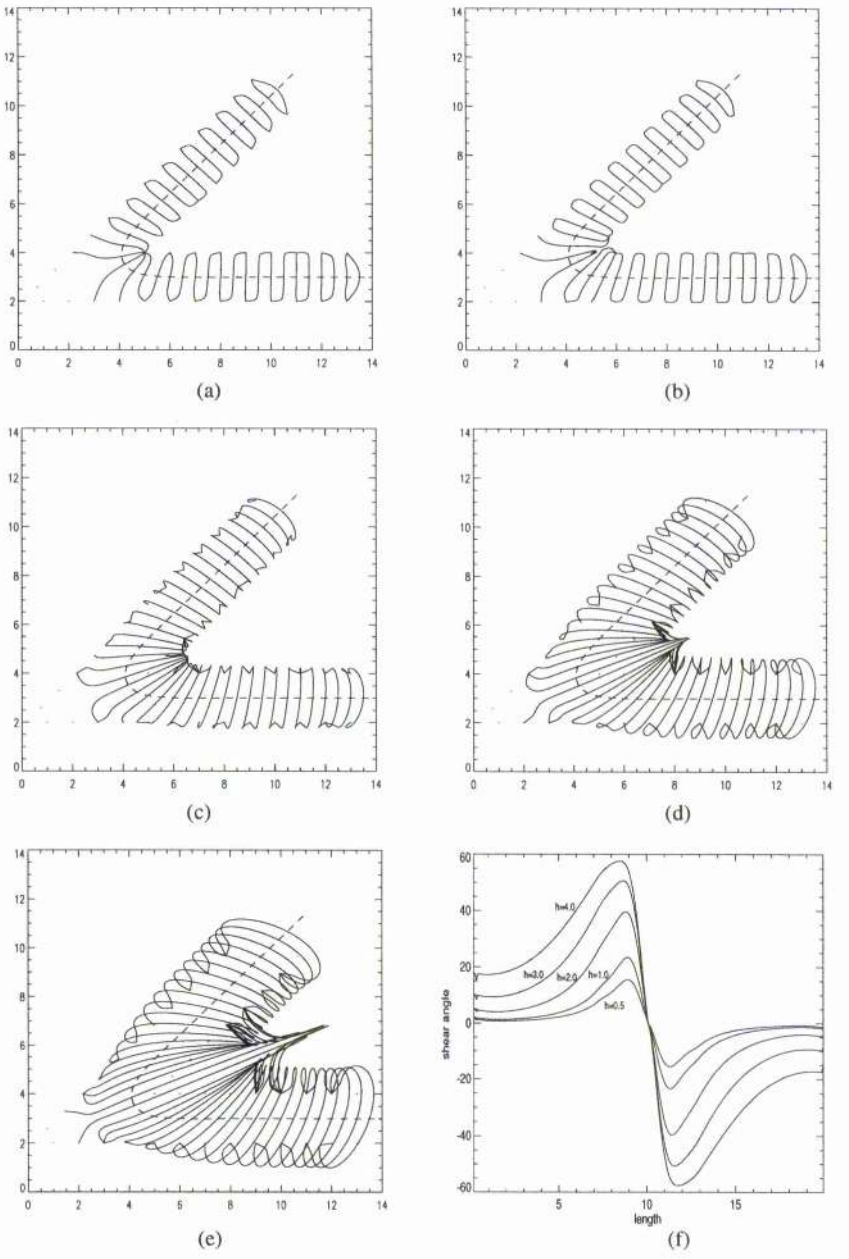

Figure 3.6: A selection of field lines along both arms of the switchback when $\theta_s = \pi/4$ at heights of a) 15,000 km, b) 30,000 km, c) 60,000 km, d) 90,000km and e) 120,000km. (f) a graph of shear versus length along an arm of the switchback for these heights.

half a solar radius across the surface of the Sun. The model of the region is carried out on a flat plane and so has not so far taken into account the effect of the curvature of the solar surface, which will be included in future (see van Ballegooijen *et al.* 1997). The plots shown in Figure 3.6(a)-(e) show the field lines that cross the P.I.L. at various heights. In Figure 3.6(a) the height is 0.5 units (15,000 km), at which the field lines are not greatly skewed with respect to the P.I.L. The positive source at the centre connects to many of the surrounding negative sinks and so the flux from the source only reaches low heights. This is why the P.I.L. lies closer to the positive source rather than the negative sinks at the corner.

The second plot, (Figure 3.6(b)) shows the field lines that cross at a height of 1 unit (30,000 km), at which there is more skew on the field lines and the skew exists much further along both arms. Less flux from the positive source at the corner reaches this height due to the fact that it connects to so many negative sinks at lower heights. In Figures 3.6(c)-(e) the field lines are plotted that cross at heights of 60,000 km, 90,000 km and 120,000 km, respectively. Again as we go up higher the skew of the field lines relative to the P.I.L. increases; it is non-zero along the entire length of each arm in Figures 3.6(d),(e). The higher the field lines the more flux connects over the top of the positive sources on the inside of the corner to the negative sinks on the outside of the corner, which gives long, skewed field lines. In Figure 3.6(f) graphs of the skew of the field lines against the length along the P.I.L. are plotted. The length along the P.I.L. is the distance along the P.I.L. from the west-most point of the horizontal arm to the northern tip of the diagonal arm. The skew angle (γ) is the angle that a field line makes to a normal from the P.I.L. as it passes over the P.I.L. (Figure 3.5(d)). Along the arms of the switchback where the P.I.L. lies parallel to the x-axis, a field line that is parallel to the P.I.L. will have a skew angle of 90° and a field line that is not skewed will be perpendicular to the P.I.L. and have a skew angle of 0°. The changing skew from one arm of the switchback to the other will be represented by a changing sign of the skew angle. The two types of skew are left skew and right skew. An arcade is said to have left skew if, when seen from above and on the positive polarity side, the arcade goes from the observer's left to right. This will be represented by a positive skew angle (γ), Figure 3.5(e). Correspondingly, a right-skewed arcade is when the arcade goes from the observer's right to left again when seen from above and on the positive polarity side and is represented by a negative value of gamma, Figure 3.5(e). The graph shows how the skew angle varies with length for heights of $h = 0.5$,

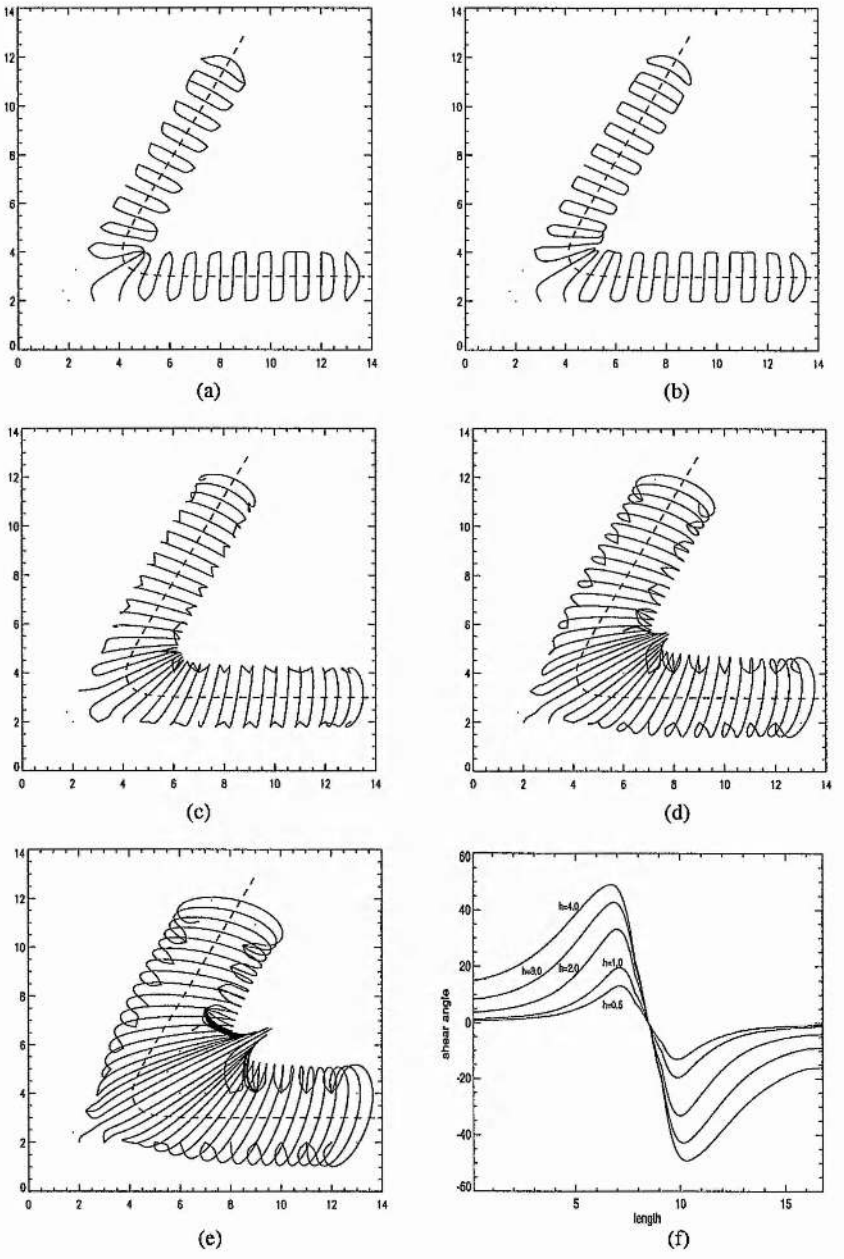

Figure 3.7: The same as Figure 3.6 but with the angle (θ_s) between the arms being $\pi/3$.

1.0, 2.0, 3.0 and 4.0 units. At the west-most point of the horizontal arm the skew is its smallest (positive value) for any given height. As the corner is approached the skew increases until a maximum is reached. It then falls sharply to zero at the corner of the switchback and reverses sign on the diagonal arm. The same feature is then repeated but with negative values of gamma along the diagonal arm. On the horizontal arm we have a left-skewed arcade and on the diagonal arm a right-skewed arcade. Thus there is a different skew on each arm of the switchback. As can be seen from the graph, the skew angle of the field lines at any point along the P.I.L. increases with height. Since there is a changing skew with height we have a shear of the field lines.

(ii) $\theta_s = \pi/3$

For a switchback angle of $\theta_s = \pi/3$, the positive flux region is again represented by 17 positive sources and opposite each of them a negative sink is placed at a distance of two units. Six extra negative sinks are then added, three onto each arm to complete the negative flux region of the switchback. The plots of the field lines are shown in Figures 3.7(a)-(e). The plots are again for field lines crossing the P.I.L. at heights of 15,000 km, 30,000 km, 60,000 km, 90,000 km and 120,000 km, respectively. As before, the skew angle of the field lines is small at low heights and increases with height. At a height of 60,000 km no flux comes from the positive source at the corner. This encourages a skewing of the higher field lines from the sources along the arm. The field lines connect over the top of the positive source and produce long skewed field lines. In Figures 3.7(d) and 3.7(e) the skew can be seen along the entire length of the arms. Figure 3.7(f) shows the skew angle against length along the P.I.L. at heights of $h = 0.5$, 1.0, 2.0, 3.0 and 4.0 units. Again the higher the height the greater the skew of the field lines. The skew is again small at the west-most point of the horizontal arm and increases with distance along the arm till a maximum is reached and then falls to zero at the corner. Again, as we pass from the horizontal arm to the diagonal arm, the angle reverses from a positive value (left-skewed structure) to a negative (right-skewed structure) and a similar pattern is repeated on the diagonal arm. It can be seen that there is less skew in the field lines than in the case when $\theta_s = \pi/4$. This is due to the fact that there is a smaller flux imbalance at the corner due to the increased value of the switchback angle θ_s. With the smaller flux imbalance fewer field lines connect to the corner of the switchback and so the shear of the field lines is less.

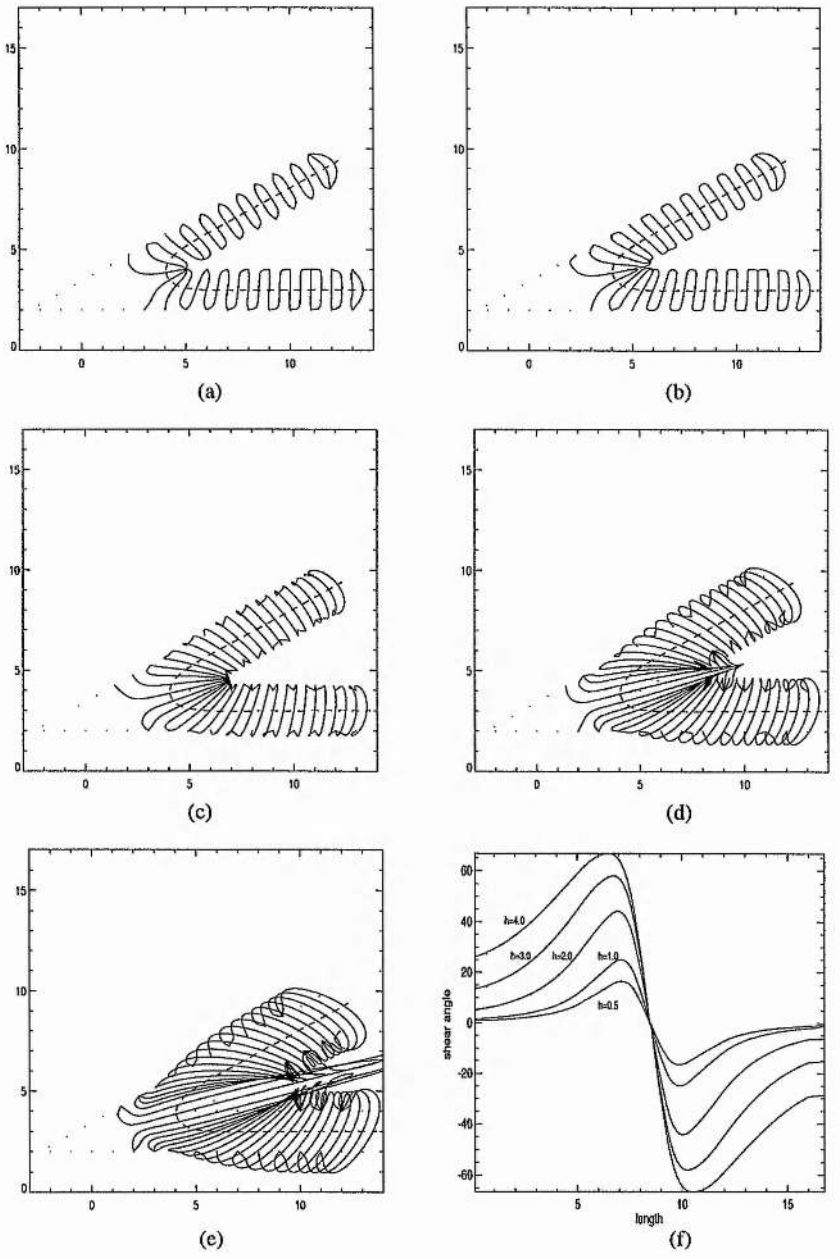

Figure 3.8: The same as Figure 3.6 but with the angle (θ_s) between the arms being $\pi/6$.

(iii) $\theta_s = \pi/6$

The above model was now repeated for a switchback angle of $\theta_s = \pi/6$. The positive flux region is again represented by 17 positive sources, but this time the negative flux region is represented by 32 sinks. Since the flux imbalance is even greater in this case, the skew of the field lines is greater at each height than when $\theta_s = \pi/4$ and $\pi/3$. Figures 3.8(a)-(e) show the field lines at the same heights as before. The graph in Figure 3.8(f) of the skew angle with respect to length along the P.I.L. shows how much the skew of the field lines has increased due to the increased flux imbalance.

Skew of field lines can be created by having a local flux imbalance at the corner of a switchback. The amount of skew of the field lines depends on the amount of flux imbalance and also the height of the field lines and their distance from the corner of the switchback. A different type of skew is obtained on each arm of the switchback due to the flux imbalance. On the Sun the imbalance of flux at the corner is due to the switchbacks lying at high latitudes on the solar surface near to the poles where there is a large region of unipolar flux.

3.2.3 Model of Observations

The general model of the switchback is next applied to a specific set of observations. By representing the flux emerging through the solar surface as a series of sources and sinks the resulting model coronal arcades will be compared with the overlying coronal arcades seen in Yohkoh images. By doing this a qualitative agreement between the orientation of the arcades in the model and the observations is found. The arcades were observed between the 24^{th} and 25^{th} February 1993. In Figure 3.9 an Hα synoptic chart shows the location of the switchback of the P.I.L. The cusp of the switchback lies between 210 and 240 degrees of heliographic longitude and in the southern hemisphere between S50 and S60 in sine latitude. To construct the model synoptic chart magnetograms were obtained from the NSO archive. The magnetograms were taken by the NSO Vacuum Telescope located in Kitt Peak, Arizona using a spectromagnetograph with the 8688 $\mathring{A}$ line. Each synoptic magnetogram represents one Carrington rotation of the Sun and is made from a weighted average of the daily maps. Each map is also corrected to provide a best estimate of the average magnetic flux density in Gauss at each pixel and represents the magnetic field at central

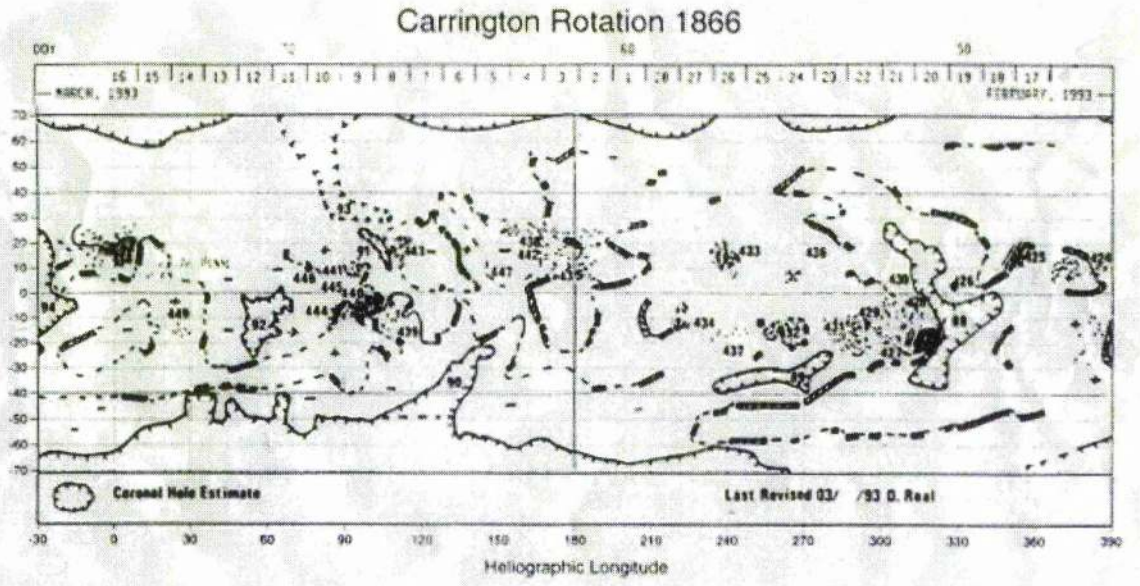

Figure 3.9: Hα synoptic chart showing a switchback of the P.I.L. in Carrington rotation 1866.

meridian passage (Harvey 1994). The maps are of size 360 $\times$ 180 pixels where each pixel in the x-direction represents 1 degree of longitude and each row represents an equal step in the sine of latitude ranging from the south pole to the north pole.

The area of magnetic flux corresponding to the switchback must now be cut out of the magnetogram. To model the arcades no flux that lies at less than 180 degrees of longitude is considered since any flux before this value lies far away from the corner of the switchback. Also no flux that lies above S30 or below S70 in sine latitude is considered. Above S30 is the active-region belt of the Sun and is well above the top corner of the switchback, while below S70 is the polar crown region of coronal holes and so it is not included either.

In Figure 3.10(a) a contour plot of the magnetic field made at -4 and 4G can be seen. Positive flux is outlined by the dark lines and negative flux by the light lines. From the contour plot it can be seen that the switchback is mainly made of weak background flux and most of the flux lies between $\pm$ 10G. Since it is made up of weak background flux no boundary flux value can be chosen (as in Mackay *et al.* 1996 and Schrijver 1987) and all flux values will be included in the modelling. Even though the switchback is made up of weak background flux the distinct shape of it can be seen with the cusp lying between 220 and 240 degrees of longitude. There are several

different sets of observations that show the time-development of the switchback between the 24^{th} and 25^{th} February 1993. However, due to the fact that there is only one magnetogram and the magnetogram is not of high resolution the time-development of the arcades cannot be modelled. Instead a time snap-shot of the arcades will be constructed showing the main properties of the arcades on both the horizontal and diagonal arms. The deduced field lines give a good agreement with the observations made on the 25^{th} February at 07:03 for the arcades above the horizontal arm and at 11:36 for the arcades above the diagonal arm. At these times the skew of the arcades on the horizontal arm varies between 50°-65° and the skew on the diagonal arm is around 50°. A full description of the development of the arcades over the two days can be found in M^{c}Allister *et al.* (1997). For the switchback the horizontal arm is defined as the arm that runs nearly parallel to a line of latitude and the diagonal arm passes through different latitudes.

On the synoptic chart a common spatial scale does not exist between the equal step in sine of latitude and longitude since the Sun has a shorter cylindrical radius nearer the poles. The origin of the model coordinate system is chosen to be the point (180,-70) on the synoptic chart and all distances are measured from this point. The conversion factor from degrees of longitude (θ) to kilometres at any given latitude (ϕ) is

$$E - W_{distance} = \theta \frac{\pi}{180} R_{sun} cos(\phi), \tag{3.1.4}$$

while the conversion factor for degrees of latitude (ϕ) at any given longitude is

$$N - S_{distance} = \phi \frac{\pi}{180} R_{sun}. \tag{3.1.5}$$

Thus all lengths on the synoptic chart are such that 1 y-pixel = 1 equal step in sine of latitude = 12,147 km $\times$ ϕ where for the n^{th} pixel measured from the equator,

$$\phi = \arcsin(\frac{n}{90}) - \arcsin(\frac{n-1}{90}). \tag{3.1.6}$$

Therefore the y-pixel length scale increases with latitude. The first pixel from the equator is such that $N - S_{distance} = 7,733km$, while for the 30^{th} pixel from the equator it is $N - S_{distance} = 12,147km$. Correspondingly 1 x-pixel = 1 degree of longitude = 12147 km $\times$ cos(ϕ), so that the length decreases with increasing latitude. The magnetogram is now split up into smaller areas

of flux which are predominately of either positive or negative flux. In general, each area is 10 longitudes long and 5 steps in sine latitude wide. Each of these areas is now represented by a magnetic source or sink whose total flux is the resultant flux of the area that it represents. The field of a single source or sink is again given by Equation 2.1.1 where this time the strength πf is given by summing over the individual contributions of each pixel within its area,

$$\pi f = \sum_n f_n \times A_n, \tag{3.1.7}$$

where f_n is the magnetic flux density in Gauss of the n^{th} pixel and A_n is the area expressed in cm^2. This gives the total flux (πf) in Maxwells. To model the magnetogram 145 sources are used, 93 of which are negative and 52 are positive. The strength of each source and sink in terms of 10^{19} Mx is given in Appendix B. Each of the sources and sinks is placed at the centre of the region that it represents in terms of sine latitude and longitude corrected for the fact that there is a shorter cylindrical radius nearer the poles. With this scaling all y-coordinates match the sine latitude seen on the synoptic chart and all x-coordinates differ by a cosine factor. In the region being modelled there is an imbalance of flux towards the positive flux of 2×10^{21} Mx. This is balanced (as in the basic model) by a series of negative sinks placed at equal angles apart and large distances from the switchback. By expressing the distances in this manner the flux regions are seen as they would be looking straight on the Sun and the location of the sources can be seen on Figure 3.10(b). The flux regions have a sheared structure and this, with the local flux imbalance towards the negative flux at the corner of the switchback, gives the sheared structure of the arcades.

The P.I.L. is now calculated for the 145 sources and in Figure 3.10 (b) it is shown as the dashed line that divides up regions of positive and negative flux. From the plot it can be seen that the deduced P.I.L. gives a good agreement to the one seen on the Hα synoptic chart. The centre of the cusp is located at (35,15) units or when transferred to heliographic coordinates at 235 degrees of longitude and S55 in sine latitude, which is close to the observed location. The main body of the horizontal arm lies at 11 units or S59 in sine latitude and at the western end the top of the horizontal arm lies at 20 units or S50 in sine latitude. Finally, on the diagonal arm the P.I.L. runs east-west for a distance of 18 units (218,653 km) at 25 units or S45 in sine latitude, and the horizontal region is situated 13 units west of the cusp of the switchback. Thus the P.I.L. deduced from the sources gives a very good agreement with the one on the synoptic chart.

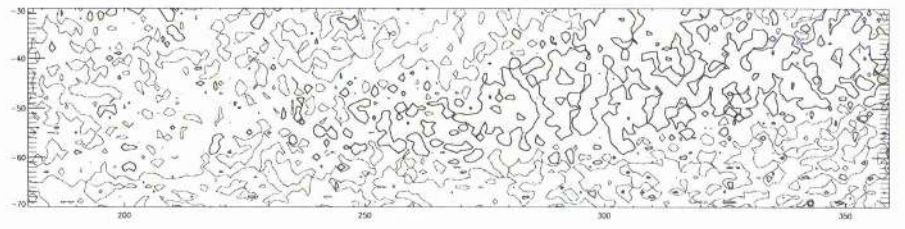

(a)

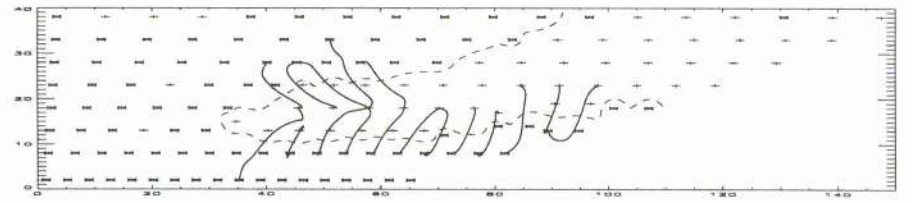

(b)

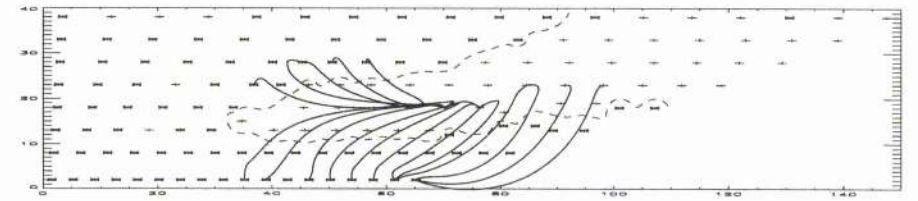

(c)

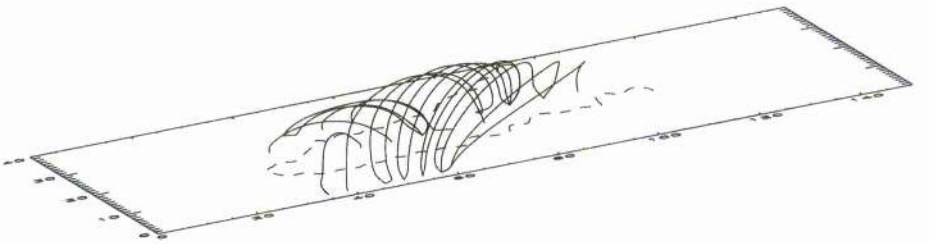

(d)

Figure 3.10: (a) Contour plot of magnetic flux regions around the switchback at ± 4 Gauss. Positive regions are given by the darker lines and negative regions by the lighter lines. (b) Field lines plotted at a height of 50,000 km showing a left skew on the horizontal arm and a right skew on the diagonal arm. Positive sources are given by the plus signs and negative sources by asterisks. (c) The same as in (b) but at a height of 140,000 km. (d) Oblique view of the field lines at heights of 200,000 km on the horizontal arm and 140,000 km on the vertical arm.

The field lines of the switchback are now plotted for various heights. Only the field lines that correspond to the observations are plotted in each case. For each of the field lines the length in kilometres and the skew angle (the angle that a field line makes to a perpendicular from the P.I.L.) are calculated. Initially, the field lines are plotted at a height of 50,000 km. From Figure 3.10(b) the field lines on the horizontal arm can be seen to have a distinctive left skew. At their southern end the feet of the arcades are located at S62 (8 units) in sine latitude and at the northern end they are located at S52 (18 units) in sine latitude in the east and at S47 in sine latitude beyond 80 units. The left skew is created by the local flux imbalance at the corner of the switchback and also by the shear in location of the sources along the arms of the switchback. If a filament formed under these arcades it would be expected to be of dextral type. The field lines along the horizontal arm have an average length of 200,000 km. On the other hand the field lines above the diagonal arm have a definite right skew which can clearly be seen to be in the opposite direction to the field lines on the horizontal arm. In contrast a filament that formed below these arcades would be of sinistral type. The southern feet of the arcades are at S52 in sine latitude and therefore intermingle with the feet of the arcades on the horizontal arm. Again the structures are on average 200,000 km long. In Figure 3.11 the shear angle of the field lines can be seen along the entire length of the P.I.L. from the west end on the horizontal arm to the northern tip of the diagonal arm. At this height the predominant skew angle on the horizontal arm is 10 to 20 degrees and on the diagonal arm it is around -30 degrees so there is slightly more skew on the diagonal arm.

Next, the field lines are plotted at a height of 140,000 km, which is closer to the height of the observed field lines (Figure 3.10(c)). Again the field lines on the horizontal arm have a distinctive left skew and the field lines on the diagonal arm have a right skew. The footpoints of the arcades on the horizontal arm at the southern end now lie at S68 in sine latitude but the northern feet lie at the same position as before. Again the feet of the two arcades intermingle. With the increased height the skew of the field lines has also increased: again the graph of skew angle against length along the P.I.L. for this height is seen in Figure 3.11. On the horizontal arm the predominant skew lies between 40-50 degrees and on the diagonal arm between 45-60 degrees. The field lines are now much longer, with lengths on average 450,000 km on the horizontal arm and 350,000 km on the diagonal arm. At this height there is a good agreement with observations.

The field lines were then finally plotted at a height of 200,000 km. At this height the field

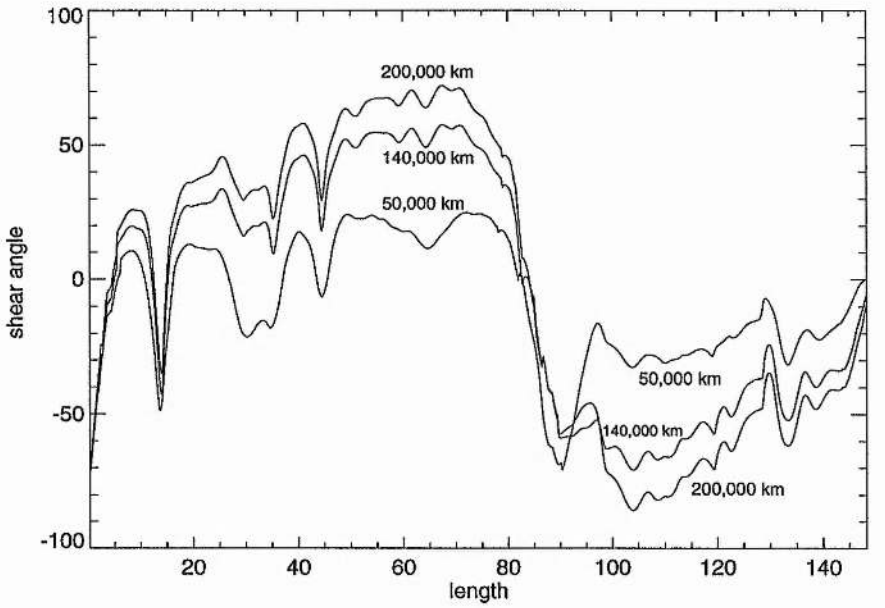

Figure 3.11: Shear of field lines along the arms of the switchback modelled from observations. Positive values denote left-skew and negative values right-skew.

lines on the horizontal arm again gave a good fit to the observations with a skew of 50-70 degrees (Figure 3.11). However, the field lines on the diagonal arm did not compare well with the observed structures from the Yohkoh images with a skew between 70 and 90 degrees. In Figure 3.10(d) an oblique view of the field lines can be seen where the height of the field lines on the horizontal arm is 200,000 km (skew 60 degrees) and the field lines on the diagonal arm are at a height of 140,000 km (skew 50 degrees). Thus a good comparison of the field lines and Yohkoh images was obtained.

3.2.4 Conclusion

In the first part of the section, it has been shown that a skewed structure can be generated along both of the arms of a switchback with a potential field model if we have a local flux imbalance at the corner of the switchback. The local flux imbalance means that on the inside of the switchback all of the flux from the positive source connects to the negative sinks at low heights. Flux from other positive sources along both of the arms can then connect to the negative sinks at the

corner over the top of the inside positive source and generate large sheared field lines as shown in Figures 3.6- 3.8. On one arm the field lines have one type of skew and on the other a different type. The amount of skew increases with height but decreases with distance along the arms of the switchback. When the amount of flux imbalance is increased, the skewing of field lines is also increased. In the second part the general model was applied to a specific set of observations and it was found that a good agreement with the orientations of the observed coronal arcades above the switchback can be obtained. The arcades on the horizontal arm have a definite left skew while the arcades on the diagonal arm have the opposite right skew. The best fit is obtained when the height of the field lines on the horizontal arm is 200,000 km (giving a skew of around 60 degrees) and the height on the diagonal arm is 140,000 km (giving a skew of around 50 degrees). Again the higher the field lines the greater the skew. The shear was again created by the local flux imbalance at the corner of the switchback and the asymmetry in physical location of the sources. The model gave a surprisingly good agreement with the observations, considering that the switchback was made up of weak background flux and low-resolution synoptic charts were used. The modelling has shown that in the corona low-lying field lines are often not greatly skewed, while the overlying field lines may be greatly skewed. The shear of field lines can be generated by a purely potential field if there is a local imbalance in flux location. Thus, unlike the case of a straight infinitely long uniform arcade, a force-free field is not required in order to produce sheared field lines. The addition of currents to produce a force-free switchback may on the other hand increase the skew still further.

3.3 Model of a Particular Filament.

In Chapter 2 a simple potential model of a filament channel was set up. We now develop it further by applying it to a specific example of a filament and filament channel.

3.3.1 Observations.

The two filament channels modelled in this section are shown in Figure 3.12. The images on the left are Hα filtergrams which show the chromosphere and on the right are videomagnetograms which give the line of sight component of the magnetic field at the photosphere. The images are from a series of time-lapse films taken on the 29^{th} and 30^{th} August at the Big Bear Solar Observatory (Martin 1985,1986). By comparing the two images, the structure of the filament can be seen relative to the photospheric magnetic fragments that lie under the filament. The filament is bounded by mostly positive flux below and negative flux above. The filament therefore lies along the polarity inversion zone between the two flux regions. There are also many sites of cancelling magnetic features near the filament. In the magnetogram the negative fields are black and the positive fields are white except within contours where there are stronger fragments of flux. Each successive contour represents an increase in field strength by a factor of two. The lowest contours correspond to field strengths of around 50G. It can also be seen that the strong concentrations of magnetic flux correspond to bright plage regions in the Hα picture.

The Hα images show many distinctive properties of the filaments. They are long, thin dark structures that bend and weave their way between regions of opposite polarity flux. When the filaments pass between regions of opposite polarity flux they tend to become very narrow (see Section 3.1).

By using the method of Foukal (1971) it is possible to determine the direction of the field inside the filament from the fibrils in the chromosphere, since the fibrils are aligned parallel to the filament's axis. In the top Hα image the fibrils on the positive polarity side emanate to the right of the plagettes (concentrations in the network magnetic field). By comparison, on the negative polarity side the fibrils emanate to the left. This suggests the horizontal component of the field is in the same direction on both sides of the filament. Thus the field in the filament goes from left to right. When standing on the positive polarity side the horizontal component of the field points

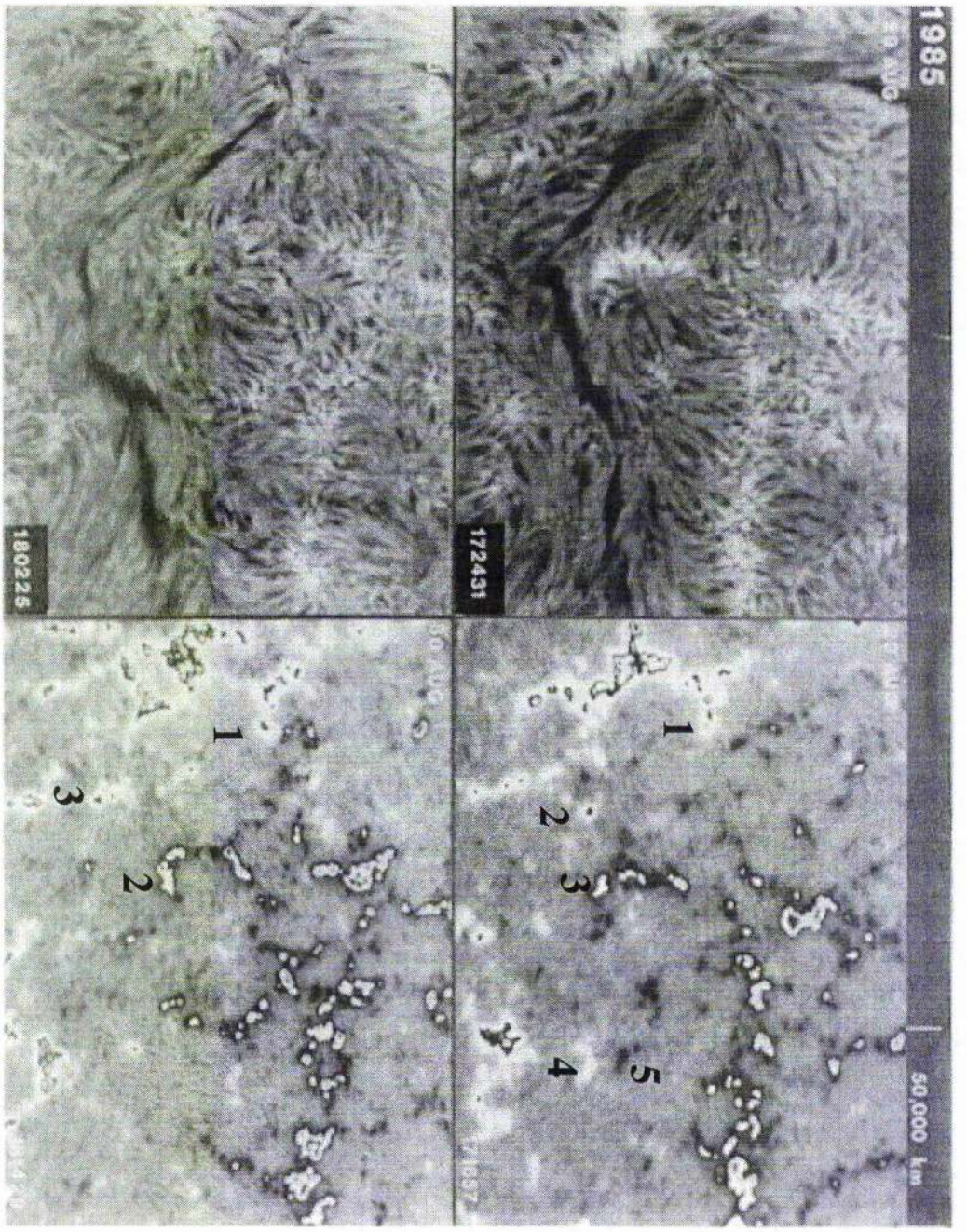

Figure 3.12: $H\alpha$ (left) and photospheric magnetogram (right) pictures of a filament channel on two days shown top and bottom (From Martin, 1985).

to the right, so this filament may be described as being "dextral". The legs of the filament leave the main body of the filament and go to the right into the chromosphere and so, as expected, this filament is also "right bearing".

The top Hα image shows a filament that seems to emerge from a region of positive flux on the left-hand side (region 1). It passes between the positive and negative regions of flux (regions 2 and 3 , 4 and 5) and becomes very narrow as it passes between them. It also has a bend or kink in the middle where the filament changes direction. The end of the filament passes off the Hα image. The same filament on the next day (bottom Hα image) has broken up into two smaller filaments (both "dextral"). The top filament emanates from flux region 1 to flux region 2 and is a very straight structure. The second filament emerges from flux region 3 and ends off the Hα image. It bends and kinks as it passes between regions of different flux. The features described above are the main ones that will be modelled.

3.3.2 Potential Model.

A potential field model is set up consisting of a series of sources and sinks representing the regions of positive and negative flux in the photosphere. It is assumed that nearly all of the sources on the magnetogram affect the filament to some degree. The magnetic field at a point (x, y, z) due to a source or sink at ($a, b, 0$) is given by :

$$\mathbf{B} = \frac{f}{2}\left(\frac{(x-a)}{((x-a)^2+(y-b)^2+z^2)^{3/2}}, \frac{(y-b)}{((x-a)^2+(y-b)^2+z^2)^{3/2}}, \right.$$

$$\left. \frac{z}{((x-a)^2+(y-b)^2+z^2)^{3/2}}\right), \qquad (3.3.1)$$

where πf is the strength of the source or sink. It is assumed that the poles are situated in the photosphere (i.e. z=0 plane). The relative strengths of each region are estimated roughly from the field strength and area of each region on the magnetogram. The strengths are only estimates since no raw data was available for the magnetogram. A more accurate calculation of this type using the exact flux values from a magnetogram is carried out in Chapter 4. All of the plots are drawn first looking vertically down on the field lines and then looking side on. The dashed box

in Figures 3.13 and 3.14 represents the magnetogram box which contains all the magnetogram sources. One unit in the box corresponds to 9200 km or $13''$.

(i) Magnetogram 1.

It is assumed that the filament's magnetic field starts in pole 1 and an extra pole (pole 2) is added outside the magnetogram box for the field lines to end in. It is also assumed that there is an overlying uniform field, created by some surrounding flux regions (see Section 2.2). The magnetic field is therefore given by :

$$\mathbf{B} = \sum_{i=1}^{21} \frac{f_i \mathbf{r_i}}{2r_i^3} + B_{0x}\hat{\mathbf{x}} + B_{0y}\hat{\mathbf{y}}, \tag{3.3.2}$$

where $\mathbf{r}_i = (x - a_i)\hat{\mathbf{x}} + (y - b_i)\hat{\mathbf{y}} + (z)\hat{\mathbf{z}}$ is the distance between the point (x, y, z) and the i^{th} pole. The strengths f_i are given in Appendix C, and we set B_{ox} = 6.0, B_{oy} = -2.0, $|\mathbf{B}|$ = 6.3. Only field lines that pass between poles 3 and 4 and 11 and 12 on the magnetogram are considered since the filament is seen to pass between these regions.

In the first model the field lines were plotted for the sources seen on the magnetogram and the overlying uniform field given above. Figure 3.13(a) shows that no field lines that pass between poles 3 and 4 connect poles 1 and 2. The majority of field lines connect poles 5 and 2. Thus the simplest potential model for the filament with only the poles in the magnetogram box and the overlying uniform field will not produce the required connections of the field lines following the path of the filament. Figure 3.13(b) shows how the field lines vary with height. They are long low-lying structures which may be able to support the prominence mass having a height of about 10,000 km.

The Hα and magnetogram images are of high resolution and only show part of the surrounding active-region flux. There may be large regions of flux lying outside the magnetogram box which may effect the field line and filament connections. The next two models show how improvements can be made to the simple potential model by adding extra sources so that the field lines connect poles 1 and 2 and so that they follow the structure of the filament. However, there is no direct evidence for the existence of these flux regions. Synoptic chart magnetograms from the NSO

archive in Tuscon were considered but were not of the required resolution to determine the location of the channel or whether the neighbouring flux regions exist.

In the second model the magnetogram poles have the same positions and strengths as before, except that a new pole is included outside the magnetogram box so that the correct connections between poles 1 and 2 are produced. The pole is added at (0,10.5) and has a relative strength of 240. This pole would represent a large region of positive flux lying outside the upper left-hand region of the magnetogram. Figure 3.13(c) shows that the correct connections are produced. The field lines shown are the only ones that connect poles 1 and 2 and pass between poles 3 and 4 and 11 and 12 (i.e. follow the path of the filament when seen from above). The field lines give a much better fit to the path of the filament than in model 1. When viewed from the side the field lines are long low-lying structures which have a central dip. The field lines are of a topology that is suitable for the formation of mass having a height of about $10,000$ km. One feature of the filament that is not reproduced in the model is the bend in the middle of the filament as it passes close to pole 6. No field lines that connect 1 and 2 and pass between 3 and 4 and 11 and 12 pass near pole 6. It was therefore decided to add extra poles to try and give the bend seen on the Hα image.

In the third model in order to create the bend two extra poles were added outside the magnetogram box at positions (8.1,0),(9.3,0). The poles have relative strengths of -220 and 260, respectively. It can be seen in Figure 3.13(e) that the effect of the poles is indeed to create a bend in the filament that makes the potential model fit the path of the filament much better. Again the variation of field lines with height is shown in Figure 3.13(f).

With the regions of positive and negative flux seen on the magnetogram and an overlying field it was found that in the simple potential model the correct path of the filament from the magnetic field lines was not given. By adding flux sources and sinks outside the magnetogram box it was found that the correct connections and a better shape for the filament could be obtained. However, these flux regions were very large and there is no direct evidence for their existence, since the only magnetogram available of the channel is of high resolution. This may mean that the filament is significantly altered by the surrounding fields that lie outside the magnetogram image.

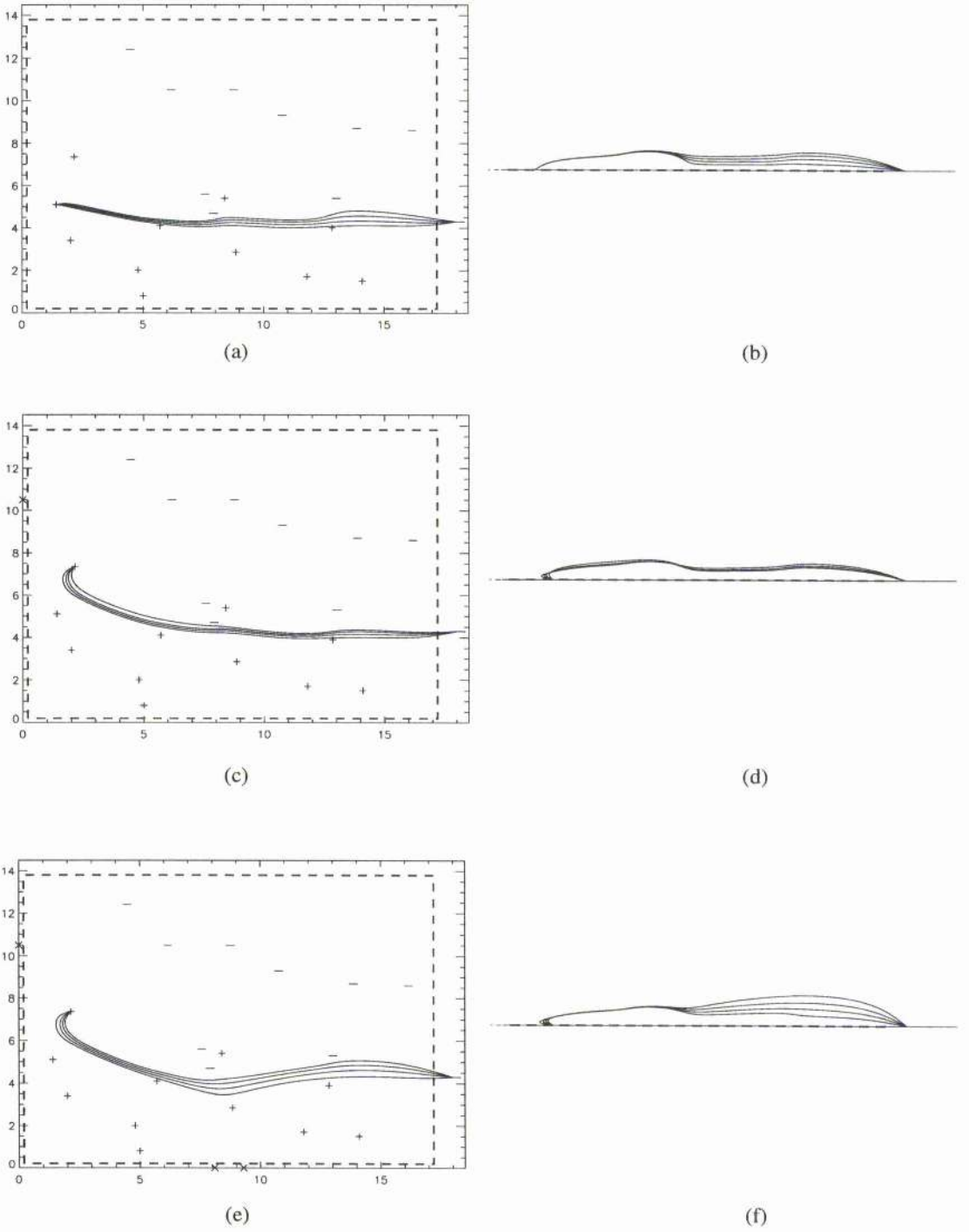

Figure 3.13: Field lines and sources (plus), sinks (minus) for model 1 from (a) above, (b) side. (c) and (d) same but for model2. (e) and (f) same but for model 3.

(ii) Magnetogram 2.

The relative flux values were then recalculated for the second magnetogram (lower-part of Figure 3.12) which is of the same region taken a day later. It can be seen that there is much flux cancellation over the 24 hours since the first magnetogram. In the Hα picture the filament has split up into two smaller parts. As before, the filaments are first modelled with the poles seen on the magnetogram and it is assumed that the same uniform field exists overlying the filament channel. The field is given by :

$$\mathbf{B} = \sum_{i=1}^{23} \frac{f_i \mathbf{r_i}}{2{r_i}^3} + B_{ox}\hat{\mathbf{x}} + B_{oy}\hat{\mathbf{y}}, \tag{3.3.3}$$

and the relative flux values are given in Appendix C.

The fourth model considers only the sources seen on the magnetogram. It can be seen (Figure 3.14(a)) that the correct connections between the poles are made but the field lines do not follow very closely the observed path of the filament. The top filament curves much more than in the Hα image and the bottom filament does not pass between poles 13 and 14. Thus the sources on the magnetogram give the correct connections but not reasonable paths for the filaments. Figure 3.14(b) gives a side on view of the two structures. They are both long, low-lying structures which could support the prominence mass.

In the first magnetogram the field lines gave a better fit to the Hα observations when extra sources lying outside the magnetogram were added. The next two models show how adding these same sources also improves the field line path in the second magnetogram. First of all, in the fifth model the pole with position (0.0,10.5) is added with its relative flux of 240. It can be seen in Figure 3.14(c) that the top filament has a much straighter structure and gives a better fit to the shape seen in the Hα image. The bottom filament has changed slightly but has the same basic shape and still does not have the field lines passing between poles 13 and 14. Thus by adding the extra pole a much better fit for the top filament is obtained. Figure 3.14(d) gives a side-on view of the field lines.

In the sixth model the two extra poles are added to see if they give a better structure for the bottom filament. They have coordinates (8.1,0) and (9.3,0) and strengths -220 and 260, respectively. With these extra poles added it was found that the correct connection could not be made.

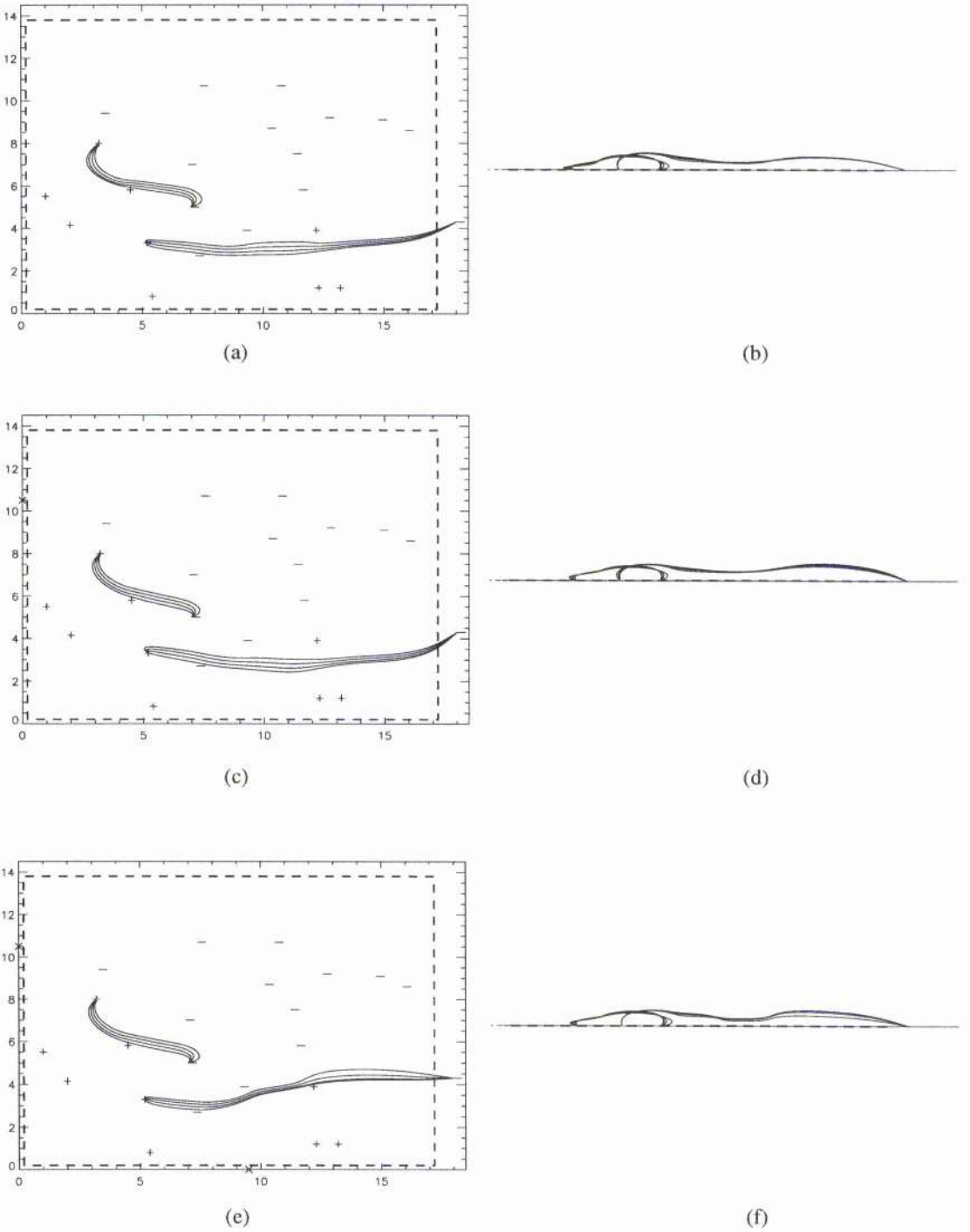

Figure 3.14: Field lines and sources (plus), sinks (minus) for model 4 from (a) above, (b) side. (c) and (d) same but for model5. (e) and (f) same but for model 7.

The large negative pole connects poles 5 and 6 while the positive pole connects to pole 2. Thus by adding the two extra poles the filament at the bottom breaks up.

Between the first and second magnetogram there is, however, much flux cancellation in the region of the magnetogram, and it is possible that the regions of flux outside the magnetogram have cancelled also. If the two extra poles cancel each other, a positive pole of strength 40 is left. The field lines in this case (model 7) are shown in Figure 3.14(e). The field lines give a good agreement with the Hα image of the filament. In Figure 3.14(f) a side-on view of the filament shows the field lines to be long low-lying structures with a height of around $10,000$ km. In Figures 3.14(b),(d),(e) it can be seen that there is always a central dip in the field lines. The dips in the field lines are due to the location of the sources and sinks in the channel. The field lines in the channel are plotted so that they follow the path of the filament. The dip in the middle is due to the location and sign of the sources 9,12 and 13 (Figure C2). The field lines emerge out of pole 7 where the vertical component of field is positive. Near poles 9 and 12 the sign of B_z changes from positive to negative so the field lines decrease in height. Around pole 13 the sign of B_z changes again to become positive so the field lines rise to avoid pole 13 and create the dip. Thus it is the location and sign of the sources 9,12 and 13 that create the dip in the structure. The dip in the field lines comes from the location and size of flux regions seen on the magnetogram. It is in this type of magnetic topology that the process described by Antiochos and Klimchuck (1993) could easily take place.

3.3.3 Conclusion.

The filaments here have been modelled with a simple potential field consisting of magnetic sources and sinks. By representing the magnitudes and locations of the flux sources observed in the magnetogram a surprisingly good representation of the filament channel and its filaments was found, considering how simple the model is. However, it is assumed that there is an overlying uniform field created by some surrounding regions. The relative strength of the overlying field is much stronger than the one considered in Section 2.2. At a height of 30,000 km it is more than 3 times stronger than the field due to the sources. However, without more extensive data the magnitude of the field in Gauss cannot be calculated, so it is unknown if it is a realistic value. In the next chapter using a different example, the magnitude of the uniform field required can be calculated.

To obtain the best fit some external sources had to be added to the field outside the magnetogram. These sources represent large regions of neighbouring flux that lie outside the field of view of the magnetogram. Due to the lack of data, the existence of these flux regions could not be established. However, an interesting point in the model is that dips in the magnetic structure of the filament can result just due to the locations of flux lying below the filament. The model here is very rough so a more detailed calculation is carried out in Chapter 4.

Chapter 4

Force-Free and Potential Models of a Filament Channel in which a Filament Forms

Few examples of the creation of a filament channel or filament have ever been documented. In a recent paper, Gaizauskas and coworkers observed the early stages of creation of such a channel and then the formation of a filament in it. The filament channel was born when a new activity complex emerged near to an old decaying bipolar active region. The filament itself then formed after convergence of flux in the channel.

In this chapter force-free models are constructed for two phases of the channel's development. For the early days the models show that the formation of the filament channel seen in Hα is due to the emerging activity complex. Later, when the activity complex has matured and a filament has formed between it and the adjacent decaying bipolar region, models which include both flux regions give a good representation of the path of the filament in the channel. The magnetic field lines of the filament form a narrow vertical, sheet-like, flux-tube corridor that is flat and low-lying. The role of the remnant region in the changing topology of the channel is investigated. It is found that the presence of flat or dipped field lines and of converging flux are necessary but not sufficient conditions for filament formation.

4.1 Observations.

In the paper by Gaizauskas *et al.* (1997) the emergence of a small activity complex and the subsequent formation of a filament channel and filament are described. The formation of the filament channel and filament occurred between the 19^{th} and 25^{th} July, 1979 during the ascending phase of cycle 21. By comparing $H\alpha$ images from the Ottawa River Solar Observatory (ORSO), (Gaizauskas 1976) and full disc magnetograms from the National Solar Observatory (NSO) they were able to describe fully the development of the channel. A brief summary of their observations is given below.

On July 20^{th}, 1979, a small activity complex M^{c}Math 16166 emerged just south of the equator, in an area free of active regions. The activity complex consisted of two dipoles in close proximity. To the east of the activity complex lay an old decaying region of plage, M^{c}Math 16159. In Figure 4.1 (bottom right panel) the newly emerged region is enclosed by an oval while the bright region to the south-east is the old remnant plage. On the previous day (July 19, bottom left panel) it can be seen that the area of emergence is free of any flux regions or strong fibril structures. The newly emerged activity complex grew rapidly on the 21^{st} and 22^{nd} but began to decay away slowly after the 23^{rd}. The old remnant region's total flux remained relatively constant for the period of filament channel and filament formation. One day after the complex started to emerge a system of curved fibrils in Hα surrounded most of it. The fibrils are in the region labelled B in Figure 4.1(top right panel). The fibrils twist in a N-S direction and at the south side they bend back into the activity complex. Near where they end Arch Filament Systems (AFS) can be seen, giving a transverse structure across the P.I.L. rather than a horizontal field along it. These AFS denote the end of the channel. The swath of fibrils, as wide as a supergranule, is in a region that was previously free of strong magnetic fields or patterns of coaligned fibrils. The fibril alignment occurred over a period of three hours (compare Figure 4.1 top panels); once formed, it lasted many days with mass forming erratically along different strands in a matter of hours (Figures 4.2,4.3, top panels). The alignment of fibrils at B indicates a strong horizontal component there and the formation of a filament channel at that location. Since that alignment takes place in a few hours and occurs when there is rapid flux emergence in the new activity complex, this suggests that the pattern is due to the extended magnetic field of the newly emerged activity complex. The strong

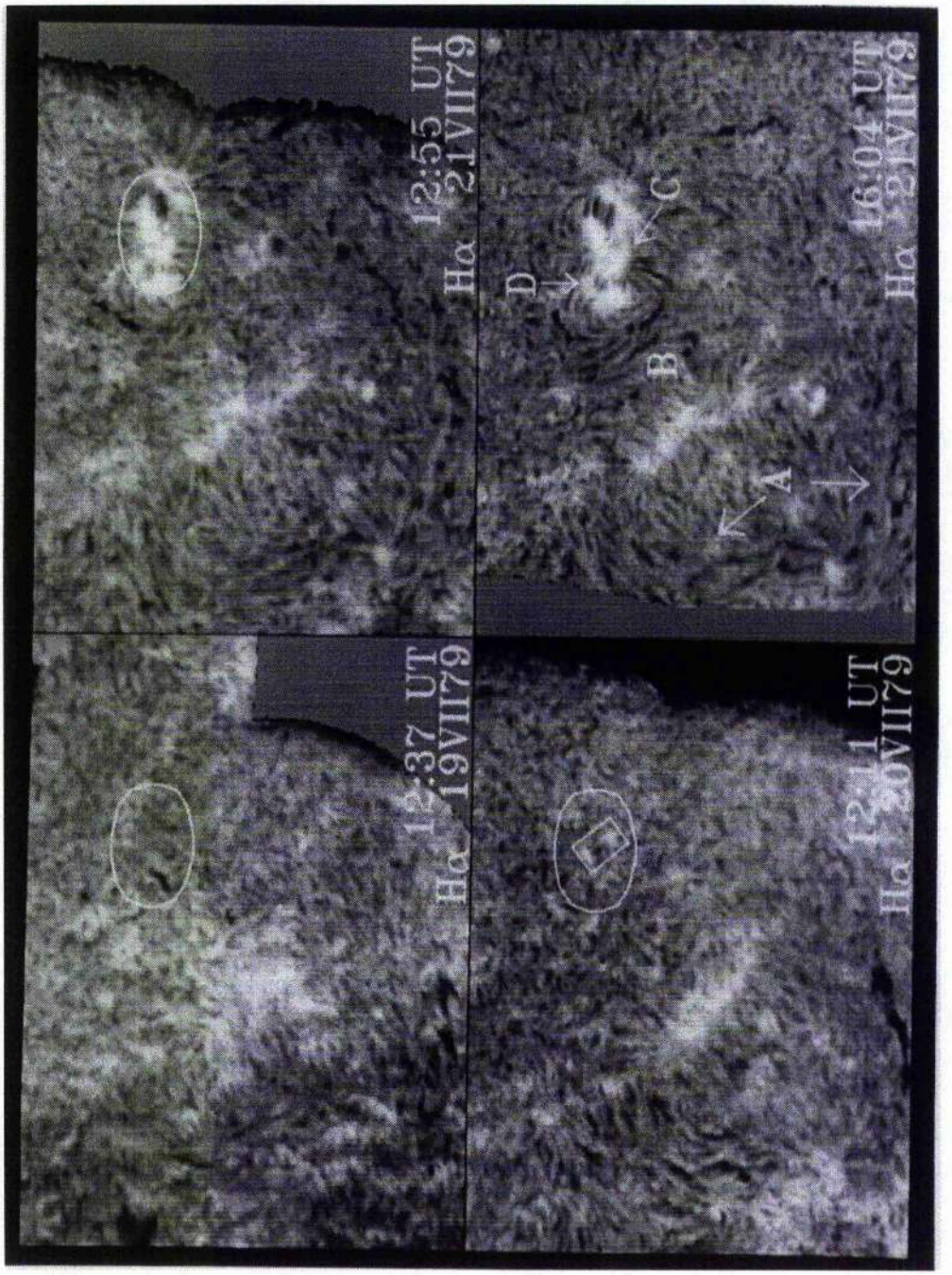

Figure 4.1: Emergence of M^{c}Math 16166 (oval) on July 20^{th}, 1979 (lower right panel) and its rapid growth by July 21^{st} (top left panel). On the 21^{st} a C-shaped ring of fibrils surround the trailing side of M^{c}Math 16166 (labelled B, top right panel) (from Gaizauskas *et al.* 1997).

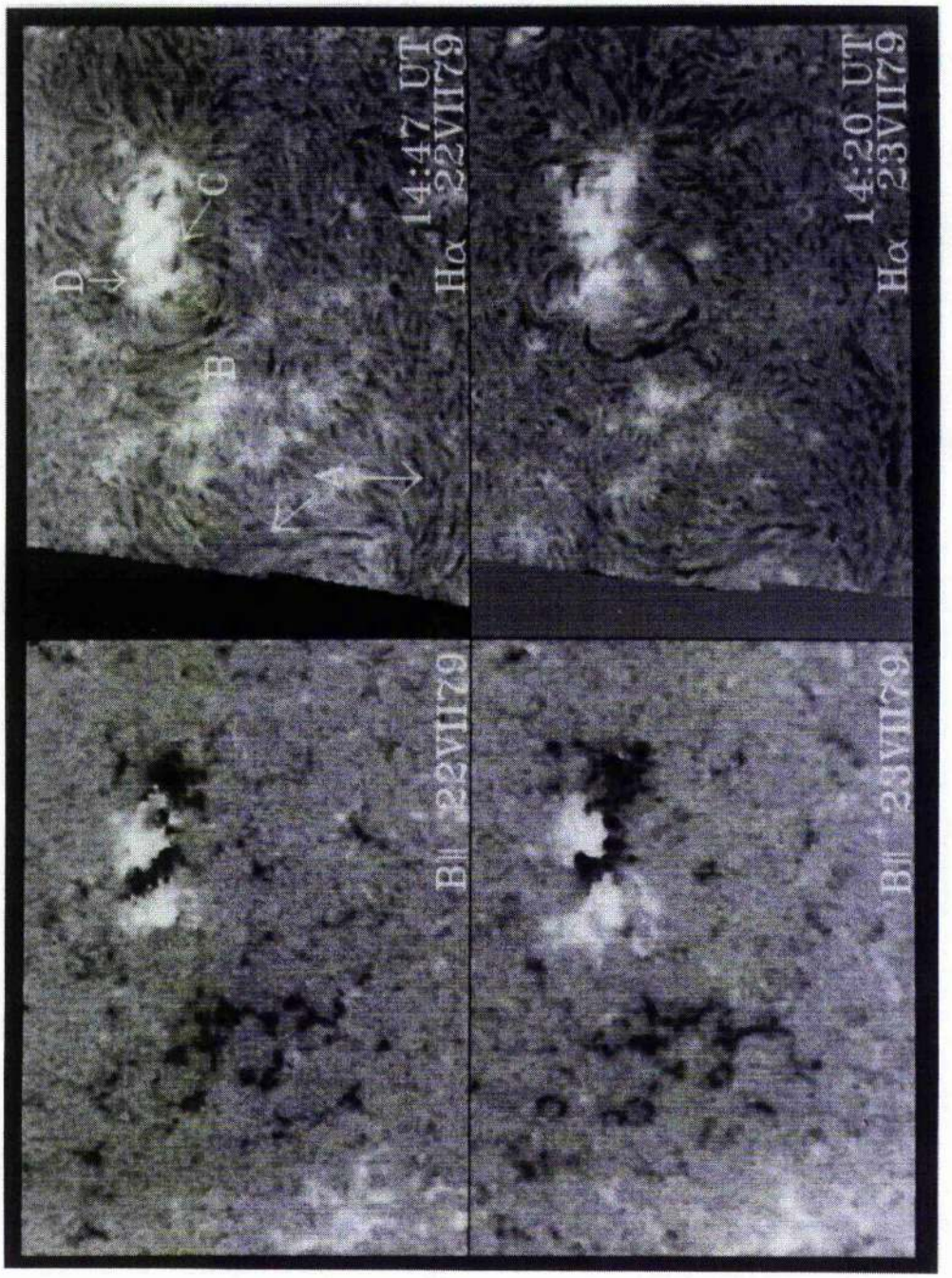

Figure 4.2: Comparison of ORSO Hα filtergrams and magnetograms from NSO/Kitt Peak for July 22^{nd} and 23^{rd}. On the magnetograms white is +ve flux and black -ve flux (from Gaizauskas *et al.* 1997).

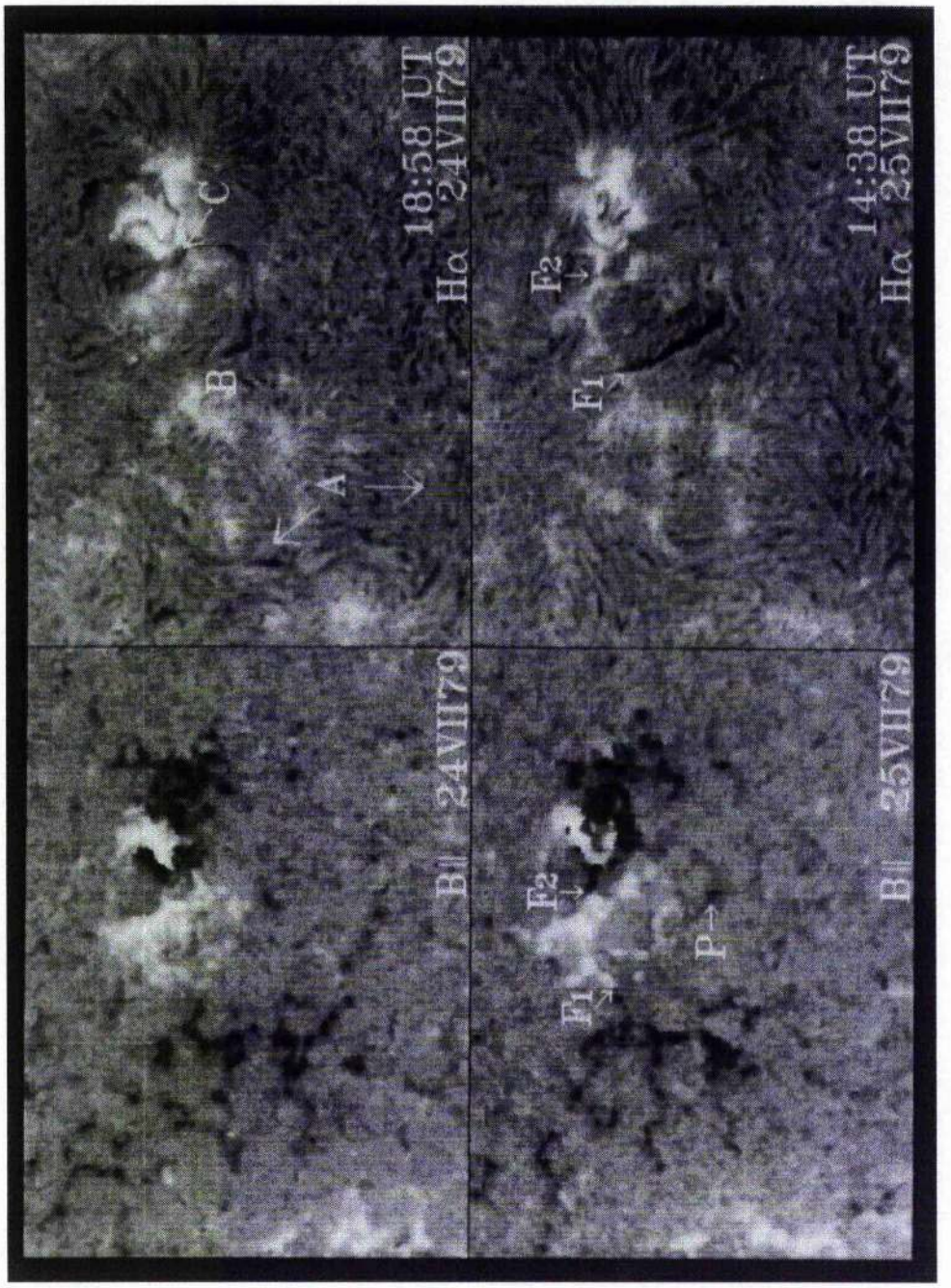

Figure 4.3: Same as Figure 4.2 but for 24^{th} and 25^{th} July. A small quiescent filament forms on the 25^{th} (upper right) where opposite polarity fragments converge (F1, lower right) (from Gaizauskas *et al.* 1997).

twisting in the N-S direction suggests that the field is non-potential. On the 22^{nd}, 23^{rd} and 24^{th} mass accumulated along strands in a period of hours as though attempting to form a filament at B. The newly emerged activity complex started to decay after the 23^{rd}; on the magnetograms of the 23^{rd} (Figure 4.2, bottom right), 24^{th} and 25^{th} (Figure 4.3, bottom panels) the flux can be seen to disperse slowly. The dispersion of flux in the channel is manly due to the eastward expansion of the positive polarity of the activity complex.

On the 25^{th} magnetic flux converged at the point F1 between the trailing positive polarity of M^{c}Math 16166 and the old remnant negative plage region M^{c}Math 16159 (Figure 4.3, bottom right panel). With the convergence a filament formed at F1 and linked excess positive flux with the negative flux in a plagette south of 16166 (Figure 4.3, top right panel). The newly formed filament persisted until its passage over the limb three days later. The formation of the filament occurred overnight and there was no smooth transition of the fibrils to the filament on the period of days. In contrast to this, neither a filament nor a filament channel formed at the point F2 where there was also convergence of flux. At this point the magnetic field has a strong transverse structure across the polarity inversion line (P.I.L.) rather than along it shown by the AFS, so there is no filament channel.

With the observations in mind, force-free models of the newly emerged activity complex are first constructed and produce the same type of fibril alignment as seen on the 21^{st} and 22^{nd}. This shows that the pattern of fibrils and therefore the filament channel is most likely created by the extended non-potential field of the newly emerged activity complex. Consequently, the old remnant plage region will not be included in the force-free modelling for these dates.

On the later days when the filament has formed, the new and remnant regions have interacted with each other. For the 25^{th} it is shown that, while a potential model fails to give the correct connectivity of the field to represent the filament, force-free models do. Thus the magnetic field of a small active-region filament cannot be described by a potential field. Force-free models of the entire channel show that the global field of the filament channel and filament can be described well by a highly sheared force-free field, even though a magnetostatic model would be required to describe the local internal structure of the filament. By modelling the channel without the old remnant bipolar active region forming a boundary on one side, the role of this region in the evolving global topology of the channel is investigated.

4.2 Force-Free Models of the Activity Complex.

4.2.1 Introduction

One day after the activity complex started to emerge, a system of curved fibrils surrounded most of it. The fibrils outline the magnetic lines of force and imply that there is a strong horizontal component of field there (Foukal 1971). The alignment of fibrils is due to the newly emerged region's extended magnetic field. Each individual fibril lasts from minutes to a few hours with mass forming erratically along them; therefore the fibrils field may be described as being in a quasistatic state. These fibrils lie in the chromosphere and lower corona where the magnetic field dominates over other forces such as pressure or gravity (see Section 1.4). Accordingly, the magnetic field that outlines them may be described as being a force-free field so that it satisfies Equations (1.4.3), (1.4.4), (1.4.10). To start with, in Section 4.2.2 a simple analytical force-free model is constructed of the newly emerged activity complex. By a topological comparison of the fibril alignment and magnetic lines of force, the field on the 21^{st} (Figure 4.1, top right panel) surrounding the activity complex is shown to be in an approximately force-free state. A numerical force-free model, with the flux through the photosphere obtained from the magnetogram, is then constructed for the 22^{nd} (Section 4.2.3) and again the field lines are compared with observations.

4.2.2 Analytical Model for the 21^{st} July.

For a general function $\alpha(\mathbf{r})$ the force-free equation(1.4.10) is very difficult to solve. However a great simplification occurs when α is uniform and linear theory applies. In previous papers by Nakagawa *et al.* (1971), Raadu and Nakagawa (1971) and Nakagawa and Raadu (1972) a topological similarity between certain classes of constant-α force-free fields and Hα structures was found. By taking observations from a longitudinal magnetogram a full boundary-value problem was then solved by Nakagawa *et al.* (1973). The magnetogram gave the horizontal (x,y) distribution of the vertical component of the magnetic field. In this method there was, however, a limitation in their manner of representation due to α being constant over the entire region. To ensure that the field was bounded, the value of α had always to be less than the minimum value of the wavenumber k_{min} ($\alpha < k_{min}$), which was determined from the size of the domain: a large domain meant that the value of k_{min} was small and therefore α had to be small. Therefore, Hα structures which had

a large local curvature could not be reproduced successfully from the computed field in a large domain. The same problem that Nakagawa encountered also appears for the data sets here when solving the full boundary-value problem. The features seen in Figure 4.1 have a large local curvature and therefore a large value of α is required. The domain of analysis containing the four patches of flux in M^{c}Math 16166 is however much larger than the region modelled in Nakagawa *et al.* (1973), which implies that the maximum value of α is even smaller than in their modelling. So, by having α constant everywhere, the large-scale curvature effects cannot be reproduced. For the activity complex M^{c}Math 16166 there are four distinct flux patches, two positive and two negative, so an analysis similar to Nakagawa and Raadu (1972) can be carried out. Single terms in the solution to the force-free equation will be considered, without solving the full boundary-value problem. Due to the geometry the analysis will be carried out above a flat plane in Cartesian coordinates.

To find a linear force-free field we have to solve Equation 1.4.10 with α = constant, and determine **B** such that it satisfies the solenoidal constraint Equation 1.4.3. To simplify the problem and to adopt a poloidal/toroidal representation (Morse & Feshbach 1953) the magnetic field may be written in terms of two arbitrary scalar functions, P and T, such that

$$\begin{aligned} \mathbf{B} &= \nabla \times \nabla \times (P\hat{\mathbf{z}}) + \nabla \times (T\hat{\mathbf{z}}) \\ &= \left(\frac{\partial^2 P}{\partial x \partial z} + \frac{\partial T}{\partial y}\right)\hat{\mathbf{x}} + \left(\frac{\partial^2 P}{\partial y \partial z} - \frac{\partial T}{\partial x}\right)\hat{\mathbf{y}} - \left(\frac{\partial^2 P}{\partial^2 x} + \frac{\partial^2 P}{\partial^2 y}\right)\hat{\mathbf{z}}. \end{aligned} \tag{4.2.1}$$

By substituting this form for **B** into the force-free equation and splitting it into its poloidal and toroidal terms (which each separately vanish), the force-free equation reduces to,

$$\nabla \times \nabla \times \{(T - \alpha P)\hat{\mathbf{z}}\} - \nabla \times \left\{(\nabla^2 P + \alpha T)\hat{\mathbf{z}}\right\} = 0, \tag{4.2.2}$$

or

$$T = \alpha P, \tag{4.2.3}$$

$$\nabla^2 P = -\alpha^2 P. \tag{4.2.4}$$

Equation 4.2.4 is then solved subject to the boundary conditions:

1. the field is bounded as z $\rightarrow \infty$;

2. the vertical component of the field B_z(x,y) at the photospheric level is given from the horizontal distribution of the observed line-of-sight component.

The appropriate solution to Equation 4.2.4 is

$$P = \sum_{k \neq 0} \frac{1}{k^2} B_k e^{i\mathbf{k}.\mathbf{x} - (k^2 - \alpha^2)^{\frac{1}{2}} z}, \tag{4.2.5}$$

where

$$\mathbf{k} = k_x \hat{\mathbf{x}} + k_y \hat{\mathbf{y}}, \quad \mathbf{x} = x\hat{\mathbf{x}} + y\hat{\mathbf{y}}, \quad k^2 = k_x^2 + k_y^2, \tag{4.2.6}$$

and the values of B_k are the Fourier coefficients of the observed magnetic field. The corresponding magnetic field components are,

$$B_x = \sum_{k \neq 0} \frac{i}{k^2} \left[\alpha k_y - k_x \left(k^2 - \alpha^2 \right)^{\frac{1}{2}} \right] B_k e^{i\mathbf{k}.\mathbf{x} - (k^2 - \alpha^2)^{\frac{1}{2}} z}, \tag{4.2.7}$$

$$B_y = \sum_{k \neq 0} - \frac{i}{k^2} \left[\alpha k_x + k_y \left(k^2 - \alpha^2 \right)^{\frac{1}{2}} \right] B_k e^{i\mathbf{k}.\mathbf{x} - (k^2 - \alpha^2)^{\frac{1}{2}} z}, \tag{4.2.8}$$

$$B_z = \sum_{k \neq 0} B_k e^{i\mathbf{k}.\mathbf{x} - (k^2 - \alpha^2)^{\frac{1}{2}} z}. \tag{4.2.9}$$

An important property to note from Equation 4.2.5 is that, since all of the field components must be bounded, the β = (k^2 - α^2)$^{\frac{1}{2}}$ appearing in the z-dependence cannot be imaginary. This means that the maximum value of $\alpha(\alpha_{max})$ must always be less than the minimum value of k(k_{min}), $\alpha_{max} < k_{min}$, which limits the amount of curvature that can be obtained for the field lines. In order to compare the topology of the deduced magnetic field with the Hα observations, single terms of the Fourier series are picked by choosing a suitable horizontal wave number k_0 = (k_x^2 + k_y^2)$^{\frac{1}{2}}$ to fit the observations. Since we are dealing with a single term, the vertical dependence β = (k_0^2 - α^2)$^{\frac{1}{2}}$ now becomes constant and Equation 4.2.1 can be written in the form

$$\mathbf{B} = \alpha \left(\nabla_H P \right) \times \hat{\mathbf{z}} - \beta \left(\nabla_H P \right) + k_0^2 P \hat{\mathbf{z}}, \tag{4.2.10}$$

where

$$\nabla_H = \frac{\partial}{\partial x} \hat{\mathbf{x}} + \frac{\partial}{\partial y} \hat{\mathbf{y}}.$$

The value of α will be determined from the twist angle γ, which is the angle that a magnetic line of force makes with a contour of B_z (P= constant). Since $\nabla_H P$ is a vector that is perpendicular to the contour of B_z (P= constant), and $(\nabla_H P) \times \hat{\mathbf{z}}$ is a vector that is tangential to the contour

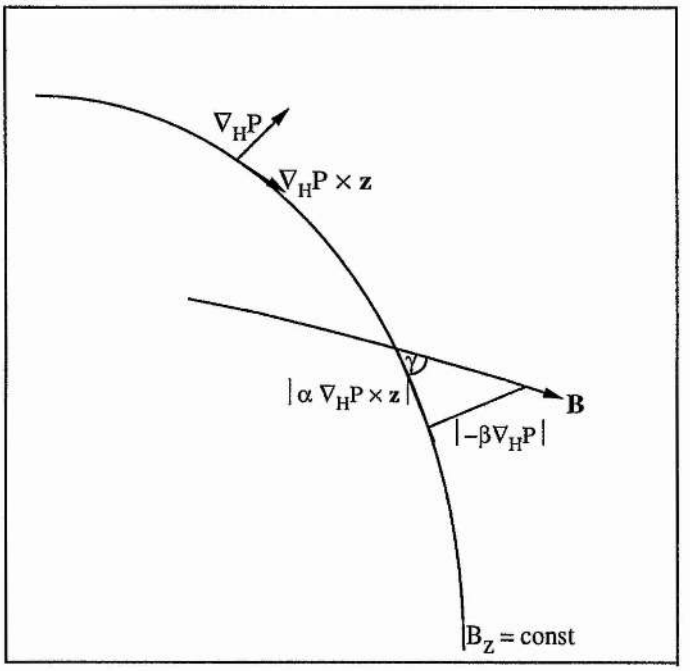

Figure 4.4: Diagram showing the definition of the twist angle γ, as the angle at which a field line cuts the contour of B_z.

of B_z, (Figure 4.4), the magnetic lines of force cut the contour of B_z at an angle γ, given by

$$\tan\gamma = \frac{|-\beta \nabla_H P|}{|\alpha(\nabla_H P \times \hat{\mathbf{z}})|} = \frac{\beta}{\alpha}, \tag{4.2.11}$$

$$\alpha = k_0 \cos\gamma. \tag{4.2.12}$$

By this representation the value of α^2 will always be less than k_0^2 so that the solution is bounded. When $\gamma = 90°$ the field lines are radial and $\alpha = 0$ so this corresponds to the potential case.

The analytical method will now be applied to the observations from the 21^{st} July. The magnetograms of the activity complex show four distinct flux patches emerging in M^{c}Math 16166. Two patches are of positive flux and two are of negative flux. To model this a suitable single term from Equation 4.2.5 is chosen, namely

$$P = \frac{1}{k^2} \sin k_x x \cos k_y y e^{-\beta z}, \tag{4.2.13}$$

where $k_x = 4$, $k_y = 1$ and $k^2 = 17$. This gives the field components as

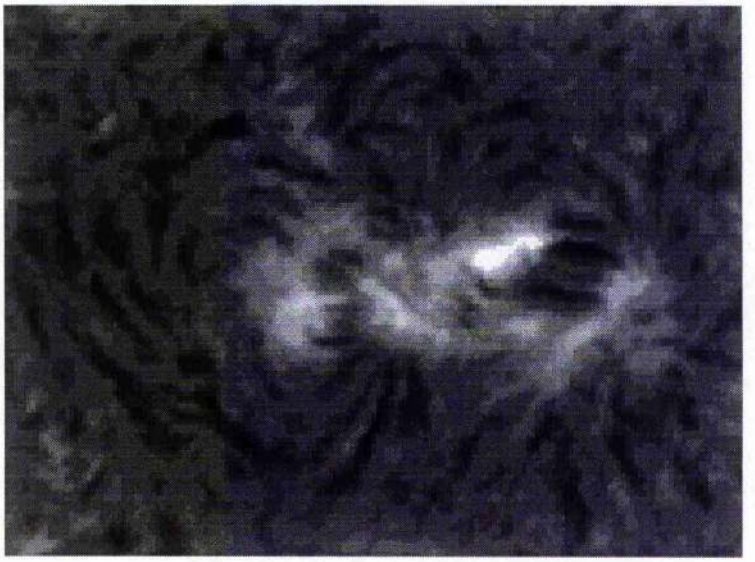

(a)

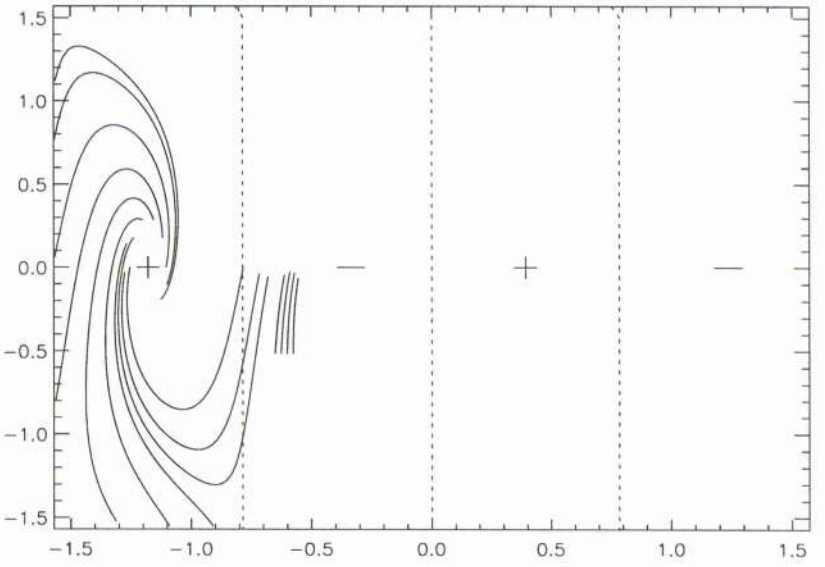

(b)

Figure 4.5: Force-free model of 21^{st} July, showing (a) the curved fibril alignment around the activity complex and (b) a plot of the deduced field lines for $\gamma = 29°$.

$$B_x = \frac{1}{k^2}\left(-\alpha k_y \sin k_x x \sin k_y y - \beta k_x \cos k_x x \cos k_y y\right) e^{-\beta z}, \quad (4.2.14)$$

$$B_y = \frac{1}{k^2}\left(\beta k_y \sin k_x x \sin k_y y - \alpha k_x \cos k_x x \cos k_y y\right) e^{-\beta z}, \quad (4.2.15)$$

$$B_z = \sin k_x x \cos k_y y e^{-\beta z}. \quad (4.2.16)$$

Before the field lines are fitted to the observations of the 21^{st} July, a limitation in this type of modelling should be mentioned. Since currents are imposed on all field lines with a magnitude proportional to field strength, the field lines have a strange behaviour at large distances, where they become periodic and form closed magnetic cells. Thus the field cannot be extended into infinite space, where the energy content becomes infinite. The field must be confined by localised artificial boundaries such as planes in Cartesian geometry. This problem can, however, be overcome in principle by considering a nonlinear force-free field, reducing α with distance from the sheared region and so avoiding the field reversals. Here, however, the field lines are plotted in the range,

$$-\frac{\pi}{2} \leq x \leq \frac{\pi}{2}, -\frac{\pi}{2} \leq y \leq \frac{\pi}{2}. \quad (4.2.17)$$

Equation 4.2.16 gives two positive areas centred at x = $-\frac{3}{8}\pi$ and $\frac{\pi}{8}$ and two areas of negative flux centred at x = $-\frac{\pi}{8}$ and $\frac{3}{8}\pi$. Thus this simple choice of P gives four distinct flux areas each of equal strength and area. The value of α is now determined so that the field lines are topologically similar to the fibril pattern seen on the 21^{st} (Figure 4.5(a)). The value of α is obtained from the twist angle γ using Equation 4.2.12. The best fit to the fibrils was obtained for $\gamma = 29°$ or $\alpha = 3.6$ and β= 2.01 . The field lines are shown in Figure 4.5(b). The plus and minus signs denote the areas of positive and negative flux and the dashed line shows where B_z= 0 on the z = 0 plane. By comparing the two images, a good agreement could be obtained for the field lines emanating from the positive source at x = $-\frac{3}{8}\pi$. The field lines are plotted so that they closely follow the path of the fibrils and are only integrated as far as they can be followed on the Hα image. The field lines obtained for the rest of the area did not match the Hα structures so well, suggesting that α is not uniform over the whole activity complex.

The simple analytical model of four flux areas with the field components given by Equation 4.2.14- 4.2.16 was therefore able to reproduce the curved fibril alignment that was seen on the left of the Hα image. A more detailed numerical model of the activity complex on the 22^{nd} is constructed in the next section.

4.2.3 Numerical Model for the 22^{nd} July.

A numerical, constant-α, force-free model of the newly emerged activity complex will now be constructed. A contour plot of the magnetogram of M^{c}Math 16166 on the 22^{nd} is shown in Figure 4.6(a). Solid contours represent areas of positive flux and dashed contours negative flux. Only flux values that lie above 50 Gauss or below -50 Gauss are considered. The newly emerged activity complex is contained within an array of 151 $\times$ 81 pixels, where 1 pixel = $1''$ = 720 km. The four discrete flux patches are labelled 1 to 4 from left to right.

For the numerical modelling, the total flux in the box representing the activity complex must be balanced and the flux can only enter or leave the box through the bottom surface. Details of the numerical method used, can be found in the papers by Finn *et al.* (1994) and Longbottom *et al.* (1996) and in Appendix D. The total flux density and flux of each patch is calculated from the magnetogram and the results are shown in Table 4.1.

Patch	Total Flux Density (G)	Total Flux (Mx)	Model Flux Value F_i
1	251233	1.3×10^{21}	1.3×10^{21}
2	-172246	-8.93×10^{20}	-9×10^{20}
3	244133	1.265×10^{21}	1.3×10^{21}
4	-322402	-1.67×10^{21}	-1.7×10^{21}

Table 4.1 Measured flux values for M^{c}Math 16166.

In the area considered there is a very good flux balance for the flux above or below $\pm$ 50G. The slight imbalance of 3 $\times$ 10^{18} Mx could be accounted for by having long-range connections to other parts of the Sun, or due to unresolved magnetic features. Since there is such a good flux balance and the regions of flux emerged together, this suggests that the activity complex at its early stages of development is an isolated system. The fourth column shows the flux values in Maxwells that are used in the modelling to ensure total flux balance.

The field lines are plotted in a cube whose sides range over (-1:1, -1:1, -1:1). All lengths are scaled so that 0.01 units = $1''$ = 720 km. Each of the flux patches is represented in the model by a

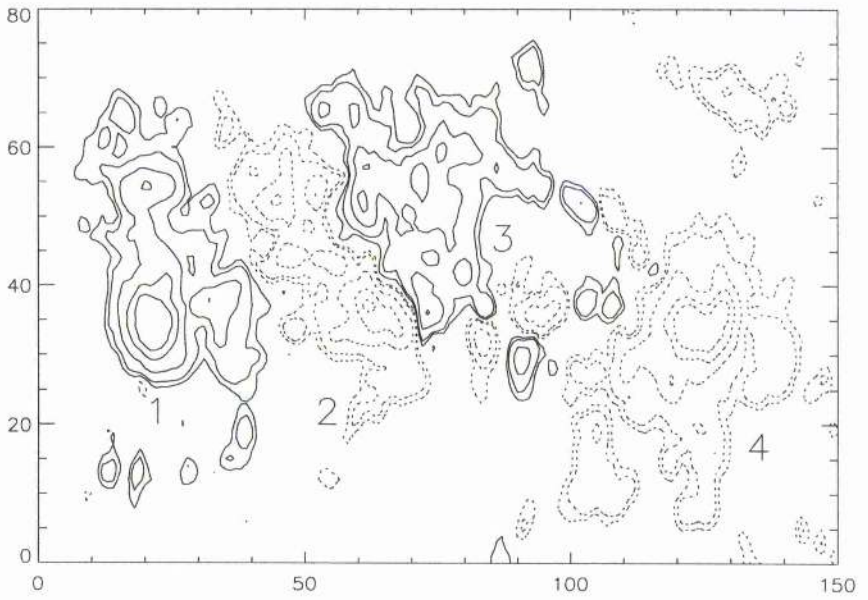

(a)

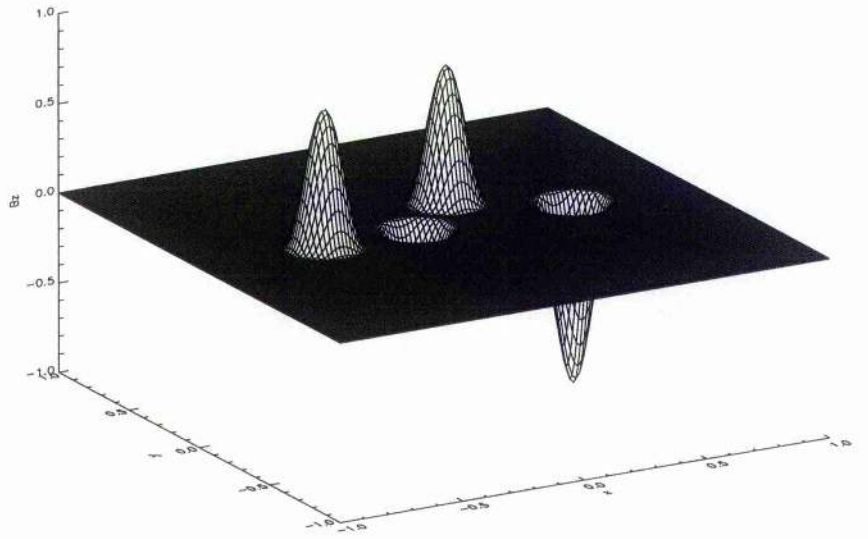

(b)

Figure 4.6: (a) Contour plot of M^{c}Math 16166 with contour levels of -800, -600, -300, -100, -50, 50, 100, 300, 600, 800 Gauss, respectively. (b) A surface plot of the vertical component of the magnetic field in the numerical model.

flux area whose vertical component at the photosphere (z= -1) plane is given by

$$B_z = \frac{B_o}{2}\left(1 + \cos\left(\frac{\pi r}{r_o}\right)\right), \quad 0 \leq r \leq r_0, \tag{4.2.18}$$

where r_o is the radius of the source which is centred at the point x_o,y_o and $\mathbf{r} = (x - x_o)\,\hat{\mathbf{x}} + (y - y_o)\,\hat{\mathbf{y}}$. All of the components are centred at the maximum/minimum flux value of the patch that they represent. The total flux emerging through a single discrete flux area is given by

$$Flux = \int_A \mathbf{B}.\mathbf{dA} = \frac{\pi}{2} B_o \left(1 - \frac{4}{\pi^2}\right) r_o^2, \tag{4.2.19}$$

where $\mathbf{dA} = r dr d\theta\,\hat{\mathbf{z}}$. The radius r_o of each area is set to be 0.15 units or 1.08×10^9cm. From Equation 4.2.19 the value of B_o in Gauss for each area can be obtained using the model flux values F_i in Table 4.1. In Table 4.2 the position (x_o,y_o) and the value of B_o for each of the sources is given.

Area	x_o	y_o	B_o G	Relative Value
1	-0.438	0.0	1193	0.7647
2	-0.125	0.0	-826	-0.5294
3	0.125	0.23	1193	0.7647
4	0.5	0.0	-1560	-1.0

Table 4.2: Position and strength of sources in model.

In Figure 4.6(b) a surface plot of the vertical component of the magnetic field at z= -1 is shown for 129 × 129 grid-points. For this number of grid-points the function can be seen to be well resolved.

The field lines inside the box are now plotted for the four flux areas given in Table 4.2 and are shown in Figure 4.7(b). The best comparison between the field lines and the fibrils seen in Hα (Figure 4.7(a)) was obtained for α=3. The values of α are scaled differently in the numerical and analytical models, so the two sets of values for the 21^{st} and 22^{nd} cannot be directly compared. However, in both cases a large value of α was required to give the best fit to the observations.

On the left-hand side the field lines bend round from the positive region to the negative region in a north-south direction and give a very good comparison with the Hα fibrils. From this topological agreement it can be seen that the C-shaped arc of fibrils observed on the 22^{nd} is aligned with

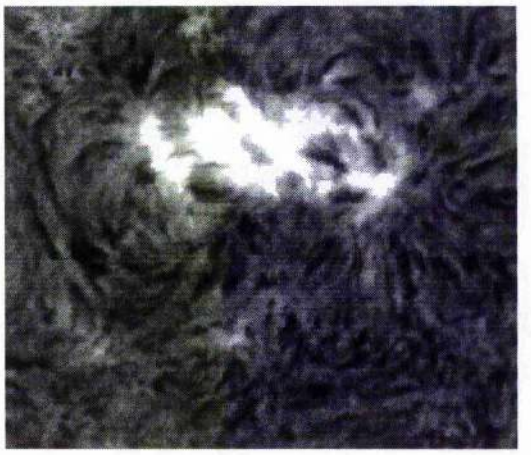

(a)

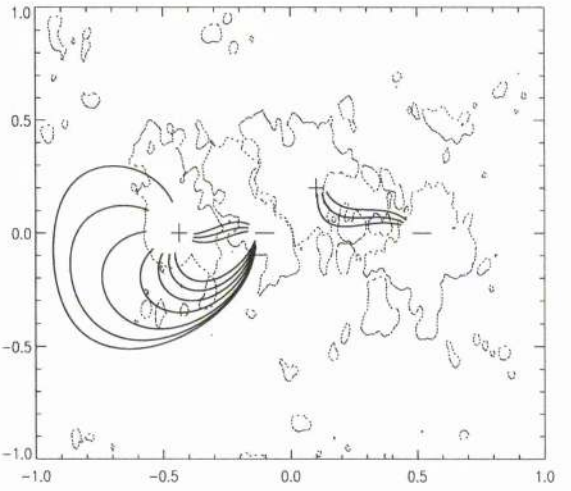

(b)

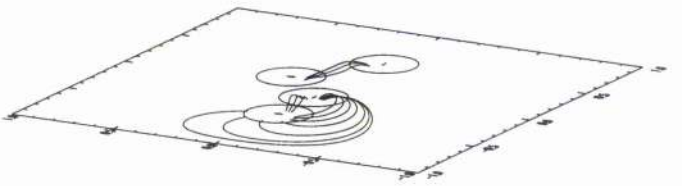

(c)

Figure 4.7: (a) The alignment of fibrils in Hα for the 22^{nd}. (b) The deduced field lines from the numerical model placed on a contour of the magnetogram. (c) The same set of field lines from an oblique view.

the extended non-potential magnetic field of the emerging activity complex. These fibrils outline the filament channel and the model shows that the formation of the filament channel is due to the magnetic field of the newly emerged activity complex. The channel is of sinistral type, since when viewed from the positive polarity side the magnetic field points to the left. The formation of the sinistral channel is due to currents that are parallel to the field (α +ve). If α had been negative (currents antiparallel to the field) the field lines would have closed south-north instead of north-south and a dextral channel would have been produced. Thus the formation of the sinistral channel (in the southern hemisphere) is due to the type of currents that are built up in the convection zone before the flux emerged through the photosphere.

Also in Figure 4.7(b) two sets of field lines that correspond to the arch-filament systems are drawn. The first set of field lines, between sources 1 and 2, show that there is transverse structure across the polarity inversion line (P.I.L.) between the two areas and no horizontal fields along the P.I.L. This transverse structure still exists four days later and is one of the reasons why a filament does not form at the P.I.L. between the two patches when flux converges between them (Gaizauskas *et al.* (1996)). The set of field lines on the right-hand side between sources 3 and 4 shows the arch-filament system that connects between the two leading sunspots. Figure 4.7(c) shows an oblique view of the field lines. The circles outline the areas of emerging or submerging flux. The maximum height of the field lines is 8,000 km so they all lie in the lower corona, just below the projected height of the filament (10,000 km). From this it can be seen that the field lines that give the best fit to the Hα image are low-lying and very flat structures. Since they are flat, mass can lie along their entire length and therefore they appear as dark strands in Hα. The plot shows that, as early as the 22^{nd}, there is a dominant horizontal component down the filament channel at the level of the lower corona. In Hα this horizontal component is seen to develop over a period of three hours and the modelling shows that it is due to the non-potential nature of the newly emerged activity complex. The Hα images of the 23^{rd} and 24^{th} (Figures 4.1, 4.2) show that the filament channel is maintained throughout the next few days as the activity complex develops.

4.3 Potential Model for the 25^{th} July.

A potential model of the filament channel magnetic field is now constructed for the 25^{th} July, in the same manner as in Chapter 3, Section 3.3. The field in the channel is given by a series of poles representing the regions of positive and negative flux at the photosphere. Potential modelling is carried out for this day since the emerged activity complex has dispersed and is now slowly evolving. For the 25^{th} July there is a magnetogram and an Hα image, so the calculated field can be compared with the image and position of the filament.

Figure 4.8(a) shows a contour plot of the magnetogram containing the newly emerged activity complex M^{c}Math 16166 and the region of plage M^{c}Math 16159 where 1 pixel = $1''$ = 720 km. The solid curves represent the patches of positive flux while the dashed curves show the negative flux. To define the perimeters of the flux patches a boundary flux value ϕ_b must be chosen. The best boundary flux values were found to be the $\pm$ 50 G contours for the positive and negative areas. When the 100 G contours were plotted the inner parts of the flux patches were fragmented, so this value is too high. Thus from now on only flux values above 50 G or below -50 G will be considered (Schrijver 1987). Also in Figure 4.8(a) a contour plot of the filament is placed on the magnetogram. The contour does not show the entire length of the filament but shows its location with respect to the flux areas. By considering this image and overlaying the magnetograms and Hα images, the origin of the filament's field can be seen to be the positive patch labelled 1 which connects to the negative plage region 2.

To model the flux distribution in the channel each of the flux patches on the contour plot are split up into smaller areas. The cuts in the patches are made across the lowest contours wherever possible ($\pm$ 50, $\pm$ 100 G). Each of these areas will now be represented by a source (positive) or sink (negative) whose field in Cartesian coordinates (x,y,z) is given by Equation 3.3.1. For the 25^{th} the magnetogram is modelled by a series of 19 sources and 27 sinks. In previous work such as Démoulin *et al.* (1992), (1993), it has been shown that the topology of an active region can be described by such magnetic sources and the more sources used the better the fit to the magnetogram.

To obtain the total flux (f_i) of each of the sources the total flux density (Φ_i) in Gauss must first be obtained for each of the areas from the magnetogram. This is done by summing over the

individual contributions of the $1''$ elements that lie within each area. To obtain the total flux for each pole in Maxwells (Mx = G cm^2) the total flux density is multiplied by the area of one pixel (cm^2),

$$f_i = \Phi_i \times (5.184 \times 10^{15} cm^2). \tag{4.3.1}$$

Each of the sources/sinks is now placed on the photospheric plane (z=0) at the maximum or minimum value of the area that they represent. The flux values and the position of each of the poles can be seen in Appendix E. In the region being modelled there is a flux imbalance of 1.74×10^{21} Mx towards the negative flux. To balance this, a system of positive sources is placed at large distances outside the field of view and spaced at equal angles. All of the lengths are scaled such that 1 unit = $1''$ = 720 km.

The field lines are now plotted at various heights (h = 0, 5, 14, 20, 30 units) for the sources seen on the magnetogram. At all of these heights it was found that the poles representing the areas of flux 1 and 2 (Figure 4.8(a)) did not connect. All of the field lines connected across the channel from the edge of the trailing positive flux to the remnant negative region. No field lines connected down the channel along the path of the filament, evidently because there is a component of field that the model is not taking into consideration. The magnetogram only gives the vertical component of field emerging through the surface and therefore may not give us all the field components in the channel. To improve the model a background field is added down the channel. This background field is added as a uniform field and may represent for example the field due to the axial dipole field of the Sun. Typical strengths of this field would be a few Gauss (Wang *et al.* (1991)).

In order to determine the exact strength of the uniform field, the field lines are plotted on top of the Hα image. The strength is then changed until the best fit obtained. The field lines give the best fit to the path of the filament when a uniform field of B_{ox} = 21 G and B_{oy} = -11.5G is added ($\mid B \mid$ = 24 G). A large uniform field is required since the connectivity has to be changed from across the channel to along the channel. In Figure 4.8(b) the field lines can be seen plotted on top of the magnetogram.

It can be seen that the field lines give a good fit to the observed path of the filament. The field lines are plotted at a height of 10,000 km and their width is 6000 km. Since a very strong uniform

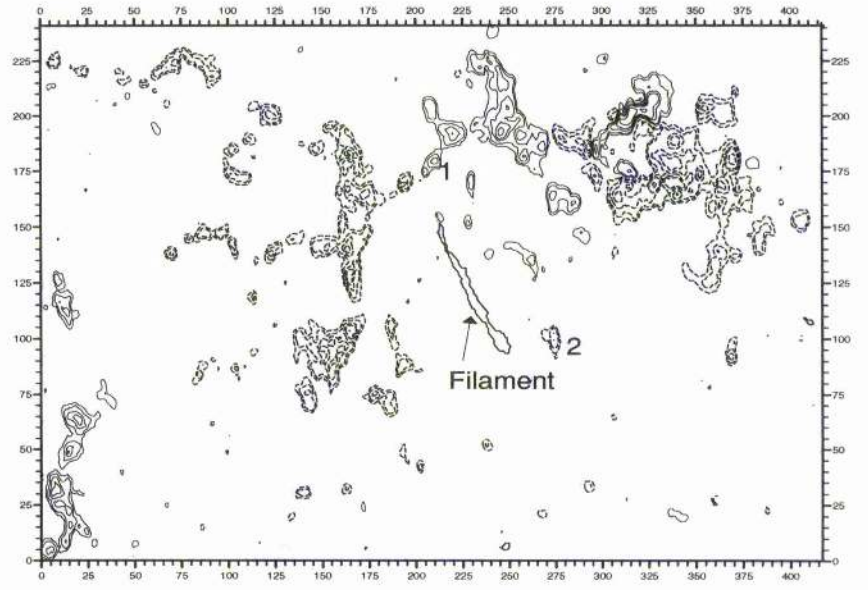

(a)

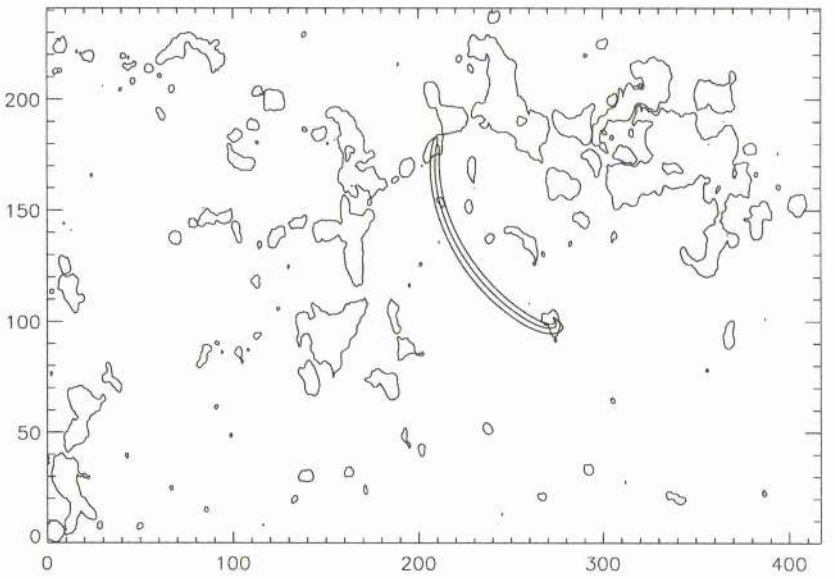

(b)

Figure 4.8: (a) Contour plot of the magnetic field in the filament channel for 25^{th} July 1979. Solid contours represent positive flux and dashed contours negative flux. On top of the plot an outline of the filament is placed showing its location. The contour levels are -500, -300, -200, -100, 50, 50, 100, 200, 300, 500 respectively. (b) The field lines obtained from the potential model superimposed on the magnetogram and viewed from the top.

field has to be applied down the channel, only field lines locally in the region of the filament agree with the Hα image. No field lines at any other part of the image agree with the Hα structures when the uniform field is added. This shows that a very strong localised horizontal component of field is required to give the correct connectivity of the filament. Thus the filament cannot be represented adequately by a potential field and a force-free field will be required to describe its global structure. The result here is also consistent with that obtained in Chapter 2, Section 2.2 for the strength of a uniform field required around active region belts of the Sun. It therefore shows that the potential model fails at active-region latitudes.

4.4 Force-free Model for the 25^{th} July.

A linear force-free model of the entire filament channel will now be constructed for the 25^{th} July. The aim is to find whether or not the global field of the filament channel can be represented by a force-free field. The connectivity of the field down the channel and the dominant horizontal component of field will be shown to be due to the force-free nature of the channels field. Again, in order to construct a simple force-free model the channel must be in total flux balance. In Figure 4.10(a) a contour plot of the positive and negative patches is shown. The patches that are labelled are the main ones that will be considered. From the magnetogram four positive patches will be considered (labelled 1-4) and five negative patches (labelled 5-9). With these flux patches there is a large imbalance towards the negative flux in the channel. This imbalance is due to the old remnant region of plage M^{c}Math 16159. In Table 4.3 the total positive and negative flux in the field of view is calculated for flux values that lie above 50 G and below -50 G.

Positive Flux	Negative Flux	Imbalance
Mx	Mx	Mx
2.32×10^{21}	-3.67×10^{21}	-1.35×10^{21}

Table 4.3: Total flux values in channel for 25^{th} July.

The imbalance is large and a region of positive flux must be found to balance it. In Figure 4.9 a synoptic chart of the appropriate carrington rotation that covers the filament channel and filament formation can be seen. The regions M^{c}Math 16166, 16159 lie in the centre of the image. Below

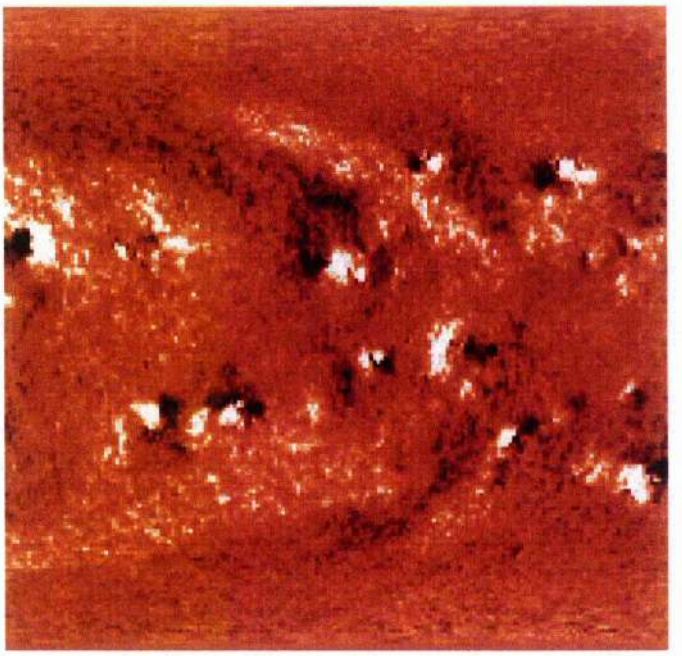

Figure 4.9: Kitt Peak synoptic chart m1684f showing filament channel and region of diffuse flux lying south of it.

them lies an extended region of positive flux which is weak and diffuse. The extended region of positive flux balances the excess negative flux in M^{c}Math 16159. To represent this region a source of the correct size required to balance the channel will be placed south-east of the main flux concentrations and out of the field of view of the magnetogram (called region 10). This source will not represent the correct distribution of flux but will give the correct direction of connectivity. Since the source is placed far from the centre of the channel it should not effect the local structure of the field in the centre of the channel. Each of the flux patches is now represented by either a circular or elongated area of flux.

For the circular areas of flux the vertical component of field (B_z) at z=-1 is given by Equation 4.2.18 and the total flux through the area is given by Equation 4.2.19 as before. For the elongated areas of flux the vertical component of field is given as follows, where the coordinates (x_o,y_o) and (x_1,y_1) describe the opposite ends of the main body of the region :

$$B_z = \frac{B_o}{2}\left(1 + \cos\left(\frac{\pi x}{r_o}\right)\right), \quad y_o \leq y \leq y_1, \quad 0 \leq x \leq r_o, \tag{4.4.1}$$

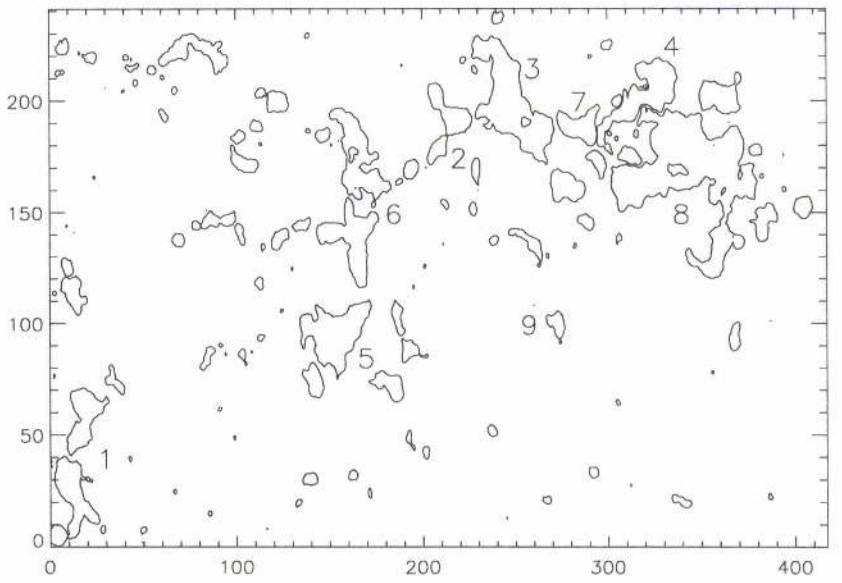

(a)

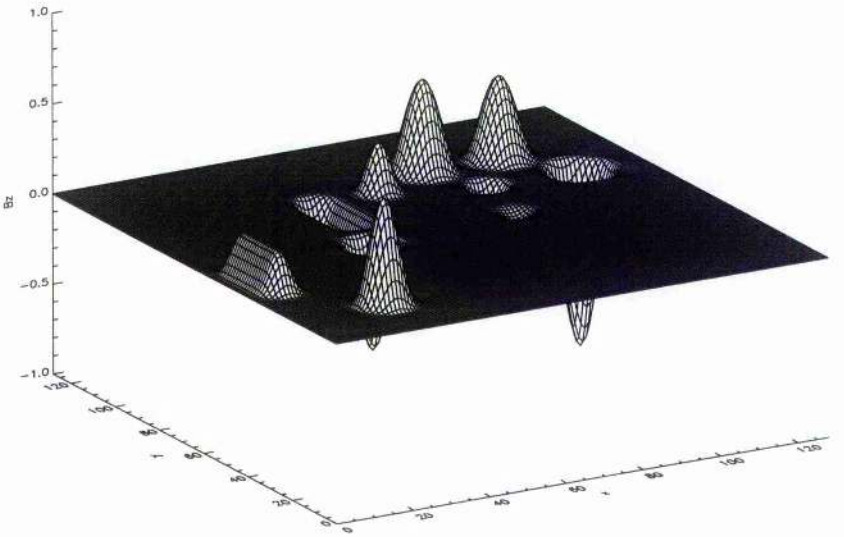

(b)

Figure 4.10: (a) Contour plot of magnetogram showing labelling of the patches of flux in the numerical model for the 25^{th} (contour levels -50,50 G). (b) A surface plot of the vertical component of magnetic field in the numerical model of the filament channel for the 25^{th}.

$$B_z = \frac{B_o}{2}\left(1+\cos\left(\frac{\pi r}{r_o}\right)\right), \quad y \le y_o, y \ge y_1, \quad 0 \le r \le r_o,$$

where

$$\mathbf{r} = (x-x_o)\hat{\mathbf{x}} + (y-y_o)\hat{\mathbf{y}}, \quad y \le y_o \tag{4.4.2}$$
$$\mathbf{r} = (x-x_1)\hat{\mathbf{x}} + (y-y_1)\hat{\mathbf{y}}, \quad y \ge y_1.$$

The total flux emerging through the area is

$$Flux = \int_A \mathbf{B}.\mathbf{dA} = B_o\left[\frac{\pi}{2}\left(1-\frac{4}{\pi^2}\right)r_o^2 + Lr_o\right], \tag{4.4.3}$$

where $L = y_1 - y_0$ is the length of the main body of the elongated area.

The sources are now scaled so that the dimensions of the box fit the magnetogram. In the box 0.01 units = 15000 km = $2''$. The resolution is now half of that used when the activity complex was modelled in Section 4.2.3 since a much larger area of the Sun is being considered. In Table 4.4 the total flux, centre and radius of each area is given. The value of B_o for each area can be determined from equations 4.2.19 and 4.4.3 for the circular and elongated areas.

Source	Flux (Mx)	x_o,y_o	r_o	B_o
1	6.5× 10^{20}	-0.875,-0.375	0.0956	0.233
		-0.875,-0.125		
2	2.2× 10^{20}	0.0,0.4375	0.0956	0.292
3	9× 10^{20}	0.25,0.5625	0.143	0.528
4	8× 10^{20}	0.5625,0.5625	0.143	0.472
5	-7.2× 10^{20}	-0.3125,-0.0625	0.12	-0.61
6	-6.5× 10^{20}	-0.25,0.1875	0.0956	-0.233
		-0.25, 0.4375		
7	-1.8× 10^{20}	0.375,0.3125	0.0956	-0.237
8	-1.7× 10^{21}	0.75,0.3125	0.143	-1.0
9	-4× 10^{19}	0.3125,0.0	0.0956	0.055
10	7.2× 10^{20}	-0.625,0.6875	0.12	0.61

Table 4.4: Position and strength of sources for 25^{th} July in force-free model.

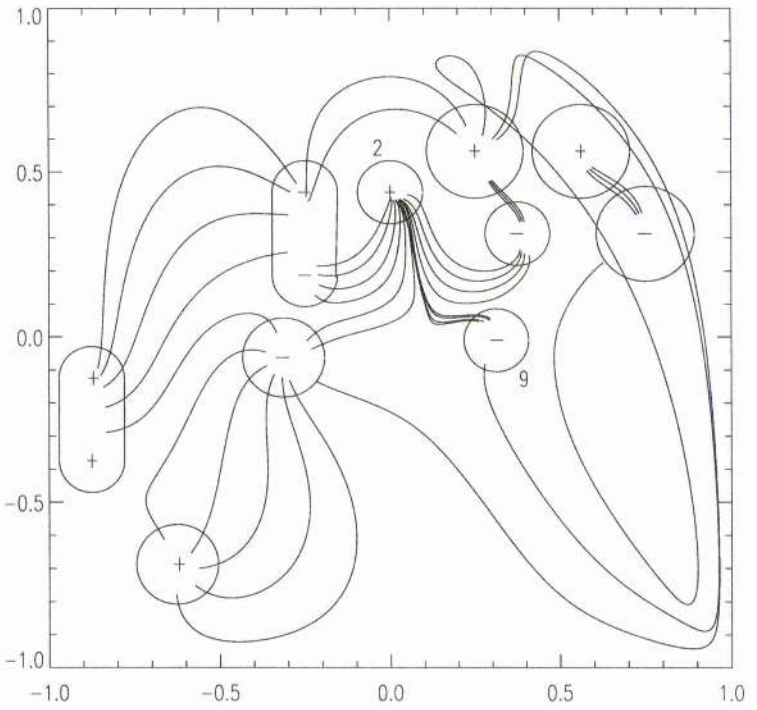

(a)

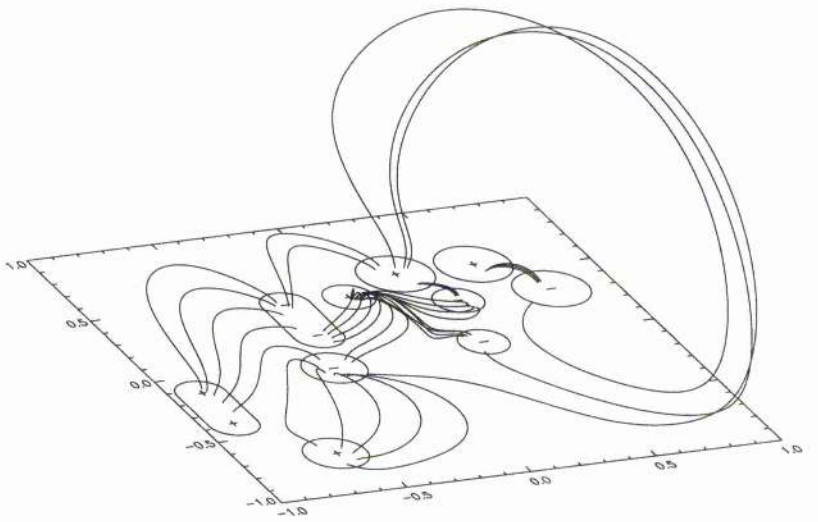

(b)

Figure 4.11: (a) Field lines in the channel for α= 2.3 showing the connectivity of the field lines in the region of the filament. (b) Same set of field line but shown from an oblique angle.

In Figure 4.10(b) a surface plot of the vertical component of the magnetic field can be seen at the photospheric (z=-1) plane. Again for 129 $\times$ 129 grid points the function is well resolved as before. The field lines in the channel are computed for various values of alpha and it is found that the best representation of the filament in the channel is for alpha = 2.3. In Figure 4.11(a) the field lines that connect between areas 2 and 9 and give the best representation of the path of the filament are shown. They form a very thin linear structure that runs down the channel parallel to the P.I.L. and near their end there is a steep bend to the right when they enter the small region of negative plage. Also, on both sides of the flux connecting areas 2 and 9, some field lines are plotted showing the global topology of the channel. The same field lines are then shown from an oblique angle in Figure 4.11(b). Thus the modelling shows that the magnetic structure of the filament channel and the global field of the filament can be well described by a force-free field. The best representation of the filament in the channel is a highly sheared force-free field in agreement with Schmieder *et al.* (1996). Also in Figure 4.11(a) two sets of field lines that correspond to the arch-filament systems are drawn. Again between regions 3 and 7 there are transverse fields across the P.I.L. between the two regions and no horizontal fields along the P.I.L. The transverse fields are still maintained on the 25^{th}, which is why no filament forms at the location P2 even though there is convergence of flux there (Gaizauskas 1997).

The separatrix surface that encloses the flux connecting regions 2 and 9 is shown in Figure 4.12. All of the field lines that represent the path of the filament lie within this surface. In Figure 4.12(a) the surface is viewed from above. The dashed lines represent the separatrix lines that divide up regions of connectivity in the z=-1 plane. A neutral point is located at $x = 0.12, y = 0.02$ and is shown by the star. The neutral point is at the intersection of four of the separatrices. The other separatrix to the north of the neutral point shows the outer (northern) boundary of the field lines that connect between regions 2 and 9. The field lines map from a small area on region 2 to a much larger area of weaker field on region 9, shown as the enclosed ovals on both regions.

In Figure 4.12(b) the separatrix surface is shown from an oblique angle and viewed from the North. From this angle it can be seen that the flux forms a thin vertical sheet structure that extends down the channel. Near source 2 the sheet is inclined at an angle to the vertical and becomes more vertical as it reaches further down the channel, before fattening out near the neutral point, where the magnetic field is very weak. Since the angle of inclination of the sheet changes as we

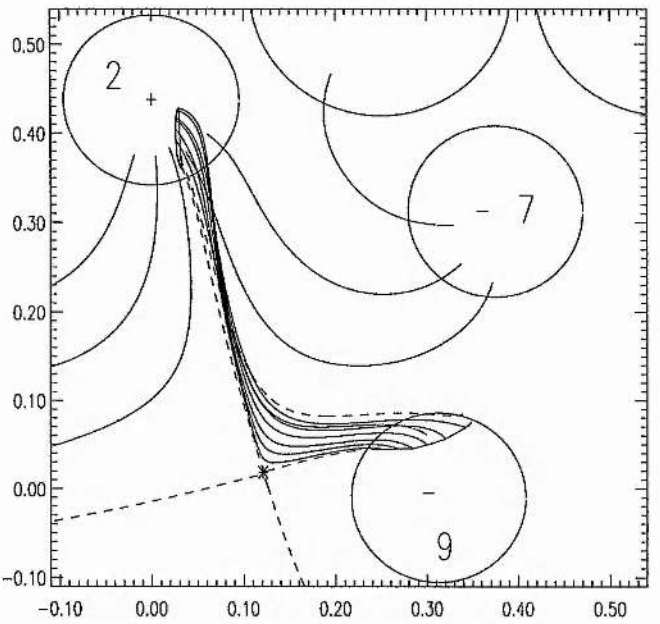

(a)

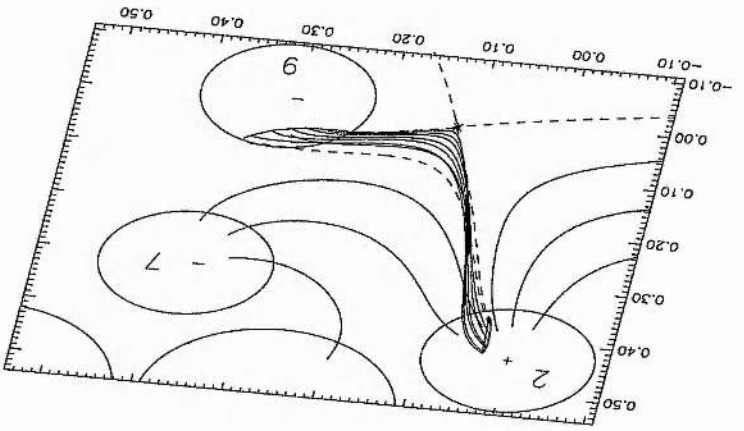

(b)

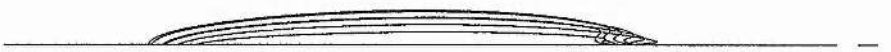

(c)

Figure 4.12: Separatrix structure for flux connecting between regions 2 and 9 view from (a) above, (b) an oblique angle, showing the thin vertical sheet structure and (c) the side showing long, low-lying field lines.

go down the channel this gives the appearance of twist of the field lines. However, this is largely a projection effect and when viewed from the side in Figure 4.12(c) it can be seen that there is very little twist in the structure. The two areas of flux are connected over a small width but over a wide range of heights from the photospheric plane to a height of 22,000 km. The flux that connects between the two regions forms a thin vertical sheet structure that resembles well the topology of a filament. The maximum height of the field lines is slightly above the projected height of the filament (10 ~15,000 km) but the effect of gravity would lower them still further. The field lines that connect between the two regions are on average 90,000 km long, and are five times longer than they are high so they are very flat, low-lying structures.

It will now be shown that M^{c}Math 16159 is a necessary boundary on the east side of the channel for the global magnetic topology to represent the connectivity of the filament. This will indicate the effect of this region on the evolving global structure of the channel. To construct the model only the newly emerged activity complex and the small plage region where the filament ends are included. Sources 1,5,6,10 are removed, and the field lines are plotted for various values of alpha. It was found that for no values of alpha (positive or negative) could a good representation of the path of the filament be found. Typical results for the channel are shown for $\alpha = 1.0$ and 2.3.

In Figure 4.13(a) the field lines are plotted in the channel for $\alpha = 1.0$. Only field lines emerging from the south of area 2 are plotted. The field lines here are shown at a height of 12,000km. Some flux does connect between areas 2 and 9; however, the field lines are not at the location of the filament and they are highly curved structures. The field lines near the location of the filament connect between regions 2 and 8 but again are strongly curved. The filament itself is a long straight structure and it can be seen that none of the field lines here gives a good representation of its magnetic topology. The field lines seen here are very similar to the fibril structures that are seen from the 21^{st} to the 24^{th} before the two regions interact and the filament forms.

The value of alpha was then changed to 2.3, the value that gives the best representation of the global topology of the filament in the channel before. Again field lines at a height of 12,000 km are shown in Figure 4.13(b). For this value of alpha no field lines connect between areas 2 and 9 along the path of the filament . The field lines have a geometry that represents the type of fibril structure that was seen on the earlier days of formation. These plots show that the filament could not have formed in the channel with its same global topology if M^{c}Math 16159 had not formed

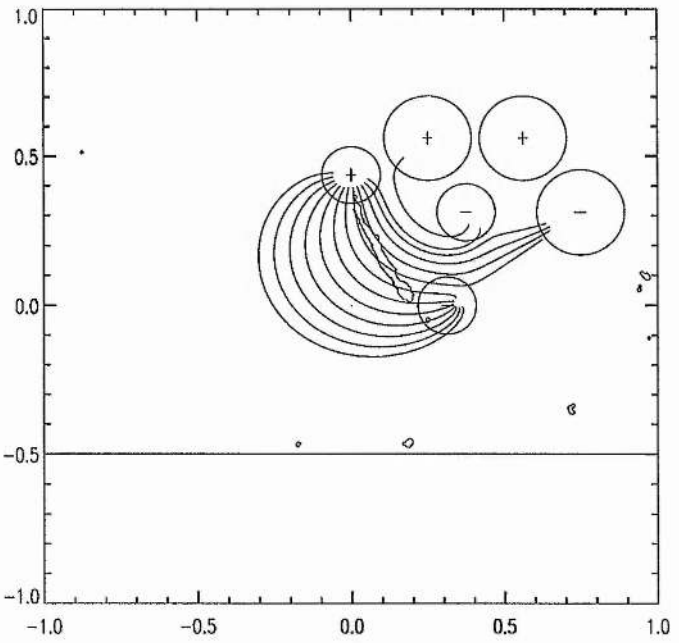

(a)

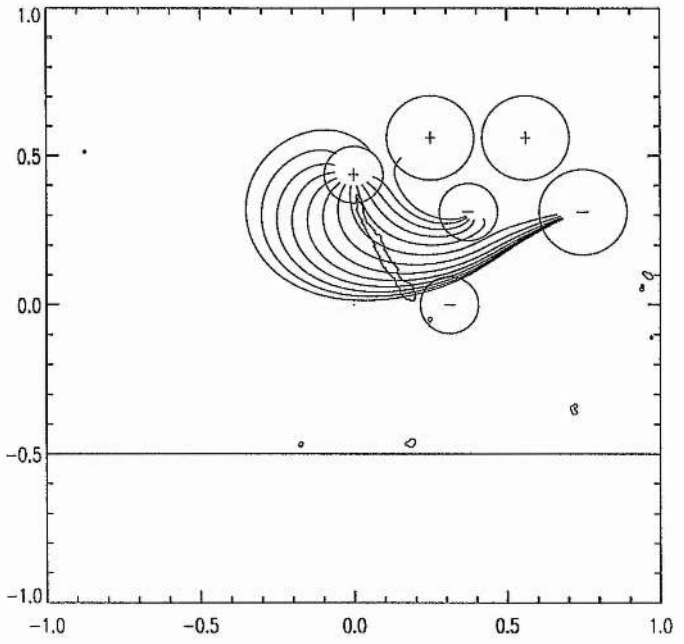

(b)

Figure 4.13: Field lines for the 25^{th} July when M^{c}Math 16159 is excluded from the modelling. This gives very curved structures that do not represent the path of the filament for (a) α=1.0 and (b) α=2.3.

a boundary on the east side of the channel. The interaction of the two regions is what generates long straight field lines that connect down the channel, with some of these field lines lying along the path of the filament. This shows that on the 25^{th} the global topology of the channel cannot be described without including M^{c}Math 16159 in the modelling.

These results indicate the role of M^{c}Math 16159 on the evolving magnetic topology of the filament channel and filament formation. On the early days of formation the fibril alignment and formation of the channel can be attributed to the emergence of the activity complex M^{c}Math 16166. This region then evolves and spreads out over the next few days with continued circular fibril alignment. Near the time the filament forms, the two regions interact with each other. This interaction generates long, straight field lines that connect down the channel in comparison to the curved field lines that existed around the activity complex on earlier days. These long straight field lines give a good representation of the global magnetic topology of the filament. Thus the role of 16159 is to allow a thin vertical sheet of flux to connect down the channel representing the path of the filament. This shows that M^{c}Math 16159 plays an important role in the evolving global magnetic topology of the channel on the latter days of formation.

4.5 Origin of Filament Mass

The main features of the magnetic topology and the role played by each patch of magnetic flux in the channel has been described. One question that still has to be answered is "Where does the filament mass come from and why is it located in the thin structure of the filament ?". From Figure 4.12 (c) it can be seen that the field lines that represent the filament are very flat, low-lying structures. This is a type of topology that may be suitable for the support of mass. Since they are flat the extra inclusion of mass may make them dip down and help further the accumulation of mass. The angle that the field lines make to the horizontal is now calculated at a height of 12,000 km to see if the field lines that represent the filament are the flattest in the channel. In Figure 4.14 the regions where the field lines are inclined less than 5 degrees to the horizontal are shown. The area where the field lines are their flattest runs across the channel and not down the channel. From this it can be seen that the field lines that represent the filament are no flatter than many of the surrounding ones. This implies that the presence of flat or dipped field lines is a necessary but not

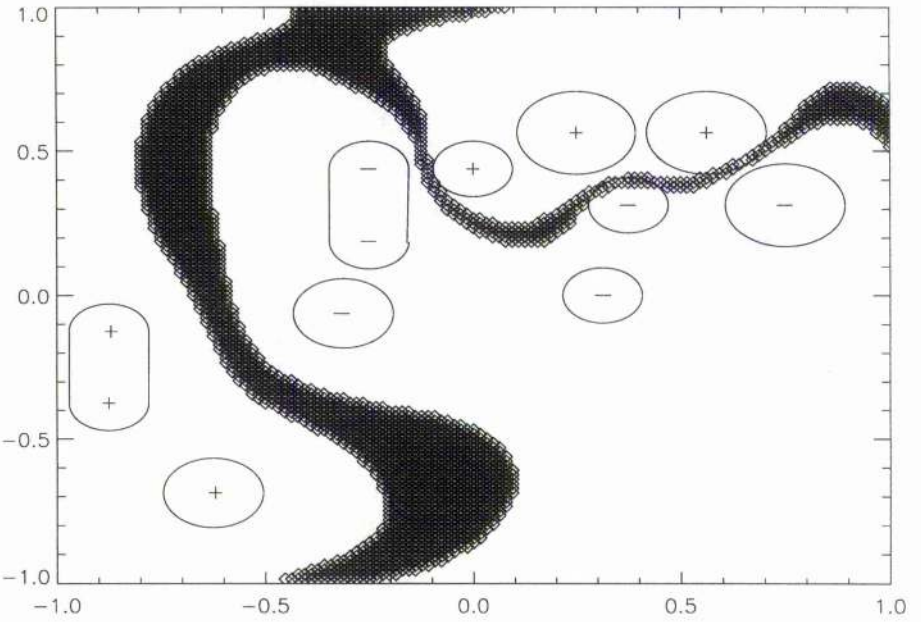

Figure 4.14: The locations (shaded) in the channel where the field lines make an angle of less than 5 degrees to the horizontal at a height of 12,000 km.

sufficient condition for the formation of a filament. To explain why the mass accumulates in the filament other mechanisms such as thermal instability, injection processes or the convergence of flux at the polarity inversion line below the filament have to be considered. A review of thermal instabilities and injection processes can be found in Priest 1989, chapter 5 and references therein. On the other hand the convergence of flux below the filament may lead to the constant supply of mass by a pick-up process (S. Martin, private communication, Priest *et al.* (1996)). It would be invaluable to investigate the role of each of these mechanisms in the formation of the filament with SoHO (CDS,SUMER,MDI) observations.

4.6 Conclusion

In this chapter both force-free and potential models of a filament channel and filament formation have been constructed. The modelling shows that, during the early stages of development, the C-shaped fibril alignment is consistent with that of a force-free field. To start with, a simple

analytical model was constructed for the 21^{st} July. The deduced field lines gave a good agreement with the observed fibril structure. A numerical model of the 22^{nd} was then constructed from the magnetogram of that day. By using the observed flux values a very good representation of the fibrils in the channel was obtained. The field lines that give the best fit are very low-lying and have a dominant horizontal component. The force-free modelling shows that the horizontal component seen from the pattern of fibrils can be attributed to the extended non-potential field of the newly emerging activity complex. This suggests that the formation of the filament channel may be due to the emerging activity complex. It is also consistent with the fact that the fibril alignment in Hα improves when fresh magnetic flux is injected into the complex.

For the 25^{th}, when the filament had formed, a potential model fails to give the correct connectivity for the filament in the filament channel. To obtain the correct connectivity a strong uniform field has to be added down the channel. With this field added, agreement with the Hα image only occurs in the immediate location of the filament. Thus a localised strong horizontal field has to be added to obtain the correct connections. This suggests that the field of the filament is not potential and to describe the global structure at least a force-free field is required. A force-free model was then found to give a good representation of the filament in the filament channel, with the filament best described by a highly sheared force-free field. The field lines that give the best fit form a thin vertical sheet of flat low-lying flux that connects down the channel and is bounded from the remnant region and most of the new flux by separatrix surfaces. The role of each region was then investigated and it was found that on later days only when M^{c}Math 16159 creates a boundary on one side of the channel can its global topology be well represented. M^{c}Math 16159 has an important effect on the magnetic topology on later days. It was then shown that the flatness of a field line is not a sufficient condition for filament formation and so additional mechanisms need to be considered, such as for instance convergence and cancellation of flux.

This modelling has highlighted some of the main features of both filament channel and filament formation. To describe the process in more detail high-resolution images taken at different levels in the atmosphere with good time resolution are required along with high-resolution vector magnetograms, which are not available for the channel considered in this chapter. The formation of the filament seems to be directly linked to the formation and development of the filament channel and future observations and theories should address both of them together.

Chapter 5

Role of Helicity in the Formation of Intermediate Filaments.

In the last few years new observations have shown that solar filaments and filament channels have a surprising hemispheric pattern (Section 1.3.1). To explain this pattern, a new theory for filament channel and filament formation is put forward. It describes the formation in terms of the emergence of a sheared activity complex. The complex then interacts with remnant flux and, after convergence and flux cancellation, the filament forms in the channel. A key feature in the model is the net helicity of the complex. With the correct sign a filament channel can form; with the opposite sign no filament channel forms after convergence. It is then shown that the hemispheric pattern of helicity in emerging flux regions gives a hemispheric pattern for filaments. A comparison between this theory and previous ones is given.

5.1 Introduction.

Filaments are one of the most interesting but mysterious of all solar phenomena. Martin, Bilimoria and Tracadas (1995) have shown that these objects and their birth grounds (filament channels) have a surprising hemispheric pattern. In the northern hemisphere most quiescent filaments are dextral, and in the southern hemisphere most are sinistral. No pattern was found for low-latitude active-region filaments (Section 1.3.1). Such a pattern for quiescent filaments shows that there is an organisational principle of some kind behind the global nature of filaments and this needs to be identified. The idea of a global organisational principle was reinforced by observations of X-Ray arcades seen above filaments by Martin and M^{c}Allister (1995). They found that stationary arcades above dextral filaments are always left-bearing, while those above sinistral filaments are always right-bearing (as seen from above). The arcade orientation and filament channel orientation have a one-to-one correspondence (Section 1.3.2). All post-eruption arcades that reform at successive heights above dextral filaments do so with a counter-clockwise rotation with height and above sinistral filaments with a clockwise rotation with height. A full description of these hemispheric patterns and others can be found in Zirker *et al.* (1997).

In response to these observations new theories of filament formation have been put forward by Rust and Kumar (1995), Priest, Van Ballegooijen and Mackay (1996) and Zirker *et al.* (1997). Each of these authors recognised that surface differential rotation would give the wrong axial component in each hemisphere and so put forward a different scenario for the origin of the hemispheric pattern. Priest *et al.* (1996) explain it by the combined effects of differential rotation acting on sub-photospheric flux, its subsequent emergence by magnetic buoyancy and then the rearrangement of the emerged elements by magnetic reconnection to give the correct axial component. On the other hand Rust and Kumar (1995) considered the filament as a twisted (helical) flux rope. This helical flux rope is organised by sub-photospheric differential rotation to give the correct axial component and then emerges into the solar atmosphere as a twisted magnetic field. The filament mass then rests in the bottom of the helix in static support. More recently, however, Zirker *et al.* (1997) explain the hemispheric pattern by surface flows acting on surface fields with magnetic reconnections to give the correct axial component. This process is considered for a mid or high-latitude bipolar magnetic region that has been acted on by differential rotation and meridional flows. The

latter authors prefered not to ascribe the patterns to unobservable subsurface flows which could not be tested. All of the authors above give convincing theoretical and observational arguments to support their models. The readers are left to consider the validity of the respective arguments for themselves.

An alternative explanation to these, which does use surface differential rotation along with reconnections and flux cancellation, has been put forward by Kuperus (1996). However to obtain the correct axial component in each hemisphere, reconnections and cancellations of flux must occur after a specific amount of differential rotation. Too much differential rotation and the wrong axial component is produced. It therefore seems unlikely that this method is robust enough to produce such a dominant hemispheric pattern.

Although there are many theories for the formation of filaments, very few examples of formation have ever been observed. One such example was seen by Gaizauskas *et al.* (1997) and then modelled by Mackay *et al.* (1997) (see Chapter 4). The observations and models showed the development of the filament channel with the emergence of an activity complex and then the formation of a filament in the channel. An important feature in creating the channel with the correct chirality was the net helicity of the complex. In this chapter we will consider how the net helicity (positive or negative) of activity complexes is related to the formation and hemispheric patterns of filaments. This is a feature which none of the above authors have included in their models. To begin with, in this chapter the process of filament channel and filament formation deduced from Chapter 4 will be described and the role of helicity in the formation discussed. Next the hemispheric pattern deduced from the models is described and finally a comparison between the model described here and that of Priest *et al.* (1996) and Rust and Kumar (1995) is given. The model is not compared with the formation process of Zirker *et al.* (1997) since their model deals with formation in an old developed magnetic region, rather than around a newly emerged region as considered here.

5.2 Process of the Formation of Filament Channels and Filaments.

On the Sun there are many different classes of filament. Each of these classes form at different locations and have different scaling properties. The process outlined below describes the formation

of an "intermediate" or "boundary" filament. It is a filament that forms between single bipolar regions of flux or activity complexes and unipolar background fields. In general they circle the periphery of the main flux concentrations but have one end rooted in one of the flux polarities. In a survey carried out by Tang (1987) it was found that the majority of filaments (63 %) form above polarity inversion lines between adjacent regions of flux rather than above polarity inversion lines contained in a single bipole. The formation process is deduced by considering the observations of Gaizauskas *et al.* (1997) and the modelling of Chapter 4 which described the magnetic field of the observed structures by force-free fields. In terms of the hemispheric pattern of Martin, Bilimoria and Tracadas (1995), the intermediate (boundary) filaments have been included with quiescent filaments but so far no individual study has been undertaken solely for them.

To begin with, the emergence of a new region of flux is required in the form of an activity complex (or a bipolar region). In a recent survey of 152 active regions by Gaizauskas and Zwaan (1997) it was found that the majority of low-latitude filaments form either inside or around *activity complexes* rather than inside *single bipolar regions*. The activity complex will therefore be considered from now on, although the details of the model are the same for both types of region. The complex must emerge close enough to a remnant region so that the two can interact. Not only convergence but also cancellation of flux has to take place so the neighbouring magnetic polarities of the new region and remnant region must have the opposite sign. The activity complex must therefore emerge on one side, either east or west of the remnant region (see Figure 5.1(a), where a complex emerges on the west side in southern hemisphere). The remnant region will have previously been acted on by differential rotation, meridional flows and supergranular diffusion and therefore will be more elongated and extend to higher latitudes than the activity complex. The effect of the remnant region on the field of the complex is small at the initial stages of development (i.e both regions are independent from each other). This is supported by the observations of Gaizauskas *et al.* (1983), who found that most emerging activity complexes are in good flux balance. The flux of the activity complex must also be in a sheared state. This gives a dominant direction and horizontal field component at the level of the chromosphere and lower corona between the two regions and therefore helps the formation of a filament channel. It is the sheared nature of the field that gives the sinistral/dextral nature of the channel (see Figure 5.1(b), where the force-free alpha is positive and gives rise to a sinistral channel).

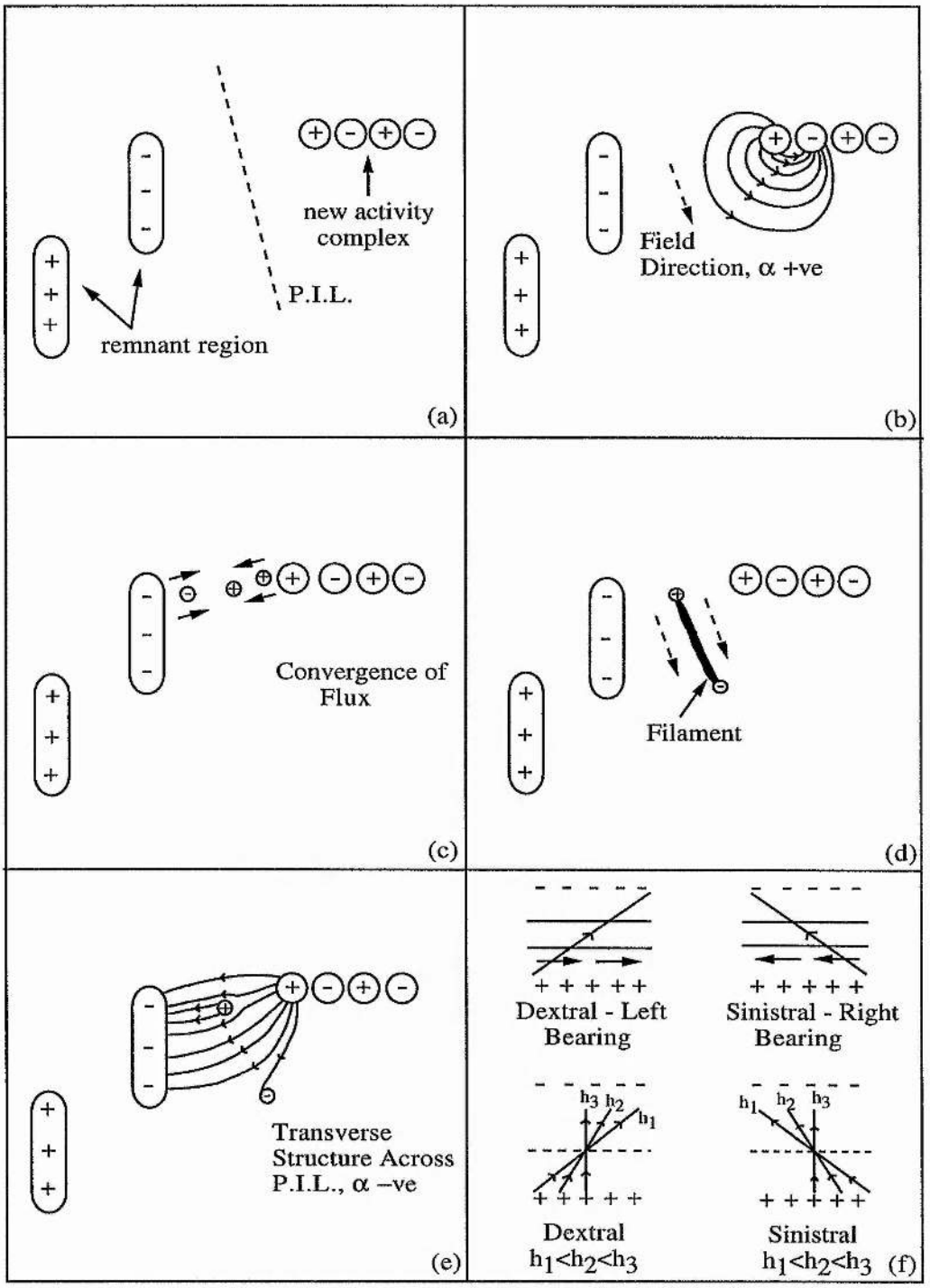

Figure 5.1: Stages of formation of the filament channel and filament (a-e). (f) Coronal arcade structure deduced from model.

Convergence of flux now occurs between the two topologically distinct regions as the component bipoles inside the activity complex expand and some of their flux is transported outwards as Moving Magnetic Features (MMF, Harvey and Harvey, 1973) into the surrounding network. With the convergence the two regions interact and reconnection takes place. The remnant region forms a boundary on one side of the channel and allows flux to connect down along the polarity inversion line between the two regions. Flux from the trailing positive polarity of the activity complex is transported into the filament channel as MMF towards the polarity inversion line. Elements of flux from the negative region also move into the channel (Figure 5.1(c)). At the point of maximum convergence, flux elements from the two regions cancel and the filament forms. It links excess flux from the convergence to other flux down the channel but not to the large remnant region (Figure 5.1(d)). The arrows give the direction of the horizontal component of field on either side of the filament structure. Since the flux that connects down the channel is small compared to the neighbouring regions it takes the form of a thin vertical sheet (Chapter 4, Figure 4.12). The filament therefore forms in the field due to an imbalance of flux along the channel but with a sheared field rather than a potential field as previously suggested in Chapter 2, Section 2.1. Although the field is sheared, the filament structure does not necessarily have helical twist. It is suggested that the mass is fed into the filament by the convergence and cancellation of flux (Priest *et al.* 1996).

For the magnetic field of the filament to connect down the channel so that it lies along the polarity inversion line the activity complex must have the correct sign of alpha with respect to the remnant region. Consider now what happens for the opposite (- ve) sign of alpha. In Figure 5.1(b) the fibrils would point in a S-N direction and the field direction would be reversed. After convergence and reconnection the field configuration of the channel shown in Figure 5.1(e) is produced. In this case transverse structures across the polarity inversion line are formed rather than a strong field along it. In other words, the configuration required for the formation of a filament channel and filament is not set up (Chapter 4, Figure 4.12).

The most important feature of this scenario is that a channel with sinistral or dextral nature is created when the complex emerges with the correct sign of alpha. The correct sign with respect to the neighbouring region (in this example +ve) gives a dominant horizontal component along the polarity inversion line between the two regions (i.e a filament channel), while the opposite sign gives transverse structure and no filament channel after convergence.

The following questions naturally arise. First, how common is this method of formation ? For this process to occur the emergence of new flux in a sheared state and then its interaction with existing remnant flux is required. This will best occur during a phase of the solar cycle when there is much old flux lying around. It is not the only method that forms a filament but it may be a predominant one at low latitudes during the ascending phase of the solar cycle. As we approach solar maximum this hypotheses could easily be tested using SoHO and ground based instruments. The second question is, how is the mass introduced into the filament and what keeps it there? This question is more difficult and presently a matter of debate, so a definite answer cannot be given. One possibility is that mass is introduced when the flux elements cancel. The cancellation of topologically distinct flux elements may create a current sheet which then "shoots" mass down the channel along the field lines that represent the filament. The mass then lies on field lines that are sufficiently long and flat to support it for a period of time. However, since the mass is not held in static support it will need to be continually replenished. Thus a process of continual small-scale flux convergence and reconnection below the filament (as suggested by Priest, Van Ballegooijen and Mackay (1996) and observed by Martin (1990)) would be required. Another possible means of mass supply is that flux is picked up from the chromosphere as the two regions converge. Recent simulations by Galsgaard and Longbottom (1997) have shown that it is possible to have density enhancement between regions of opposite polarity flux as they converge and reconnect. The full details of this are as yet unknown and more observations and theoretical work will be required to answer the question. The method described above only considers the evolution of the magnetic topology of the filament channel and filament. There is not enough information at present to describe in detail the plasma process involved. However, the model does show that helicity can be important for the formation of filaments.

5.3 Hemispheric Patterns

In a recent paper by Pevstov *et al.* (1995) it was found that there is a hemispheric pattern for the net helicity of active regions. In the northern hemisphere 76 % of active regions have negative helicity (alpha -ve) and in the southern hemisphere 69 % have positive helicity (alpha +ve). The dominant values of alpha in each hemisphere do not change with the solar cycle or with class of

Cycle	Side	Northern alpha	Southern alpha
21	west	-ve (76%) dextral	+ve (69%) sinistral
21	east	+ve (24%) sinistral	-ve (31%) dextral
22	west	-ve (76%) dextral	+ve (69%) sinistral
22	east	+ve (24%) sinistral	-ve (31%) dextral

Table 5.1: Sign of helicity (alpha) necessary to form filaments.

flux region (unipolar, active region, activity complex). In the present model the net helicity of the activity complex plays an important role in determining the chirality of the channel. The correct sign of helicity gives connections down the channel along the P.I.L. and the wrong sign gives connections across the channel. Can a hemispheric pattern for this type of formation be explained by the hemispheric pattern of helicity ?

To see if this is the case force-free models of the channel analysed before, which formed on the 25^{th} July 1979, are constructed but we consider the effects of flux emerging on both the east and west side of the remnant region and in each hemisphere according to the polarity emergence law for both cycle 21 and 22. The sign and value of alpha is deduced that produces connectivity down the channel rather than across it so that a filament-type structure can be obtained as before. The results are presented in Table 5.1 for different solar cycles, hemispheres, and sides of emergence of the new flux relative to the old flux.

If the flux regions emerge to the west of the activity complex in cycle 21 a positive value of alpha is required to give the correct connectivity in the southern hemisphere and a negative value of alpha is required in the northern hemisphere. With this, sinistral channels are produced in the southern hemisphere and dextral channels in the northern hemisphere (Figure 5.2(a)), which is consistent with the results of Martin, Bilimoria and Tracadas (1995). If the opposite value of

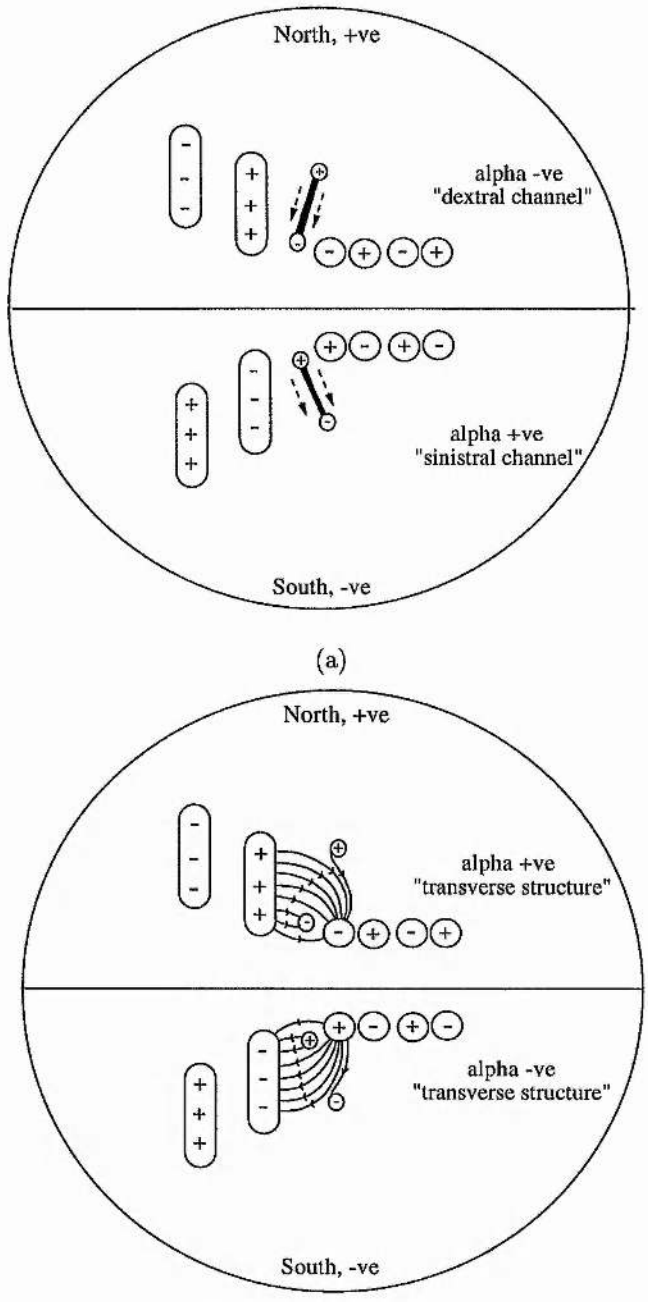

Figure 5.2: Emergence west of remnant region for cycle 21, showing (a) filament channel formation for dominant values of alpha in each hemisphere. Arrows give direction of horizontal component of field on either side of channel. (b) Transverse structure across P.I.L. for minority values of alpha in each hemisphere.

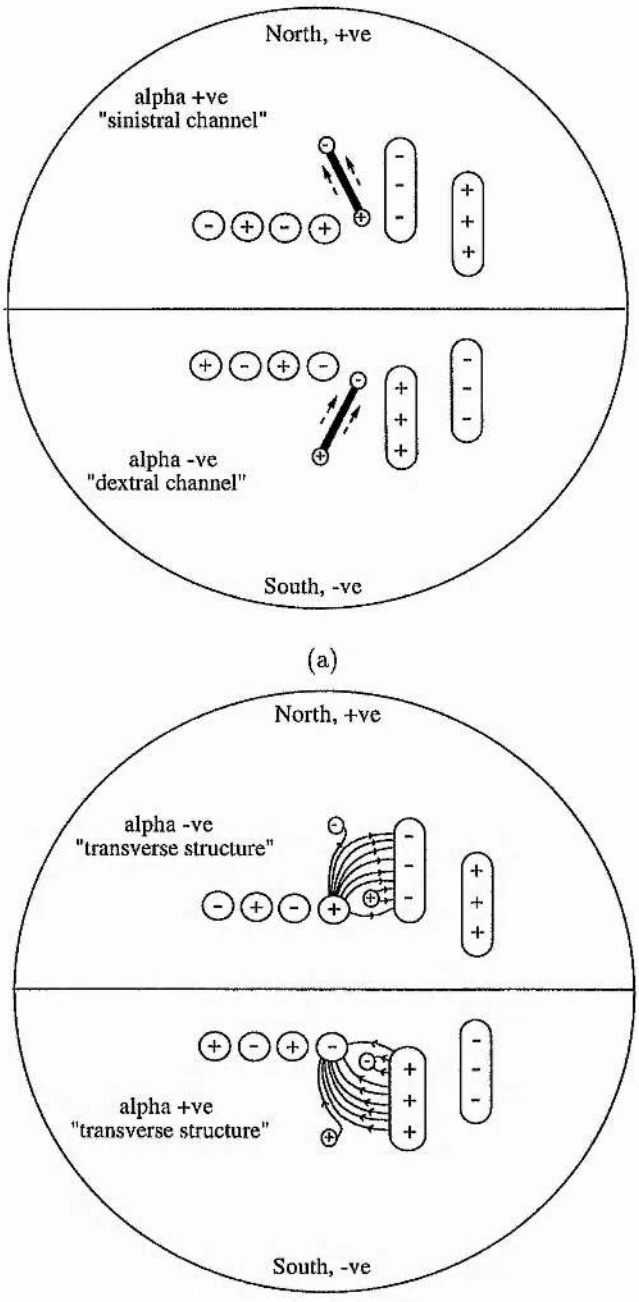

Figure 5.3: Emergence east of remnant region for cycle 21, showing (a) filament channel formation for minority values of alpha in each hemisphere. Arrows give direction of horizontal component of field on either side of channel. (b) Transverse structure across P.I.L. for dominant values of alpha in each hemisphere.

alpha is used in each case, a transverse structure is obtained across the channel and no flux connects down the channel to produce a filament-type structure (Figure 5.2(b)). If the flux emerges on the east side of the remnant region the opposite occurs. A negative value of alpha is required in the southern hemisphere and gives a dextral channel and a positive value is required in the northern hemisphere to give a sinistral channel (Figure 5.3(a)). Again if the opposite sign of alpha is used in each case flux connects across the channel and not down it (Figure 5.3(b)). Emergence on the west side needs the dominant sign of alpha in each hemisphere to obtain the correct magnetic structure while emergence on the east side needs the minority sign of alpha. The minority values of alpha in each hemisphere give the wrong chirality, while the dominant values give the correct chirality. Thus statistically there is a much higher chance of having dextral filaments in the northern hemisphere and sinistral filaments in the southern hemisphere. However, both can be produced by this mechanism in each hemisphere. The same pattern is found for the next cycle (22) with the polarity of the flux regions reversed accordingly; thus the results are independent of the solar cycle as Martin, Bilimoria and Tracadas (1995) found. This shows the significance of helicity in the hemispheric patterns of filaments, a feature not considered until recently. In this chapter a hemispheric pattern known from observations has been used along with theory to predict that there is a hemispheric pattern for intermediate filaments.

The models constructed are also consistent with the results of Martin and M^{c}Allister (1995) for the overlying arcades. The axial component of field in the channel is created from the type of twisting due to the sign of alpha in the complex. The arcades overlying the filament channel must have the same direction of axial field as the filament channel lying below them or there would be a field reversal with height. Thus all stable arcades lying above dextral filament channels should be left-bearing and all arcades above sinistral filament channels correspondingly right-bearing (Figure 5.1(f)).

The filament channel in this model is represented by a sheared force-free field. As we go higher up into the corona we would expect the field to relax more to a potential field with height. Thus the higher up, the more transverse the field should be across the P.I.L. The relaxation time for the coronal field through a tearing mode instability would be typically a few days. When eruptions occur some energy will be lost but not all of it. The field that closes down is then seen as a dynamical loop system and loops that were not seen before are now lit up. If the field is relaxing

towards a potential field with height (as Schmieder *et al.* (1996) found) then a clockwise rotation of the loops with height would occur for sinistral filament channels and a counter-clockwise rotation for dextral filament channels (Figure 5.1(f)). This is indeed what is seen in the observations. The arcade orientation must be consistent with the axial component of field in each channel and that is why there is a one-to-one correspondence between them.

5.4 Comparison with Previous Models

It is now useful to compare the method of formation described above with the models of Rust and Kumar (1995) and Priest, Van Ballegooijen and Mackay (1996) to show how well the previous theoretical models compare with the present one deduced from observations.

5.4.1 Rust and Kumar (1995)

In their model the authors describe the formation of a filament as the emergence of a horizontal, twisted flux rope. The flux ropes are produced by a global, subsurface velocity that twists the field. Subsurface differential rotation then acts on the flux rope to give the correct axial component in each hemisphere. To support this they describe the barbs of pre-eruptive filaments as a filled helix and interpret the cancelling magnetic features seen during formations as the emergence of a U-shaped loop that lifts mass up into the corona. With each new, U-loop emergence the total length of the emerged flux rope increases and helicity and mass are added to the filament. The model does not use shearing motions of surface fields or magnetic reconnections to form the filament.

While their scenario is appealing due to its simplicity it does not fit the picture deduced from the observations. First of all, it does not include the role of the filament channel in the formation of the filament. For the type of filament considered here, the filament channel is observed to be created by the emergence of a new region of flux in a sheared state. It is then the shear of this region that produces the sinistral/dextral nature and a dominant horizontal component of field in the channel long before the actual filament forms. The fibrils of the channel represent arches that connect regions of positive and negative flux, they do not represent emerging horizontal flux ropes. Secondly, cancellation of flux does occur in our model but it is interpreted differently. The cancellation is observed to occur between elements of the new and remnant regions. If it

represented the emergence of a U-shaped loop that connected the cancelling fragments below the surface, the emergence of the loop would give a flux rope that stretched across the polarity inversion line and not along it. The emerging structure would be at a large angle to the dominant direction of field in the channel. In our opinion the cancellation is of two topologically distinct structures that are not necessarily connected below the surface because one structure had emerged many months before the other. These elements cancel out and in the process inject mass down the channel to form the filament. Reconnections also play an important role in the changing topology of the channel as the two flux systems converge. In our opinion the Rust and Kumar scenario does not fit well the method of formation seen here. However, our mechanism is for a specific type of filament formation so it does not rule out their process for other types of filaments such as those of the polar crown.

5.4.2 Priest, Van Ballegooijen and Mackay (1996)

The above authors put forward a dynamical model for the formation of filaments where the filament is maintained by the continual input of mass and magnetic flux from cancelling magnetic fragments. Subsurface differential rotation is used to give the correct axial component in each hemisphere. However, the build-up of this component in the chromosphere and corona is described in terms of small-scale emergences and reconnections along the polarity inversion line. These emergences and reconnections create the filament as a flux tube along the filament channel with cool plasma lifted up from the photosphere and chromosphere by each reconnection. The flux tube may have twist but it is not an essential ingredient. Continual reconnections are required to maintain the filament channel and filament.

This scenario also differs greatly from the one described in Section 5.2. To begin with, it describes the filament channel formation through the systematic alignment of small-scale fields that have emerged once subsurface differential rotation has acted upon them. In contrast, the mechanism of the present chapter forms the channel by the emergence of a sheared region. The formation of the channel occurs with one large-scale emergence, rather than with a series of small-scale emergences as Priest, Van Ballegooijen and Mackay (1996) suggest. To form the filament, reconnections are required in both scenarios. In our model the new and remnant regions interact with the remnant region forming a boundary on one side of the channel. The filament then forms

after there is a large-scale cancellation of flux at the top of the channel. Thus the filament is formed by one large cancellation building up the mass and flux rather than by many small-scale cancellations. However, a process of many small-scale cancellations below the filament would be required to maintain it after it has formed. The method of Priest *et al.* (1996) may be more suitable for high-latitude filaments where there are no clear large-scale emergences of flux. At high latitudes where the fields are weaker, small-scale emergences and reconnections may more easily orientate the field to the sinistral/dextral direction in each hemisphere. However, at lower latitudes where the fields are stronger the process is less likely.

5.5 Conclusion

In this chapter a new scenario has been put forward for the formation of filament channels and filaments. It involves the emergence of new flux and its interaction with remnant flux. The key ingredient in the model is the net helicity of the new region that emerges. With the correct sign of helicity a filament channel and filament can form between the two regions; with the incorrect sign, transverse structure is obtained across the polarity inversion line and no filament can form. The observed hemispheric pattern of helicity then naturally leads to a hemispheric pattern for this type of filament, with dextral filaments dominating in the northern hemisphere and sinistral filaments in the southern hemisphere. This method, however, is appropriate for a specific type of filament, namely the intermediate or boundary filament. The formation of polar-crown filaments is more likely to be caused by one of the alternative methods given above. However, the present model stresses that helicity can have an important effect on the hemispheric patterns of filaments, a feature that should be included in future modelling.

Chapter 6

Conclusions and Future Work.

This thesis has mainly dealt with the magnetic structure of filament channels and filaments. To model these objects, potential and force-free approximations have been used. Throughout this thesis, an emphasis has been given to the modelling of specific observations. In Chapter 1 both a potential and a force-free model of a filament channel were set up. The potential model consisted of two point sources that represent the origin of the flux of the filament and two line sources that produce the flux of the overlying arcade. With this model, the filament channel was created by an asymmetry of flux locations along a finite length of the polarity inversion line in the channel. An interesting feature of the model is the presence of a separatrix surface that envelopes the flux that connects along the channel. For the initial model, the lower bound of the separatrix was consistent with the lower bound of a prominence, whereas the upper bound was far to high to be the upper bound of the prominence, though it did correspond in altitude roughly to the top of the coronal cavity. For the lower field lines within the separatrix the free-fall time was around 3000 s which is the same as the coronal condensation time. Therefore, it may be possible for a filament to form on the lower field lines while the higher ones represent those of the coronal cavity. When a weak background field was added to the filament channel it was found that a large change in the heights of the separatrices could occur. For quiet-region flux values and a background field of around 1G the lower and upper separatrices could be reduced to the heights of the lower and upper bounds of quiescent filaments. With the uniform field added the field lines were much flatter and had a free-fall time of 4000-5000 s. With the increased free-fall time and flatter field

lines the topology was much more suitable for the formation of a filament. However, when active-region flux values were considered a background field of over 40G was required and a field of this magnitude could not be justified. This showed that the potential model may be suitable for large quiescent filaments but not for small active-region filaments. After the simple potential model a more detailed numerical linear force-free model was constructed. With this, the effect of magnetic shear on the separatrix surface was considered. Again similar results were found to the potential model with the possibility of both upper and lower bounds existing. This time the heights and widths of the separatrices could be increased or decreased as the sign of alpha was changed to both positive and negative values. Dextral channels existed for a wider range of negative values of alpha and sinistral channels for positive values of alpha. For the cases considered here there was a wide range of possible structures that could represent the magnetic field of a filament. It was also found that the exact dimensions of the structure depended very much on the boundary conditions, with the potential model and open boundary conditions giving the highest possible solution.

In Chapter 3 potential modelling was used to model a variety of coronal structures. First the bending of a filament in the filament channel was considered as the interaction of the horizontal component of the filament field with regions of opposite polarity flux called plagettes. With this, the bending and narrowing of the filament as it passed between the plagettes was obtained and a possible mechanism for determining the horizontal component of the filament field from Hα and magnetogram images was put forward. The potential modelling was then used to model the opposite skew of arcades above each arm of a switchback of a polarity inversion line. The initial modelling showed that the skew on each arm could result from an imbalance of flux at the corner of the switchback. This imbalance was due to the switchbacks lying close to the polar regions on the Sun. As the flux imbalance increased the amount of skew also increased. The modelling showed that changing skew of field lines with height or shear of the field could be obtained with a potential field, as long as there was a flux imbalance in that field. A specific example of a switchback was then modelled and a good comparison between the model and observations was found. The skew on the horizontal arm was found to be right-skew and roughly 60 degrees while on the diagonal arm it was left-skew and 50 degrees. Finally, a specific example of a filament in a filament channel was modelled. However, to obtain a good representation a background uniform field had to be added along with extra regions of flux. Since the region being modelled was of high resolution the

existence of the extra regions of flux was not ascertained. It was, however, shown that dips in a filament's magnetic field could be due to the locations of opposite polarity flux that lie below the filament.

In Chapter 4 the formation of a filament channel and filament over a period of five days was modelled from a sequence of Hα and magnetogram images. The modelling showed that the formation of the filament channel was due to the emergence of an activity complex in a highly sheared state. Both analytical and numerical force-free models were considered. It was found that the field lines that give the best fit to the Hα images were flat and low-lying. Further modelling then showed that the magnetic field of a small active-region filament could not be represented by a potential field but was described well by a highly sheared force-free field. The field lines that gave the best fit to the filament formed a thin vertical sheet of flat low-lying flux that connected down the channel. The changing angle of inclination of the structure gave the appearance of twist. It was then shown that interaction between the new activity complex and the old remnant region was a necessary condition for the filament to form at its observed location. This suggested that magnetic reconnections play an important role in the formation of filaments, a feature which some models do not include. In Chapter 5 the process described above was generalised to suggest a new scenario for the formation of filament channels and filaments. It involves both the emergence of new flux and its interaction with remnant flux. A key feature in the model is the net helicity of the newly emerged region. With the correct sign a filament channel and filament could form after convergence; with the incorrect sign no filament channel or filament could form. The observed pattern of helicity in each hemisphere then naturally leads to a hemispheric pattern for filament channels, with dextral channels dominating in the northern hemisphere and sinistral channels in the southern hemisphere with an average ratio of 70:30. This result shows the importance of helicity in the hemispheric patterns of filaments, a feature which should be incorporated in future modelling.

One interesting feature that has been observed throughout the modelling work carried out in this thesis is that it is very difficult to determine whether field lines are potential or force-free just by considering their topology. In Chapter 3, Section 3.2 it was shown that a changing skew or "shear" of field lines could be obtained with height (see Figures 3.6 (f), 3.7 (f), 3.8 (f)) from a purely potential field (as long as there was a flux imbalance in that field). However, in Chapter

4, Section 4.2.3 the two sets of field lines that correspond to the "arch filament systems" can be seen to give a very transverse (unsheared) structure across their respective polarity inversion lines (Figure 4.7), even though these field lines are highly sheared. This shows that the only way to determine whether an observed structure is really potential or not is to consider the flux locations and sizes and to compute the resulting potential and non-potential field lines.

There are many outstanding problems in the area of prominence research and future work may proceed in many directions. To begin with, the modelling of the observed region in Chapter 4 could be repeated with non-linear force-free field models. If vector magnetograms were available these could be used to determine alpha in the various flux regions. With this a much better model of the filament channel could be constructed and possibly the arcades lying above the filament included. With the present model (using a linear force-free field) the solution is only reasonable in a localised region (the region of the filament where alpha is roughly constant).

Another unanswered question relates to the hemispheric pattern of filament channels and filaments. Progress has been made with the results in Chapter 5 but it does not give the full answer. To determine how helicity affects the hemispheric patterns of filaments throughout the solar cycle, helicity could be added into the global diffusion code developed by Aad van Ballegooijen. This code simulates the effects of differential rotation, diffusion, and meridional flows on photospheric flux distributions. With this, the authors van Ballegooijen, Cartledge and Priest (1997) were able to show that these effects could not give rise to the hemispheric patterns of filaments. However, they neglected one important effect, namely the observed helicity of emerging flux regions. By determining the amount and location of helicity emergence from the results of Pevtsov (1994,1995) the evolution of this preferential twisting in each hemisphere throughout the solar cycle could be followed. It would be interesting to note whether these effects allow a preferential survival of dextral channels in the northern hemisphere and sinistral in the southern.

Another use of the code would be to take the channel modelled in Chapter 4 and evolve the field for one month. The computed field could then be compared with that observed on the next rotation to see if differential rotation, diffusion and meridional flows can explain the changing appearance and evolution of the filament channel through the next solar rotation. These are just two of the many possible applications of the code in the context of filament channels and filaments.

A further area of future work relates to the barbs of filaments. Very little research to date has

been undertaken on these structures. Models are needed to address fundamental questions about suitable magnetic topologies for barbs. They will have to explain how the mass is supported and why there is a hemispheric pattern. By considering the magnetic topologies of the barbs a fuller understanding of the three-dimensional nature of magnetic fields in filaments could be obtained. If the barbs join to the top of the filament, it would suggest that the field of the filament has a helical structure. However, if the barbs connect to the bottom of the filament, the field is likely to have more of a straight tube-like structure. Both two-dimensional analytical and three-dimensional numerical models could be constructed. Such models should also consider how the barbs are connected to the photosphere. Observations suggest that the barbs are located in regions of parasitic (opposite) polarity photospheric flux, but it is unclear whether they connect to the centres or boundaries of supergranular cells. The modelling has important theoretical and observational consequences. In order to maintain a close relationship between theoretical and observational results the models could be applied to observations to test how well the theories deal with specific cases.

The magnetic topologies of barbs are also of fundamental importance for understanding the source of mass in filaments. One possibility is that mass is injected from the chromosphere along the barbs into the filament. The modelling could be compared with SOHO (CDS,SUMER) observations of filament flows. Again, models need to be constructed which allow both upflows and downflows in filaments. An alternative explanation for supplying the mass is to lift it as dense photospheric material up into the corona by flux cancellation events that occur at the footpoints of barbs. In a preliminary paper Priest *et al.* (1996) address this problem and outline the process. More detailed calculations could consider whether the mass pickup process does indeed work.

As another area of research, filament eruptions and CME's could be considered in terms of the switchbacks of polarity-inversion lines. At these locations, frequent CME events occur in conjunction with erupting filaments lying along the arms of the switchback. Yohkoh images of the overlying arcades could be studied. By constructing models of both the pre-eruption and post-eruption arcades from magnetograms, calculations of the change in energy state could be made. The Yohkoh data could also be compared with Hα images of filaments. By doing this, a possible mechanism for the CME could be sought. The global diffusion model would be useful in this study, to test whether or not the arcades are formed due to differential rotation on the footpoints and whether it could describe the evolution of the switchback. There are, therefore, many possible

areas of work that can be undertaken as natural steps from the research carried out in this thesis.

A. Comparison of Order of Magnitude Estimates and Numerical Results.

The tables below compare the order of magnitude estimates of the separatrix heights with those obtained numerically for $a = 1.0, 3.0, 5.0$. It can be seen that as the value of a and f grows larger the estimate becomes worse.

$a = 1.0$

Property	Order of Magnitude Estimate	Numerical Value
Poles join in y=0 plane	$f > 2.0$	$f > 1.9$
Poles initially join	$f = 2.0$ $y = 0.0$	$f = 1.9$ $y = 0.0$
Sep. heights when $f = 10.0$	2.3	3.0

$a = 3.0$

Property	Order of Magnitude Estimate	Numerical Value
Poles join in y=0 plane	$f > 18.0$	$f > 31.0$
Poles initially join	$f = 11.0$ $y = 2.8$	$f = 6.0$ $y = 5.0$
Sep. heights when $f = 10.0$	6.0 0.7	14.0 1.25

$a = 5.0$

Property	Order of Magnitude Estimate	Numerical Value
Poles join in y=0 plane	$f > 50.0$	$f > 135.0$
Poles initially join	$f = 19.6$ $y = 5.0$	$f = 7.0$ $y = 8.6$
Sep. heights when $f = 25.0$	10.0 2.2	29.0 2.2

B. Position and Labelling of Sources in Switchback Model.

In Figure B1 the position and labelling of the sources and sinks that represent the switchback are shown. Below a list of the flux values of the sources and sinks can be seen with the flux values scaled in terms of 10^{19} Mx.

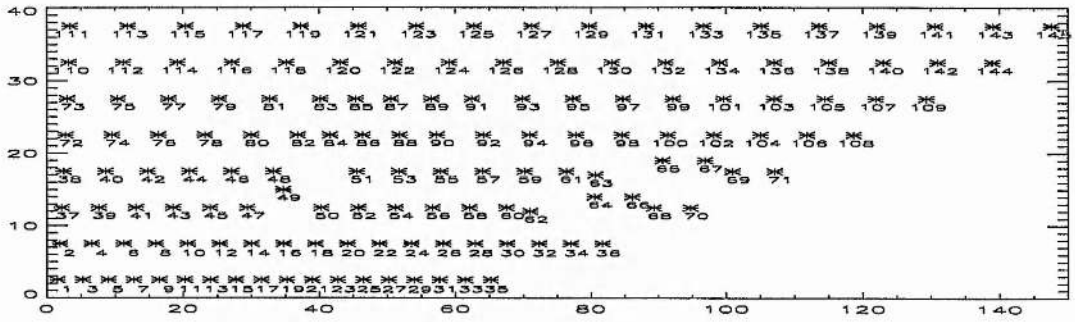

Figure B1: Position and labelling of sources and sinks in switchback model.

$f_1 = -27.6$	$f_2 = -8.0$	$f_3 = -22.7$	$f_4 = -7.2$	$f_5 = -27.4$	$f_6 = -6.2$
$f_7 = -26.4$	$f_8 = -8.5$	$f_9 = -27.2$	$f_{10} = -24.0$	$f_{11} = -30.0$	$f_{12} = -11.1$
$f_{13} = -30.6$	$f_{14} = -17.4$	$f_{15} = -22.8$	$f_{16} = -13.3$	$f_{17} = -35.7$	$f_{18} = -5.4$
$f_{19} = -45.4$	$f_{20} = -9.4$	$f_{21} = -32.0$	$f_{22} = -15.2$	$f_{23} = -15.4$	$f_{24} = -19.8$
$f_{25} = -25.0$	$f_{26} = -18.7$	$f_{27} = -31.0$	$f_{28} = -24.8$	$f_{29} = -19.0$	$f_{30} = -17.0$
$f_{31} = -24.7$	$f_{32} = -24.4$	$f_{33} = -30.8$	$f_{34} = -15.4$	$f_{35} = -26.1$	$f_{36} = -26.2$
$f_{37} = -10.1$	$f_{38} = -16.7$	$f_{39} = -8.3$	$f_{40} = -4.9$	$f_{41} = -4.1$	$f_{42} = -7.5$
$f_{43} = 3.2$	$f_{44} = -4.8$	$f_{45} = -8.6$	$f_{46} = -5.1$	$f_{47} = -8.7$	$f_{48} = -0.4$
$f_{49} = 9.4$	$f_{50} = 9.4$	$f_{51} = 18.2$	$f_{52} = 18.8$	$f_{53} = 10.9$	$f_{54} = 11.2$
$f_{55} = 36.9$	$f_{56} = 6.5$	$f_{57} = 32.9$	$f_{58} = 6.3$	$f_{59} = 43.6$	$f_{60} = 16.3$
$f_{61} = 46.0$	$f_{62} = 2.5$	$f_{63} = 32.6$	$f_{64} = -7.0$	$f_{65} = 11.8$	$f_{66} = -19.2$

$f_{67} = 8.0$	$f_{68} = -23.8$	$f_{69} = -12.9$	$f_{70} = -21.6$	$f_{71} = -15.4$	$f_{72} = -27.4$
$f_{73} = -12.2$	$f_{74} = -18.4$	$f_{75} = -13.4$	$f_{76} = -9.9$	$f_{77} = -15.5$	$f_{78} = 3.4$
$f_{79} = -17.2$	$f_{80} = -11.7$	$f_{81} = -19.6$	$f_{82} = -9.4$	$f_{83} = -18.1$	$f_{84} = -3.4$
$f_{85} = -25.0$	$f_{86} = 0.65$	$f_{87} = -9.8$	$f_{88} = 1.9$	$f_{89} = -21.9$	$f_{90} = 1.5$
$f_{91} = -27.7$	$f_{92} = 15.5$	$f_{93} = -11.5$	$f_{94} = 40.4$	$f_{95} = 26.7$	$f_{96} = 44.0$
$f_{97} = 67.5$	$f_{98} = 47.0$	$f_{99} = 48.8$	$f_{100} = 47.0$	$f_{101} = 32.0$	$f_{102} = 50.2$
$f_{103} = 58.9$	$f_{104} = 55.9$	$f_{105} = 90.1$	$f_{106} = 76.8$	$f_{107} = 86.9$	$f_{108} = 38.7$
$f_{109} = 36.1$	$f_{110} = -17.4$	$f_{111} = -50.3$	$f_{112} = -12.2$	$f_{113} = 6.9$	$f_{114} = -7.7$
$f_{115} = 7.1$	$f_{116} = -6.7$	$f_{117} = 0.6$	$f_{118} = -22.8$	$f_{119} = -3.8$	$f_{120} = -25.1$
$121 = -25.3$	$122 = -28.9$	$f_{123} = -6.8$	$f_{124} = -40.5$	$f_{125} = -16.7$	$f_{126} = -68.6$
$f_{127} = -20.9$	$f_{128} = -53.8$	$f_{129} = -70.8$	$f_{130} = -2.9$	$f_{131} = -31.7$	$f_{132} = 64.7$
$f_{133} = -4.7$	$f_{134} = 81.9$	$f_{135} = 102.7$	$f_{136} = 58.7$	$f_{137} = 113.6$	$f_{138} = 14.6$
$f_{139} = 20.5$	$f_{140} = 69.4$	$f_{141} = -4.9$	$f_{142} = 49.5$	$f_{143} = 28.6$	$f_{144} = 110.5$
$f_{145} = 29.2$					

C. Position and Labelling of Sources for Model of Particular Filament.

Diagrams showing the position and labelling of the sources and sinks in the filament channel for both magnetogram 1 (Figure C1) and magnetogram 2 (Figure C2). The sources are represented by '+' signs and the sinks by '-' signs. Below each of the diagrams are the relative flux values of the sources (f_i).

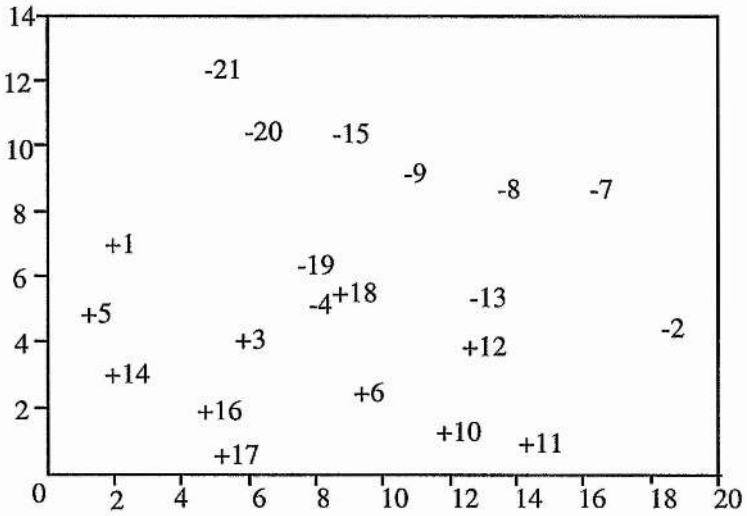

Figure C1: Position of sources and labelling for magnetogram 1.

Magnetogram 1

$f_1 = 20.0$	$f_2 = -100.0$	$f_3 = 3.0$	$f_4 = -4.0$	$f_5 = 10.0$	$f_6 = 2.0$	$f_7 = -13.0$
$f_8 = -13.0$	$f_9 = -13.0$	$f_{10} = 12.0$	$f_{11} = 10.0$	$f_{12} = 2.0$	$f_{13} = -2.0$	$f_{14} = 8.0$
$f_{15} = -13.0$	$f_{16} = 3.0$	$f_{17} = 3.0$	$f_{18} = 1.0$	$f_{19} = -6.0$	$f_{20} = -3.0$	$f_{21} = -3.0$

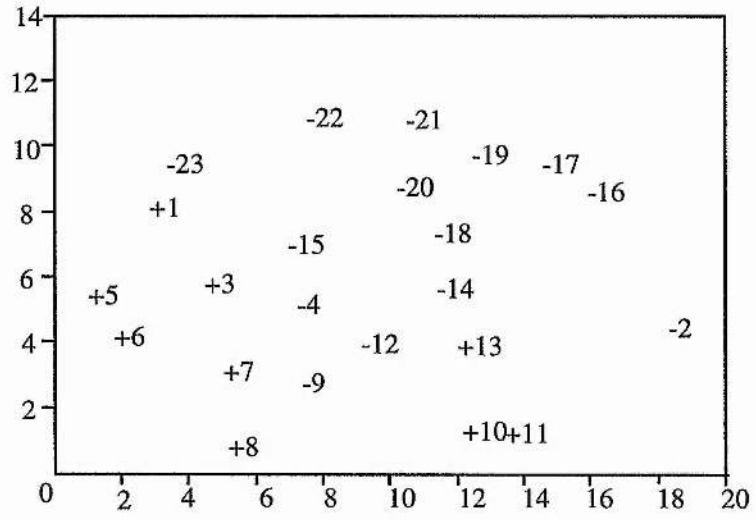

Figure C2: Position of sources and labelling for magnetogram 2.

Magnetogram 2

$f_1 = 26.0$ $f_2 = -100.0$ $f_3 = 3.0$ $f_4 = -8.0$ $f_5 = 10.0$ $f_6 = 10.0$ $f_7 = 7.0$

$f_8 = 7.0$ $f_9 = -3.0$ $f_{10} = 10.0$ $f_{11} = 10.0$ $f_{12} = -3.0$ $f_{13} = 3.0$ $f_{14} = -4.0$

$f_{15} = -6.0$ $f_{16} = -16.0$ $f_{17} = -16.0$ $f_{18} = -4.0$ $f_{19} = -16.0$ $f_{20} = -5.0$ $f_{21} = -10.0$

$f_{22} = -12.0$ $f_{23} = -1.0$

D. Numerical Method used to Obtain Linear Force-Free Fields.

A brief description of the method used to obtain the 3-D force-free equilibria is given here. For a more detailed description of the method used, the papers by Finn *et al.* (1994) and Longbottom *et al.* (1997) and references therein should be considered. To find a 3-D linear ($\alpha = const$) force-free equilibria the equation

$$\nabla \times \mathbf{B} = \alpha \mathbf{B}, \tag{D.1}$$

must be solved. One method of doing this is to reduce the problem to one involving the vector potential $\mathbf{A}$ ($\mathbf{B} = \nabla \times \mathbf{A}$). The problem is then solved in a cube whose sides range from $-1 < x, y, z < 1$. With this form for $\mathbf{B}$ the force-free equation reduces to solving

$$\nabla^2 \mathbf{A} + \alpha \nabla \times \mathbf{A} = 0, \tag{D.2}$$

subject to the boundary conditions

1. The tangential components of $\mathbf{A}$ ($A_t = -\hat{\mathbf{n}} \times (\hat{\mathbf{n}} \times \mathbf{A})$) on each face are consistent with the normal component of $\mathbf{B}$ ($B_n = \mathbf{B}.\hat{\mathbf{n}}$).

2. The normal component of $\mathbf{A}(A_n = \mathbf{A}.\hat{\mathbf{n}})$ satisfies $\nabla.\mathbf{A} = 0$ on the boundary. In fact with convergence to the solution of Equation D.2, $\nabla.\mathbf{A} = 0$ everywhere.

The cube represents an isolated region of the solar surface and flux can only enter or leave through the bottom surface ($z = -1$). This means that B_n the normal component of $\mathbf{B}$, is zero on each of the faces except $z = -1$ (which represents the photosphere). To satisfy boundary condition 1 it is assumed that the tangential components of $\mathbf{A}$ are zero on each of the faces except the $z = -1$. With this the second boundary condition is satisfied by having the normal derivative of the normal component of $\mathbf{A}$ zero on each of these faces.

The base flux now needs to be specified. This is done by specifying the normal component of the magnetic field ($B_n = B_z$) at $z = -1$. To do this it is first assumed that on the base

$$\frac{\partial A_z}{\partial z} = 0 \tag{D.3}$$

and conditions 1 and 2 give

$$B_z = \frac{\partial A_y}{\partial x} - \frac{\partial A_x}{\partial y} \tag{D.4}$$

$$\frac{\partial A_x}{\partial x} + \frac{\partial A_y}{\partial y} = 0 \tag{D.5}$$

To find A_x,A_y on the base from B_z, the vector potential $\mathbf{A}$ is written in the form of a flux function Φ such that

$$\mathbf{A} = \nabla \times (\Phi(x, y)\hat{\mathbf{z}}) + A_z\hat{\mathbf{z}}. \tag{D.6}$$

With this form for $\mathbf{A}$ Equation D.4 becomes

$$\frac{\partial^2 \Phi}{\partial x^2} + \frac{\partial^2 \Phi}{\partial y^2} = -B_z$$

This equation is then solved subject to the boundary conditions that

$$\frac{\partial \Phi}{\partial n} = 0 \tag{D.7}$$

on the boundaries. This is required so that on the boundaries the tangential components of $\mathbf{A}$ are zero. With A_x,A_y determined from B_z on the base the full problem can then be solved. It is solved by linear multigrid including V-cycles on a regular cartesian grid and with a Gauss-Seidel smoother.

Each of the problems considered in Chapters 2 and 4 is solved on three different grid spacings, namely 33^3, 65^3 and 129^3 grid points. This is done so that convergence of the solution can be shown. In all of the problems the radius and location of the sources are chosen so that they are independent on the lowest grid (33^3). As the number of grid points is increased the sources are centred on the same grid points as on the 33^3 grid. This is to ensure that exactly the same problem is solved as the number of grid points is increased. In all cases, as the number of grid points is increased it is generally found that the footpoints of the field lines lie within one grid spacing of those carried out on the previous grid size. However, if a field line passes close to a separatrix surface or lies on the separatrix surface, as the surface becomes better resolved, a large displacement of footpoints can occur. This just represents the nature of these surfaces. To show that convergence of the solution has occurred as the number of grid points is increased global

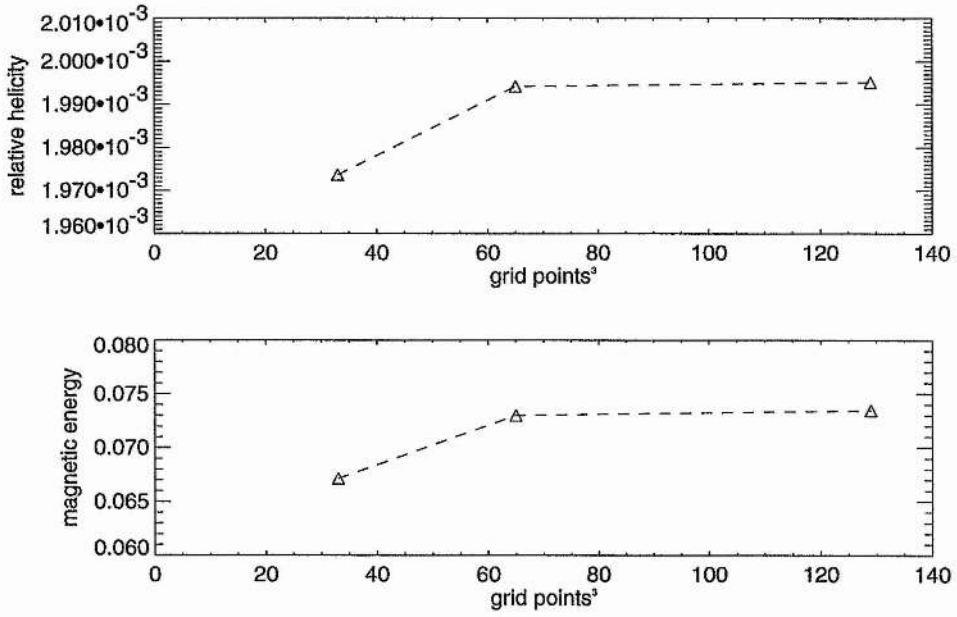

Figure D1. Graphs of (a) Relative Helicity versus grid spacing and (b) magnetic energy versus grid spacing. Both show convergence of the solution as the number of grid points in increased.

properties of the field are considered such as the magnetic energy and relative helicity (Berger 1985) of the field. The magnetic energy and relative helicity are given by

$$MagneticEnergy = \int_v \frac{B^2}{2\mu} dV \tag{D.8}$$

and

$$RelativeHelicity = \int_v \mathbf{A}.\mathbf{B} dV. \tag{D.9}$$

The magnetic energy tells us how much energy is stored in the field. When the field is potential we have the minimum amount of energy and this energy is unavailable. However, as alpha increases (magnetic shear added) the energy increases. The relative helicity measures the linkage of the field and gives a measure of the amount of twisting. When $\alpha = 0$ the relative helicity is zero. In Figure D1 the graphs of (a) relative helicity and (b) magnetic energy versus grid spacing in dimensionless units can be seen for $\alpha = 2.3$ and the problem considered in Chapter 4, Section 4.5. These show that as the grid spacing is doubled the solutions quickly converge. Convergence for the other problems considered in this thesis was also checked and similar results found.

E. Position and Labelling of Sources for Potential Model of July 25^{th} 1979.

Flux values in terms of 10^{19} Mx for each of the poles representing the magnetic field of the filament channel. In Figure E1 we see the position and labelling of the sources, '+' signs and the sinks, '-' signs for the potential model of the 25^{th} July.

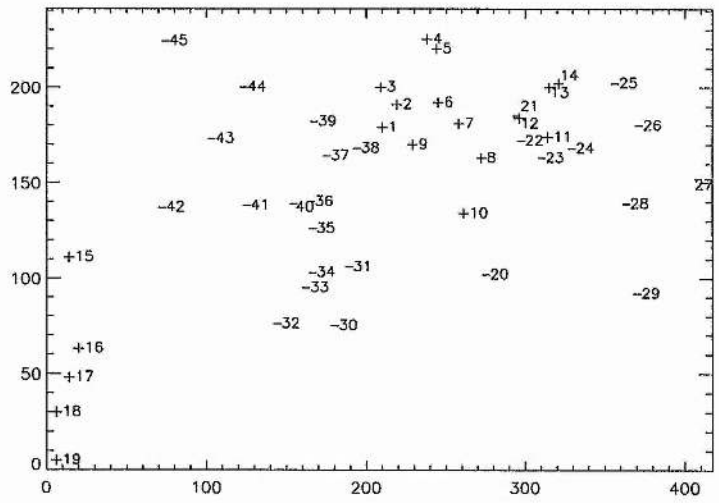

Figure E1. The positions and labelling of the sources in the channel for the potential model of the 25^{th} July.

f_1 = 4.9	f_2 = 11.1	f_3 = 4.4	f_4 = 7.9	f_5 = 13.1	f_6 = 44.0
f_7 = 16.3	f_8 = 12.5	f_9 = 1.9	f_{10} = 3.7	f_{11} = 4.5	f_{12} = 4.4
f_{13} = 25.3	f_{14} = 34.4	f_{15} = 10.0	f_{16} = 16.7	f_{17} = 7.4	f_{18} = 20.7
f_{19} = 12.6	f_{20} = -4.0	f_{21} = -15.9	f_{22} = -3.4	f_{23} = -28.9	f_{24} = -91.5
f_{25} = -17.0	f_{26} = -45.5	f_{27} = -11.2	f_{28} = -15.5	f_{29} = -3.2	f_{30} = -7.5
f_{31} = -6.1	f_{32} = -6.5	f_{33} = -43.8	f_{34} = -12.0	f_{35} = -13.3	f_{36} = -16.9
f_{37} = -14.8	f_{38} = -3.6	f_{39} = -18.4	f_{40} = -6.7	f_{41} = -4.8	f_{42} = -8.7
f_{43} = -7.2	f_{44} = -6.9	f_{45} = -16.0			

References

Athay, R.G.: 1976, "The Solar Chromosphere and Corona: Quiet Sun", D.Reidel, Dordrecht, Holland.

Athay, R.G., Querfield, C.W., Smartt, R.N., Landi Degl'innocenti, E. and Bommier V.: 1983, "Vector Magnetic Fields in Prominences", *Solar Phys.*, **89**, 3.

Antiochos, S.K. and Klimchuck, J.A.: 1991, "A Model for the Formation of Solar Prominences", *Astrophys. J.*, **378**, 372.

Antiochos, S.K., Dahlburg, R.B. and Klimchuck, J.A.: 1994, "The magnetic field of solar prominences", *Astrophys. J.*, **420**, L41.

Babcock, H.W. and Babcock, H.D.: 1955, "The Sun's magnetic Field, 1952-1954", *Astrophys. J*, **121**, 349.

Berger, M.A.: 1985, "Structure and Stability of Constant α Force-Free Fields", *Astrophys. J. Supp. Series*, **59**, 433.

Cartledge, N.P.: 1995, "External and Internal Magnetohydrostatic Models of Quiescent Solar Prominences ", PhD Thesis, University of St. Andrews.

Cartledge, N.P., van Ballegooijen, A.A. and Priest, E.R.: 1997, "Origins of the Axial Magnetic Field in Prominences", in preparation.

Demoulin, P., Henoux, J. C. and Mandrini, C. H.: 1992, "Development of a Topological Model for Solar Flares", *Solar Phys.*, **139**, 105.

Demoulin, P., van Driel-Gesztelyi, L., Schmieder, B., Henoux, J. C., Csepura, G. and Hagyard, M. J.: 1993, "Evidence for Magnetic Reconnection in Solar Flares" , *Astron. and Astro.* , **271**, 292.

Engvold, O.: 1976, "The fine Structure of Prominences", *Solar Phys.*, **49**, 283.

Engvold, O.: 1987, "Prominence Environment" in Dynamics and Structure of Solar Prominences (eds. J.L. Ballester and E.R. Priest), 51.

Fielder, R.A.S. and Hood, A.W.: 1993, "The effect of Shear on Normal Polarity Prominences",

Solar Phys., **147**, 297.

Finn, J.M., Guzdar, P.N. and Usikov, D.: 1994, "Three-Dimensional Force-Free Looplike Magnetohydrodynamic Equilibria", *Astrophys. J.* , **427**, 475.

Foukal, P.: 1971, "Morphological relations in the chromospheric Hα fine structure", *Solar Phys.*, **19**, 59.

Gaizauskas, V.: 1976, "The Ottawa River Solar Observatory", *R.A.S.C. JOUR.*, **70**, 1.

Gaizauskas, V., Harvey, K.L., Harvey, J.W. and Zwaan, C.: 1983, "Large Scale Patterns Formed By Solar Active Regions During the Ascending Phase of Cycle 21", *Astrophys. J.*, **265**, 1056.

Gaizauskas, V., Zirker, J., Sweetland C. and Kovacs A.: 1997, "Formation of a Solar Filament Channel", *Astrophys. J.*, **479**, 448.

Gaizauskas, V. and Zwaan, C.: 1997, "Why and Where Do Filaments Form In Active Regions", in preparation.

Galsgaard, K., and Longbottom, A.W.: 1997, "Are Filaments Formed by the Convergence of Flux", in preparation.

Harvey, K.L. and Harvey, J.W.: 1973, "Observations of Moving Magnetic Features Near Sunspots ", *Solar Phys.*, **28**, 61.

Harvey, K.L.: 1994, "Irradiance Models Based on Solar Magnetic Fields", IAU Colloquium No. 143, "The Sun as a Variable Star: Solar and Stellar Irradiance Variations", eds. Pap, J. *et al.*

Hood, A.W.: 1992, "Instabilities in the Solar Corona", *Plasma Physics and Controlled Fusion*, **34.4** , 411.

Kippenhahn, R. and Schluter, A.: 1957, "Eine Theorie der Solaren Filamente", *Zs. Ap.*, **43**, 36.

Kuperus, M. and Raadu, M.A.: 1974, "The support of prominences formed in neutral sheets ", *Astron. Astrophys.*, **31**, 189.

Kuperus, M.: 1996, "The Double Inverse Polarity Paradigm", *Solar Phys.*, **169**, 349.

Leroy, J.L., Bommier, V. and Sahal-Brechot, S.: 1983, "The magnetic field in the Prominences of the Polar Crown", *Solar Phys.*, **83**, 135.

Leroy, J.L.: 1989, "Observations of prominence magnetic fields", in *Dynamics and Structure of Quiescent Solar Prominences* (ed. E.R. Priest), 77.

Longbottom, A.W., Fiedler R.A.S. and Rickard, G.J.: 1997, "On some Practical Aspects of Multigrid Methods In Obtaining Three-Dimensional Coronal Equilibrium Solutions", *Astron. Astrophys. Supp.*, submitted.

Low, B.C. and Hundhausen, J.R.: 1995, "Magnetostatic structures of the solar corona. II. The magnetic topology of quiescent prominences", *Astrophys. J.*, **443**, 818.

M^{c}Allister, A. , Mackay, D.H. and Hundhausen, J.R.: 1997, "The Skew of Polar Crown X-ray Arcades", in preparation.

Mackay, D.H. and Priest, E.R.: 1996, "Potential Field Models of a Sinistral or Dextral Filament Channel", *Solar Phys.*, **167**, 281.

Mackay, D.H. , Gaizauskas, V. , Rickard, G.J. and Priest, E.R.: 1997a, "Force Free and Potential Models of a Filament Channel In Which a Filament Forms", *Astrophys. J*, **486**.

Mackay, D.H., Priest, E.R., Gaizauskas, V. and van Ballegooijen, A.A.: 1997b, "Role of Helicity in the Formation of Intermediate Filaments", *Solar Phys.*, submitted.

Malherbe, J.M., Schmieder, B., Ribes, E. and Mein, P.: 1983, "Dynamics of Solar Filaments", *Astron. Astrophys.* , **119**, 197.

Malherbe, J.M.: 1989, " The Formation of Solar Prominences" in *Dynamics and Structure of Quiescent Solar Prominences* (ed. E.R. Priest), 115.

Marsh, G.E.: 1996, "Force-Free Magnetic Fields; Solutions, Topology and Applications.", World Scientific, Singapore.

Martin, S.F.: 1973, "The Evolution of Prominences and their Relationship to Active Centres ", *Solar Phys.*, **31**, 3.

Martin, S.F., Livi, S.H.B. and Wang, J.: 1985, "The cancellation of magnetic flux. II. In a decaying active region", *Aust. J. Phys.*, **38**, 929.

Martin, S.F.: 1986, "Recent observations of the formation of filaments", *Coronal and*

Prominence Plasmas (ed A. Poland) NASA CP 2442, 73.

Martin, S.F.: 1990, "Conditions for the formation of prominences as inferred from optical observations" in *Dynamics of Quiescent Prominences, Proc. IAU Colloq. 117, Lecture Notes in Physics* 363, Springer-Verlay, New York, 1.

Martin, S.F., Bilimoria, R. and Tracadas, P.W.: 1995, "Magnetic field configurations basic to filament channels and filaments" in *Solar Surface Magnetism*, R.J. Rutten and C.J. Schrijver (eds.), Springer-Verlag, New York, 303.

Martin, S.F. and M^{c}Allister, A.H.: 1995, "The Skew of X-ray Coronal Loops Overlying H-alpha Filaments", BAAS, **27**, 961.

Martres, M.J., Mein, P., Schmeider, B. and Soru-Escaut, I.: 1981, "Structure and Evolution of Velocities in Quiescent Filaments", *Solar Phys.*, **69**, 301.

Morse, P. M. and Feshbach, H.: 1953, *Methods in Theoretical Physics*, M^{c}Graw-Hill, New York, p.1767.

Nakagawa, Y., Raadu, M. A., Billings, D. E. and M^{c}Namera, D.: 1971, "On the Topology of Filaments and Chromospheric Fibrils ", *Solar Phys.*, **19**, 72.

Nakagawa, Y. and Raadu, M.A.: 1972, "On the Practical Representation of Magnetic Fields ", *Solar Phys.*, **25**, 127.

Nakagawa, Y., Raadu, M.A. and Harvey, J.W.: 1973, "The Topological Association of Hα Structures and Magnetic Fields ", *Solar Phys.*, **30**, 421.

Narain, U. and Ulmschneider, P., Chromospheric and Coronal Heating Mechanisms, Space SCIENCE REVIEW **54**, 377

Parnell, C.E.: 1994, "Models of X-Ray Bright Points and Cancelling Magnetic Features", PhD Thesis, University of St. Andrews.

Pevstov, A.A., Canfield, R.C. and Metcalf, T.R.: 1994, "Patterns of Helicity in Solar Active Regions", *Astrophys. J.*, **435**, L117.

Pevstov, A.A., Canfield, R.C. and Metcalf, T.R.: 1995, " Latitudinal Variations of Helicity of

Photospheric Magnetic Fields", *Astrophys. J.*, **440**, L109.

Philips, K.J.H.: 1995, "Guide to the Sun", Cambridge University Press.

Poland, A.I. and Mariska, J.T.: 1986, "A Syphon Mechanism for Supplying Prominence Mass", *Solar Phys.*, **104**, 303.

Priest, E.R.: 1982, *Solar Magnetohydrodynamics*, Reidel, Dordrecht, Holland.

Priest, E.R.: 1989, *Dynamics and Structure of Quiescent Solar Prominences*, Kluwer, Dordrecht, Holland.

Priest, E.R., Hood, A.W. and Anzer, U.: 1989, "A Twisted Flux Tube Model for Solar Prominences", *Astrophys. J.* **344**, 1010.

Priest, E.R. , Van Ballegooijen, A.A. and Mackay, D.H.: 1995, "A model for dextral and sinistral prominences", *Astrophys. J.*, **460**, 530.

Querfield, C.W., Smartt, R.N., Bommier, V., Landi Degl'innocenti, E. and House, L.L.: 1985, "Vector Magnetic Fields in Prominences", *Solar Phys.*, **96**, 277.

Raadu, M. A. and Nakagawa, Y.: 1971, "The Topology of Force-Free Magnetic Fields Near Bipolar Sunspots ", *Solar Phys.*, **20**, 64.

Richardson, R.S.: 1941, "The Nature of Solar Hydrogen Vortices", *Astrophys. J*, **93**, 24.

Rust, D.M. and Kumar, A.: 1995, "Helical Magnetic Fields in Filaments", *Solar Phys.*, **155**, 69.

Solberg, F.C.R. and M^{c}Allister, A.: 1997. "Axial Soft X-ray Brightenings Associated with Hα Filaments" in *New perspectives on Solar Prominences*, IAU Colloqiuim 167, ASP.

Schmieder, B., Malherbe, J.M., Poland, A.I. and Simon, G.: 1985, "Dynamics of Solar Filaments", *Astron. Astrophys.* , **153**, 64.

Schmieder, B.: 1989, "Overall Properties and Steady Flows" in *Dynamics and Structure of Quiescent Prominences, Proc. IAU Colloq. 117, Lecture Notes in Physics* 363, Springer-Verlay, New York, p1.

Schmieder, B., Demoulin, P., Aulanier, G. and Golub, L.: 1996, "Differential Magnetic Field Shear in an Active Region", *Astrophys. J.*, **467**, 881.

Schrijver, C.J.: 1987, "Solar Active Regions: radiative intensities and large-scale parameters of the magnetic field", *Ast. and Astro.*, **180**, 241.

Tandberg - Hansen, E.: 1974, *Solar Prominences*, Reidel, Dordrecht, Holland.

Tang, F.: 1987, "Quiescent Prominences-Where are they Formed", *Solar Phys.*, **107**, 233.

van Ballegooijen, A.A. and Martens, P.C.H.: 1989, "Formation and Eruption of Solar Prominences", *Astrophys. J*, **361**, 283.

van Ballegooijen, A.A. and Martens, P.C.H.: 1990, "Magnetic Fields in Quiescent Prominences", *Astrophys. J*, **343**, 917.

van Ballegooijen, A.A., Cartledge, N.P., and Priest, E.R.: 1997, "Magnetic Flux Transport and the Formation of Filament Channels on the Sun", *Astrophys. J.*, accepted.

Verwichte, E.: 1997, PhD thesis, University of St. Andrews. in preparation.

Wang, Y.M. and Sheeley, N.R.: 1991, "Magnetic Flux Transport and the Suns Dipole Moment: New Twists to the Babcock-Leighton Model", *Astrophys. J* , **375**, 761.

Wesson, J.: 1987, "Tokamaks" , Oxford Engineering Science Series, Oxford Science Publications.

Zirin, H.: 1988, "Astrophysics of the Sun", Cambridge University Press.

Zirker, J.B.: 1993, "Coronal Heating", *Solar Phys.*, **148**, 43.

Zirker, J.B., Martin, S.F., Harvey, K. and Gaizauskas, V.: 1997, "Global Magnetic Patterns of Chirality", *Solar Phys.*, accepted.